

***Metal Nanohole Arrays: From Self-Assembly to  
Light-Harvesting***

DISSERTATION

zur Erlangung des akademischen Grades eines  
Doktors der Naturwissenschaften (Dr. rer. nat.)  
an der Fakultät für Biologie, Chemie und Geowissenschaften  
der Universität Bayreuth

vorgelegt von

***Christian Stelling***

aus *Pfaffenhofen*

Bayreuth, 2018



Die vorliegende Arbeit wurde in der Zeit von 01/2014 bis 02/2018 in Bayreuth am Lehrstuhl Physikalische Chemie I unter Betreuung von Herrn Professor Dr. Markus Retsch angefertigt.

Vollständiger Abdruck der von der Fakultät für Biologie, Chemie und Geowissenschaften der Universität Bayreuth genehmigten Dissertation zur Erlangung des akademischen Grades eines Doktors der Naturwissenschaften (Dr. rer. nat.).

Dissertation eingereicht am: 22. Februar 2018

Zulassung durch die Promotionskommission: 21. März 2018

Wissenschaftliches Kolloquium: 09. Oktober 2018

Amtierender Dekan: Prof. Dr. Stefan Peiffer

Prüfungsausschuss:

Prof. Dr. Markus Retsch (Gutachter)

Prof. Dr. Mukundan Thelakkat (Gutachter)

Prof. Dr. Birgit Weber (Vorsitz)

Jun.-Prof. Dr. Anna Schenk



# Table of Contents

Summary.....	5
Zusammenfassung .....	9
1 Introduction.....	13
1.1 Self-Assembly of Colloidal Particles in Two Dimensions.....	16
1.2 Nanosphere Lithography .....	24
1.3 Surface Plasmon Polaritons .....	30
1.3.1 The Drude Theory of Metals.....	30
1.3.2 Bound Electromagnetic Waves .....	32
1.3.3 Nanohole Arrays .....	38
1.4 Colloidal Light Management in Thin-Film Photovoltaics.....	44
2 Overview of the Thesis .....	67
2.1 Graphical Table of Content .....	84
2.2 Contributions to Joint Publications.....	87
3 Subwavelength Etched Colloidal Monolayers: A Model System for Tunable Antireflective Coatings .....	93
3.1 Introduction.....	94
3.2 Results and Discussion .....	96
3.3 Conclusion .....	103
3.4 Experimental Section.....	104
3.5 Supporting Information .....	108
4 Vibrational Dynamics of a Two-Dimensional Microgranular Crystal .....	113
4.1 Introduction.....	114
4.2 Methodology.....	115
4.3 Contact-Based Modes .....	118
4.4 Spheroidal Vibrational Modes .....	121
4.5 Conclusion .....	124
4.6 Appendices .....	127
5 Ordered Particle Arrays via a Langmuir Transfer Process: Access to Any Two-Dimensional Bravais Lattice .....	131
5.1 Introduction.....	132
5.2 Results and Discussion .....	134
5.3 Conclusion .....	141
5.4 Experimental Section.....	142
5.5 Supporting Information .....	146

6	Showing Particles their Place: Deterministic Colloid Immobilization by Gold Nanomeshes.....	151
6.1	Introduction.....	152
6.2	Results and Discussion.....	154
6.3	Conclusion.....	166
6.4	Experimental Section.....	167
6.5	Supporting Information.....	173
7	Nanomeshes at Liquid Interfaces: From Free-Standing Hole Arrays toward Metal-Insulator-Metal Architectures.....	183
7.1	Introduction.....	184
7.2	Results and Discussion.....	186
7.3	Conclusion.....	193
7.4	Experimental Section.....	193
7.5	Supporting Information.....	198
8	Surface Plasmon Modes of Nanomesh-on-Mirror Nanocavities Prepared by Nanosphere Lithography.....	199
8.1	Introduction.....	200
8.2	Results and Discussion.....	201
8.3	Conclusion.....	210
8.4	Experimental Section.....	210
8.5	Supporting Information.....	215
9	Plasmonic Nanomeshes: Their Ambivalent Role as Transparent Electrodes in Organic Solar Cells.....	223
9.1	Introduction.....	224
9.2	Results and Discussion.....	227
9.3	Conclusion.....	241
9.4	Experimental Section.....	242
9.5	Supplementary Information.....	249
10	Outlook.....	261
	List of Publications.....	263
	List of Contributions.....	265
	Danksagung.....	267
	(Eidesstattliche) Versicherungen und Erklärungen.....	269

## Summary

This thesis is dedicated to progress in the field of colloidal self-assembly and colloidal crystals as well as their potential application for the preparation of transparent, conducting electrodes. Colloidal crystals are periodic structures formed by particles with dimensions between 1 nm and 1  $\mu\text{m}$  and are widely used for the preparation of functional surfaces with tailored physical properties. Their application requires the fast production of large-area, homogeneous structures with nanometer-sized features and minimal defect-densities. Colloidal self-assembly meets these expectations and offers a rapid and cost-effective fabrication of periodic patterns by employing the intrinsic properties of the single particles.

This thesis is divided into three parts, which present contributions to (I) the defined self-assembly of polymer particles and the properties of particle monolayers (chapters 3 - 5), (II) the directed self-assembly of polymer colloids into gold nanohole arrays (chapter 6), and (III) the fabrication of optical devices based on gold nanohole arrays (chapters 7 - 9). For this purpose, the self-assembly of spherical polystyrene particles with diameters between 0.1  $\mu\text{m}$  and 2.5  $\mu\text{m}$  was induced at the water/air interface, which yields purely two-dimensional colloidal crystals with large single-crystalline domains.

In chapter 3, I analyzed the optical properties of colloidal monolayers with subwavelength-scale particle diameters ( $< 0.2 \mu\text{m}$ ). These monolayers can be regarded as an effective medium and can act as single-layer antireflective coatings. Thereby, the effective refractive index of the coating and the wavelength of maximum transmittance can be adjusted independently. This supplements the optical characterization of colloidal particle arrays with the properties of monolayers with subwavelength-sized particles.

Based on the exceptionally high long-range order of the colloidal crystal, collective vibrational modes were detected for the first time across the entire Brillouin zone in a monolayer of large polystyrene spheres (1.5  $\mu\text{m}$ ) (chapter 4). An analytical model was developed, which well describes the experimental results, taking into account the particle-particle and particle-substrate contacts.

Usually, colloidal assembly methods yield hexagonal, close-packed particle monolayers limiting the variety of structures attainable with colloidal self-assembly. In chapter 5, I demonstrated the fabrication of non-close-packed particle arrays with symmetries of all possible two-dimensional Bravais lattices starting from hexagonal, close-packed monolayers

floating at the water/air interface. As the monolayers are purely one-dimensionally stretched upon transfer onto hydrophobic substrates, this presents a scalable method for the preparation of colloidal crystals with arbitrary lattice symmetry.

Via colloidal lithography, the structures generated by colloidal particles can be replicated into various materials. In chapter 6, I used gold nanohole arrays, prepared by colloidal lithography, as templates for the directed self-assembly of polymer colloids. Exploiting a tailored surface charge contrast with feature sizes in the range of the single particles, negatively charged polymer particles were site-selectively trapped from the bulk dispersion, forming non-close-packed particle monolayers. Thus, hierarchical structures are accessible with high structural control over large areas.

Nanohole arrays in thin metal films, prepared by colloidal lithography, offer a versatile platform for optically active surfaces that support surface plasmon polaritons (SPP). These SPP resonances, collective oscillations of the conduction band electrons, efficiently couple to incident light due to the periodic perforation of the metal film and are easily tunable by adjusting the nanoscale geometry. Therefore, nanohole arrays are highly attractive as an electrode material for solar cells.

A drawback of employing colloidal lithography for the fabrication of metal nanohole arrays is that it is limited to few substrate materials due to the inherent plasma etching step. By introducing a plasma-stable sacrificial layer, the transfer of nanohole arrays onto arbitrary substrates via the water/air interface was shown (chapter 7). This broadens the fabrication flexibility considerably and enables the preparation of plasmonic metal-insulator-metal multilayers and free-standing nanohole arrays.

The optical properties of these multilayers were drastically altered compared to the single layer nanohole array, which was in good agreement with numerical and analytical models (chapter 8). This detailed analysis of the optical effects occurring in nanoscale materials is essential for the specific manipulation of light in potential applications.

Finally, I integrated gold nanohole arrays into polymer solar cells as transparent, conducting electrodes (chapter 9). A cavity SPP, confined between the nanohole array electrode and the silver back-electrode, was observed and increased the power conversion efficiency at the absorption edge of the photoactive polymer. However, the nanohole arrays exhibited high losses due to reflection and absorption in the gold layer leading to an overall lower efficiency compared to indium tin oxide reference electrodes.

Altogether, the interface-assisted self-assembly of colloidal polystyrene particles was used to prepare functional surface patterns on a macroscopic scale. This thesis revealed fundamental optical and acoustic properties of self-assembled colloidal crystals and considerably extended the range of structures attainable with colloidal self-assembly. Furthermore, the complex optical properties of gold nanohole arrays, integrated into metal-insulator-metal absorbers as well as organic solar cells, were investigated.



## Zusammenfassung

Diese Arbeit behandelt Fortschritte auf den Gebieten der kolloidalen Selbstanordnung und kolloidalen Kristalle sowie deren mögliche Anwendung zur Herstellung von transparenten Elektroden. Kolloidale Kristalle sind periodische Strukturen aus Partikeln mit einer Größe zwischen 1 nm und 1  $\mu\text{m}$  und werden zur Herstellung funktionaler Oberflächen mit definierten physikalischen Eigenschaften verwendet. Voraussetzung für die praktische Anwendung kolloidaler Kristalle ist die Möglichkeit Strukturen im Nanometer-Bereich großflächig, homogen und mit minimaler Defektdichte herstellen zu können. Das Verfahren der kolloidalen Selbstanordnung erfüllt diese Voraussetzung indem es die intrinsischen Eigenschaften der einzelnen Kolloidpartikel ausnutzt.

Diese Dissertation ist in drei Teile gegliedert und enthält Beiträge zu (I) der definierten Selbstanordnung von Polymerpartikeln und den Eigenschaften von Partikelmonolagen (Kapitel 3 - 5), (II) der hierarchischen Anordnung von Polymerpartikeln in Lochgittern (Kapitel 6) und (III) der Herstellung optischer Bauelemente basierend auf Goldlochmasken (Kapitel 7 - 9). Für diese Arbeit wurden rein zweidimensionale kolloidale Kristalle mit großen, einkristallinen Domänen verwendet. Diese wurden durch die Selbstanordnung von sphärischen Polystyrolpartikeln mit Durchmessern zwischen 0.1  $\mu\text{m}$  und 2.5  $\mu\text{m}$  an der Wasser/Luft-Grenzfläche gebildet.

In Kapitel 3 untersuchte ich die optischen Eigenschaften kolloidaler Monolagen mit Partikeldurchmessern unterhalb der Wellenlänge des sichtbaren Lichts ( $< 0.2 \mu\text{m}$ ). Diese Monolagen können als effektives Medium betrachtet werden und fungieren als Antireflexbeschichtung. Der effektive Brechungsindex der Beschichtung und die Wellenlänge mit den optimalen Antireflexeigenschaften können dabei unabhängig voneinander eingestellt werden. Dies ergänzt die bekannten, optischen Eigenschaften kolloidaler Kristalle mit den Eigenschaften von Partikelmonolagen mit Partikeldurchmessern, die unterhalb der betrachteten Wellenlänge liegen.

Aufgrund der außergewöhnlich langreichweitigen Ordnung der kolloidalen Kristalle wurden in Monolagen aus großen Polystyrolpartikeln (1.5  $\mu\text{m}$ ) zum ersten Mal kollektive Vibrationsmoden in der gesamten Brillouin-Zone detektiert (Kapitel 4). Die experimentellen Daten konnten durch ein analytisches Modell, welches die Partikel-Partikel- sowie die Partikel-Substrat-Kontakte berücksichtigt, gut beschrieben werden.

Kolloidale Selbstanordnungsverfahren ergeben normalerweise hexagonal dicht gepackte Partikelmonolagen. Dadurch ist die Zahl der Strukturen, die über kolloidaler Selbstanordnung erreicht werden können, stark eingeschränkt. In Kapitel 5 zeigte ich die Herstellung nicht dicht gepackter Partikelmonolagen mit Symmetrien aller möglichen zweidimensionalen Bravaisgitter, ausgehend von hexagonal dicht gepackten Monolagen an der Wasser/Luft-Grenzfläche. Da diese beim Übertrag auf hydrophobe Substrate ausschließlich eindimensional verstreckt werden, stellt dies eine einfache und skalierbare Methode zur Herstellung von Kolloidkristallen mit beliebiger Gittersymmetrie dar.

Mit Hilfe der Kolloidlithographie können durch Kolloidpartikel erstellte Strukturen in zahlreiche Materialien überführt werden. In Kapitel 6 verwendete ich durch Kolloidlithographie hergestellte Goldlochmasken als Überstruktur zur gerichteten Anordnung kolloidaler Polymerpartikel. Dazu wurde auf dem Substrat gezielt ein Kontrast in der Oberflächenladung in der Größenordnung der Partikel erzeugt. Anschließend konnten negativ geladene Partikel einer Polymerdispersion selektiv in der Templatstruktur adsorbiert werden und bildeten nicht dicht gepackte Partikelmonolagen. Dies ermöglicht die Herstellung großflächiger, hierarchischer Strukturen.

Geordnete Lochstrukturen in dünnen Metallfilmen sind außerdem ein vielseitiger Baustein für optisch aktive Oberflächen, die Oberflächenplasmonen nutzen. Oberflächenplasmonen sind kollektive Oszillationen der Leitungsbandelektronen, welche aufgrund der periodischen Struktur des Metallfilms durch eingestrahktes Licht angeregt werden können. Die Eigenschaften der Oberflächenplasmonen sind dabei durch die geometrischen Parameter der Nanostruktur bestimmt. Deshalb sind per Kolloidlithographie hergestellte Lochmasken attraktive Kandidaten als Elektrodenmaterial für Solarzellen.

Ein Nachteil der Kolloidlithographie besteht in der geringen Auswahl an verfügbaren Substraten aufgrund der inhärenten Plasmabehandlung während der Strukturbildung. Indem eine plasmastabile Opferschicht eingefügt wurde, konnte der Übertrag von Lochmasken auf beliebige Substrate über die Wasser/Luft-Grenzfläche gezeigt werden (Kapitel 7). Dies erhöht die Zahl der möglichen Strukturen beträchtlich und ermöglicht die Herstellung plasmonisch aktiver Metall-Isolator-Metall Multilagen sowie freistehender Lochmasken.

Die optischen Eigenschaften dieser Multilagen unterscheiden sich stark von denen der einlagigen Lochmasken, was durch numerische und analytische Modelle bestätigt wurde

(Kapitel 8). Solch detaillierte Untersuchungen der optischen Effekte in derartigen nanoskaligen Materialien sind für potentielle Anwendungen unablässig.

Schließlich integrierte ich Goldlochmasken als transparente Elektrode in Polymer-Solarzellen (Kapitel 9). Ein Oberflächenplasmon, lokalisiert zwischen der Lochmaske und der rückseitigen Silberelektrode, erhöhte die Effizienz der Solarzelle an der Absorptionskante des fotoaktiven Polymers. Allerdings führten die gleichzeitig auftretenden, hohen Verluste aufgrund der Reflexion der Goldschicht und der Absorption in der Goldschicht zu einer insgesamt niedrigeren Effizienz verglichen mit den Referenzelektroden aus Indiumzinnoxid.

Zusammenfassend wurde die Selbstanordnung von kolloidalen Polystyrolpartikeln an der Wasser/Luft-Grenzfläche zur Herstellung makroskopischer, funktionaler Oberflächenstrukturen verwendet. Diese Arbeit enthüllte dabei fundamentale optische und akustische Eigenschaften selbstangeordneter kolloidaler Kristalle und vergrößerte die Bandbreite der Strukturen, welche durch die Selbstanordnung von Kolloiden verwirklicht werden können. Außerdem wurden die komplexen optischen Eigenschaften von Goldlochmasken in Metall-Isolator-Metall Absorbern und organischen Solarzellen untersucht.



## 1 Introduction

The term nanotechnology has attracted tremendous attention during the last decade, not only in the respective scientific areas but also in public life. Regularly present in mass media, nanotechnology is often praised for revolutionizing the world as we know it today. Futuristic images are drawn showing incredible possibilities such as miniaturized machines traveling through our blood vessels to fight diseases.<sup>1</sup> Others visualize a lift leaving the earth atmosphere ascending along cables consisting of carbon nanotubes.<sup>2</sup>

Although these scenarios remain science-fiction, many applications indeed already entered our daily life. They range from transistors with features only a few nanometers in size,<sup>3</sup> quantum dot emitters enhancing the brightness in liquid crystal displays,<sup>4</sup> self-cleaning surfaces,<sup>5</sup> antibacterial clothing<sup>6</sup> to light-absorbing particles in sunscreens.<sup>7</sup>

Nanotechnology is highly interdisciplinary, covering several fields of science including physics, chemistry, and biology as well as material science and engineering. The criterion combining these fields under the term nanotechnology is merely the dimension of the structures that are used. According to the definition of the International Organization for Standardization (ISO), nanotechnology explores materials with at least one dimension typically, but not necessarily, being below 100 nm.<sup>8</sup>

In this size range, the properties of materials can be significantly different from those of the bulk materials.<sup>9</sup> The surface to volume ratio drastically increases when decreasing the structure dimensions, changing, for example, the catalytic properties of a material. Additionally, the small size leads to an electronic confinement giving rise to strongly size-dependent quantum effects, which influence properties such as color or conductivity.

A fast progressing subfield within nanotechnology is nanophotonics and more specific plasmonics. Nanophotonics studies the manipulation of light by objects on the nanometer scale. With its help, new applications are developed in the fields of microscopy, lighting or lasers. Plasmonics more specifically studies the interaction of light with nanometer-sized metal structures. When metal structures of deep-subwavelength dimensions are excited at resonance, collective oscillations of electrons arise.<sup>10</sup> These oscillations result in a substantial absorption and scattering of the incident light. Consequently, plasmonic structures are already used in several applications such as plasmonic sensors<sup>11,12</sup> or surface enhanced Raman spectroscopy.<sup>13</sup> Furthermore, plasmonic structures are discussed as waveguiding materials for optical circuits with nanometer-sized features,<sup>14</sup> color filtering,<sup>15-19</sup> drug-delivery<sup>20</sup> or nanometer-sized lasing

devices.<sup>21-23</sup> In optoelectronic devices like photodetectors, light emitting diodes or solar cells plasmonic structures might increase the conversion efficiency.<sup>24-27</sup>

The recent progress in the field of nanotechnology, and plasmonics in particular, is benefitted by advances in fabrication and characterization techniques with nanometer resolution, which were mainly driven by the miniaturization in the semiconductor industry. Extraordinary high control over size, shape, orientation, and arrangement of the nanostructures is vital to achieve the desired properties.<sup>28,29</sup> Applying top-down lithographic approaches like electron beam lithography, interference lithography or focused-ion-beam milling arbitrary nanostructures can be deliberately designed with high precision.<sup>30,31</sup> At the same time, characterization methods like transmission electron microscopy or atomic force microscopy have further advanced, now being able to study matter in the sub-nanometer regime.<sup>32-34</sup>

Top-down lithographic methods start from the bulk material, “writing” the desired structure into the material. However, these techniques suffer from several severe limitations. Sophisticated equipment is needed for the processes, which often need a high vacuum (electron beam lithography, focused-ion-beam milling). Moreover, the processes are very time-consuming and thus hardly scalable, leading to high production costs. Finally, lithographic processes are still limited in resolution. Thus, alternative techniques for the large-scale, high-resolution fabrication of nanostructures is still subject to intensive research.

In contrast, solution processed bottom-up approaches could offer a fast, cost-effective and large-scale production of nanomaterials.<sup>35</sup> Bottom-up approaches rely on the fabrication of structures starting from smaller building blocks such as atoms, molecules or particles. For this, the building blocks are combined into larger structures using self-assembly or self-organization strategies exploiting the intrinsic properties of the individual building blocks. Further control can be achieved using directed self-assembly methods providing a templating structure, which defines the dimensions of the self-assembled structure.<sup>36</sup> Nevertheless, self-assembly methods still suffer from a lack of reproducibility and precision regarding the structural control and defect density.

In this work, the fabrication and characterization of photonic and plasmonic surfaces by colloidal means is described. In the beginning, the theoretical background is summarized, starting with the principal self-assembly concepts for colloidal particles (chapter 1.1). Following this, the technique of nanosphere lithography is introduced in chapter 1.2 as a simple bottom-up approach towards nanostructured surfaces. In chapter 1.3 the fundamentals of surface plasmon polaritons are briefly covered followed by a brief description of the optics of

gold nanohole arrays. Chapter 1.4 gives insight into the application of colloids for light management purposes in optoelectronic devices including dielectric and plasmonic particles as well as structures prepared by colloidal lithography. On this basis, the main results of this thesis and its integration into the field of research are reviewed in chapter 2. In this context, the contribution of all authors is outlined. In the second part of the thesis, the publications are presented in detail (chapter 3 - 9). Finally, the future perspectives of colloidal self-assembly strategies for optical devices are discussed.

## 1.1 Self-Assembly of Colloidal Particles in Two Dimensions

According to the IUPAC definition, colloids are objects dispersed in a medium with at least one dimension in between 1 nm and 1  $\mu\text{m}$ .<sup>37</sup> In this size range the interaction forces and dynamics are ranged in between those of single molecules and macroscopic objects. While still being subject to Brownian motion, the particles are already affected by gravitational forces, which are strongly dependent on the size and density of the particles.<sup>38</sup> Thus colloidal systems are usually metastable, and phase separation only takes place on a relatively large time scale. Due to the complex interaction of forces in this so-called “mesoscale”, colloidal particles can self-assemble into ordered structures. These have been named “colloidal crystals” because of their resemblance to atomic crystal structures.

The interactions present in colloidal systems and thus the ability to self-assemble thereby are highly sensitive towards the size, shape, and uniformity of the dispersed particles. Especially, an extremely high uniformity is a prerequisite for the preparation of highly ordered colloidal assemblies. Consequently, a vast variety of synthesis methods has been developed to obtain highly monodisperse colloids. Polymerization methods including emulsion polymerization,<sup>39-41</sup> dispersion polymerization,<sup>42</sup> precipitation polymerization<sup>43</sup> or suspension polymerization<sup>44</sup> readily yield spherical polymer particles. Analogously, sol-gel synthesis<sup>45</sup> or particle formation via the reduction of ionic precursors<sup>46</sup> are used to obtain inorganic colloids.

Colloidal crystals are widely used for the preparation of functional surfaces featuring an immense range of applications. Particle arrays on solid substrates have been used to generate self-cleaning<sup>5,47</sup> or antireflective properties,<sup>48-50</sup> as well as to tune wettability.<sup>51</sup> Using nanosphere lithography, complex nanostructures can be prepared in various materials starting from self-assembled colloids.<sup>52</sup> The possibility to create structures with periodic changes in refractive index in the wavelength range of visible light fosters unique optical properties like waveguiding<sup>53</sup> or photonic band gaps.<sup>54,55</sup> The emergence of photonic band gaps readily results in structural colors<sup>56-58</sup> and is regularly exploited for sensing applications.<sup>59,60</sup> Similarly, regular arrangements can be used to control the propagation of mechanical waves inside the colloidal crystal.<sup>61,62</sup> Moreover, two-dimensional colloidal crystals can be used to study defect formation in crystalline structures.<sup>63,64</sup>

The wide range of applications leads to the development of myriads of assembly methods for two-dimensional colloidal crystals, which are discussed in plenty of reviews.<sup>35,36,65</sup> As a straightforward technique for the preparation of large-area monolayers, the dry assembly of

spherical polymer colloids by rubbing was described.<sup>66</sup> However, most assembly methods start from particles dispersed in a liquid medium. Here, multiple forces are acting simultaneously. Achieving control over the complex forces interacting thereby is essential for high quality, defect-free assemblies.

In the bulk phase, colloidal particles are mainly stabilized by Coulomb interactions and steric stabilization. Coulomb interactions act between charged particles. Owing to their high surface area, colloidal particles usually are highly charged in polar, liquid media due to ion adsorption or the dissociation of functional groups. Thus, Coulomb interactions are one of the most important forces for colloidal systems. For like-charged particles, the electrostatic potential is repulsive preventing particle agglomeration. Quantitatively, the potential is given by the Poisson-Boltzmann equation. Analogously to capacitors, the Poisson-Boltzmann equation describes the electrical potentials of ions accumulated in a double-layer near the surface of the charged particles.<sup>67</sup> Directly derived from the Poisson-Boltzmann equation, the Debye length provides the length scale of electrostatic repulsion. At a distance from the charged interface equal to the Debye length, the potential decays to  $1/e$  of the potential at the interface. The Debye length is inversely proportional to the square root of the ionic strength in the medium. Therefore, increasing the ionic strength decreases the Debye length and thus the electrostatic stabilization of the colloid.

Attractive van-der-Waals forces counteract the repulsive forces and favor particle agglomeration once the particles are in contact. The interplay of electrostatic interactions and van-der-Waals forces is described by the DLVO theory, a fundamental theory of colloidal stability (Figure 1.1a).<sup>68,69</sup> In DLVO theory, the net attractive or repulsive potential depending on the distance between two particles is derived from the sum of electrostatic and van-der-Waals forces. This results in a global minimum at small interparticle distances and a second minimum at larger distances resulting from attractive van-der-Waals forces. At intermediate distances, the electrostatic repulsion dominates. To attain a high degree of order, controlling the balance of repulsive and attractive interactions is vital. The repulsive interactions at intermediate distances act as an energy barrier impeding the random aggregation of particles, stabilizing only the minimum free-energy position with a maximum of adjacent particles, which is within the (hexagonal) lattice. A more detailed insight into the interaction forces in liquid systems is given in several articles.<sup>36,67,70</sup>

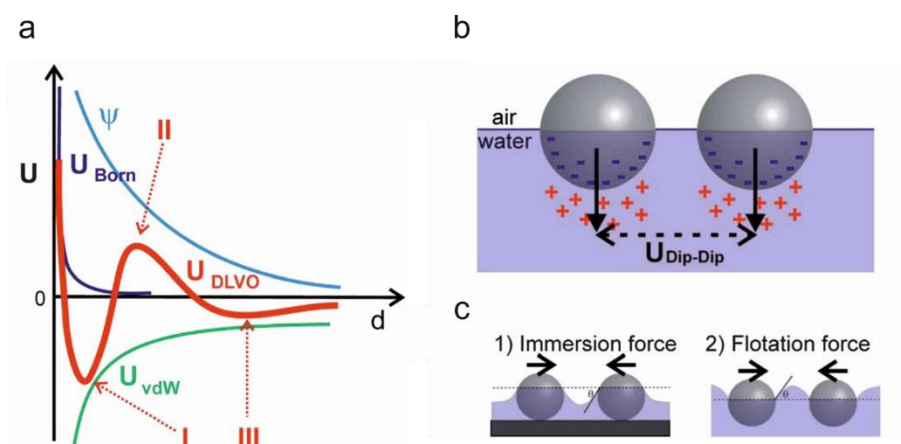


**Figure 1.1.** Forces acting in the colloidal regime. (a) Potential  $U$  vs. interparticle distance  $d$  plot of the forces relevant for the DLVO theory: The interaction of repulsive electrostatic forces ( $\Psi$ ) and attractive van-der-Waals forces ( $U_{\text{vdW}}$ ) results in a net force ( $U_{\text{DLVO}}$ ) comprising a global minimum at small interparticle distances (I), a net repulsion at intermediate distances (II) and a minimum at larger distances (III). The Born potential ( $U_{\text{Born}}$ ) prevents particle overlapping. (b) The symmetric dissociation of ionic groups on the surface of particles trapped at the interface induces a repulsive dipole force. (c) Immersion capillary forces and flotation capillary forces of particles sitting at the interface. Reproduced from Ref. 35 with permission from The Royal Society of Chemistry.

The colloidal stability can be further influenced by additional forces. Apart from electrostatic interactions, colloids can be stabilized sterically by large polymer ligands.<sup>71,72</sup> Moreover, the addition of dissolved polymers or smaller particles can yield attractive flocculation and depletion forces.<sup>73,74</sup>

Especially for larger particles, gravitational forces cause particle sedimentation, which can result in the formation of colloidal crystals depending on the distinct height of the energy barrier caused by the repulsive interactions. However, sedimentation generally yields three-dimensional colloidal crystals.<sup>75</sup> Electrostatic attraction to an oppositely charged substrate leads to random sequential adsorption of the particles giving particle monolayers with low surface coverage and high degree of disorder.<sup>76-78</sup>

External forces such as electrophoretic direct current<sup>79</sup> and alternating current<sup>80</sup> can be applied to electrical conductive substrates immersed into the particle dispersion to generate ordered particle monolayers.

Other forces dominate for particles near interfaces. As discovered by Pieranski *et al.*, colloidal particles are trapped at liquid/gas or liquid/liquid interfaces.<sup>81</sup> When trapped at an interface between media with different polarity, the asymmetric dissociation of ionic groups on the particle surface provides dipole like charge distributions (Figure 1.1b). As these dipoles are oriented parallel for all particles at the interface, a repulsive force emerges.

Moreover, flotation and immersion capillary forces have to be considered (Figure 1.1c).<sup>82,83</sup> Particles at an interface deform the interface depending on the wettability of the particles. For large particles, gravitational and buoyancy forces further influence the deformation of the interface. When the curvature of the meniscus extends into the same direction, the urge to minimize the free-energy by minimizing the interfacial area of the system results in an attractive flotation force between two particles. Attractive immersion capillary forces act when particles are trapped at a solid interface in a liquid film distinctly thinner than the particle diameter. Immersion capillary can influence even very small colloidal particles. Flotation and immersion capillary forces thereby are susceptible towards the particle wettability, size, shape, the density of the particles compared to the density of the liquid media as well as surface modifications of solid substrates.

Convective assembly is a commonly used method for the production of two-dimensional and three-dimensional colloidal crystals capitalizing on immersion capillary forces on solid substrates. On hydrophilic substrates, a thin liquid film is formed at the three-phase-contact line, and immersion capillary forces drag the particles into the colloidal crystal. Driven by solvent evaporation in the meniscus region, the particles are convectively transported from the bulk dispersion to the three-phase-contact line.<sup>82</sup>

Convective assembly can be observed in drying colloid dispersions drop cast onto hydrophilic substrates.<sup>84</sup> By slowly moving the meniscus across the substrate the colloidal crystal film is continuously deposited, and the coffee-ring effect is avoided. Experimentally, this can be realized by vertical<sup>85</sup> or horizontal<sup>86</sup> deposition techniques or by confining the dispersion in wedge-shaped evaporation cells (Figure 1.2).<sup>87,88</sup> Similarly, immersion capillary forces are exploited in spin-coating based assembly methods.<sup>89,90</sup> However, spin-coating often results in small domain sizes and the realization of high quality, defect-free monolayers is challenging.

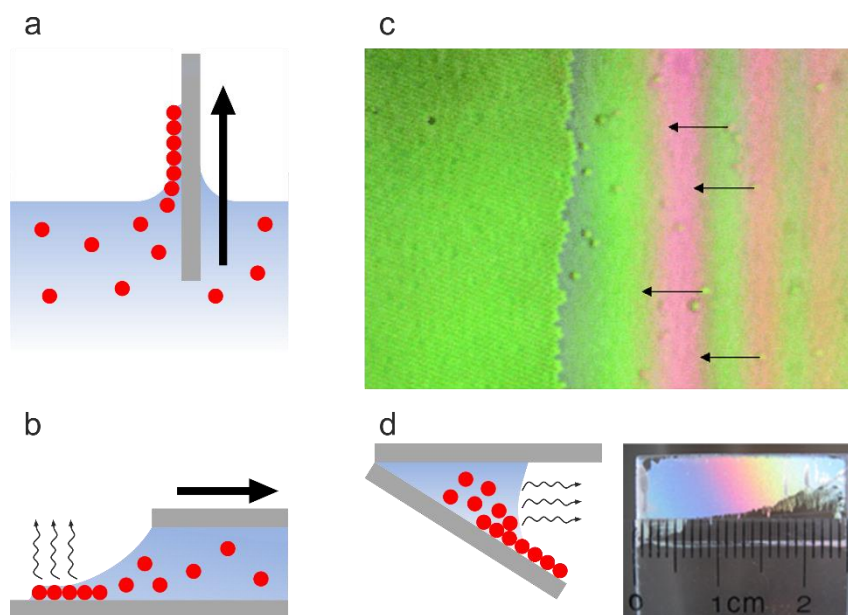


**Figure 1.2.** Convective assembly methods. The meniscus is formed by (a) vertically lifting the substrate out of a particle dispersion or (b) horizontally withdrawing the particle dispersion. (c) Optical microscopy image of a close-packed particle monolayer growing at the three-phase-contact line. The meniscus is moving from left to right. The particles are driven to the contact line by convection. (d) Convective assembly in a wedge-shaped cell. The photograph depicts a monocrystalline colloidal crystal assembled in a wedge-shaped cell. (c) Reprinted with permission from Ref. 86. ©2007 American Chemical Society. (d) Reprinted with permission from Ref. 88. ©2013 American Chemical Society.

In general, high degrees of order can be achieved with interface assisted methods. Here, the colloidal crystal is generated at a liquid interface and transferred to a solid substrate in a subsequent step. During the assembly stage, the particles are trapped at the interface and are subject to a purely lateral motion. The Langmuir-Blodgett method is highly reproducible but needs sophisticated equipment.<sup>91</sup> The particles at the liquid interface are compressed mechanically by barriers to form a close-packed monolayer. This technique can be supported by a simultaneous measurement of pressure-area isotherms.

In a more convenient method, the particles are applied directly to the liquid/air interface through a thin cannula.<sup>92,93</sup> The cannula tip is positioned in contact with the interface forming a meniscus. Based on the Marangoni effect, the particles are radially pushed away from the cannula tip, and a close-packed particle monolayer is growing from the boundaries of the interface inwards. By carefully controlling the flow rate and spreading of the particle dispersion, large-area monolayers can be generated very fast.

Likewise, particles can be applied to water/oil interfaces. Thus, attractive capillary forces can be reduced, and non-close-packed monolayers are obtained.<sup>94-96</sup> By additionally introducing a curvature to the water/oil interface, Ershov *et al.* were able to create non-close-packed square

arrays of colloidal particles.<sup>97</sup> However, the transfer of non-close-packed particle arrays from the water/oil interface to solid substrates is not trivial due to the onset of capillary forces.

Vogel *et al.* introduced a method for the wafer-scale production of particle monolayers (Figure 1.3a,b).<sup>98</sup> The aqueous colloidal dispersion, diluted with the same amount of ethanol, is applied to the water interface via a hydrophilic glass slide immersed in a sodium dodecyl sulfate solution with a tilt angle of approximately 45°. Thus, the particle flow into the subphase is considerably reduced, minimizing defect formation when transferring the monolayer onto solid substrates. A close-packed particle monolayer is formed directly at the three-phase contact line.

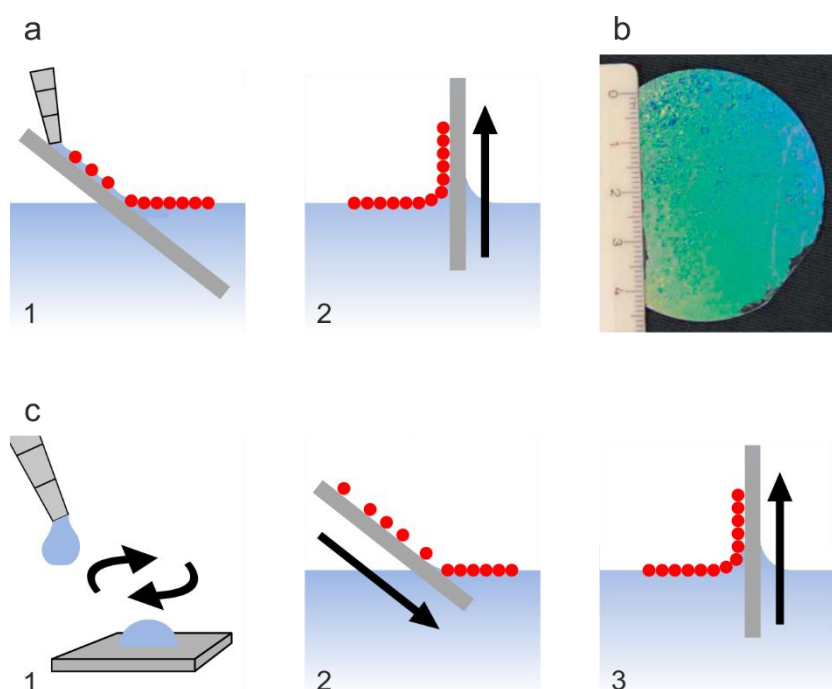


**Figure 1.3.** Colloidal crystal formation at the water/air interface. (a) Colloidal crystal assembly by addition of the colloid dispersion via a tilted glass slide. (b) Silicon wafer covered with a monolayer of 1  $\mu\text{m}$  polymer colloids. (c) A substrate with sparsely distributed particles is prepared by spin-coating of the particle dispersion onto a positively charged substrate. The colloidal crystal is formed by immersion of the particle coated substrate. (b) Reprinted with permission from Ref. 98. ©2011 Wiley-VCH.

An alternative method to trap colloidal particles at the water/air interface was developed by Retsch *et al.*<sup>99</sup> The particles are spin-coated on a cationically functionalized glass slide to form a layer of sparsely distributed particles (Figure 1.3c). Subsequently, the coated glass slide is immersed into the subphase. Upon immersion, the particles detach from the glass slide at the three-phase-contact line and immediately form a close-packed particle monolayer. A small amount of sodium dodecyl sulfate is added to the subphase to provide an additional force, which pushes the particles together when detaching from the glass slide. Thus, the assembly via

flotation or immersion capillary forces is confined to a single particle monolayer, and the evolution of particle multilayers is avoided. The particle monolayer can then be transferred to an arbitrary substrate either by draining the subphase or pushing or lifting the substrate through the floating monolayer. Simultaneously, the dissociation of functional groups on the particle surface and thus the interparticle repulsion by electrostatic forces can be tuned by adjusting the pH of the subphase. This drastically influences the quality of the particle monolayer.

Post processing at the water/air interface can further enhance the order of the floating monolayer. While floating at the interface, defects in the monolayer can be eliminated by annealing with expansion-compression cycles or ultrasound.<sup>100</sup> Similarly, recrystallization was induced by shear forces generated with a stream of compressed nitrogen.<sup>101</sup>

Binary colloidal crystals consisting of two different sizes have been prepared with several of the methods discussed above.<sup>35,36</sup> Depending on the size ratio and stoichiometry of the particles, complex superstructures can be formed.

Substrate-supported, non-hexagonally ordered arrays are not directly accessible with colloidal self-assembly. Instead, non-hexagonal assemblies can be obtained starting from hexagonal monolayers on elastomeric substrates. By swelling or stretching the substrate, the particle arrays can be distorted, and different geometries can be generated.<sup>102</sup>

Finally, topographical or chemical patterning of the substrate allows for the creation of hierarchical structures with colloidal particles. Topographically patterned substrates are usually coated via convective assembly methods. When moving across the structure, the meniscus is pinned to the topographical features, which results in a directed deposition of the colloids.<sup>86,103-105</sup> With feature sizes in the range of single particles, individually separated particles can be deposited,<sup>86,106-108</sup> (Figure 1.4a) and close-packed or non-close-packed arrays with various lattice geometries can be prepared.<sup>86,106</sup> Feature sizes much larger than the single particle are usually used to generate superstructures with patches of hexagonal, close-packed monolayers.<sup>109</sup> By confining multiple particles in patterns tuned to the lattice period, the lattice symmetry and orientation can be controlled.<sup>106,107</sup>

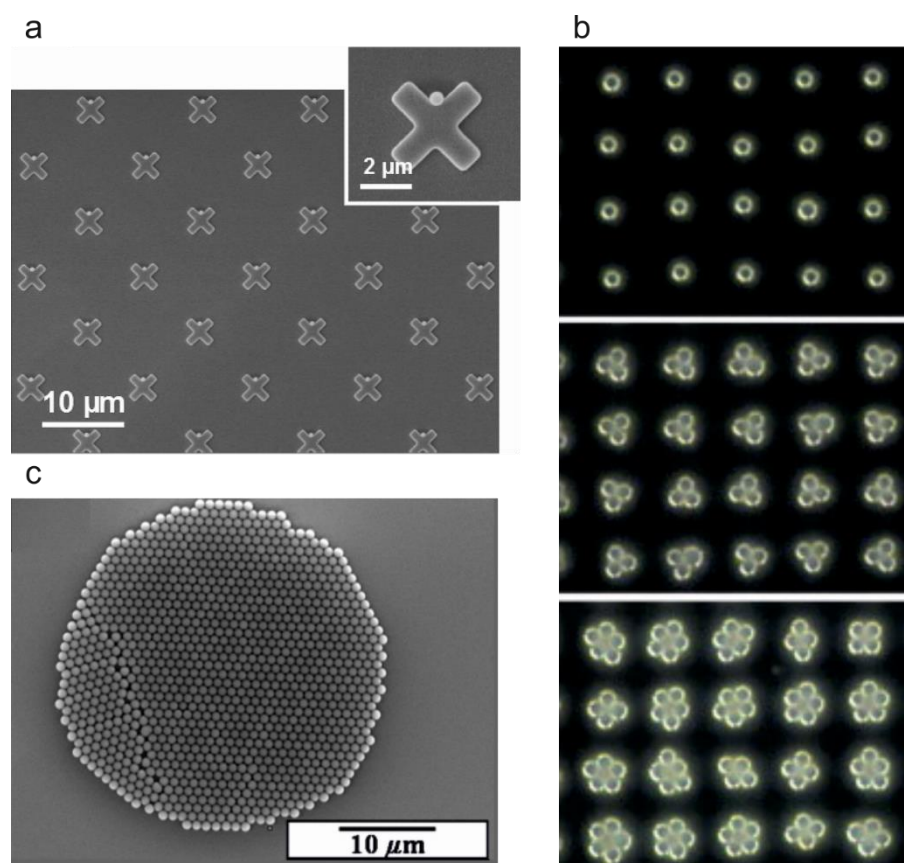


**Figure 1.4.** Particle deposition on patterned substrates. (a) Single particles deposited in topographical features via capillary assembly. (b) Deposition of single particles and particle clusters using a contrast in the surface charge by patterning with polyelectrolytes. (c) Patterned, close-packed colloidal crystal deposited on a substrate with wettability contrast. (a) Reprinted with permission from Ref. 86. ©2007 American Chemical Society. (b) Reprinted with permission from Ref. 110. ©2002 Wiley-VCH. (c) Reprinted with permission from Ref. 111. ©2005 American Chemical Society.

Chemical patterning of the substrate can generate surface areas with a contrast in surface charge or wettability. This contrast is often achieved using polyelectrolytes, silane or thiol chemistry.<sup>111-113</sup> By structuring the surface charge, the placement of single particles or small particle clusters is possible via electrostatic attraction (Figure 1.4b).<sup>110</sup> Larger domains of ordered close-packed arrays, however, are not directly accessible due to the strong binding of the particles to the surface. Thus the particle assembly driven by capillary forces is impeded.<sup>112</sup> On the contrary, introducing a contrast in wettability may result in larger, ordered assemblies directed to the areas preferably wetted by the particle dispersion (Figure 1.4c).<sup>111,114</sup> More complex geometries are possible using the directed self-assembly of non-isotropic particles with engineered binding sites.<sup>115,116</sup>

## 1.2 Nanosphere Lithography

Starting from self-assembled colloidal structures, nanosphere lithography or colloidal lithography presents a simple and cheap alternative to top-down lithographic techniques. Therefore, since its introduction by van Duyne *et al.*<sup>117</sup> in 1995, the method evolved rapidly and has been used to prepare a plethora of different nanostructures.<sup>35,52,65,118-122</sup>

Van Duyne *et al.* used hexagonal, close-packed monolayers and double-layers of polystyrene spheres as a template for metal evaporation.<sup>117</sup> After lift-off of the particle array by dissolving in dichloromethane, ordered arrays of triangularly shaped nanoparticles as well as round nanodots remained for the monolayer and double-layer masks, respectively (Figure 1.5a,b). Soon after, the plasmonic properties of these nanoparticle arrays were investigated with regard to the dielectric environment<sup>123</sup> as well as the size,<sup>124</sup> shape,<sup>125</sup> and material<sup>126</sup> of the particles. Kosiorek *et al.* thermally annealed a polystyrene particle monolayer with microwave pulses partially closing the interstices of the monolayer. Like this, Co nanodots were fabricated with diameters as small as 30 nm but large interparticle spacings at the same time.<sup>127</sup>

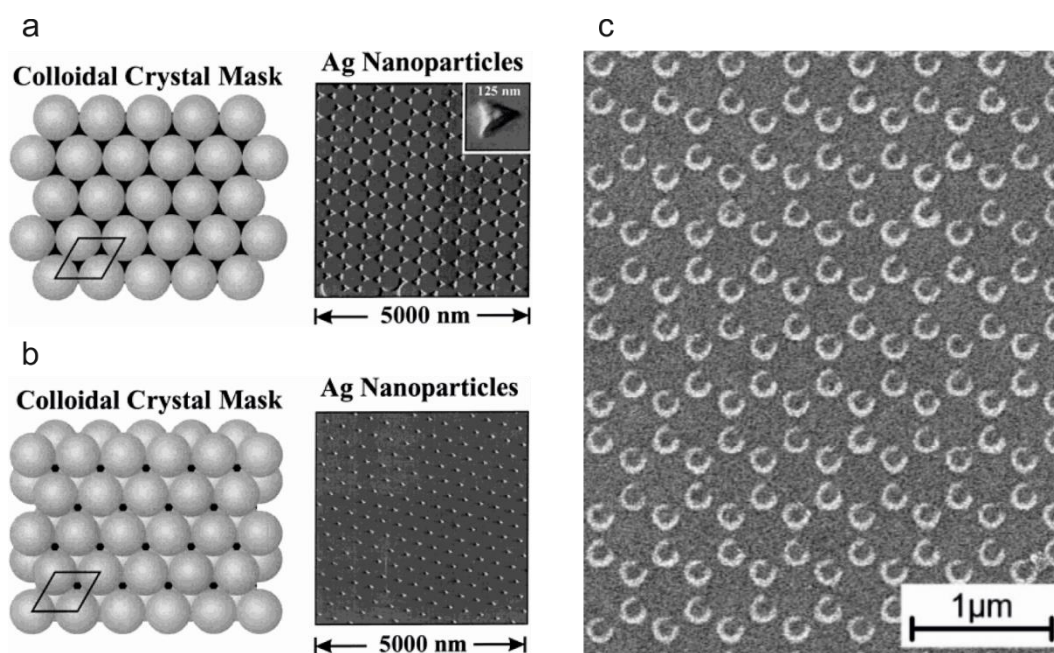


**Figure 1.5.** Plasmonic particle arrays prepared templated by close-packed colloidal crystals. (a) Triangularly shaped Ag nanoparticles were prepared by Ag deposition through a monolayer of polystyrene particles. (b) The Ag deposition through the interstices of a bilayer of polystyrene spheres results in Ag nanodot arrays. (c) Split-ring resonators formed by incomplete sample rotation during gold evaporation. (a,b) Reprinted with permission from Ref. 125. ©2001 American Chemical Society. (c) Reprinted with permission from Ref. 128. ©2009 Wiley-VCH.

The small apertures prepared by monolayer annealing were also used for the fabrication of nanorings. For this, a further level of complexity was added by varying the sample angle for metal evaporation. During evaporation at an angle of  $25^\circ$ , the sample stage was rotated yielding Fe nanoring arrays<sup>129</sup>. Similarly, an incomplete sample rotation during evaporation results in split-ring resonators (Figure 1.5c).<sup>128</sup>

An additional parameter is introduced when using non-close-packed monolayers as shadow masks. Most often, non-close-packed arrays are produced by plasma etching.<sup>36,98</sup> Starting from a close-packed monolayer, the particle diameter is reduced depending on the etching time without changing the interparticle distance.<sup>130,131</sup> Analogously, the particle diameter can be reduced by shrinking close-packed hydrogel particles<sup>89,132</sup> or degrading<sup>133,134</sup> the polymer shell of core/shell particles without affecting the order of the colloidal crystal. Alternatively, non-close-packed particle monolayers are accessible by swelling elastomeric substrates bearing a close-packed monolayer<sup>135</sup> or directly via spin-coating.<sup>136</sup> Metal evaporation onto non-close-packed particle monolayers readily yields nanohole arrays after lift-off of the particle template (Figure 1.6a).<sup>137</sup>

Line structures and grid structures can be fabricated by multiple, angled deposition and rotating the sample in between the deposition steps (Figure 1.6b).<sup>138</sup>

By combining angled metal evaporation with reactive ion beam etching nanocrescent arrays<sup>139,140</sup> and binary nanocrescent arrays<sup>141,142</sup> were fabricated (Figure 1.6c). For this, the metal is deposited through a non-close-packed particle layer at an oblique angle. Then, the structure is exposed to reactive ion beam etching perpendicular to the substrate removing all excess metal not shaded by the particle template. Finally, the particle template is removed revealing the nanocrescents.

A more sophisticated two-step method for the preparation of split-ring resonators<sup>143</sup> or metal nanodiscs<sup>144</sup> is based on hole-mask colloidal lithography (Figure 1.6d). For hole-mask colloidal lithography, a metal nanohole array is prepared by colloidal lithography on top of a sacrificial polymer layer. After the polymer layer is selectively etched beneath the holes of the metal film, the apertures in the metal film are finally used as evaporation mask.<sup>144</sup>

Etching colloidal particle multilayers results in anisotropically etched particles as the upper particle layers act as shadow masks for the underlying layers.<sup>145</sup> Thus, various more complex geometries such as binary particle arrays can be realized. Using a double layer of hexagonal, close-packed polystyrene spheres as evaporation mask, in which the particles of the second layer sit in the interstices of the bottom layer, resulted in shuttlecock-shaped particles.<sup>146</sup> If the

second particle layer is rotated with respect to the bottom layer, Moiré patterns emerge, which were used as evaporation mask in a method coined Moiré nanosphere lithography.<sup>147,148</sup>

Further, metal evaporation presents a simple method for the fabrication of Janus particles<sup>149</sup> or hollow metal hemispheres.<sup>150</sup>

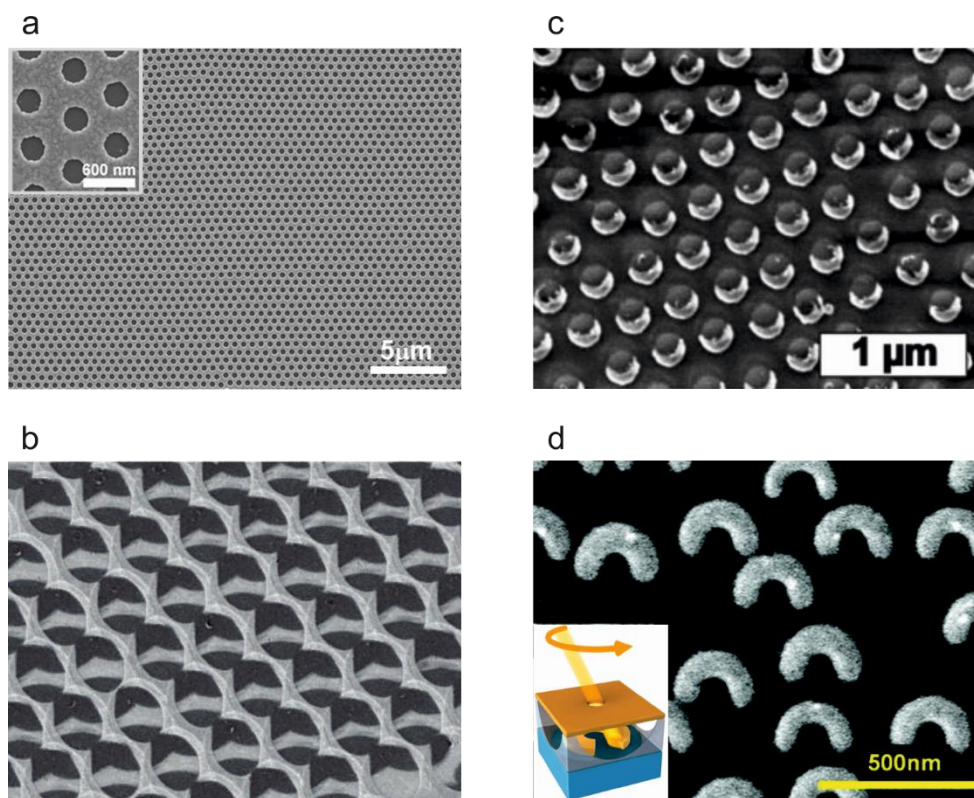


**Figure 1.6.** Metal nanostructures prepared using non-close-packed particle monolayers as a template. (a) Ag nanohole array prepared by evaporation normal to the surface. (b) Grid structures are accessible via angled metal evaporation. (c) Nanocrescent arrays can be prepared by angled metal evaporation and subsequent reactive ion beam etching normal to the surface. (d) Split-ring resonators produced by hole-mask colloidal lithography. The inset shows a schematic of the fabrication. The sample is rotated during evaporation of metal through a nanohole template. (a) Reprinted with permission from Ref. 137. ©2009 American Chemical Society. (b) Reprinted with permission from Ref. 138. ©2007 American Chemical Society. (c) Reprinted with permission from Ref. 139. ©2009 Wiley-VCH. (d) Reprinted with permission from Ref. 143. ©2012 American Chemical Society.

As an alternative to metal evaporation, which requires high vacuum, metal can be deposited by electroless plating. Here, the metal film is formed in a wet chemical process by reduction of ionic metal precursors in solution. Controlling the nucleation is vital to achieve smooth films and impede secondary nucleation yielding metal particles. Gold nanohole arrays<sup>151,152</sup>, as well as nanoring arrays<sup>153</sup> made of platinum, gold, and copper, have been prepared using electroless plating and colloidal crystals as templates.

Electrochemical deposition can be used to fabricate gold hole arrays<sup>154</sup> as well as hollow particles made of ZnO<sup>155</sup> or Ag.<sup>156</sup> For this, however, a conductive substrate is needed.

Silver honeycomb meshes were prepared by coating a close-packed monolayer of polystyrene particles using ink bar coating and a commercial silver ink followed by thermal annealing and lift-off of the particle template.<sup>157</sup>

Nanobowl arrays were fabricated using atomic layer deposition of TiO<sub>2</sub>,<sup>158</sup> electropolymerization,<sup>159</sup> or the infiltration of a colloidal monolayer with WO<sub>3</sub> precursors.<sup>160</sup>

The infiltration of three-dimensional colloidal crystals results in a material class called inverse opals. However, inverse opals are a research field on its own and will not be covered here.<sup>161-163</sup> Nevertheless, a two-dimensional inverse opal can be prepared by infiltration of a colloidal monolayer.<sup>164</sup>

Furthermore, colloidal monolayers can be used as a shadow mask to etch the structure into the substrate itself. Nanowires were etched into a silicon substrate through non-close-packed particle monolayers by SF<sub>6</sub><sup>165</sup> or chlorine<sup>5</sup> reactive ion etching (Figure 1.7a). Analogously, “candle stands” were etched into a gallium antimonide substrate with chlorine reactive ion etching.<sup>166</sup> Nanotriangles prepared by colloidal lithography were used as an etching mask to obtain Si nanopillars.<sup>167</sup> Moreover, colloidal monolayers can be employed for the preparation of etching masks to pattern thin polymer films.<sup>168</sup> Nanodiscs composed of Co/Pt alloy were created using perpendicular reactive ion beam etching of a thin Co/Pt film shaded by non-close-packed particle monolayers.<sup>169</sup>

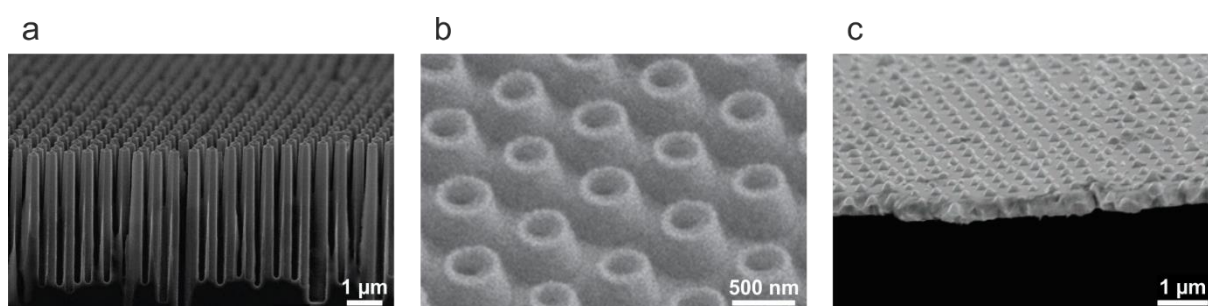


**Figure 1.7.** Patterned substrates via colloidal lithography. (a) Silicon nanowires were fabricated via SF<sub>6</sub> reactive ion etching through a non-closed-packed particle monolayer. (b) Nanovolcanos were prepared by metal evaporation onto photoresist nanocones and subsequent removal of the resist. The nanocones were prepared via reactive ion etching through a close-packed colloidal crystal. (c) Anisotropic silicon etching through a chromium nanohole array yields inverted nanopyramid arrays, which can be replicated into metal films by template-stripping. (a) Reprinted with permission from Ref. 165. ©2010 American Chemical Society. (b) Reprinted with permission from Ref. 170. ©2013 Wiley-VCH. (c) Reprinted with permission from Ref. 171. ©2007 American Chemical Society.

Ai *et al.* etched nanocones into a photoresist layer using a close-packed monolayer of polystyrene spheres as a template (Figure 1.7b). Subsequent metal deposition and particle lift-off resulted in an array of nanovolcanos.<sup>170</sup>

Anisotropic silicon etching was used by Sun *et al.* to fabricate periodic arrays of metal nanopyramids (Figure 1.7c). During the wet etching of the silicon substrate, the KOH preferentially etches the <100> plane of silicon. To obtain the array of nanopyramids, a non-close-packed monolayer of silica particles was prepared by spin-coating and used as a template for the deposition of a chromium mask. The resulting chromium nanohole array then acted as an etching mask defining the size and spacing of the inverted nanopyramids. After removing the chromium, a metal film was deposited and finally template-stripped yielding the metal nanopyramids.<sup>171</sup>

When depositing the metal layer without previously removing the chromium mask, free-standing metal nanopyramids can be produced.<sup>172</sup>

Nanopillars can also be prepared by directed growth techniques. Hexagonally shaped, single crystalline ZnO pillars were grown from solution on zinc foils using a colloidal monolayer template.<sup>173</sup> Thereby, the pillars grew in the interstices of a monolayer of polystyrene spheres itself or in the unmasked area of the inverted hole structure.

Amorphous TiO<sub>2</sub> was deposited by pulsed laser deposition by Li *et al.*<sup>174</sup> Upon annealing, the amorphous TiO<sub>2</sub> crystallized into polycrystalline anatase TiO<sub>2</sub> nanopillars.

Au nanoparticle arrays prepared by colloidal lithography were used to grow vertically aligned silicon<sup>175</sup> and ZnO<sup>176-178</sup> nanopillars by vapor-liquid-solid mechanisms with several techniques. Similarly, Ni catalyst arrays can be used to grow periodic carbon nanotube arrays.<sup>179-181</sup>

Recently, colloidal monolayers were used as templates not only on solid substrates but directly at the liquid/gas interface. By chemical polymerization of aniline or pyrrole in the presence of a floating particle monolayer, nanobowls of conducting polymers were fabricated.<sup>182</sup> Ag nanobowls<sup>183</sup> and Ag<sub>2</sub>S nanonets<sup>184</sup> were prepared via interface reactions with reactive gas and metal precursors dissolved in the liquid phase. Ye *et al.* obtained ZnS nanobowl arrays by floating a colloidal monolayer on a precursor solution. The decomposition of the precursors was then triggered by temperature.<sup>185</sup> Similarly, Sun *et al.* trapped a monolayer of polystyrene spheres at the liquid/air interface above a solution of H<sub>2</sub>AuCl<sub>4</sub> and Na<sub>2</sub>SO<sub>3</sub>. The irradiation with UV light then induced the formation of Au hollow sphere arrays.<sup>186</sup>

A three-dimensional gold nanohole array was created by Ai *et al.* using a close-packed monolayer of polystyrene spheres.<sup>187</sup> After gold deposition, the gold hemispheres were partially embedded in P4VP to selectively etch the exposed top layer using a commercial gold etching solution. After removing the P4VP layer and the particle template by dissolution in ethanol and toluene, respectively, the three-dimensional gold nanohole array remained.

Colloidal monolayers have also been used for evaporation induced self-assembly. CdSe quantumdots<sup>188</sup> or carbon nanotubes<sup>189</sup> were driven into the interstices between the substrate and the colloidal particles by capillary forces, thus creating nanoring arrays.

Finally, self-assembled polymer spheres containing metal particles were converted into ordered arrays of metallic nanoparticles by plasma combustion of the organic content followed by thermal annealing.<sup>190</sup>

Altogether, colloidal lithography offers the possibility to prepare a tremendous variety of nanostructures relying on colloidal building blocks. Most prominently, nanosphere lithography is used to transfer the structures obtained by colloidal self-assembly into metallic surfaces. Due to the possibility to create structures with a feature size smaller than the wavelength of visible light, these structures feature exceptional plasmonic properties in this wavelength range.<sup>118,191</sup> Thus, nanosphere lithography has been exploited to produce nanostructures for sensing,<sup>185,192</sup> surface enhanced fluorescence,<sup>193</sup> and Raman spectroscopy.<sup>13</sup>

Moreover, plasmonic nanostructures are discussed to enhance the power conversion efficiency in light emitting diodes<sup>194,195</sup> and solar cells<sup>24-27,196</sup> because of their ability to confine light in deep subwavelength volumes.<sup>197</sup> Colloidal lithography also features a simple approach towards metamaterials.<sup>128,139,198</sup> The fascinating plasmonic properties of nanostructured metallic surfaces are described in the following chapter.

## 1.3 Surface Plasmon Polaritons

### 1.3.1 The Drude Theory of Metals

As already mentioned, plasmons are collective oscillations of electrons in a solid. Three types of plasmons can be distinguished: Bulk plasmons are longitudinal electron density oscillations in the bulk material. Surface plasmon polaritons (SPP) are two-dimensional, transverse oscillations of electrons bound to a metal/dielectric interface. Localized surface plasmon (LSP) resonances are in-phase oscillations of electrons in deep-subwavelength-scale particles.

In general, a high density of free electrons is needed in a material to excite these oscillations. Thus, although also found in metal oxides<sup>199</sup> and organic materials<sup>200</sup> plasmons are mainly observed in metals. This chapter focuses on the fundamental properties of metals and their connected ability to support surface plasmon polaritons.

The most apparent macroscopic properties of metals are their conductivity and their high reflectivity. Both can be well described, though simplified, on a microscopic level by the Drude theory, which was proposed by Paul Drude around 1900.<sup>201</sup> In the Drude theory, metals are described as compounds consisting of positively charged ions and much smaller, negatively charged electrons. In contrast to the heavy ions, which are assumed immobile, the electrons are considered to be delocalized, forming a freely floating “electron gas” within the matter. When an electric field  $\vec{E}$  is applied, these electrons follow the field. Otherwise, based on the kinetic gas theory, the electrons are regarded to be moving in a constant, random motion and electron-electron interactions are neglected. However, collisions of electrons with the positively charged ions lead to changes in the direction and velocity of the electrons, which is described by a damping factor

$$\gamma = \frac{1}{\tau}, \quad 1.1$$

with  $\tau$  being the average time between two collisions.<sup>202</sup> Following these assumptions, the time-dependent motion equation of an electron in an electric field  $\vec{E}$  equals to

$$-e\vec{E}(t) = m\ddot{x} + m\gamma\dot{x}, \quad 1.2$$

with  $e$  and  $m$  being the charge and mass of an electron,  $t$  being the time and  $x$  being the displacement. Applying an oscillating electric field

$$\vec{E}(t) = \vec{E}_0 e^{-i\omega t}, \quad 1.3$$

with an amplitude  $\vec{E}_0$  and the angular frequency  $\omega$  the displacement of the electron can be expressed as

$$\vec{x}(t) = \frac{e}{m(\omega^2 + i\gamma\omega)} \vec{E}(t). \quad 1.4$$

For a linear, isotropic medium  $i$ , the relation between the macroscopic polarization  $\vec{P}$  and the electric field is given by

$$\vec{P}(t) = -Ne\vec{x}(t) = (\varepsilon_i - 1)\varepsilon_0\vec{E}(t), \quad 1.5$$

with the number density of charge carriers  $N$ , the vacuum permittivity  $\varepsilon_0$  and the relative permittivity of the medium  $\varepsilon_i$ . This directly yields the dielectric function of metals with the plasma frequency  $\omega_p$ :

$$\varepsilon_i = 1 - \frac{Ne^2}{\varepsilon_0 m(\omega^2 + i\gamma\omega)} = 1 - \frac{\omega_p^2}{(\omega^2 + i\gamma\omega)} \quad 1.6$$

$$\omega_p^2 = \frac{Ne^2}{\varepsilon_0 m} \quad 1.7$$

The dielectric function can be separated into its real part and its imaginary part:

$$\varepsilon_i(\omega) = \varepsilon_i'(\omega) + i\varepsilon_i''(\omega) \quad 1.8$$

$$\varepsilon_i' = 1 - \frac{\omega_p^2 \tau^2}{(1 + \omega^2 \tau^2)} \quad 1.9$$

$$\varepsilon_i'' = \frac{\omega_p^2 \tau}{\omega(1 + \omega^2 \tau^2)} \quad 1.10$$

In Figure 1.8 the wavelength dependent real and imaginary part of the dielectric function of gold is depicted. The real part changes its sign at the plasma frequency. The plasma frequency is the eigenfrequency of the bulk plasmon, which is a longitudinal, collective oscillation of the electron gas within its volume. Below the plasma frequency, the real part becomes negative, connected to a very high imaginary part. This is reflected in a high reflectivity of the metal as the electrons respond to an external electric field. Above the plasma frequency, however, the real permittivity of the metal is positive, and the oscillations of an electromagnetic wave are too fast for the electrons to follow. Thus, the metal becomes transparent above its plasma frequency.

For real metals, the plasma frequency is usually located in the ultraviolet region. In this region, interband transitions occur, which are not considered in the Drude theory.

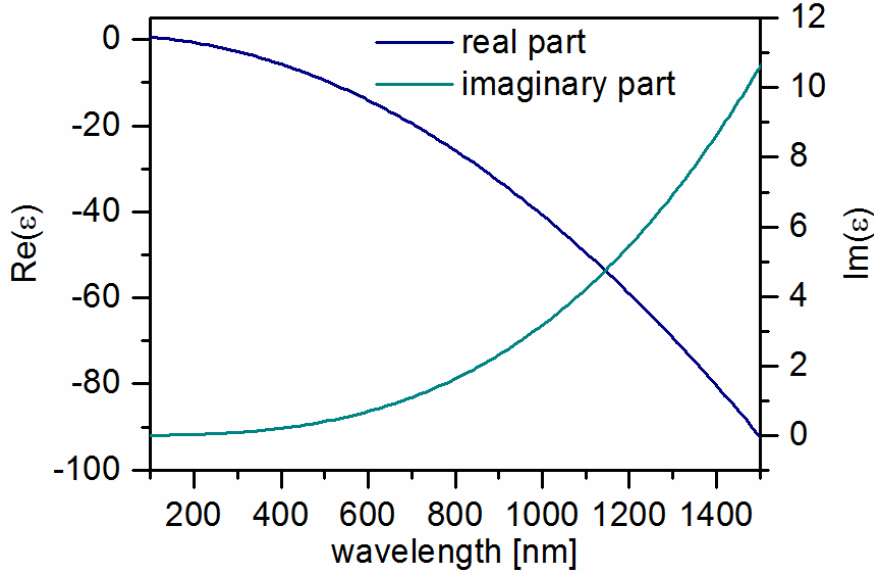


**Figure 1.8.** Real and imaginary part of the dielectric function of gold calculated by the Drude model. The values of  $\tau = 7 * 10^{-15} \text{ s}$  and  $\omega_p = 1.22 * 10^{16} \frac{1}{\text{s}}$  were adapted from Ref. 203.

### 1.3.2 Bound Electromagnetic Waves

In modern physics, the interaction of light and matter is described by Maxwell's equations, which form the fundament of classical electromagnetism. Maxwell's equations explain how charges and currents evoke electric and magnetic fields, respectively. Furthermore, the interaction between electric and magnetic fields can be explained as well as their spatial- and time-dependent evolution.

The interaction of an electromagnetic wave with a metal/dielectric interface can be derived from the macroscopic Maxwell's equations, which involve matter given by macroscopic parameters: the relative permittivity  $\epsilon_i$  and the relative permeability  $\mu_i$ .<sup>202</sup> Additionally, free and bound charges and currents are taken into account by using the electric displacement field  $\vec{D}$  and the magnetizing field  $\vec{H}$ . In a linear, isotropic medium, these values are connected to the electric field  $\vec{E}$  and the magnetic field  $\vec{B}$  by the following expressions:

$$\vec{D} = \epsilon_i \epsilon_0 \vec{E} \quad 1.11$$

$$\vec{B} = \mu_i \mu_0 \vec{H} \quad 1.12$$

Implying only harmonic oscillations, a time-independent form of Maxwell's equations can be used:

$$\vec{\nabla} \cdot \vec{D} = \rho_f \quad 1.13$$

$$\vec{\nabla} \cdot \vec{B} = 0 \quad 1.14$$

$$\vec{\nabla} \times \vec{E} = -i\omega\vec{B} = -i\omega\mu_i\mu_0\vec{H} \quad 1.15$$

$$\vec{\nabla} \times \vec{H} = \vec{J}_f + i\omega\vec{D} = \sigma\vec{E} + i\omega\varepsilon_i\varepsilon_0\vec{E} \quad 1.16$$

$\rho_f$  equals the density of free charges,  $\sigma$  is the conductivity, and  $\vec{J}_f$  is the free current density. For electromagnetic waves, free charge carriers can be neglected ( $\rho_f = 0$ ,  $\vec{J}_f = 0$ ,  $\sigma = 0$ ). Thus, Maxwell's equations simplify to

$$\vec{\nabla} \cdot \vec{D} = 0 \quad 1.17$$

$$\vec{\nabla} \cdot \vec{B} = 0 \quad 1.18$$

$$\vec{\nabla} \times \vec{E} = -i\omega\mu_i\mu_0\vec{H} \quad 1.19$$

$$\vec{\nabla} \times \vec{H} = i\omega\varepsilon_i\varepsilon_0\vec{E}. \quad 1.20$$

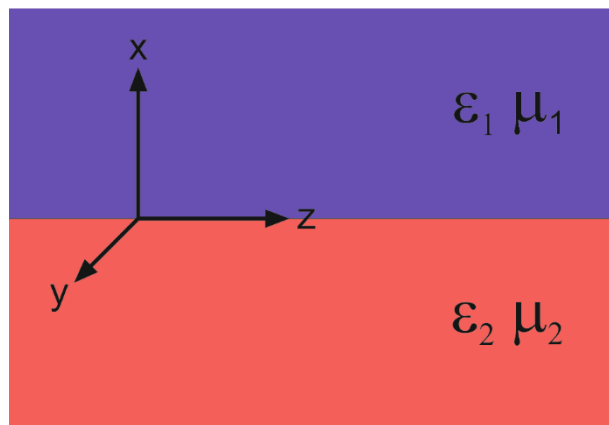


**Figure 1.9.** Scheme of an interface between two half-spaces of materials  $i$  with relative permittivities  $\varepsilon_i$  and relative permeabilities  $\mu_i$ .

For the description of surface waves, Maxwell's equations are solved for an interface between two half-spaces with relative permittivities  $\varepsilon_i$  and relative permeabilities  $\mu_i$  (Figure 1.9). By implying that neither the geometry nor the fields changes in  $y$  direction, it follows that:

$$\frac{\partial}{\partial y} = 0 \quad 1.21$$

Thus, the curl equations (equations 1.19 and 1.20) can be split into an equation system:

$$\frac{\partial E_x}{\partial z} - \frac{\partial E_z}{\partial x} = -i\omega\mu_i\mu_0 H_y \quad 1.22$$

$$-\frac{\partial H_y}{\partial z} = i\omega\varepsilon_i\varepsilon_0 E_x \quad 1.23$$

$$-\frac{\partial H_y}{\partial x} = i\omega\varepsilon_i\varepsilon_0 E_z \quad 1.24$$

$$\frac{\partial H_x}{\partial z} - \frac{\partial H_z}{\partial x} = -i\omega\mu_i\mu_0 E_y \quad 1.25$$

$$-\frac{\partial E_y}{\partial z} = i\omega\varepsilon_i\varepsilon_0 H_x \quad 1.26$$

$$-\frac{\partial E_y}{\partial x} = i\omega\varepsilon_i\varepsilon_0 H_z \quad 1.27$$

In the following, only the TM-mode (equations 1.22 - 1.24) is considered with the electric field aligned perpendicular to the interface. Moreover, the propagation constant  $\beta$  is introduced, with

$$\frac{\partial E_x}{\partial z} = i\beta E_x \quad 1.28 \quad \text{and} \quad \frac{\partial H_y}{\partial z} = i\beta H_y, \quad 1.29$$

which leads to

$$i\beta E_x - \frac{\partial E_z}{\partial x} = -i\omega\mu_i\mu_0 H_y \quad 1.30$$

$$-i\beta H_x = i\omega\varepsilon_i\varepsilon_0 E_x \quad 1.31$$

$$-\frac{\partial H_y}{\partial x} = i\omega\varepsilon_i\varepsilon_0 E_z. \quad 1.32$$

A surface wave, which is bound to the interface, has to decay exponentially in x-direction with the decay constant  $\kappa_i$ , while being periodic in z-direction. Therefore, the following solution can be assumed:

$$\vec{E}_i(z) = \begin{bmatrix} E_{x,i} \\ E_{z,i} \end{bmatrix} e^{-\kappa_i|x|} e^{i\beta z} \quad 1.33$$

$$\vec{H}_i(z) = H_{y,i} e^{-\kappa_i |x|} e^{i\beta z} \quad 1.34$$

Introducing this possible solution results in the following equation systems for the two respective media:

$$i\beta E_{x,1} + \kappa_1 E_{z,1} = -i\omega\mu_1\mu_0 H_{y,1} \quad 1.35$$

$$-i\beta H_{y,1} = i\omega\varepsilon_1\varepsilon_0 E_{x,1} \quad 1.36$$

$$-\kappa_1 H_{y,1} = i\omega\varepsilon_1\varepsilon_0 E_{z,1} \quad 1.37$$

$$i\beta E_{x,2} + \kappa_2 E_{z,2} = -i\omega\mu_2\mu_0 H_{y,2} \quad 1.38$$

$$-i\beta H_{y,2} = i\omega\varepsilon_2\varepsilon_0 E_{x,2} \quad 1.39$$

$$-\kappa_2 H_{y,2} = i\omega\varepsilon_2\varepsilon_0 E_{z,2} \quad 1.40$$

Solving these equation systems directly yields the dispersion relation of a surface wave, with  $k_0$  being the free space wavevector in vacuum:

$$k_0^2 \mu_i \varepsilon_i = \beta^2 - \kappa_i^2 \quad 1.41$$

Moreover, at the interface, the tangential components of the electric and magnetic fields have to be continuous across the interface:

$$E_{z,1} = E_{z,2} \quad 1.42 \quad \text{and} \quad H_{y,1} = H_{y,2} \quad 1.43$$

This gives the existence condition for surface plasmon polaritons:

$$\varepsilon_2 = -\varepsilon_1 \frac{\kappa_2}{\kappa_1} \quad 1.44$$

For surface waves, the decay constants have to be positive values. Thus, the dielectric constants have to have opposite signs, which is only possible when using a metal below its plasma frequency for one of the materials.

Combining equations 1.41 and 1.44, and assuming non-magnetic media ( $\mu_i = 1$ ) the dispersion relation of surface plasmon polaritons can be expressed as:

$$\beta = k_0 \sqrt{\frac{\varepsilon_1 \varepsilon_2}{\varepsilon_1 + \varepsilon_2}} \quad 1.45$$

As one of the materials has to be a metal, the permittivity  $\varepsilon_2$  can be approximated using the Drude theory. For a very small damping term  $\gamma$  the dielectric function can be reduced to

$$\varepsilon_2 = 1 - \frac{\omega_P^2}{\omega^2}. \quad 1.46$$

The surface plasma frequency  $\omega_{SP}$  is obtained when inserting the dielectric function into the dispersion relation (equation 1.45) and assuming  $\omega = \omega_{SP}$ ,  $k_0 = \omega_{SP}/c$ , and  $\beta \rightarrow \infty$ :

$$\omega_{SP} = \frac{\omega_P}{\sqrt{1 + \varepsilon_1}} \quad 1.47$$

The received dispersion relation for surface plasmon polaritons is depicted in Figure 1.10. At low frequencies, the SPP nearly behaves like free-space electromagnetic waves. For high frequencies, it approaches  $\omega_{SP}$ . Above the plasma frequency, the dispersion of the bulk plasmon is visible. Over the whole frequency range, however, the SPP dispersion is below the dispersion of the free photons.

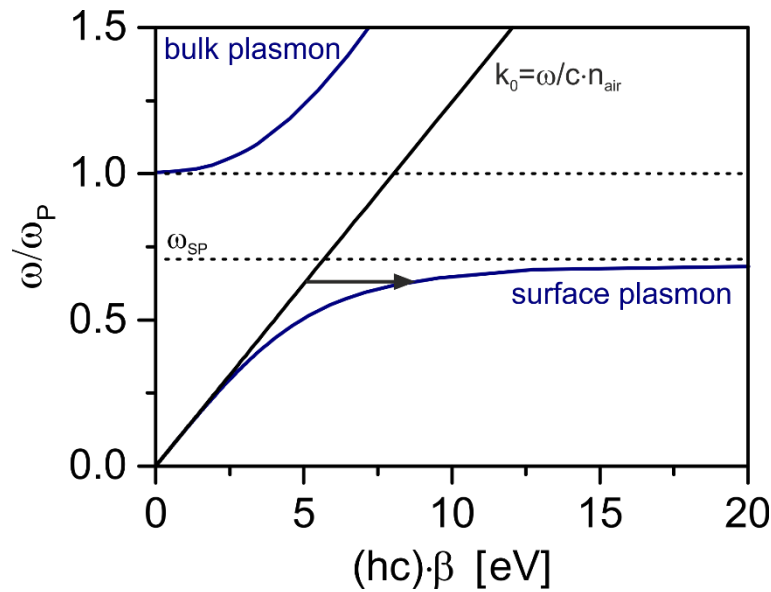


**Figure 1.10.** Dispersion relation of a surface plasmon at the gold/air interface. The dashed lines denote the plasma frequency  $\omega_P$  and the surface plasma frequency  $\omega_{SP}$  of gold, the solid black line the momentum of the free photon in air. The arrow indicates the momentum mismatch between the surface plasmon polariton and the free photon.

As shown in Figure 1.10, the dispersion of the surface plasmon polariton does not cross the light line of a free-space photon. Therefore, independent of the incident frequency, the SPP cannot be excited due to a momentum mismatch. To still be able to excite SPPs, this momentum mismatch, which is denoted by the arrow in Figure 1.10, has to be overcome. The missing

momentum can be provided by using high index dielectric materials. In the Kretschmann and Otto configuration, the total internal reflection in high index prisms is used. When the prism is close enough to the metal surface, the evanescent wave caused by the total internal reflection can excite a surface plasmon polariton. For a given frequency, the momentum is then matched by tuning the angle of incidence.

Alternatively, the momentum mismatch can be compensated by introducing a periodic corrugation of the metal/dielectric interface. According to the grating equation, the grating provides an additional momentum, equal to a multiple integer  $m$  of the reciprocal lattice vector  $\vec{K}$ , which adds to the in-plane component  $\vec{k}_x$  of the incident light (Figure 1.11).<sup>204</sup> This directly yields the excitation condition for surface plasmon polaritons using a grating coupler:

$$\beta = \vec{k}_x + m\vec{K} = \vec{k}_0 * n_1 * \sin \theta + m\vec{K} \quad 1.48$$

$$n_1 = \sqrt{\epsilon_1} \quad \text{refractive index of the dielectric}$$

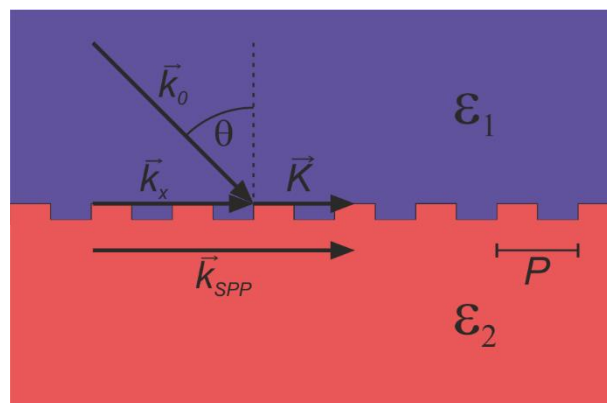


**Figure 1.11.** Coupling of a surface plasmon polariton with incident light via a metal grating with period  $P$ .

The period of the grating thereby has to be in the order of the wavelength of the incident light. Therefore, a metal surface has to be patterned with sub-micron resolution to allow for the excitation of surface plasmon polaritons in the visible spectrum.

### 1.3.3 Nanohole Arrays

Metal nanohole arrays or nanomeshes present a prevalent example for nanostructured materials that support surface plasmon polaritons. These structures have attracted much interest since the discovery of their extraordinary optical transmission.<sup>205</sup> For infinitely thin metal films, Bethe theoretically derived a simple correlation between the transmission efficiency and the radius  $r$  of the holes, in which the transmission efficiency scales with  $(r/\lambda)^4$ .<sup>206</sup> Thus, the transmittance is expected to decay exponentially as soon as the radius of the hole is smaller than the wavelength of interest. However, this assumption did not hold for optical thick metal layers perforated with subwavelength holes. For both, single apertures and subwavelength hole arrays, a transmittance maximum was observed that was much higher than predicted by Bethe's law.<sup>207</sup> This phenomenon was assigned to the excitation of surface plasmons.<sup>208-210</sup> The incident light excites the surface plasmon, which then tunnels the energy through the holes to the surface plasmon confined to the other metal/dielectric interface.<sup>211</sup> There, the energy is re-emitted again by coupling back to the free wave.

Metal nanohole arrays have been prepared by various methods. Electron beam lithography or focused ion beam milling (FIB) are often used as they give nanohole arrays with arbitrary symmetries and without lattice defects, nevertheless with the aforementioned drawbacks of low throughput and small sample sizes.<sup>209,212</sup> Instead, nanoimprint lithography can be applied to fabricate large areas.<sup>213,214</sup>

An elegant method to produce large-scale nanohole arrays without sophisticated equipment is based on nanosphere lithography (Figure 1.12). The preparation of nanohole arrays via nanosphere lithography starts from close-packed polymer particle monolayers, which are obtained from arbitrary self-assembly strategies (Figure 1.12a). For hard spheres, such as polystyrene particles, the particles are then etched using reactive ion etching, which allows for a precise tuning of the particle diameter (Figure 1.12b). Subsequently, the desired metal can be deposited by thermal evaporation (Figure 1.12c). The optical properties of these metal coated particle arrays already resemble those of nanohole arrays as their spectral properties are governed by the underlying lattice.<sup>215</sup> Finally, the particle template is removed using adhesive tape and ultrasonication, leaving behind the nanohole array (Figure 1.12d). Whereas the hole diameter  $d$  is given by the etching time, the period  $P$  of the received nanohole array is solely defined by the initial diameter  $d_0$  of the polymer spheres.

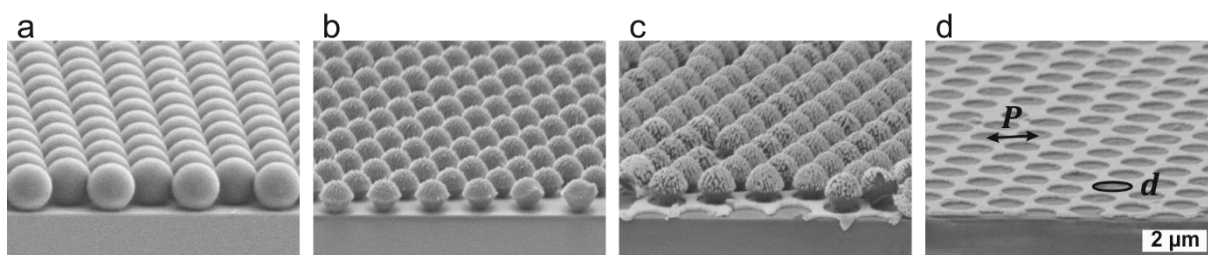


**Figure 1.12.** Fabrication of nanohole arrays by nanosphere lithography. (a) Side-view scanning electron microscopy image of a hexagonal, close-packed monolayer of polystyrene particles. (b) Non-close-packed monolayer after plasma etching. (c) 100 nm gold deposited onto non-close-packed particle monolayer by thermal evaporation. (d) Gold nanohole array.

However, in contrast to top-down lithographic methods, nanosphere lithography typically yields multi-crystalline monolayers, with domains of different crystal orientation, and includes lattice defects. Furthermore, the tunability of the hole size is bound to the array period. Hole diameters much smaller than 60 % of the initial particle diameter are hardly accessible, as the particles lose their shape after prolonged plasma treatment.<sup>130,216</sup> Moreover, nanosphere lithography is usually confined to a hexagonal symmetry.

Nevertheless, nanosphere lithography is a widespread technique for the lab-scale production of nanohole arrays due to its simplicity. The tunability of the spectral properties of nanohole arrays alongside with their dimensions makes metal nanohole arrays an ideal system for fundamental research in the fields of sensing applications,<sup>212,217</sup> color filters,<sup>15,17,18,218</sup> metamaterials,<sup>217</sup> and transparent electrodes.<sup>219</sup>

As metal nanohole arrays are also two-dimensional gratings, they can provide the momentum that is necessary to excite SPP modes. Figure 1.13 shows the denotation of the direct lattice vectors  $\mathbf{i}$  and  $\mathbf{j}$  for a hexagonal array. The reciprocal lattice vector  $\vec{K}$  for this lattice can be written as

$$K = |\vec{K}| = \frac{2\pi}{\sqrt{3}/2P} \sqrt{i^2 + ij + j^2}. \quad 1.49$$

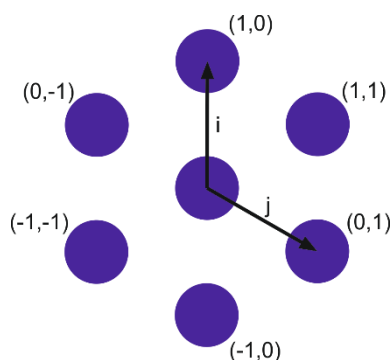


**Figure 1.13.** Definition of the direct lattice vectors.

Combined with the excitation condition for SPPs in grating couplers (equation 1.48) and the dispersion relation of SPPs (equation 1.45), this yields an expression for the SPP resonance wavelengths  $\lambda_0$  at normal incidence:

$$\lambda_0 = \frac{P}{\sqrt{\frac{4}{3}(i^2 + ij + j^2)}} * \sqrt{\frac{\varepsilon_1 \varepsilon_2}{\varepsilon_1 + \varepsilon_2}} \quad 1.50$$

For non-normal illumination, an additional term for the angle of incidence  $\Theta$  is added:<sup>220</sup>

$$\lambda_0 = \frac{P}{\sqrt{\frac{4}{3}(i^2 + ij + j^2)}} * \left( \sqrt{\frac{\varepsilon_1 \varepsilon_2}{\varepsilon_1 + \varepsilon_2}} - n_1 * \sin \Theta \right) \quad 1.51$$

These equations, however, do not consider the metal thickness or the influence of the holes on the permittivity and thus have to be regarded as a rough approximation.<sup>221</sup> It can be seen, that multiple diffraction orders (i,j) exist, which propagate in distinct directions, defined by the symmetry of the lattice. Some of these diffraction orders are degenerated at normal incidence and can be separated by increasing the angle of incidence, which results in a rich plasmonic behavior (Figure 1.14).

In experiments, usually two sets of resonances appear because the metal nanohole arrays are typically prepared on solid substrates and the dielectric constant  $\varepsilon_1$  of the medium in contact with the metal film is different on either side.<sup>213</sup> Therefore, one can allocate the resonances to the respective metal/dielectric interfaces as denoted in Figure 1.14a. Higher diffraction orders (i,j) are expected at shorter wavelengths but are not visible in the present spectra. At wavelengths shorter than the onset of interband transitions at approximately 516 nm for gold, no SPP is observed due to strong damping.<sup>222</sup>

In Figure 1.14b, the transmittance, reflectance, and absorption of the gold nanohole array are given for an angle of incidence of 6 °. The SPP resonance of gold nanohole arrays prepared by nanosphere lithography is characterized by a rather weak and broad absorption, which in transmittance measurements expresses itself as a minimum in transmittance followed by a transmittance maximum. Concomitantly, the reflectance spectrum shows a nearly mirrored trace with a reflectance maximum followed by a minimum. Due to this asymmetry, the line shape can be described as a Fano resonance, in which constructive and destructive interference between a continuum state and a discrete state lead to an asymmetric resonance.<sup>223</sup> For metal nanohole arrays, the coupling of directly transmitted light or hole LSP resonances with the SPP resonances is proposed to cause this interference.<sup>224,225</sup> Alternatively, Sannomiya *et al.* assigned

the transmittance maxima to LSP resonances of the holes and the transmittance minima to the SPP resonances.<sup>226</sup> This is substantiated experimentally by large spectral shifts of the transmittance maximum when the shape of the holes is altered without changing the lattice period.<sup>227</sup>

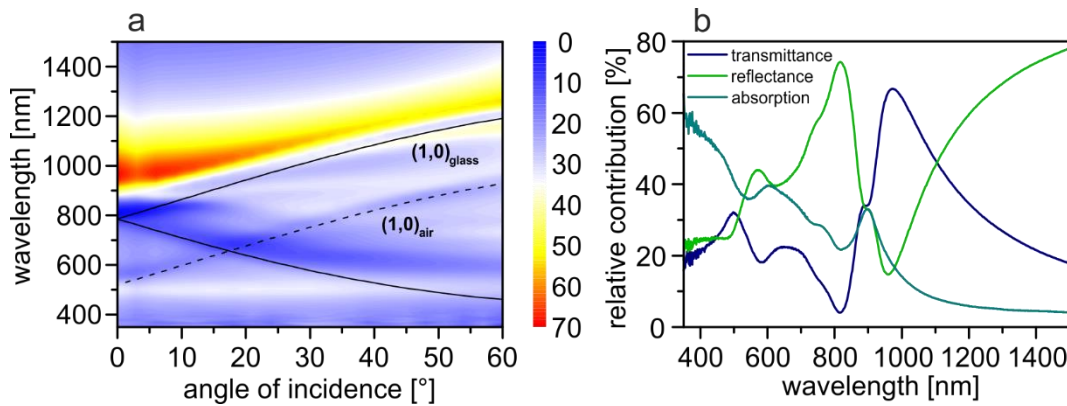


**Figure 1.14.** Optical properties of a gold nanohole array with  $P = 570$  nm. (a) Angle-resolved UV-vis spectroscopy. The solid and dashed lines indicate the theoretical values for the SPP resonances confined to the Au/glass and Au/air interface according to equation 1.51. The colors denote the transmittance in percent. (b) Transmittance, reflectance and absorption spectra at an angle of incidence of  $6^\circ$ .

In Figure 1.15 the influence of the geometrical parameters on the transmittance spectra of gold nanohole arrays is illustrated. Increasing the lattice period  $P$  leads to a strong shift of the resonances towards longer wavelengths (Figure 1.15a). Thus, by adjusting the lattice period, the resonances can be easily tuned across the whole visible and near-infrared (NIR) spectral range.

The effect of the hole size is depicted in Figure 1.15b. For large  $d/d_0$  ratios (equivalent to short etching times during fabrication) isolated, triangularly shaped nanoparticles are obtained, which show one reflectance dip in the NIR region associated with the LSP resonances of the particles. Increasing the etching time first results in larger nanoparticles and a shift of the resonance wavelength to longer wavelengths.<sup>124</sup> When further decreasing the  $d/d_0$  ratio, the interstices between the nanoparticles vanish, and the particles fuse to larger structures. Once a continuous gold film is formed, the optical properties change drastically. This sharp transition upon closing the interparticle gaps was thoroughly addressed by several groups.<sup>198,228,229</sup> For continuous nanohole arrays, the hole diameter has only little influence on the resonance wavelength. Instead, the thickness of the gold layer has a much higher influence on the spectral properties. Equation 1.51 is only valid for thick metal films ( $> 50$  nm), in which the SPP resonances of the two interfaces are not coupled. In thin metal films, the SPP modes

on the different interfaces of the film are strongly coupled. This coupling results in the evolution of two new modes, a symmetric mode at lower energy and an anti-symmetric mode at higher energy than the SPP mode in the uncoupled case.<sup>211,230,231</sup> While the low-energy mode broadens, the high-energy mode is very sharp and shows an unusually long propagation length. Thus, the low-energy and high-energy modes are also denoted as short-range and long-range SPP modes, respectively.<sup>232</sup> Indeed, for thinner gold layers the resonances increasingly broaden and shift to longer wavelengths (Figure 1.15c). These resonances thus correspond to the low-energy mode. The high-energy modes are not visible in the spectra.<sup>233</sup>

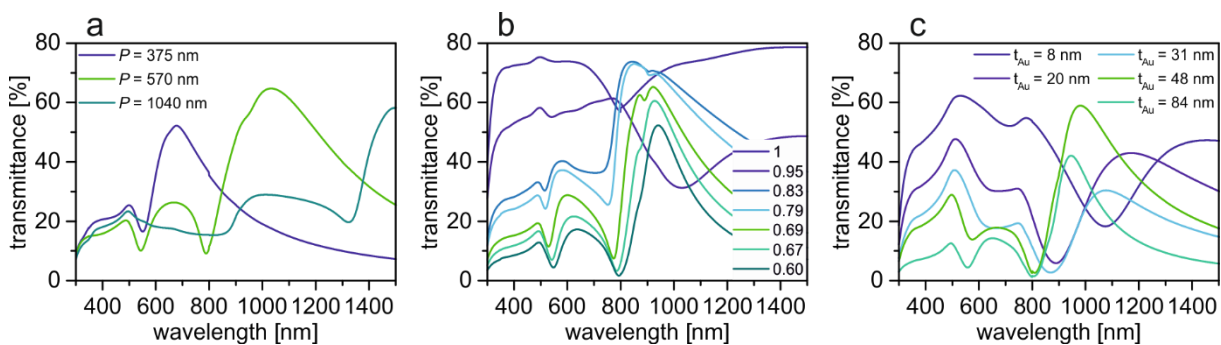


**Figure 1.15.** Correlation of geometrical parameters and optical response of gold nanohole arrays. (a) Transmittance spectra of nanohole arrays with a thickness of  $t_{Au} = 100$  nm and varying periods. The hole diameters are adjusted to a  $d/d_0$  ratio of 0.7. (b) Transmittance spectra of nanohole arrays with  $t_{Au} = 100$  nm,  $P = 570$  nm, and varying hole diameters. The numbers represent different  $d/d_0$  ratios. (c) Transmittance spectra of nanohole arrays with  $P = 570$  nm,  $d/d_0 = 0.7$  and varying film thicknesses.

As the SPP resonances are highly sensitive towards the surrounding refractive index, metal nanohole arrays have been employed for molecular sensing devices.<sup>226</sup> According to equation 1.51, the resonances shift to longer wavelengths with increasing refractive index of the adjacent medium. For thick metal films ( $> 50$  nm), the resonances bound to the interfaces on either side of the film can be tuned independently as shown in Figure 1.16.<sup>212</sup>

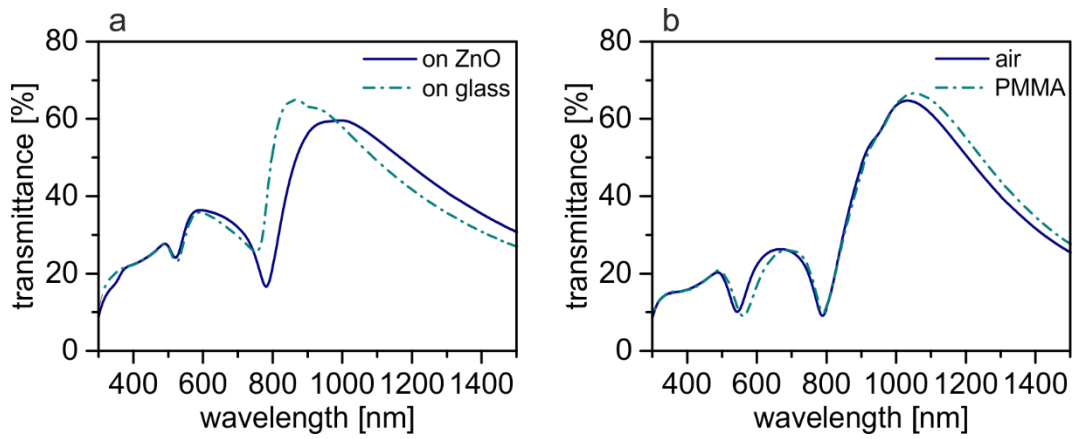


**Figure 1.16.** Influence of the surrounding medium. (a) Comparison of the transmittance spectra of gold nanohole arrays ( $t_{Au} = 100$  nm,  $P = 570$  nm,  $d/d_0$  ratio of 0.7) on substrates with different refractive index ( $n_{\text{glass}} \approx 1.54$ ;  $n_{\text{ZnO}} \approx 1.9$ ). (b) Comparison of the transmittance spectra of gold nanohole arrays ( $t_{Au} = 100$  nm,  $P = 570$  nm,  $d/d_0$  ratio of 0.7) on glass covered with air ( $n_{\text{air}} \approx 1.00$ ) or 30 nm PMMA ( $n_{\text{PMMA}} \approx 1.48$ ).

## 1.4 Colloidal Light Management in Thin-Film Photovoltaics

The term “thin-film photovoltaics” summarizes several new types of solar cells and is primarily based on the production process of the solar cells rather than the materials used, as the absorbing layer can be organic or inorganic. Typical inorganic materials, which are commercially used in thin-film solar cells, are cadmium telluride (CdTe), copper indium gallium diselenide (CIGS) or amorphous silicon (a-Si).<sup>234</sup> Apart from that, organic and hybrid materials are still part of ongoing research such as polymer solar cells, perovskite solar cells or dye-sensitized solar cells.<sup>235-237</sup> Thin-film solar cells are prepared by coating processes like printing or vacuum deposition and rely on extremely thin layers of the photoactive material, with a thickness of usually below one micrometer. This allows for a cheaper production and a shorter energy payback time compared conventional solar cells made of crystalline silicon, which are very costly, especially regarding the high energy needs in production. Moreover, thin-film solar cells can be prepared on flexible substrates or curved surfaces, making them attractive for mobile and integrated applications.<sup>238</sup> Furthermore, the cells are very efficient at weak (diffuse) light conditions.

However, the thickness of the absorbing layer is limited not only because of the coating processes but also due to the limited exciton diffusion length and low charge carrier mobility in these materials. Commercial, crystalline silicon solar cells use light harvesting layers with a thickness of up to 200  $\mu\text{m}$  to ensure a complete absorption of the incident light above the bandgap. In thin-film solar cells, the absorber thickness is often not sufficient for an efficient absorption of the incident light. Thus, semiconductor materials with high absorption coefficients are needed. One promising candidate is perovskite, which exhibits high charge carrier mobilities and an absorption near unity within its bandgap for only 400 nm thick films.<sup>235,239</sup>

Apart from new absorber materials, light management is used in state-of-the-art solar cells to optimize the absorption within the light-harvesting layer. For this, the cell structures are modified by introducing antireflective coatings, waveguiding structures, structured back-electrodes, microlens arrays or microcavity structures.<sup>196,240-245</sup> Wet-chemically prepared colloidal structures can be a very cheap and simple way to realize light management concepts and thus to overcome the inefficient light absorption in thin-film solar cells.<sup>24,25</sup> Here, the colloids are not implemented to allow for the solution-processability of the photoactive layers or electrodes but to enhance the efficiency of the devices.<sup>246-251</sup>

Colloidal particles have been introduced at various positions in thin-film solar cells. Dielectric particles can act as antireflective coatings when placed at the glass/air interface on top of the

transparent electrode (Figure 1.17a).<sup>252,253</sup> Analogously, metal nanoparticles can scatter light into a higher-index substrate and have been used as antireflective coating on top of a thin-film silicon solar cell.<sup>254-256</sup>

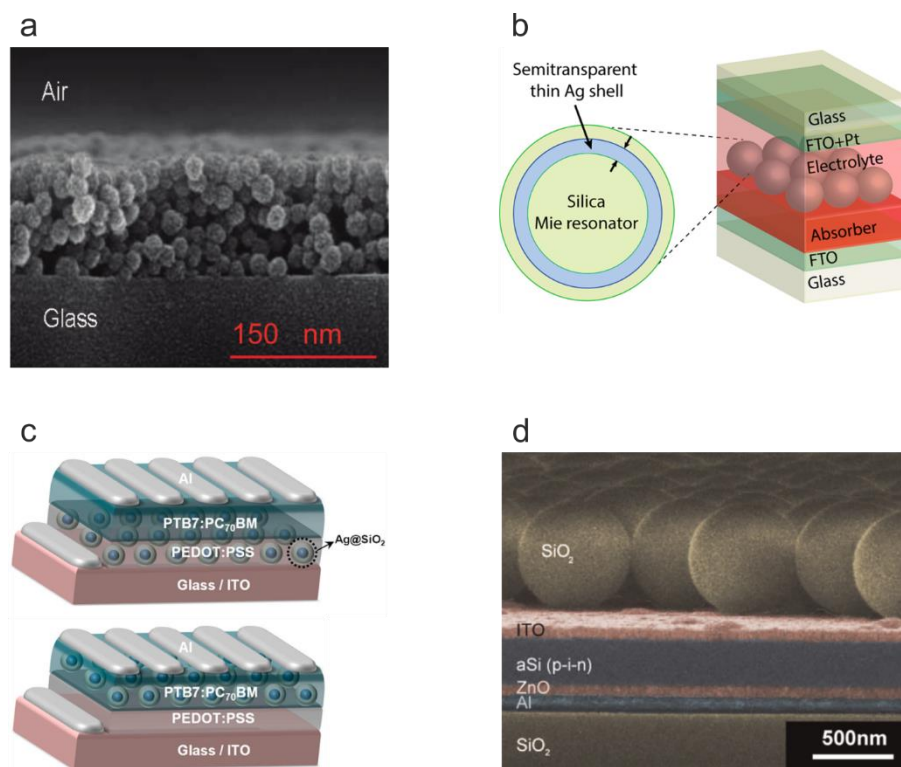


**Figure 1.17.** Light management in thin-film solar cells with colloidal particles. (a) Antireflective coating based on mesoporous silica nanoparticles. (b) SiO<sub>2</sub>/Ag/SiO<sub>2</sub> core/shell/shell particles as back-scatterers on top of the absorber layer of a dye-sensitized solar cell. (c) Ag/SiO<sub>2</sub> core/shell particles placed in the hole-transport layer and the active layer of polymer solar cells as light-scattering centers. (d) Monolayer of SiO<sub>2</sub> spheres assembled on the transparent electrode of an amorphous silicon thin-film solar cell for light incoupling into the photoactive layer. (a) Reprinted with permission from Ref. 253. ©2012 American Chemical Society. (b) Reprinted with permission from Ref. 257. ©2016 American Chemical Society. (c) Reprinted with permission from Ref. 258. ©2013 American Chemical Society. (d) Reprinted with permission from Ref. 259. ©2013 Wiley-VCH.

Moreover, metal nanoparticles have been incorporated into the active layer or the charge transport layer. The impact of metal particles and the exact mechanisms leading to enhanced efficiencies are complex and hard to distinguish. Metal nanoparticles show strong absorption peaks at the LSP resonance and concomitantly exhibit very high scattering cross-sections. Usually, the noble metals gold or silver are used due to the overlap of their LSP resonances with the solar spectrum and their relatively low absorption losses. In many cases, the enhanced efficiency is assigned to scattering of the incident light at the particles and thus a longer path

length of the photons in the absorber resulting in a higher absorption probability. This typically results in an increased short-circuit current density of the devices.<sup>260,261</sup>

The balance between absorption and scattering can be adjusted by tuning the size and shape of the particles.<sup>24</sup> Baek *et al.* introduced silver nanoparticles of distinct sizes into the hole conducting layer near the ITO electrode.<sup>260</sup> The optimum efficiency was found for particles with a diameter of 67 nm, which showed the highest ratio of forward scattered power. Particles with more corners were found to exhibit stronger scattering and thus a higher efficiency enhancement when mixed into the hole transport layer or the active layer.<sup>262,263</sup>

When placed near the back-electrode, metal nanoparticles can efficiently scatter light that is transmitted through the active layer back into the absorber (Figure 1.17b).<sup>264,265</sup> Dabirian *et al.* placed wavelength-scale SiO<sub>2</sub>/Ag/SiO<sub>2</sub> core/shell/shell particles on top of the mesoporous layer in a dye-sensitized solar cell. The particles efficiently scattered the transmitted light and significantly improved the short-circuit current density of the devices.<sup>257</sup>

Scattering was also identified as the primary mechanism for enhanced efficiencies in solar cells with particles introduced into or near the active layer.<sup>261</sup> Choi *et al.* additionally ascribed the increase in efficiency to a contribution of the enhanced electric near-field. Therefore, silver nanoparticles placed in the active layer outperformed particles in the hole conducting layer due to the shorter distance between the particles and the active layer (Figure 1.17c).<sup>258</sup> The increased absorption spectrally coincides with the LSP resonances of the particles. Thus, by incorporating both, silver and gold nanoparticles, the absorption can be enhanced in a broader absorption region.<sup>266</sup> A broader absorption enhancement can also be reached by using metal nanoparticle clusters.<sup>267,268</sup> Moreover, the impact of metal nanoparticles on the electrical device properties has been studied. A passivation with a dielectric shell is often used to prevent exciton quenching and charge recombination at the metal surface.<sup>258,269,270</sup> However, the shell has to be thin enough for the electric field induced by the metal core to protrude into the active layer.<sup>271</sup> Furthermore, metal nanoparticles mixed into the active layer or the charge transport layers have been discussed to enhance the exciton dissociation as well as the hole transport properties.<sup>266,272,273</sup> While the open circuit voltage is usually not affected by the integration of metal nanoparticles, this results in a slightly increased fill factor.

In order to obtain reproducible and controllable devices, self-assembled structures can be used for a higher control over the particle density and distribution.<sup>274</sup> Besides, particle arrays can evoke collective coupling effects, which can prove beneficial in thin-film solar cells.<sup>24,196</sup> For example, a monolayer of dielectric spheres on top of a thin-film amorphous silicon solar cell can enhance the efficiency of the device by coupling light into the absorber by Fabry-Pérot

resonances and resonant photonic crystal modes (Figure 1.17d).<sup>259</sup> Moreover, this coupling mechanism is mostly insensitive towards the angle of incidence.

Instead of directly introducing particles into the solar cells, colloids can also act as a template structure. By evaporating metal through a close-packed monolayer of polymer spheres, highly uniform metal nanoparticle arrays were fabricated on the ITO electrode of bulk-heterojunction polymer solar cells (Figure 1.18a).<sup>275,276</sup> In both examples from literature, the device absorption and thus the short-circuit current density was increased around the LSP resonance of the particles.

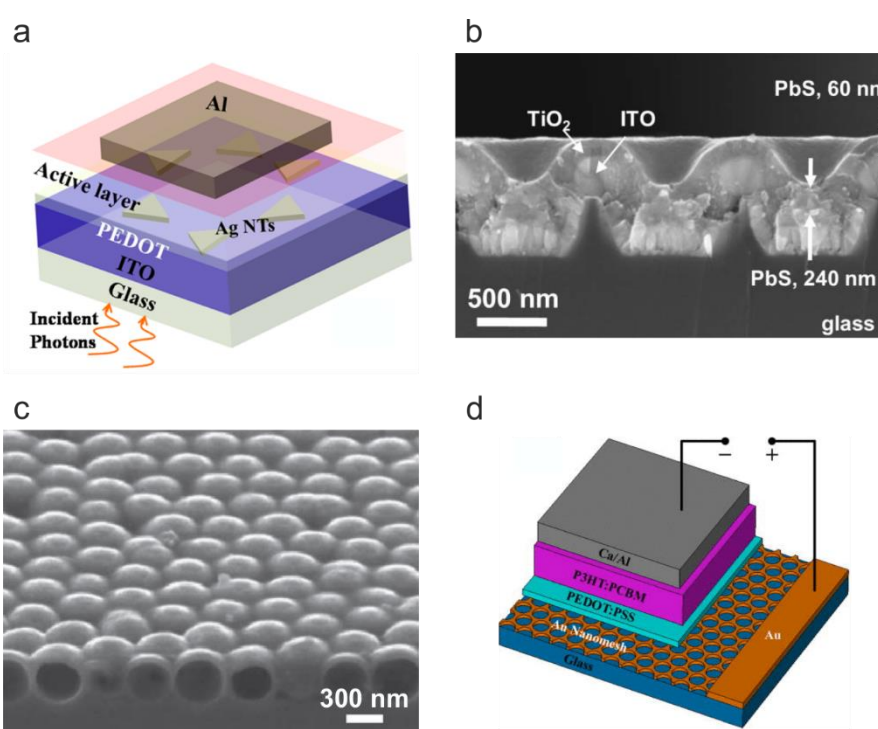


**Figure 1.18.** Light management structures in thin-film solar cells fabricated by colloidal lithography. (a) Nanopyramid array on the transparent ITO electrode for near-field enhancement in the active layer. (b) Colloidal quantum dot solar cell prepared on a nanohole patterned glass substrate. (c) Silicon nanoshell absorber fabricated by chemical vapor deposition of silicon onto colloidal silica spheres. (d) Gold nanohole array integrated as transparent electrode in a polymer solar cell. (a) Reprinted with permission from Ref. 276. ©2012 American Chemical Society. (b) Reprinted with permission from Ref. 277. ©2013 Nature Publishing Group. (c) Reprinted with permission from Ref. 278. ©2012 Nature Publishing Group. (d) Reprinted with permission from Ref. 279. ©2012 AIP Publishing LLC.

Furthermore, colloidal lithography can be applied to pattern specific elements of the device such as the front- or back-electrode or the substrate. Colloidal monolayers of silica or polymer particles have been applied to etch the glass substrate<sup>280,281</sup> or the active material.<sup>282-285</sup> The

resulting nanocone or nanopillar arrays exhibit highly efficient antireflective properties over a broad range of incident angles.

Alternatively, Li *et al.* used a close-packed monolayer of polystyrene spheres to create an array of TiO<sub>2</sub> nanopillars on top of a thin-film quantum-well solar cell.<sup>286</sup> The array acted as a gradient refractive index antireflective coating and scattered light into guided modes within the semiconductor.

Thin-film silicon solar cells have also been prepared on nanohole structured glass substrates (Figure 1.18b).<sup>277</sup> The nanohole arrays were prepared by depositing metal onto non-close-packed particle monolayers and using the resulting metal nanohole array as an etching mask. Due to the conformal coating of the device layers, the colloidal quantum dot solar cells benefited from both, an antireflective effect at the glass/ITO interface and an enhanced electric field at the back-electrode.

Similarly, patterned back-electrodes have been fabricated by metal deposition on metal nanohole arrays<sup>287</sup> as well as on nanohole<sup>288</sup> and nanocone<sup>289</sup> structured glass substrates, which were made by colloidal lithography. Alternatively, electrodeposition of silver through close-packed particle monolayers readily yields nanobowl arrays, which were used as back-electrode for thin-film silicon solar cells by Lal *et al.*<sup>290</sup> In all studies, the absorption of the devices was effectively increased. This was explained with an efficient back-scattering of the light impinging on the electrode and enhanced field intensities within the absorber layer due to the excitation of SPP and LSP resonances as well as guided modes. Nishimura *et al.* prepared TiO<sub>2</sub> inverse opals on dye-sensitized photoelectrodes. The inverse opals acted as a dielectric mirror and the device exhibited an increased short-circuit photocurrent efficiency.<sup>291</sup>

Alternatively, the semiconductor itself can be structured using colloids as a sacrificial template. Wavelength-scale silicon nanoshells show an enhanced absorption compared to flat silicon due to the absorption of resonant whispering gallery modes (Figure 1.18c).<sup>278</sup> The nanoshells were prepared via chemical vapor deposition of silicon onto silica particles as a template. In another study, Wei *et al.* formed PEDOT nanobowl arrays on ITO by electrodeposition through close-packed colloidal monolayers.<sup>292</sup> This led to an increased light path in the active layer in the assembled device as well as an increased interface between the PEDOT and the absorber CuPc and thus a higher charge collection efficiency.

Finally, the metal nanohole arrays described in chapter 1.3.3 have been studied as transparent conducting electrodes for thin-film solar cells (Figure 1.18d).<sup>157,293,294</sup> In addition to the possible

light trapping properties of the nanohole pattern, nanohole arrays could be used as a replacement for ITO.

Indeed, metal nanohole array electrodes prepared by colloidal lithography have been shown to enhance the efficiency of small-molecule thin-film solar cells. The enhanced efficiency was ascribed to the increased interfacial area between hole and electron conductor and high electric fields in close vicinity to the perforated electrode due to the excitation of surface plasmons.<sup>295</sup> Moreover, guided modes localized in the active layer were discussed to contribute to the light trapping capability of metal nanohole arrays.<sup>296,297</sup>

However, in polymer solar cells, the incorporation of metal nanohole arrays resulted in high losses in the short-circuit current density due to the limited transmittance of the electrodes.<sup>279,298,299</sup> Unfortunately, this loss in transmittance compared to ITO cannot be avoided by increasing the hole size without sacrificing the high conductivity of metal nanohole arrays due to the percolation threshold.<sup>219,300</sup> Obviously, it is not a trivial task to replace ITO by nanohole electrodes while retaining or even enhancing the power conversion efficiency of the device. Nevertheless, metal nanohole arrays remain an attractive tool to reveal the distinct interactions of plasmonic resonances and diffracted modes with absorber layers in general and thin-film solar cell devices in specific.

## References

1. Ozin, G. A., Manners, I., Fournier-Bidoz, S. & Arsenault, A. Dream Nanomachines. *Adv. Mater.* **17**, 3011-3018 (2005).
2. Edwards, B. C. The Space Elevator NIAC Phase II Final Report. (Nasa Institute for Advanced Concepts, 2003).
3. Franklin, A. D. DEVICE TECHNOLOGY. Nanomaterials in transistors: From high-performance to thin-film applications. *Science* **349**, aab2750 (2015).
4. Shirasaki, Y., Supran, G. J., Bawendi, M. G. & Bulović, V. Emergence of colloidal quantum-dot light-emitting technologies. **7**, 13 (2012).
5. Min, W. L., Jiang, B. & Jiang, P. Bioinspired Self-Cleaning Antireflection Coatings. *Adv. Mater.* **20**, 3914-+ (2008).
6. Moritz, M. & Geszke-Moritz, M. The newest achievements in synthesis, immobilization and practical applications of antibacterial nanoparticles. *Chem. Eng. J.* **228**, 596-613 (2013).
7. Shi, H., Magaye, R., Castranova, V. & Zhao, J. Titanium dioxide nanoparticles: a review of current toxicological data. *Particle and Fibre Toxicology* **10**, 15 (2013).
8. International Organization for Standardization. *ISO/TC 229 Nanotechnologies*, <https://www.iso.org/committee/381983.html> (2005).
9. Schmid, G. *Nanoparticles: From Theory to Application*. (WILEY-VCH Verlag GmbH & Co. KGaA, Weinheim, 2003).

10. Sarid, D. & Challener, W. *Modern Introduction to Surface Plasmons*. (Cambridge University Press, Cambridge, 2010).
11. Anker, J. N., Hall, W. P., Lyandres, O., Shah, N. C., Zhao, J. & Van Duyne, R. P. Biosensing with plasmonic nanosensors. *Nat Mater* **7**, 442-453 (2008).
12. Nakamoto, K., Kurita, R., Niwa, O., Fujii, T. & Nishida, M. Development of a mass-producible on-chip plasmonic nanohole array biosensor. *Nanoscale* **3**, 5067-5075 (2011).
13. Camden, J. P., Dieringer, J. A., Zhao, J. & Van Duyne, R. P. Controlled Plasmonic Nanostructures for Surface-Enhanced Spectroscopy and Sensing. *Acc. Chem. Res.* **41**, 1653-1661 (2008).
14. Corcoran, B., Monat, C., Grillet, C., Moss, D. J., Eggleton, B. J., White, T. P., O'Faolain, L. & Krauss, T. F. Green light emission in silicon through slow-light enhanced third-harmonic generation in photonic-crystal waveguides. *Nat. Photonics* **3**, 206-210 (2009).
15. Inoue, D., Miura, A., Nomura, T., Fujikawa, H., Sato, K., Ikeda, N., Tsuya, D., Sugimoto, Y. & Koide, Y. Polarization independent visible color filter comprising an aluminum film with surface-plasmon enhanced transmission through a subwavelength array of holes. *Appl. Phys. Lett.* **98**, 093113 (2011).
16. Tan, S. J., Zhang, L., Zhu, D., Goh, X. M., Wang, Y. M., Kumar, K., Qiu, C. W. & Yang, J. K. Plasmonic color palettes for photorealistic printing with aluminum nanostructures. *Nano Lett.* **14**, 4023-4029 (2014).
17. Lu, B. R., Xu, C., Liao, J., Liu, J. & Chen, Y. High-resolution plasmonic structural colors from nanohole arrays with bottom metal disks. *Opt. Lett.* **41**, 1400-1403 (2016).
18. Cheng, F., Yang, X., Rosenmann, D., Stan, L., Czuplewski, D. & Gao, J. Enhanced structural color generation in aluminum metamaterials coated with a thin polymer layer. *Opt. Express* **23**, 25329-25339 (2015).
19. Park, H. J., Xu, T., Lee, J. Y., Ledbetter, A. & Guo, L. J. Photonic color filters integrated with organic solar cells for energy harvesting. *ACS Nano* **5**, 7055-7060 (2011).
20. Sun, T., Zhang, Y. S., Pang, B., Hyun, D. C., Yang, M. & Xia, Y. Engineered Nanoparticles for Drug Delivery in Cancer Therapy. *Angew. Chem. Int. Ed.* **53**, 12320-12364 (2014).
21. Wu, H. Y., Liu, L. J., Lu, M. & Cunningham, B. T. Lasing Emission from Plasmonic Nanodome Arrays. *Advanced Optical Materials* **4**, 708-714 (2016).
22. Zhou, W., Dridi, M., Suh, J. Y., Kim, C. H., Co, D. T., Wasielewski, M. R., Schatz, G. C. & Odom, T. W. Lasing action in strongly coupled plasmonic nanocavity arrays. *Nat Nano* **8**, 506-511 (2013).
23. Meng, X., Liu, J., Kildishev, A. V. & Shalaev, V. M. Highly directional spaser array for the red wavelength region. *Laser & Photonics Reviews* **8**, 896-903 (2014).
24. Karg, M., König, T. A. F., Retsch, M., Stelling, C., Reichstein, P. M., Honold, T., Thelakkat, M. & Fery, A. Colloidal self-assembly concepts for light management in photovoltaics. *Mater. Today* **18**, 185-205 (2015).
25. Atwater, H. A. & Polman, A. Plasmonics for improved photovoltaic devices. *Nat. Mater.* **9**, 205-213 (2010).
26. Petoukhoff, C. E., Shen, Z., Jain, M., Chang, A. & O'Carroll, D. M. Plasmonic electrodes for bulk-heterojunction organic photovoltaics: a review. *J. Photonics Energy* **5**, 057002 (2015).
27. Ahn, S., Rourke, D. & Park, W. Plasmonic nanostructures for organic photovoltaic devices. *J. Opt.* **18**, 033001 (2016).

28. Maurer, T., Adam, P.-M. & Lévêque, G. Coupling between plasmonic films and nanostructures: from basics to applications. *Nanophotonics* **4**, 363-382 (2015).
29. Ross, M. B., Mirkin, C. A. & Schatz, G. C. Optical Properties of One-, Two-, and Three-Dimensional Arrays of Plasmonic Nanostructures. *The Journal of Physical Chemistry C* **120**, 816-830 (2016).
30. Watt, F., Bettioli, A. A., Van Kan, J. A., Teo, E. J. & Breese, M. B. H. Ion Beam Lithography and Nanofabrication: A Review. *International Journal of Nanoscience* **04**, 269-286 (2005).
31. Chen, Y. Nanofabrication by electron beam lithography and its applications: A review. *Microelectron. Eng.* **135**, 57-72 (2015).
32. Park, J. *et al.* Nanoparticle imaging. 3D structure of individual nanocrystals in solution by electron microscopy. *Science* **349**, 290-295 (2015).
33. Van Tendeloo, G., Bals, S., Van Aert, S., Verbeeck, J. & Van Dyck, D. Advanced electron microscopy for advanced materials. *Adv. Mater.* **24**, 5655-5675 (2012).
34. Bals, S., Goris, B., Liz-Marzan, L. M. & Van Tendeloo, G. Three-dimensional characterization of noble-metal nanoparticles and their assemblies by electron tomography. *Angew. Chem. Int. Ed. Engl.* **53**, 10600-10610 (2014).
35. Vogel, N., Weiss, C. K. & Landfester, K. From soft to hard: the generation of functional and complex colloidal monolayers for nanolithography. *Soft Matter* **8**, 4044-4061 (2012).
36. Vogel, N., Retsch, M., Fustin, C. A., Del Campo, A. & Jonas, U. Advances in colloidal assembly: the design of structure and hierarchy in two and three dimensions. *Chem. Rev.* **115**, 6265-6311 (2015).
37. McNaught, A. D. & Wilkinson, A. *IUPAC. Compendium of Chemical Terminology, 2nd ed. (the "Gold Book")*. (Blackwell Scientific Publications, Oxford, 1997).
38. Dokou, E., Barteau, M. A., Wagner, N. J. & Lenhoff, A. M. Effect of Gravity on Colloidal Deposition Studied by Atomic Force Microscopy. *J. Colloid Interface Sci.* **240**, 9-16 (2001).
39. Xia, Y., Gates, B., Yin, Y. & Lu, Y. Monodispersed Colloidal Spheres: Old Materials with New Applications. *Adv. Mater.* **12**, 693-713 (2000).
40. Landfester, N. B., F. Tiarks, M. Antonietti. Formulation and Stability Mechanisms of Polymerizable Miniemulsions. *Macromolecules* **32**, 5222-5228 (1999).
41. Guo, J. S., El-Aasser, M. S. & Vanderhoff, J. W. Microemulsion polymerization of styrene. *J. Polym. Sci., Part A: Polym. Chem.* **27**, 691-710 (1989).
42. Tseng, C. M., Lu, Y. Y., El-Aasser, M. S. & Vanderhoff, J. W. Uniform polymer particles by dispersion polymerization in alcohol. *J. Polym. Sci., Part A: Polym. Chem.* **24**, 2995-3007 (1986).
43. Li, W.-H. & Stöver, H. D. H. Mono- or narrow disperse poly(methacrylate-co-divinylbenzene) microspheres by precipitation polymerization. *J. Polym. Sci., Part A: Polym. Chem.* **37**, 2899-2907 (1999).
44. Hohenstein, W. P. & Mark, H. Polymerization of olefins and diolefins in suspension and emulsion. Part II. *J. Polym. Sci.* **1**, 549-580 (1946).
45. Stöver, W., Fink, A. & Bohn, E. Controlled growth of monodisperse silica spheres in the micron size range. *J. Colloid Interface Sci.* **26**, 62-69 (1968).
46. Lee, Y. J. *et al.* Ultraspherical, highly spherical monocrystalline gold particles for precision plasmonics. *ACS Nano* **7**, 11064-11070 (2013).
47. Vogel, N., Belisle, R. A., Hatton, B., Wong, T.-S. & Aizenberg, J. Transparency and damage tolerance of patternable omniphobic lubricated surfaces based on inverse colloidal monolayers. **4**, 2176 (2013).

48. Li, Y. *et al.* Biomimetic Surfaces for High-Performance Optics. *Adv. Mater.* **21**, 4731-4734 (2009).
49. Gao, T., Jelle, B. P. & Gustavsen, A. Antireflection properties of monodisperse hollow silica nanospheres. *Appl. Phys. A* **110**, 65-70 (2013).
50. Liu, B. T. & Yeh, W. D. Antireflective surface fabricated from colloidal silica nanoparticles. *Colloid Surface A* **356**, 145-149 (2010).
51. Park, S. G., Lee, S. Y., Jang, S. G. & Yang, S. M. Perfectly hydrophobic surfaces with patterned nanoneedles of controllable features. *Langmuir* **26**, 5295-5299 (2010).
52. Nemiroski, A., Gonidec, M., Fox, J. M., Jean-Remy, P., Turnage, E. & Whitesides, G. M. Engineering shadows to fabricate optical metasurfaces. *ACS Nano* **8**, 11061-11070 (2014).
53. Romanov, S. G. *et al.* Probing guided modes in a monolayer colloidal crystal on a flat metal film. *Phys. Rev. B* **86**, 195145 (2012).
54. von Freymann, G., Kitaev, V., Lotsch, B. V. & Ozin, G. A. Bottom-up assembly of photonic crystals. *Chem. Soc. Rev.* **42**, 2528-2554 (2013).
55. Galisteo-López, J. F., Ibisate, M., Sapienza, R., Froufe-Pérez, L. S., Blanco, Á. & López, C. Self-Assembled Photonic Structures. *Adv. Mater.* **23**, 30-69 (2011).
56. Kolle, M., Salgard-Cunha, P. M., Scherer, M. R., Huang, F., Vukusic, P., Mahajan, S., Baumberg, J. J. & Steiner, U. Mimicking the colourful wing scale structure of the *Papilio blumei* butterfly. *Nat Nanotechnol* **5**, 511-515 (2010).
57. Aguirre, C. I., Reguera, E. & Stein, A. Tunable Colors in Opals and Inverse Opal Photonic Crystals. *Adv. Funct. Mater.* **20**, 2565-2578 (2010).
58. Park, C., Koh, K. & Jeong, U. Structural Color Painting by Rubbing Particle Powder. **5**, 8340 (2015).
59. Ge, J. & Yin, Y. Responsive Photonic Crystals. *Angew. Chem. Int. Ed.* **50**, 1492-1522 (2011).
60. Fenzl, C., Hirsch, T. & Wolfbeis, O. S. Photonic Crystals for Chemical Sensing and Biosensing. *Angew. Chem. Int. Ed.* **53**, 3318-3335 (2014).
61. Cheng, W., Wang, J., Jonas, U., Fytas, G. & Stefanou, N. Observation and tuning of hypersonic bandgaps in colloidal crystals. *Nat Mater* **5**, 830-836 (2006).
62. Still, T., Cheng, W., Retsch, M., Jonas, U. & Fytas, G. Colloidal systems: a promising material class for tailoring sound propagation at high frequencies. *Journal of Physics-Condensed Matter* **20**, 404203 (2008).
63. Schall, P., Cohen, I., Weitz, D. A. & Spaepen, F. Visualization of dislocation dynamics in colloidal crystals. *Science* **305**, 1944-1948 (2004).
64. Schall, P., Cohen, I., Weitz, D. A. & Spaepen, F. Visualizing dislocation nucleation by indenting colloidal crystals. *Nature* **440**, 319-323 (2006).
65. Ye, X. & Qi, L. Two-dimensionally patterned nanostructures based on monolayer colloidal crystals: Controllable fabrication, assembly, and applications. *Nano Today* **6**, 608-631 (2011).
66. Park, C., Lee, T., Xia, Y., Shin, T. J., Myoung, J. & Jeong, U. Quick, Large-Area Assembly of a Single-Crystal Monolayer of Spherical Particles by Unidirectional Rubbing. *Adv. Mater.* **26**, 4633-4638 (2014).
67. Israelachvili, J. N. *Intermolecular and surface forces*. 3rd edn, (Elsevier Ltd, Oxford, 2011).
68. Derjaguin, B. & Landau, L. Theory of the stability of strongly charged lyophobic sols and of the adhesion of strongly charged particles in solutions of electrolytes. *Prog. Surf. Sci.* **43**, 30-59 (1993).

69. Verwey, E. J. W., Overbeek, J. T. G. & van Nes, K. *Theory of the Stability of Lyophobic Colloids: The Interaction of Sol Particles Having an Electric Double Layer*. (Elsevier Publishing Company, 1948).
70. Li, Q., Jonas, U., Zhao, X. S. & Kappl, M. The forces at work in colloidal self-assembly: a review on fundamental interactions between colloidal particles. *Asia-Pac. J. Chem. Eng.* **3**, 255-268 (2008).
71. Zhulina, E. B., Borisov, O. V. & Priamitsyn, V. A. Theory of steric stabilization of colloid dispersions by grafted polymers. *J. Colloid Interface Sci.* **137**, 495-511 (1990).
72. Napper, D. H. Steric stabilization. *J. Colloid Interface Sci.* **58**, 390-407 (1977).
73. Jenkins, P. & Snowden, M. Depletion flocculation in colloidal dispersions. *Adv. Colloid Interface Sci.* **68**, 57-96 (1996).
74. Dickinson, E. & Eriksson, L. Particle flocculation by adsorbing polymers. *Adv. Colloid Interface Sci.* **34**, 1-29 (1991).
75. Nutz, F. A., Ruckdeschel, P. & Retsch, M. Polystyrene colloidal crystals: Interface controlled thermal conductivity in an open-porous mesoparticle superstructure. *J. Colloid Interface Sci.* **457**, 96-101 (2015).
76. Jonas, U., del Campo, A., Krüger, C., Glasser, G. & Boos, D. Colloidal assemblies on patterned silane layers. *Proceedings of the National Academy of Sciences* **99**, 5034-5039 (2002).
77. Tien, J., Terfort, A. & Whitesides, G. M. Microfabrication through Electrostatic Self-Assembly. *Langmuir* **13**, 5349-5355 (1997).
78. Semmler, M., Mann, E. K., Rička, J. & Borkovec, M. Diffusional Deposition of Charged Latex Particles on Water–Solid Interfaces at Low Ionic Strength. *Langmuir* **14**, 5127-5132 (1998).
79. Giersig, M. & Mulvaney, P. Preparation of ordered colloid monolayers by electrophoretic deposition. *Langmuir* **9**, 3408-3413 (1993).
80. Zhang, K.-Q. & Liu, X. Y. In situ observation of colloidal monolayer nucleation driven by an alternating electric field. *Nature* **429**, 739-743 (2004).
81. Pieranski, P. Two-Dimensional Interfacial Colloidal Crystals. *Phys. Rev. Lett.* **45**, 569-572 (1980).
82. Kralchevsky, P. A. & Nagayama, K. Capillary forces between colloidal particles. *Langmuir* **10**, 23-36 (1994).
83. Kralchevsky, P. A. & Nagayama, K. Capillary interactions between particles bound to interfaces, liquid films and biomembranes. *Adv. Colloid Interface Sci.* **85**, 145-192 (2000).
84. Denkov, N., Velev, O., Kralchevski, P., Ivanov, I., Yoshimura, H. & Nagayama, K. Mechanism of formation of two-dimensional crystals from latex particles on substrates. *Langmuir* **8**, 3183-3190 (1992).
85. Dimitrov, A. S. & Nagayama, K. Continuous Convective Assembling of Fine Particles into Two-Dimensional Arrays on Solid Surfaces. *Langmuir* **12**, 1303-1311 (1996).
86. Malaquin, L., Kraus, T., Schmid, H., Delamarche, E. & Wolf, H. Controlled particle placement through convective and capillary assembly. *Langmuir* **23**, 11513-11521 (2007).
87. Sun, J., Tang, C. J., Zhan, P., Han, Z. L., Cao, Z. S. & Wang, Z. L. Fabrication of centimeter-sized single-domain two-dimensional colloidal crystals in a wedge-shaped cell under capillary forces. *Langmuir* **26**, 7859-7864 (2010).
88. Ye, R., Ye, Y. H., Zhou, Z. & Xu, H. Gravity-assisted convective assembly of centimeter-sized uniform two-dimensional colloidal crystals. *Langmuir* **29**, 1796-1801 (2013).

89. Quint, S. B. & Pacholski, C. Extraordinary long range order in self-healing non-close packed 2D arrays. *Soft Matter* **7**, 3735-3738 (2011).
90. Mihi, A., Ocaña, M. & Míguez, H. Oriented Colloidal-Crystal Thin Films by Spin-Coating Microspheres Dispersed in Volatile Media. *Adv. Mater.* **18**, 2244-2249 (2006).
91. Vogel, N., de Viguierie, L., Jonas, U., Weiss, C. K. & Landfester, K. Wafer-Scale Fabrication of Ordered Binary Colloidal Monolayers with Adjustable Stoichiometries. *Adv. Funct. Mater.* **21**, 3064-3073 (2011).
92. Zhang, J. T., Wang, L., Lamont, D. N., Velankar, S. S. & Asher, S. A. Fabrication of large-area two-dimensional colloidal crystals. *Angew. Chem. Int. Ed. Engl.* **51**, 6117-6120 (2012).
93. Dai, Z., Li, Y., Duan, G., Jia, L. & Cai, W. Phase diagram, design of monolayer binary colloidal crystals, and their fabrication based on ethanol-assisted self-assembly at the air/water interface. *ACS Nano* **6**, 6706-6716 (2012).
94. Isa, L., Kumar, K., Müller, M., Grolig, J., Textor, M. & Reimhult, E. Particle lithography from colloidal self-assembly at liquid-liquid interfaces. *ACS Nano* **4**, 5665-5670 (2010).
95. Reynaert, S., Moldenaers, P. & Vermant, J. Control over colloidal aggregation in monolayers of latex particles at the oil-water interface. *Langmuir* **22**, 4936-4945 (2006).
96. Law, A. D., Buzza, D. M. & Horozov, T. S. Two-dimensional colloidal alloys. *Phys. Rev. Lett.* **106**, 128302 (2011).
97. Ershov, D., Sprakel, J., Appel, J., Cohen Stuart, M. A. & van der Gucht, J. Capillarity-induced ordering of spherical colloids on an interface with anisotropic curvature. *Proc. Natl. Acad. Sci. U.S.A.* **110**, 9220-9224 (2013).
98. Vogel, N., Goerres, S., Landfester, K. & Weiss, C. K. A Convenient Method to Produce Close- and Non-close-Packed Monolayers using Direct Assembly at the Air-Water Interface and Subsequent Plasma-Induced Size Reduction. *Macromol. Chem. Phys.* **212**, 1719-1734 (2011).
99. Retsch, M., Zhou, Z., Rivera, S., Kappl, M., Zhao, X. S., Jonas, U. & Li, Q. Fabrication of Large-Area, Transferable Colloidal Monolayers Utilizing Self-Assembly at the Air/Water Interface. *Macromol. Chem. Phys.* **210**, 230-241 (2009).
100. Shinotsuka, K., Kajita, Y., Hongo, K. & Hatta, Y. Crystal Perfection of Particle Monolayer at the Air-Water Interface. *Langmuir* **31**, 11452-11457 (2015).
101. Meng, X. & Qiu, D. Gas-flow-induced reorientation to centimeter-sized two-dimensional colloidal single crystal of polystyrene particle. *Langmuir* **30**, 3019-3023 (2014).
102. Li, X., Wang, T., Zhang, J., Yan, X., Zhang, X., Zhu, D., Li, W., Zhang, X. & Yang, B. Modulating two-dimensional non-close-packed colloidal crystal arrays by deformable soft lithography. *Langmuir* **26**, 2930-2936 (2010).
103. Ramiro-Manzano, F., Bonet, E., Rodriguez, I. & Meseguer, F. Colloidal crystal thin films grown into corrugated surface templates. *Langmuir* **26**, 4559-4562 (2010).
104. Hur, J. & Won, Y. Y. Fabrication of high-quality non-close-packed 2D colloid crystals by template-guided Langmuir-Blodgett particle deposition. *Soft Matter* **4**, 1261-1269 (2008).
105. Lu, C. H., Möhwald, H. & Fery, A. A lithography-free method for directed colloidal crystal assembly based on wrinkling. *Soft Matter* **3**, 1530-1536 (2007).
106. Khanh, N. N. & Yoon, K. B. Facile organization of colloidal particles into large, perfect one- and two-dimensional arrays by dry manual assembly on patterned substrates. *J. Am. Chem. Soc.* **131**, 14228-14230 (2009).

107. Yin, Y. D. & Xia, Y. N. Self-assembly of monodispersed spherical colloids into complex aggregates with well-defined sizes, shapes, and structures. *Adv. Mater.* **13**, 267-271 (2001).
108. Kraus, T., Malaquin, L., Schmid, H., Riess, W., Spencer, N. D. & Wolf, H. Nanoparticle printing with single-particle resolution. *Nat Nanotechnol* **2**, 570-576 (2007).
109. Kumacheva, E., Golding, R. K., Allard, M. & Sargent, E. H. Colloid Crystal Growth on Mesoscopically Patterned Surfaces: Effect of Confinement. *Adv. Mater.* **14**, 221-224 (2002).
110. Lee, I., Zheng, H. P., Rubner, M. F. & Hammond, P. T. Controlled cluster size in patterned particle arrays via directed adsorption on confined surfaces. *Adv. Mater.* **14**, 572-577 (2002).
111. Masuda, Y., Itoh, T. & Koumoto, K. Self-Assembly Patterning of Silica Colloidal Crystals. *Langmuir* **21**, 4478-4481 (2005).
112. Zhang, X., Zhang, J., Zhu, D., Li, X., Zhang, X., Wang, T. & Yang, B. A universal approach to fabricate ordered colloidal crystals arrays based on electrostatic self-assembly. *Langmuir* **26**, 17936-17942 (2010).
113. Friebel, S., Aizenberg, J., Abad, S. & Wiltzius, P. Ultraviolet lithography of self-assembled monolayers for submicron patterned deposition. *Appl. Phys. Lett.* **77**, 2406-2408 (2000).
114. Guo, Q., Arnoux, C. & Palmer, R. E. Guided Assembly of Colloidal Particles on Patterned Substrates. *Langmuir* **17**, 7150-7155 (2001).
115. Chen, Q., Bae, S. C. & Granick, S. Directed self-assembly of a colloidal kagome lattice. *Nature* **469**, 381-384 (2011).
116. Wang, Y., Wang, Y., Breed, D. R., Manoharan, V. N., Feng, L., Hollingsworth, A. D., Weck, M. & Pine, D. J. Colloids with valence and specific directional bonding. *Nature* **491**, 51-55 (2012).
117. Hulteen, J. C. Nanosphere lithography: A materials general fabrication process for periodic particle array surfaces. *Journal of Vacuum Science & Technology A: Vacuum, Surfaces, and Films* **13**, 1553 (1995).
118. Ai, B., Yu, Y., Möhwald, H., Zhang, G. & Yang, B. Plasmonic films based on colloidal lithography. *Adv. Colloid Interface Sci.* **206**, 5-16 (2014).
119. Yang, S. M., Jang, S. G., Choi, D. G., Kim, S. & Yu, H. K. Nanomachining by colloidal lithography. *Small* **2**, 458-475 (2006).
120. Zhang, G. & Wang, D. Colloidal lithography--the art of nanochemical patterning. *Chem Asian J* **4**, 236-245 (2009).
121. Zhang, J., Li, Y., Zhang, X. & Yang, B. Colloidal self-assembly meets nanofabrication: from two-dimensional colloidal crystals to nanostructure arrays. *Adv. Mater.* **22**, 4249-4269 (2010).
122. Li, Y., Cai, W. & Duan, G. Ordered Micro/Nanostructured Arrays Based on the Monolayer Colloidal Crystals†. *Chem. Mater.* **20**, 615-624 (2008).
123. Jensen, T. R., Duval, M. L., Kelly, K. L., Lazarides, A. A., Schatz, G. C. & Van Duyne, R. P. Nanosphere Lithography: Effect of the External Dielectric Medium on the Surface Plasmon Resonance Spectrum of a Periodic Array of Silver Nanoparticles. *The Journal of Physical Chemistry B* **103**, 9846-9853 (1999).
124. Hulteen, J. C., Treichel, D. A., Smith, M. T., Duval, M. L., Jensen, T. R. & Van Duyne, R. P. Nanosphere Lithography: Size-Tunable Silver Nanoparticle and Surface Cluster Arrays. *The Journal of Physical Chemistry B* **103**, 3854-3863 (1999).

125. Haynes, C. L. & Van Duyne, R. P. Nanosphere Lithography: A Versatile Nanofabrication Tool for Studies of Size-Dependent Nanoparticle Optics. *The Journal of Physical Chemistry B* **105**, 5599-5611 (2001).
126. Chan, G. H., Zhao, J., Hicks, E. M., Schatz, G. C. & Van Duyne, R. P. Plasmonic Properties of Copper Nanoparticles Fabricated by Nanosphere Lithography. *Nano Lett.* **7**, 1947-1952 (2007).
127. Kosiorok, A., Kandulski, W., Glaczynska, H. & Giersig, M. Fabrication of nanoscale rings, dots, and rods by combining shadow nanosphere lithography and annealed polystyrene nanosphere masks. *Small* **1**, 439-444 (2005).
128. Gwinner, M. C., Koroknay, E., Fu, L., Patoka, P., Kandulski, W., Giersig, M. & Giessen, H. Periodic large-area metallic split-ring resonator metamaterial fabrication based on shadow nanosphere lithography. *Small* **5**, 400-406 (2009).
129. Kosiorok, A., Kandulski, W., Chudzinski, P., Kempa, K. & Giersig, M. Shadow Nanosphere Lithography: Simulation and Experiment. *Nano Lett.* **4**, 1359-1363 (2004).
130. Akinoglu, E. M., Morfa, A. J. & Giersig, M. Understanding anisotropic plasma etching of two-dimensional polystyrene opals for advanced materials fabrication. *Langmuir* **30**, 12354-12361 (2014).
131. Plettl, A., Enderle, F., Saitner, M., Manzke, A., Pfahler, C., Wiedemann, S. & Ziemann, P. Non-Close-Packed Crystals from Self-Assembled Polystyrene Spheres by Isotropic Plasma Etching: Adding Flexibility to Colloid Lithography. *Adv. Funct. Mater.* **19**, 3279-3284 (2009).
132. Volk, K., Fitzgerald, J. P., Retsch, M. & Karg, M. Time-Controlled Colloidal Superstructures: Long-Range Plasmon Resonance Coupling in Particle Monolayers. *Adv. Mater.* **27**, 7332-7337 (2015).
133. Vogel, N., Fernandez-Lopez, C., Perez-Juste, J., Liz-Marzan, L. M., Landfester, K. & Weiss, C. K. Ordered arrays of gold nanostructures from interfacially assembled Au@PNIPAM hybrid nanoparticles. *Langmuir* **28**, 8985-8993 (2012).
134. Spatz, J. P., Mössmer, S., Hartmann, C., Möller, M., Herzog, T., Krieger, M., Boyen, H.-G., Ziemann, P. & Kabius, B. Ordered Deposition of Inorganic Clusters from Micellar Block Copolymer Films. *Langmuir* **16**, 407-415 (2000).
135. Yan, X., Yao, J., Lu, G., Li, X., Zhang, J., Han, K. & Yang, B. Fabrication of non-close-packed arrays of colloidal spheres by soft lithography. *J. Am. Chem. Soc.* **127**, 7688-7689 (2005).
136. Jiang, P., Prasad, T., McFarland, M. J. & Colvin, V. L. Two-dimensional nonclose-packed colloidal crystals formed by spincoating. *Appl. Phys. Lett.* **89**, 011908 (2006).
137. Lee, S. H., Bantz, K. C., Lindquist, N. C., Oh, S.-H. & Haynes, C. L. Self-Assembled Plasmonic Nanohole Arrays. *Langmuir* **25**, 13685-13693 (2009).
138. Zhang, G., Wang, D. & Möhwald, H. Fabrication of Multiplex Quasi-Three-Dimensional Grids of One-Dimensional Nanostructures via Stepwise Colloidal Lithography. *Nano Lett.* **7**, 3410-3413 (2007).
139. Retsch, M., Tamm, M., Bocchio, N., Horn, N., Foerch, R., Jonas, U. & Kreiter, M. Parallel Preparation of Densely Packed Arrays of 150-nm Gold-Nanocrescent Resonators in Three Dimensions. *Small* **5**, 2105-2110 (2009).
140. Shumaker-Parry, J. S., Rochholz, H. & Kreiter, M. Fabrication of Crescent-Shaped Optical Antennas. *Adv. Mater.* **17**, 2131-2134 (2005).
141. Vogel, N., Fischer, J., Mohammadi, R., Retsch, M., Butt, H.-J., Landfester, K., Weiss, C. K. & Kreiter, M. Plasmon Hybridization in Stacked Double Crescents Arrays Fabricated by Colloidal Lithography. *Nano Lett.* **11**, 446-454 (2011).

142. Fischer, J., Vogel, N., Mohammadi, R., Butt, H.-J., Landfester, K., Weiss, C. K. & Kreiter, M. Plasmon hybridization and strong near-field enhancements in opposing nanocrescent dimers with tunable resonances. *Nanoscale* **3**, 4788-4797 (2011).
143. Cataldo, S., Zhao, J., Neubrech, F., Frank, B., Zhang, C., Braun, P. V. & Giessen, H. Hole-mask colloidal nanolithography for large-area low-cost metamaterials and antenna-assisted surface-enhanced infrared absorption substrates. *ACS Nano* **6**, 979-985 (2012).
144. Fredriksson, H., Alaverdyan, Y., Dmitriev, A., Langhammer, C., Sutherland, D. S., Zch, M. & Kasemo, B. Hole--Mask Colloidal Lithography. *Adv. Mater.* **19**, 4297--4302 (2007).
145. Choi, D. G., Yu, H. K., Jang, S. G. & Yang, S. M. Colloidal lithographic nanopatterning via reactive ion etching. *J. Am. Chem. Soc.* **126**, 7019-7025 (2004).
146. Zhang, G., Wang, D. & Möhwald, H. Ordered binary arrays of Au nanoparticles derived from colloidal lithography. *Nano Lett.* **7**, 127-132 (2007).
147. Wu, Z., Chen, K., Menz, R., Nagao, T. & Zheng, Y. Tunable multiband metasurfaces by moire nanosphere lithography. *Nanoscale* **7**, 20391-20396 (2015).
148. Chen, K., Rajeeva, B. B., Wu, Z., Rukavina, M., Dao, T. D., Ishii, S., Aono, M., Nagao, T. & Zheng, Y. Moire Nanosphere Lithography. *ACS Nano* **9**, 6031-6040 (2015).
149. Perro, A., Reculosa, S., Ravaine, S., Bourgeat-Lami, E. & Duguet, E. Design and synthesis of Janus micro- and nanoparticles. *J. Mater. Chem.* **15**, 3745 (2005).
150. Love, J. C., Gates, B. D., Wolfe, D. B., Paul, K. E. & Whitesides, G. M. Fabrication and Wetting Properties of Metallic Half-Shells with Submicron Diameters. *Nano Lett.* **2**, 891-894 (2002).
151. Weiler, M. & Pacholski, C. Soft colloidal lithography. *RSC Adv.* **7**, 10688-10691 (2017).
152. Quint, S. B. & Pacholski, C. A chemical route to sub-wavelength hole arrays in metallic films. *J. Mater. Chem.* **19**, 5906--5908 (2009).
153. Bayati, M., Patoka, P., Giersig, M. & Savinova, E. R. An approach to fabrication of metal nanoring arrays. *Langmuir* **26**, 3549-3554 (2010).
154. Sun, F., Cai, W. P., Li, Y., Cao, B., Lu, F., Duan, G. & Zhang, L. Morphology Control and Transferability of Ordered Through-Pore Arrays Based on the Electrodeposition of a Colloidal Monolayer. *Adv. Mater.* **16**, 1116-1121 (2004).
155. Elias, J., Lévy-Clément, C., Bechelany, M., Michler, J., Wang, G.-Y., Wang, Z. & Philippe, L. Hollow Urchin-like ZnO thin Films by Electrochemical Deposition. *Adv. Mater.* **22**, 1607-1612 (2010).
156. Liu, G., Cai, W., Kong, L., Duan, G., Li, Y., Wang, J., Zuo, G. & Cheng, Z. Standing Ag nanoplate-built hollow microsphere arrays: Controllable structural parameters and strong SERS performances. *J. Mater. Chem.* **22** (2012).
157. Kwon, N., Kim, K., Sung, S., Yi, I. & Chung, I. Highly conductive and transparent Ag honeycomb mesh fabricated using a monolayer of polystyrene spheres. *Nanotechnology* **24**, 235205 (2013).
158. Wang, X., Lao, C., Graugnard, E., Summers, C. J. & Wang, Z. L. Large-Size Lifiable Inverted-Nanobowl Sheets as Reusable Masks for Nanolithography. *Nano Lett.* **5**, 1784-1788 (2005).
159. Pernites, R. B., Foster, E. L., Felipe, M. J. L., Robinson, M. & Advincula, R. C. Patterned Surfaces Combining Polymer Brushes and Conducting Polymer via Colloidal Template Electropolymerization. *Adv. Mater.* **23**, 1287-1292 (2011).

160. Zhang, H., Duan, G., Liu, G., Li, Y., Xu, X., Dai, Z., Wang, J. & Cai, W. Layer-controlled synthesis of WO<sub>3</sub> ordered nanoporous films for optimum electrochromic application. *Nanoscale* **5**, 2460-2468 (2013).
161. Phillips, K. R., England, G. T., Sunny, S., Shirman, E., Shirman, T., Vogel, N. & Aizenberg, J. A colloidoscope of colloid-based porous materials and their uses. *Chem. Soc. Rev.* **45**, 281-322 (2016).
162. Li, Q., Retsch, M., Wang, J., Knoll, W., Jonas, U., Broekmann, P., Dotz, K. & Schalley, C. Porous Networks Through Colloidal Templates. *Templates in Chemistry Iii* **287**, 135-180 (2009).
163. Stein, A., Li, F. & Denny, N. R. Morphological Control in Colloidal Crystal Templating of Inverse Opals, Hierarchical Structures, and Shaped Particles†. *Chem. Mater.* **20**, 649-666 (2008).
164. Jin Hyun, W., Ken Lee, H., Soon Oh, S., Hess, O., Choi, C.-G., Hyuk Im, S. & Park, O. O. Two-Dimensional TiO<sub>2</sub> Inverse Opal with a Closed Top Surface Structure for Enhanced Light Extraction from Polymer Light-Emitting Diodes. *Adv. Mater.* **23**, 1846-1850 (2011).
165. Garnett, E. & Yang, P. Light trapping in silicon nanowire solar cells. *Nano Lett.* **10**, 1082-1087 (2010).
166. Sun, C. H., Min, W. L. & Jiang, P. Templated fabrication of sub-100 nm periodic nanostructures. *Chem Commun (Camb)*, 3163-3165 (2008).
167. Kuo, C.-W., Shiu, J.-Y. & Chen, P. Size- and Shape-Controlled Fabrication of Large-Area Periodic Nanopillar Arrays. *Chem. Mater.* **15**, 2917-2920 (2003).
168. Acikgoz, C., Ling, X. Y., Phang, I. Y., Hempenius, M. A., Reinhoudt, D. N., Huskens, J. & Vancso, G. J. Fabrication of Freestanding Nanoporous Polyethersulfone Membranes Using Organometallic Polymer Resists Patterned by Nanosphere Lithography. *Adv. Mater.* **21**, 2064-2067 (2009).
169. Jeong, J.-R., Kim, S., Kim, S.-H., Bland, J. A. C., Shin, S.-C. & Yang, S.-M. Fabrication of Hexagonal Lattice Co/Pd Multilayer Nanodot Arrays Using Colloidal Lithography. *Small* **3**, 1529-1533 (2007).
170. Ai, B., Yu, Y., Möhwald, H. & Zhang, G. Responsive Monochromatic Color Display Based on Nanovolcano Arrays. *Advanced Optical Materials* **1**, 724-731 (2013).
171. Sun, C.-H., Linn, N. C. & Jiang, P. Templated Fabrication of Periodic Metallic Nanopyramid Arrays. *Chem. Mater.* **19**, 4551-4556 (2007).
172. Henzie, J., Kwak, E.-S. & Odom, T. W. Mesoscale Metallic Pyramids with Nanoscale Tips. *Nano Lett.* **5**, 1199-1202 (2005).
173. Li, C., Hong, G., Wang, P., Yu, D. & Qi, L. Wet Chemical Approaches to Patterned Arrays of Well-Aligned ZnO Nanopillars Assisted by Monolayer Colloidal Crystals. *Chem. Mater.* **21**, 891-897 (2009).
174. Li, Y., Fang, X., Koshizaki, N., Sasaki, T., Li, L., Gao, S., Shimizu, Y., Bando, Y. & Golberg, D. Periodic TiO<sub>2</sub> Nanorod Arrays with Hexagonal Nonclose-Packed Arrangements: Excellent Field Emitters by Parameter Optimization. *Adv. Funct. Mater.* **19**, 2467-2473 (2009).
175. Fuhrmann, B., Leipner, H. S., Hoche, H. R., Schubert, L., Werner, P. & Gosele, U. Ordered arrays of silicon nanowires produced by nanosphere lithography and molecular beam epitaxy. *Nano Lett.* **5**, 2524-2527 (2005).
176. Liu, D. F. *et al.* Periodic ZnO nanorod arrays defined by polystyrene microsphere self-assembled monolayers. *Nano Lett.* **6**, 2375-2378 (2006).
177. Wang, X., Summers, C. J. & Wang, Z. L. Large-Scale Hexagonal-Patterned Growth of Aligned ZnO Nanorods for Nano-optoelectronics and Nanosensor Arrays. *Nano Lett.* **4**, 423-426 (2004).

178. Walker, T. G. Transcatheter Arterial Embolization versus Surgery in the Treatment of Upper Gastrointestinal Bleeding after Therapeutic Endoscopy Failure. *Yearbook of Diagnostic Radiology* **2009**, 218-220 (2009).
179. Kempa, K. *et al.* Photonic Crystals Based on Periodic Arrays of Aligned Carbon Nanotubes. *Nano Lett.* **3**, 13-18 (2003).
180. Hsieh, K. C., Tsai, T. Y., Wan, D., Chen, H. L. & Tai, N. H. Iridescence of patterned carbon nanotube forests on flexible substrates: from darkest materials to colorful films. *ACS Nano* **4**, 1327-1336 (2010).
181. Huang, Z. P., Carnahan, D. L., Rybczynski, J., Giersig, M., Sennett, M., Wang, D. Z., Wen, J. G., Kempa, K. & Ren, Z. F. Growth of large periodic arrays of carbon nanotubes. *Appl. Phys. Lett.* **82**, 460-462 (2003).
182. Chen, J., Chao, D., Lu, X., Zhang, W. & Manohar, S. K. General Synthesis of Two-Dimensional Patterned Conducting Polymer-Nanobowl Sheet via Chemical Polymerization. *Macromol. Rapid Commun.* **27**, 771-775 (2006).
183. Hong, G., Li, C. & Limin, Q. Facile Fabrication of Two-Dimensionally Ordered Macroporous Silver Thin Films and Their Application in Molecular Sensing. *Adv. Funct. Mater.* **20**, 3774-3783 (2010).
184. Li, C., Hong, G. & Qi, L. Nanosphere Lithography at the Gas/Liquid Interface: A General Approach toward Free-Standing High-Quality Nanonets. *Chem. Mater.* **22**, 476-481 (2010).
185. Ye, X., Li, Y., Dong, J., Xiao, J., Ma, Y. & Qi, L. Facile synthesis of ZnS nanobowl arrays and their applications as 2D photonic crystal sensors. *Journal of Materials Chemistry C* **1**, 6112 (2013).
186. Sun, F. & Yu, J. C. Photochemical preparation of two-dimensional gold spherical pore and hollow sphere arrays on a solution surface. *Angew. Chem. Int. Ed. Engl.* **46**, 773-777 (2007).
187. Ai, B., Yu, Y., Möhwald, H. & Zhang, G. Novel 3D Au nanohole arrays with outstanding optical properties. *Nanotechnology* **24**, 035303 (2013).
188. Chen, J., Liao, W.-S., Chen, X., Yang, T., Wark, S. E., Son, D. H., Batteas, J. D. & Cremer, P. S. Evaporation-Induced Assembly of Quantum Dots into Nanorings. *ACS Nano* **3**, 173-180 (2009).
189. Motavas, S., Omrane, B. & Papadopoulos, C. Large-Area Patterning of Carbon Nanotube Ring Arrays. *Langmuir* **25**, 4655-4658 (2009).
190. Manzke, A., Pfahler, C., Dubbers, O., Plettl, A., Ziemann, P., Crespy, D., Schreiber, E., Ziener, U. & Landfester, K. Etching Masks Based on Miniemulsions: A Novel Route Towards Ordered Arrays of Surface Nanostructures. *Adv. Mater.* **19**, 1337-1341 (2007).
191. Ai, B., Möhwald, H., Wang, D. & Zhang, G. Advanced Colloidal Lithography Beyond Surface Patterning. *Adv. Mater. Interfaces* **4**, 1600271 (2017).
192. Haes, A. J., Zou, S., Schatz, G. C. & Van Duyne, R. P. A Nanoscale Optical Biosensor: The Long Range Distance Dependence of the Localized Surface Plasmon Resonance of Noble Metal Nanoparticles. *The Journal of Physical Chemistry B* **108**, 109-116 (2004).
193. Farcău, C. & Aștilean, S. Silver half-shell arrays with controlled plasmonic response for fluorescence enhancement optimization. *Appl. Phys. Lett.* **95**, 193110 (2009).
194. Ho, Y. H., Chen, K. Y., Peng, K. Y., Tsai, M. C., Tian, W. C. & Wei, P. K. Enhanced light out-coupling of organic light-emitting diode using metallic nanomesh electrodes and microlens array. *Opt. Express* **21**, 8535-8543 (2013).

195. Ding, W., Wang, Y., Chen, H. & Chou, S. Y. Plasmonic Nanocavity Organic Light-Emitting Diode with Significantly Enhanced Light Extraction, Contrast, Viewing Angle, Brightness, and Low-Glare. *Adv. Funct. Mater.* **24**, 6329-6339 (2014).
196. Brongersma, M. L., Cui, Y. & Fan, S. Light management for photovoltaics using high-index nanostructures. *Nat Mater* **13**, 451-460 (2014).
197. Tagliabue, G., Poulikakos, D. & Eghlidi, H. Three-dimensional concentration of light in deeply sub-wavelength, laterally tapered gap-plasmon nanocavities. *Appl. Phys. Lett.* **108**, 221108 (2016).
198. Tagliabue, G., Höller, C., Eghlidi, H. & Poulikakos, D. Proximal gap-plasmon nanoresonators in the limit of vanishing inter-cavity separation. *Nanoscale* **6**, 10274-10280 (2014).
199. Li, S. Q., Guo, P., Zhang, L., Zhou, W., Odom, T. W., Seideman, T., Ketterson, J. B. & Chang, R. P. H. Infrared Plasmonics with Indium–Tin-Oxide Nanorod Arrays. *ACS Nano* **5**, 9161-9170 (2011).
200. Jablan, M., Buljan, H. & Soljačić, M. Plasmonics in graphene at infrared frequencies. *Phys. Rev. B* **80**, 245435 (2009).
201. Drude, P. Zur Elektronentheorie der Metalle. *Annalen der Physik* **306**, 566-613 (1900).
202. Maier, S. *Plasmonics: Fundamentals and Applications*. (Springer, New York, 2007).
203. Kreiter, M. *Surface plasmon-related resonances on metallic diffraction gratings*, Johannes Gutenberg-Universität Mainz, (2000).
204. Knoll, W. Interfaces and thin films as seen by bound electromagnetic waves. *Annu. Rev. Phys. Chem.* **49**, 569-638 (1998).
205. Ebbesen, T. W., Lezec, H. J., Ghaemi, H. F., Thio, T. & Wolff, P. A. Extraordinary optical transmission through sub-wavelength hole arrays. *Nature* **391**, 667-669 (1998).
206. Bethe, H. A. Theory of Diffraction by Small Holes. *Phys. Rev.* **66**, 163-182 (1944).
207. Genet, C. & Ebbesen, T. W. Light in tiny holes. *Nature* **445**, 39-46 (2007).
208. Barnes, W. L., Murray, W. A., Dintinger, J., Devaux, E. & Ebbesen, T. W. Surface plasmon polaritons and their role in the enhanced transmission of light through periodic arrays of subwavelength holes in a metal film. *Phys. Rev. Lett.* **92**, 107401 (2004).
209. Ghaemi, H., Thio, T., Grupp, D., Ebbesen, T. & Lezec, H. Surface plasmons enhance optical transmission through subwavelength holes. *Phys. Rev. B: Condens. Matter* **58**, 6779-6782 (1998).
210. Liu, H. & Lalanne, P. Microscopic theory of the extraordinary optical transmission. *Nature* **452**, 728-731 (2008).
211. Martín-Moreno, L., García-Vidal, F., Lezec, H., Pellerin, K., Thio, T., Pendry, J. & Ebbesen, T. Theory of Extraordinary Optical Transmission through Subwavelength Hole Arrays. *Phys. Rev. Lett.* **86**, 1114-1117 (2001).
212. Sharma, N., Keshmiri, H., Zhou, X., Wong, T. I., Petri, C., Jonas, U., Liedberg, B. & Dostalek, J. Tunable Plasmonic Nanohole Arrays Actuated by a Thermoresponsive Hydrogel Cushion. *J. Phys. Chem. C* **120**, 561-568 (2016).
213. Lin, E.-H., Tsai, W.-S., Lee, K.-L., Lee, M.-C. M. & Wei, P.-K. Enhancing angular sensitivity of plasmonic nanostructures using mode transition in hexagonal gold nanohole arrays. *Sensors and Actuators B: Chemical* **241**, 800-805 (2017).
214. Yoo, D., Johnson, T. W., Cherukulappurath, S., Norris, D. J. & Oh, S. H. Template-Stripped Tunable Plasmonic Devices on Stretchable and Rollable Substrates. *ACS Nano* **9**, 10647-10654 (2015).
215. Farcau, C., Giloan, M., Vinteler, E. & Astilean, S. Understanding plasmon resonances of metal-coated colloidal crystal monolayers. *Appl. Phys. B* **106**, 849-856 (2012).

216. Yu, Y., Zhou, Z., Möhwald, H., Ai, B., Zhao, Z., Ye, S. & Zhang, G. Distorted colloidal arrays as designed template. *Nanotechnology* **26**, 035301 (2015).
217. Wu, Z. & Zheng, Y. Moiré Chiral Metamaterials. *Advanced Optical Materials* **5**, 1700034 (2017).
218. Mahani, F. F., Mokhtari, A. & Mehran, M. Dual mode operation, highly selective nanohole array-based plasmonic colour filters. *Nanotechnology* **28**, 385203 (2017).
219. Morfa, A. J., Akinoglu, E. M., Subbiah, J., Giersig, M. & Mulvaney, P. Transparent metal electrodes from ordered nanosphere arrays. *J. Appl. Phys.* **114**, 054502 (2013).
220. Couture, M., Liang, Y., Poirier Richard, H. P., Faid, R., Peng, W. & Masson, J. F. Tuning the 3D plasmon field of nanohole arrays. *Nanoscale* **5**, 12399-12408 (2013).
221. Sarrazin, M., Vigneron, J.-P. & Vigoureux, J.-M. Role of Wood anomalies in optical properties of thin metallic films with a bidimensional array of subwavelength holes. *Phys. Rev. B* **67**, 085415 (2003).
222. Schwind, M., Kasemo, B. & Zoric, I. Localized and propagating plasmons in metal films with nanoholes. *Nano Lett.* **13**, 1743-1750 (2013).
223. Luk'yanchuk, B., Zheludev, N. I., Maier, S. A., Halas, N. J., Nordlander, P., Giessen, H. & Chong, C. T. The Fano resonance in plasmonic nanostructures and metamaterials. *Nat. Mater.* **9**, 707-715 (2010).
224. Genet, C., van Exter, M. P. & Woerdman, J. P. Fano-type interpretation of red shifts and red tails in hole array transmission spectra. *Opt. Commun.* **225**, 331-336 (2003).
225. Chang, S. H., Gray, S. & Schatz, G. Surface plasmon generation and light transmission by isolated nanoholes and arrays of nanoholes in thin metal films. *Opt. Express* **13**, 3150-3165 (2005).
226. Sannomiya, T., Scholder, O., Jefimovs, K., Hafner, C. & Dahlin, A. B. Investigation of plasmon resonances in metal films with nanohole arrays for biosensing applications. *Small* **7**, 1653-1663 (2011).
227. Koerkamp, K. J., Enoch, S., Segerink, F. B., van Hulst, N. F. & Kuipers, L. Strong influence of hole shape on extraordinary transmission through periodic arrays of subwavelength holes. *Phys. Rev. Lett.* **92**, 183901 (2004).
228. Metin Akinoglu, E., Sun, T., Gao, J., Giersig, M., Ren, Z. & Kempa, K. Evidence for critical scaling of plasmonic modes at the percolation threshold in metallic nanostructures. *Appl. Phys. Lett.* **103**, 171106 (2013).
229. Murray, W. A., Astilean, S. & Barnes, W. L. Transition from localized surface plasmon resonance to extended surface plasmon-polariton as metallic nanoparticles merge to form a periodic hole array. *Phys. Rev. B* **69**, 165407 (2004).
230. Anatoly, V. Z. & Igor, I. S. Near-field photonics: surface plasmon polaritons and localized surface plasmons. *Journal of Optics A: Pure and Applied Optics* **5**, S16 (2003).
231. Ritchie, R. H. Plasma Losses by Fast Electrons in Thin Films. *Phys. Rev.* **106**, 874-881 (1957).
232. Sarid, D. Long-Range Surface-Plasma Waves on Very Thin Metal Films. *Phys. Rev. Lett.* **47**, 1927-1930 (1981).
233. Degiron, A., Lezec, H. J., Barnes, W. L. & Ebbesen, T. W. Effects of hole depth on enhanced light transmission through subwavelength hole arrays. *Appl. Phys. Lett.* **81**, 4327-4329 (2002).
234. Lee, T. D. & Ebong, A. U. A review of thin film solar cell technologies and challenges. *Renewable and Sustainable Energy Reviews* **70**, 1286-1297 (2017).
235. Petrus, M. L. *et al.* Capturing the Sun: A Review of the Challenges and Perspectives of Perovskite Solar Cells. *Adv. Energy Mater.* **7**, 1700264 (2017).

236. Hagfeldt, A., Boschloo, G., Sun, L., Kloo, L. & Pettersson, H. Dye-Sensitized Solar Cells. *Chem. Rev.* **110**, 6595-6663 (2010).
237. Lu, L., Zheng, T., Wu, Q., Schneider, A. M., Zhao, D. & Yu, L. Recent Advances in Bulk Heterojunction Polymer Solar Cells. *Chem. Rev.* **115**, 12666-12731 (2015).
238. Pagliaro, M., Ciriminna, R. & Palmisano, G. Flexible Solar Cells. *ChemSusChem* **1**, 880-891 (2008).
239. Gujar, T. P. & Thelakkat, M. Highly Reproducible and Efficient Perovskite Solar Cells with Extraordinary Stability from Robust CH<sub>3</sub>NH<sub>3</sub>PbI<sub>3</sub>: Towards Large-Area Devices. *Energy Technol.* **4**, 449-457 (2016).
240. Leem, J. W., Kim, S., Park, C., Kim, E. & Yu, J. S. Strong photocurrent enhancements in plasmonic organic photovoltaics by biomimetic nanoarchitectures with efficient light harvesting. *ACS Appl Mater Interfaces* **7**, 6706-6715 (2015).
241. Lin, H. W., Chiu, S. W., Lin, L. Y., Hung, Z. Y., Chen, Y. H., Lin, F. & Wong, K. T. Device engineering for highly efficient top-illuminated organic solar cells with microcavity structures. *Adv. Mater.* **24**, 2269-2272 (2012).
242. Sergeant, N. P., Hadipour, A., Niesen, B., Cheyng, D., Heremans, P., Peumans, P. & Rand, B. P. Design of transparent anodes for resonant cavity enhanced light harvesting in organic solar cells. *Adv. Mater.* **24**, 728-732 (2012).
243. Gilot, J., Barbu, I., Wienk, M. M. & Janssen, R. A. J. The use of ZnO as optical spacer in polymer solar cells: Theoretical and experimental study. *Appl. Phys. Lett.* **91**, 113520 (2007).
244. Tang, Z., Tress, W. & Inganäs, O. Light trapping in thin film organic solar cells. *Mater. Today* **17**, 389-396 (2014).
245. Albrecht, S., Schäfer, S., Lange, I., Yilmaz, S., Dumsch, I., Allard, S., Scherf, U., Hertwig, A. & Neher, D. Light management in PCPDTBT:PC70BM solar cells: A comparison of standard and inverted device structures. *Org. Electron.* **13**, 615-622 (2012).
246. De, S., Higgins, T. M., Lyons, P. E., Doherty, E. M., Nirmalraj, P. N., Blau, W. J., Boland, J. J. & Coleman, J. N. Silver Nanowire Networks as Flexible, Transparent, Conducting Films: Extremely High DC to Optical Conductivity Ratios. *ACS Nano* **3**, 1767-1774 (2009).
247. Yim, J. H., Joe, S. Y., Pang, C., Lee, K. M., Jeong, H., Park, J. Y., Ahn, Y. H., de Mello, J. C. & Lee, S. Fully Solution-Processed Semitransparent Organic Solar Cells with a Silver Nanowire Cathode and a Conducting Polymer Anode. *ACS Nano* **8**, 2857-2863 (2014).
248. Maurer, J. H., Gonzalez-Garcia, L., Reiser, B., Kanelidis, I. & Kraus, T. Templated Self-Assembly of Ultrathin Gold Nanowires by Nanoimprinting for Transparent Flexible Electronics. *Nano Lett.* **16**, 2921-2925 (2016).
249. Lee, J.-Y., Connor, S. T., Cui, Y. & Peumans, P. Solution-Processed Metal Nanowire Mesh Transparent Electrodes. *Nano Lett.* **8**, 689-692 (2008).
250. Reineck, P., Lee, G. P., Brick, D., Karg, M., Mulvaney, P. & Bach, U. A solid-state plasmonic solar cell via metal nanoparticle self-assembly. *Adv. Mater.* **24**, 4750-4755 (2012).
251. Jasieniak, J., MacDonald, B. I., Watkins, S. E. & Mulvaney, P. Solution-processed sintered nanocrystal solar cells via layer-by-layer assembly. *Nano Lett.* **11**, 2856-2864 (2011).
252. Cook, K. T., Tettey, K. E., Bunch, R. M., Lee, D. & Nolte, A. J. One-Step Index-Tunable Antireflection Coatings from Aggregated Silica Nanoparticles. *ACS Applied Materials & Interfaces* **4**, 6426-6431 (2012).

253. Moghal, J., Kobler, J., Sauer, J., Best, J., Gardener, M., Watt, A. A. R. & Wakefield, G. High-Performance, Single-Layer Antireflective Optical Coatings Comprising Mesoporous Silica Nanoparticles. *ACS Applied Materials & Interfaces* **4**, 854-859 (2012).
254. Pillai, S., Catchpole, K. R., Trupke, T. & Green, M. A. Surface plasmon enhanced silicon solar cells. *J. Appl. Phys.* **101**, 093105 (2007).
255. Catchpole, K. R. & Polman, A. Plasmonic solar cells. *Opt. Express* **16**, 21793-21800 (2008).
256. Losurdo, M., Giangregorio, M. M., Bianco, G. V., Sacchetti, A., Capezzuto, P. & Bruno, G. Enhanced absorption in Au nanoparticles/a-Si:H/c-Si heterojunction solar cells exploiting Au surface plasmon resonance. *Sol. Energy Mater. Sol. Cells* **93**, 1749-1754 (2009).
257. Dabirian, A., Byranvand, M. M., Naqavi, A., Kharat, A. N. & Taghavinia, N. Self-Assembled Monolayer of Wavelength-Scale Core-Shell Particles for Low-Loss Plasmonic and Broadband Light Trapping in Solar Cells. *ACS Appl Mater Interfaces* **8**, 247-255 (2016).
258. Choi, H. *et al.* Multipositional silica-coated silver nanoparticles for high-performance polymer solar cells. *Nano Lett.* **13**, 2204-2408 (2013).
259. Grandidier, J., Weitekamp, R. A., Deceglie, M. G., Callahan, D. M., Battaglia, C., Bukowsky, C. R., Ballif, C., Grubbs, R. H. & Atwater, H. A. Solar cell efficiency enhancement via light trapping in printable resonant dielectric nanosphere arrays. *Physica Status Solidi a-Applications and Materials Science* **210**, 255-260 (2013).
260. Baek, S.-W., Noh, J., Lee, C.-H., Kim, B., Seo, M.-K. & Lee, J.-Y. Plasmonic Forward Scattering Effect in Organic Solar Cells: A Powerful Optical Engineering Method. *Sci. Rep.* **3**, 1726 (2013).
261. Wang, D. H., Do Kim, Y., Choi, K. W., Seo, J. H., Im, S. H., Park, J. H., Park, O. O. & Heeger, A. J. Enhancement of Donor-Acceptor Polymer Bulk Heterojunction Solar Cell Power Conversion Efficiencies by Addition of Au Nanoparticles. *Angew. Chem.* **50**, 5519-5523 (2011).
262. Ng, A. *et al.* Enhanced performance of PTB7:PC(7)(1)BM solar cells via different morphologies of gold nanoparticles. *ACS Appl Mater Interfaces* **6**, 20676-20684 (2014).
263. Tseng, W.-H. *et al.* Shape-Dependent Light Harvesting of 3D Gold Nanocrystals on Bulk Heterojunction Solar Cells: Plasmonic or Optical Scattering Effect? *The Journal of Physical Chemistry C* **119**, 7554-7564 (2015).
264. Mendes, M. J., Morawiec, S., Simone, F., Priolo, F. & Crupi, I. Colloidal plasmonic back reflectors for light trapping in solar cells. *Nanoscale* **6**, 4796 (2014).
265. Wang, C., Li, C., Wen, S., Ma, P., Liu, Y., MacKenzie, R. C. I., Tian, W. & Ruan, S. Combining plasmonic trap filling and optical backscattering for highly efficient third generation solar cells. *J. Mater. Chem. A* **5**, 3995-4002 (2017).
266. Lu, L., Luo, Z., Xu, T. & Yu, L. Cooperative plasmonic effect of Ag and Au nanoparticles on enhancing performance of polymer solar cells. *Nano Lett.* **13**, 59-64 (2013).
267. Park, H. I., Lee, S., Lee, J. M., Nam, S. A., Jeon, T., Han, S. W. & Kim, S. O. High performance organic photovoltaics with plasmonic-coupled metal nanoparticle clusters. *ACS Nano* **8**, 10305-10312 (2014).
268. Pastorelli, F., Bidault, S., Martorell, J. & Bonod, N. Self-Assembled Plasmonic Oligomers for Organic Photovoltaics. *Advanced Optical Materials* **2**, 171-175 (2014).
269. Shen, W. *et al.* Enhanced efficiency of polymer solar cells by incorporated Ag-SiO<sub>2</sub> core-shell nanoparticles in the active layer. *RSC Adv.* **4**, 4379-4386 (2014).

270. Yoon, W.-J., Jung, K.-Y., Liu, J., Duraisamy, T., Revur, R., Teixeira, F. L., Sengupta, S. & Berger, P. R. Plasmon-enhanced optical absorption and photocurrent in organic bulk heterojunction photovoltaic devices using self-assembled layer of silver nanoparticles. *Sol. Energy Mater. Sol. Cells* **94**, 128-132 (2010).
271. Xu, X., Du, Q., Peng, B., Xiong, Q., Hong, L., Demir, H. V., Wong, T. K. S., Ko Kyaw, A. K. & Sun, X. W. Effect of shell thickness on small-molecule solar cells enhanced by dual plasmonic gold-silica nanorods. *Appl. Phys. Lett.* **105**, 113306 (2014).
272. Chen, F.-C., Wu, J.-L., Lee, C.-L., Hong, Y., Kuo, C.-H. & Huang, M. H. Plasmonic-enhanced polymer photovoltaic devices incorporating solution-processable metal nanoparticles. *Appl. Phys. Lett.* **95**, 013305 (2009).
273. Fu, W.-F. *et al.* Optical and electrical effects of plasmonic nanoparticles in high-efficiency hybrid solar cells. *PCCP* **15**, 17105-17111 (2013).
274. Singh, C. R., Honold, T., Gujar, T. P., Retsch, M., Fery, A., Karg, M. & Thelakkat, M. The role of colloidal plasmonic nanostructures in organic solar cells. *Phys. Chem. Chem. Phys.* **18**, 23155-23163 (2016).
275. Kirkeminde, A. *et al.* Surface-passivated plasmonic nano-pyramids for bulk heterojunction solar cell photocurrent enhancement. *Nanoscale* **4**, 4421-4425 (2012).
276. Wu, B., Oo, T. Z., Li, X., Liu, X., Wu, X., Yeow, E. K. L., Fan, H. J., Mathews, N. & Sum, T. C. Efficiency Enhancement in Bulk-Heterojunction Solar Cells Integrated with Large-Area Ag Nanotriangle Arrays. *The Journal of Physical Chemistry C* **116**, 14820-14825 (2012).
277. Adachi, M. M., Labelle, A. J., Thon, S. M., Lan, X., Hoogland, S. & Sargent, E. H. Broadband solar absorption enhancement via periodic nanostructuring of electrodes. *Sci. Rep.* **3**, 2928 (2013).
278. Yao, Y., Yao, J., Narasimhan, V. K., Ruan, Z., Xie, C., Fan, S. & Cui, Y. Broadband light management using low-Q whispering gallery modes in spherical nanoshells. *Nat Commun* **3**, 664 (2012).
279. Zhu, J., Zhu, X., Hoekstra, R., Li, L., Xiu, F., Xue, M., Zeng, B. & Wang, K. L. Metallic nanomesh electrodes with controllable optical properties for organic solar cells. *Appl. Phys. Lett.* **100**, 143109 (2012).
280. Ji, S., Park, J. & Lim, H. Improved antireflection properties of moth eye mimicking nanopillars on transparent glass: flat antireflection and color tuning. *Nanoscale* **4**, 4603 (2012).
281. Mailoa, J. P., Lee, Y. S., Buonassisi, T. & Kozinsky, I. Textured conducting glass by nanosphere lithography for increased light absorption in thin-film solar cells. *Journal of Physics D: Applied Physics* **47**, 085105 (2014).
282. Sun, C. H., Ho, B. J., Jiang, B. & Jiang, P. Biomimetic subwavelength antireflective gratings on GaAs. *Opt. Lett.* **33**, 2224-2226 (2008).
283. Sun, C.-H., Jiang, P. & Bin, J. Broadband moth-eye antireflection coatings on silicon. *Appl. Phys. Lett.* **92**, 061112 (2008).
284. Sun, C.-H., Min, W.-L., Linn, N. C., Jiang, P. & Jiang, B. Templated fabrication of large area subwavelength antireflection gratings on silicon. *Appl. Phys. Lett.* **91**, 231105 (2007).
285. Zhu, J. *et al.* Optical absorption enhancement in amorphous silicon nanowire and nanocone arrays. *Nano Lett.* **9**, 279-282 (2009).
286. Li, X. H., Li, P. C., Hu, D. Z., Schaadt, D. M. & Yu, E. T. Light trapping in thin-film solar cells via scattering by nanostructured antireflection coatings. *J. Appl. Phys.* **114**, 044310 (2013).

287. Xu, W.-F., Pan, M.-Y., Fu, P.-H., Li, S.-W., Huang, D.-W. & Wei, P.-K. Efficiency enhancement of top-illuminated ITO-free organic solar cells using plasmonic-assisted nanostructured reflective electrodes. *J. Mater. Chem. C* **3**, 9131-9136 (2015).
288. Chen, T.-G., Yu, P., Chen, S.-W., Chang, F.-Y., Huang, B.-Y., Cheng, Y.-C., Hsiao, J.-C., Li, C.-K. & Wu, Y.-R. Characteristics of large-scale nanohole arrays for thin-silicon photovoltaics. *Progress in Photovoltaics: Research and Applications* **22**, 452-461 (2014).
289. Zhu, J., Hsu, C.-M., Yu, Z., Fan, S. & Cui, Y. Nanodome Solar Cells with Efficient Light Management and Self-Cleaning. *Nano Lett.* **10**, 1979-1984 (2009).
290. Lal, N. N., Soares, B. F., Sinha, J. K., Huang, F., Mahajan, S., Bartlett, P. N., Greenham, N. C. & Baumberg, J. J. Enhancing solar cells with localized plasmons in nanovoids. *Opt. Express* **19**, 11256-11263 (2011).
291. Nishimura, S., Abrams, N., Lewis, B. A., Halaoui, L. I., Mallouk, T. E., Benkstein, K. D., van de Lagemaat, J. & Frank, A. J. Standing wave enhancement of red absorbance and photocurrent in dye-sensitized titanium dioxide photoelectrodes coupled to photonic crystals. *J. Am. Chem. Soc.* **125**, 6306-6310 (2003).
292. Wei, H.-Y., Huang, J.-H., Hsu, C.-Y., Chang, F.-C., Ho, K.-C. & Chu, C.-W. Organic solar cells featuring nanobowl structures. *Energy Environ. Sci.* **6**, 1192 (2013).
293. Wu, W. & Tassi, N. G. A broadband plasmonic enhanced transparent conductor. *Nanoscale* **6**, 7811-7816 (2014).
294. Cheng, K., Cui, Z., Li, Q., Wang, S. & Du, Z. Large-scale fabrication of a continuous gold network for use as a transparent conductive electrode in photo-electronic devices. *Nanotechnology* **23**, 425303 (2012).
295. Luhman, W. A., Lee, S. H., Johnson, T. W., Holmes, R. J. & Oh, S. H. Self-assembled plasmonic electrodes for high-performance organic photovoltaic cells. *Appl. Phys. Lett.* **99**, 103306 (2011).
296. Du, Q. G., Ren, H., Wu, L., Bai, P., Png, C. E., Sun, X. W., Kam, C. H. & Martijn de Sterke, C. Light absorption mechanism in organic solar cells with hexagonal lattice nanohole aluminum transparent electrodes. *J. Opt.* **17**, 085901 (2015).
297. Chou, S. Y. & Ding, W. Ultrathin, high-efficiency, broad-band, omni-acceptance, organic solar cells enhanced by plasmonic cavity with subwavelength hole array. *Opt. Express* **21**, A60-A76 (2013).
298. Reilly, T. H., van de Lagemaat, J., Tenent, R. C., Morfa, A. J. & Rowlen, K. L. Surface-plasmon enhanced transparent electrodes in organic photovoltaics. *Appl. Phys. Lett.* **92**, 243304 (2008).
299. Takatori, K., Nishino, T., Okamoto, T., Takei, H., Ishibashi, K. & Micheletto, R. Indium-free organic thin-film solar cells using a plasmonic electrode. *J. Phys. D-Appl. Phys.* **49**, 185106 (2016).
300. Peng, Y., Paudel, T., Chen, W. C., Padilla, W. J., Ren, Z. F. & Kempa, K. Percolation and polaritonic effects in periodic planar nanostructures evolving from holes to islands. *Appl. Phys. Lett.* **97**, 041901 (2010).



## 2 Overview of the Thesis

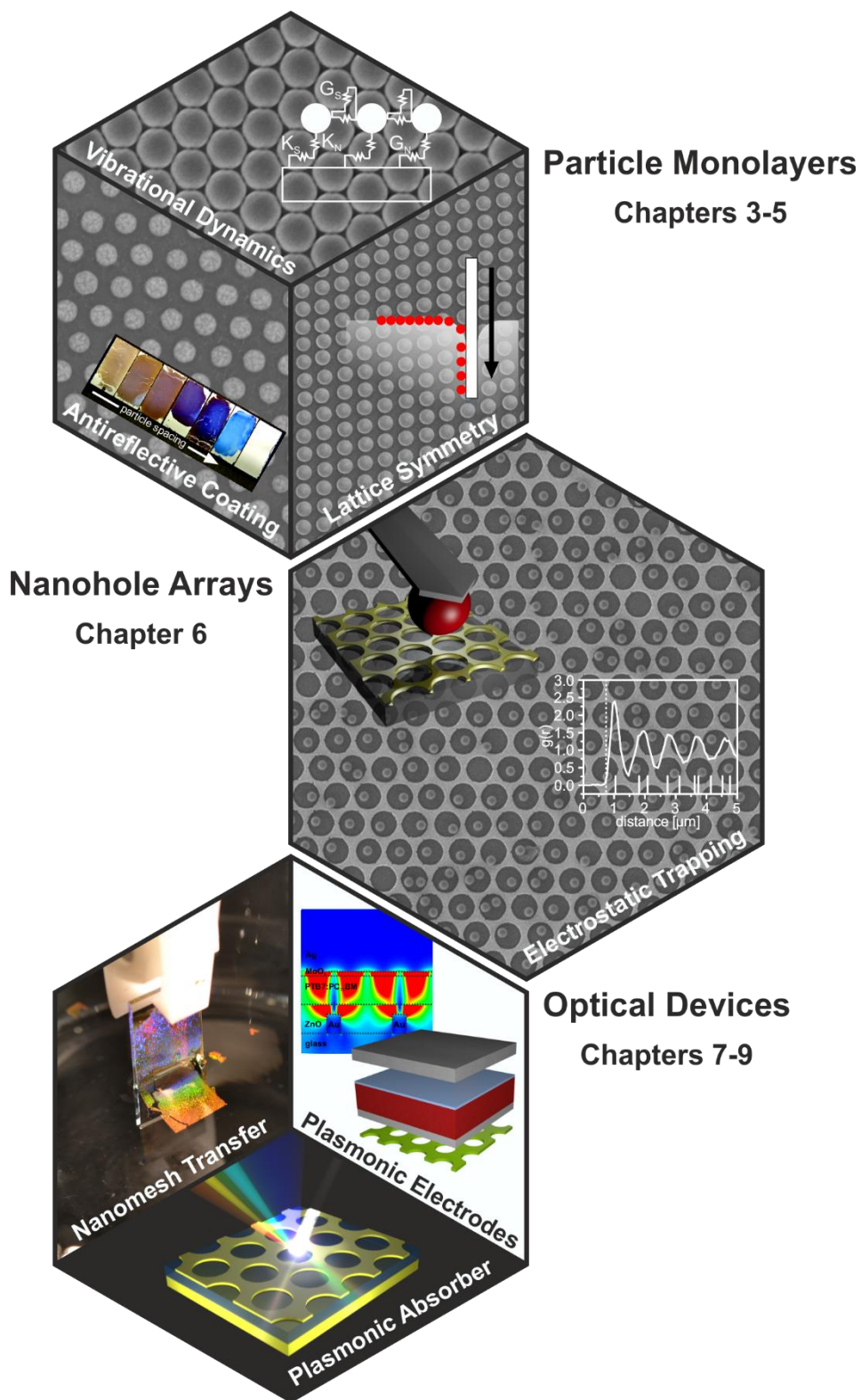


Figure 2.1. Overview of the thesis.

The objective of this thesis is the preparation of functional devices using colloidal self-assembly. The thesis consists of seven individual contributions, which all address structures prepared by colloidal self-assembly. They can be grouped into three blocks:

The first contributions are dedicated to the fabrication of highly regular colloidal monolayers via an interface-mediated self-assembly process and their optical and acoustic characterization. In chapter 3, the antireflective properties of non-close-packed monolayers of colloidal polystyrene spheres are examined. Following this, the mechanical properties of colloidal crystals are studied by determining the interaction of a close-packed particle array with surface acoustic waves (chapter 4). Next, the preparation of non-close-packed particle monolayers with all two-dimensional Bravais lattices is described in chapter 5.

In the second part, the fabrication of gold nanohole arrays with tailored adhesive properties starting from self-assembled particle monolayers and their application for directed self-assembly is presented. Precise tuning of the electrostatic forces acting at the solid-liquid interface allows for the controlled self-assembly of particles into the nanohole template (chapter 6).

The last part is devoted to the assembly and characterization of optical devices based on gold nanohole arrays. In chapter 7 metal-insulator-metal multilayer structures based on nanohole arrays were prepared by a newly developed transfer technique, followed by a thorough optical characterization of three-layered metal-insulator-metal absorbers in chapter 8. Finally, gold nanohole arrays were integrated into organic solar cells as transparent conductive electrodes (chapter 9). The following overview will summarize the main results of this thesis.

Colloidal monolayers have been widely investigated for the fabrication of photonic crystals. These photonic crystals can interact with electromagnetic waves by creating a periodic modulation of the dielectric constant. Analogously to the interaction of electrons with atomic crystals, this results in photonic band gaps. To manipulate light in the visible spectrum, the modulation of the dielectric constant has to be on the length scale of visible light. For feature sizes much smaller than the wavelength of interest, the structure does not diffract the electromagnetic wave but behaves like a homogeneous, effective medium. In this way, a subwavelength colloidal monolayer can be regarded as a layer with an effective refractive index that can be adjusted by tuning the volume fraction of the colloids. Consequently, in this first contribution, monolayers of subwavelength-sized polystyrene particles were used as antireflective coatings.

The amount of light that is reflected at an interface is dependent on the difference of the refractive indices of the two materials and can be calculated using the Fresnel equations. These reflections often limit the performance of optical components. A simple way to reduce reflections is to replace the interface by a layer of a material, which exhibits a refractive index in between that of the two materials. Although in this way two new interfaces are formed, the combined reflectivity of the two interfaces is lower than that of the original interface. For the simplified case of normal incident light and an interface between air and common glass, the Fresnel equations yield a desired refractive index of  $n_c = \sqrt{n_{glass}n_{air}} = \sqrt{1.49 \cdot 1.00} = 1.23$  for the antireflective coating. Such low refractive indices are hardly accessible with bulk materials but can be realized with colloidal monolayers due to their porous structure.

For this purpose, polystyrene particles with diameters between 102 nm and 181 nm were used to prepare monolayers via colloidal self-assembly at the water/air interface. Starting from close-packed particle arrays, the diameter  $2r$  of the polymer particles was reduced using plasma etching while the interparticle distance was defined by the initial particle diameter  $D_0$  (Figure 2.2a). This decreases the polymer volume fraction in the particle monolayer and leads to a lower refractive index.

In a first series, particle arrays with an initial particle diameter of 140 nm were etched to vary the particle diameter between 140 nm and 85 nm. Assuming spherical particles, this corresponds to a volume fraction between 60.5 % and 24.3 %. While all samples exhibit a transmittance superior to the naked glass substrate in the visible wavelength range, a maximum transmittance of 95.5 % is observed at a volume fraction of 46.3 % (a particle area fraction of 61.1 %) after 150 s of plasma treatment (Figure 2.2b). This value is close to the optimum

volume fraction of 43.3 % (the optimum particle area fraction of 64.2 %) derived from the Maxwell-Garnett effective medium approximation.

Concomitant to the decreasing volume fraction, the thickness  $d$  of the effective layer formed by the colloidal monolayer inevitably decreases with increasing etching times. This results in a shift of the wavelength of maximum transmittance  $\lambda_{max}$  to shorter wavelengths according to the condition of destructive interference of the reflected light  $\lambda_{max} = 4 \cdot n_c \cdot d$  for single layer antireflective coatings. Moreover, the optimum transmittance can be well correlated to a minimum in  $\Delta n = n_c - n_{opt}$  with  $n_{opt} = 1.23$  (Figure 2.2c). Too long or too short etching times result in a refractive index deviating from the optimum value and thus a reduced transmittance.

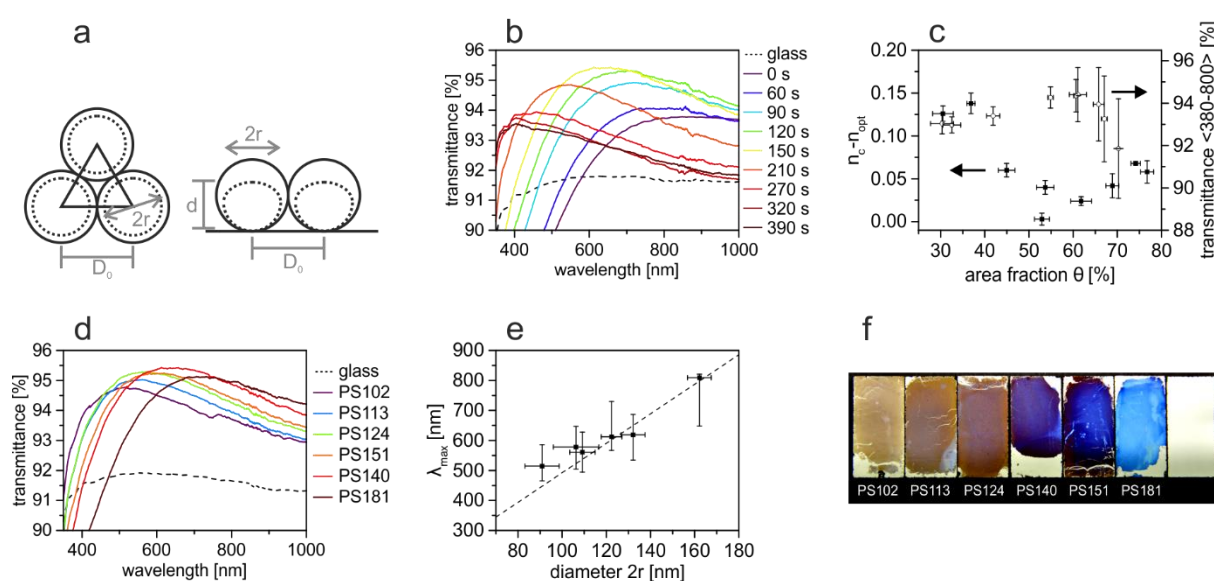


**Figure 2.2.** Antireflective properties of colloidal monolayers. (a) Top-view and side-view scheme of a colloidal monolayer. (b) Transmittance spectra of a continuously etched polystyrene monolayer with an initial particle diameter  $D_0$  of 140 nm. The dashed line represents a neat glass substrate. (c) Deviation of the refractive index of the coating  $n_c$  from the optimum refractive index  $n_{opt} = 1.23$  and averaged transmittance for particle monolayers with varying particle area fraction reached after distinct etching times. (d) Transmittance spectra of particle monolayers with different initial particle diameters approximately etched to the optimum particle area fraction of 64.2 %. (e) Peak positions from (d) as a function of the particle diameter  $2r$  after etching. The dashed line indicates the theoretical values. (f) Photograph of the reflection colors of monolayers with different initial particle diameters etched to the optimum surface coverage. Reproduced from *Macromolecular Chemistry and Physics* 216, 1682-1688 (2015) with permission from Wiley-VCH.

In a second series, monolayers with initial particle diameters between 102 nm and 181 nm were etched to the optimum volume fraction of 43.3 %. Thus, all samples exhibit a refractive index near the optimum value of  $n_{opt} = 1.23$  and consequently a peak transmittance exceeding 94.5 % (Figure 2.2d). By using different initial particle diameters, the effective layer thickness can be

tuned independently of the effective refractive index of the coating. Therefore, the wavelength of maximum transmittance can be tuned across the whole visible range from 515 nm to 810 nm (Figure 2.2e). As a result, the samples show distinct colors in reflection dependent on the initial particle size and complementary to the wavelength of maximum transmittance  $\lambda_{max}$  (Figure 2.2f).

Antireflective coatings made of colloidal monolayers are certainly not competitive to modern gradient refractive index structures with regard to the scratch resistance and angle-insensitivity. However, this work describes the optical properties of subwavelength colloidal monolayers complementary to the existing studies of wavelength-scale photonic crystals.

Apart from optical properties, the phononic properties of granular matter and colloidal crystals attract more and more attention. Rather than the periodic modulation of the refractive index, the density modulation and the modulation of the elastic modulus in colloidal crystals are responsible for exciting mechanical characteristics. Using a laser-induced transient grating technique, we analyzed the vibrational dynamics of a hexagonal, close-packed particle monolayer. For the first time, a single-crystalline domain with dimensions exceeding the measurement spot was probed, enabling the detection of vibrational modes across the entire Brillouin zone.

For this, a monolayer of polystyrene spheres with diameters of 1.5  $\mu\text{m}$  was prepared at the water/air interface and transferred onto a 100 nm aluminum film (Figure 2.3a). A transient grating was formed by the interference pattern of two laser pulses crossed at the sample inducing Rayleigh surface waves propagating in the  $\Gamma$ -K direction of the colloidal crystal. A probe laser, diffracted by the grating, was used to detect the acoustic modes present in the sample (Figure 2.3b). All modes can be described mathematically by considering rigid particles with spring contacts between the particles and the substrate ( $K_S$  and  $K_N$ ) as well as between two adjacent particles ( $G_S$  and  $G_N$ ) (Figure 2.3c).

The Rayleigh surface wave excited in the aluminum substrate shows a dispersion with constant slope and is folded back at the Brillouin zone boundary (Figure 2.3d). Additionally, spheroidal and contact-based modes of the particle monolayer are observed with rather flat dispersions. Between 50 MHz and 300 MHz, three contact-based modes are visible. The most prominent of these modes (V) can be described by a predominantly vertical motion of the particles, while the two smaller modes mainly correspond to horizontal (HR) and rotational (RH) displacements of the particles. Due to the single crystalline nature of the particle monolayer, particle-particle interactions affect the dispersion of the contact-based modes leading to a wavevector-

dependency of these modes (Figure 2.3e). This allowed for the extraction of both, the particle-substrate and particle-particle spring constants by fitting the dispersion of the vertical mode V with a mathematical model.

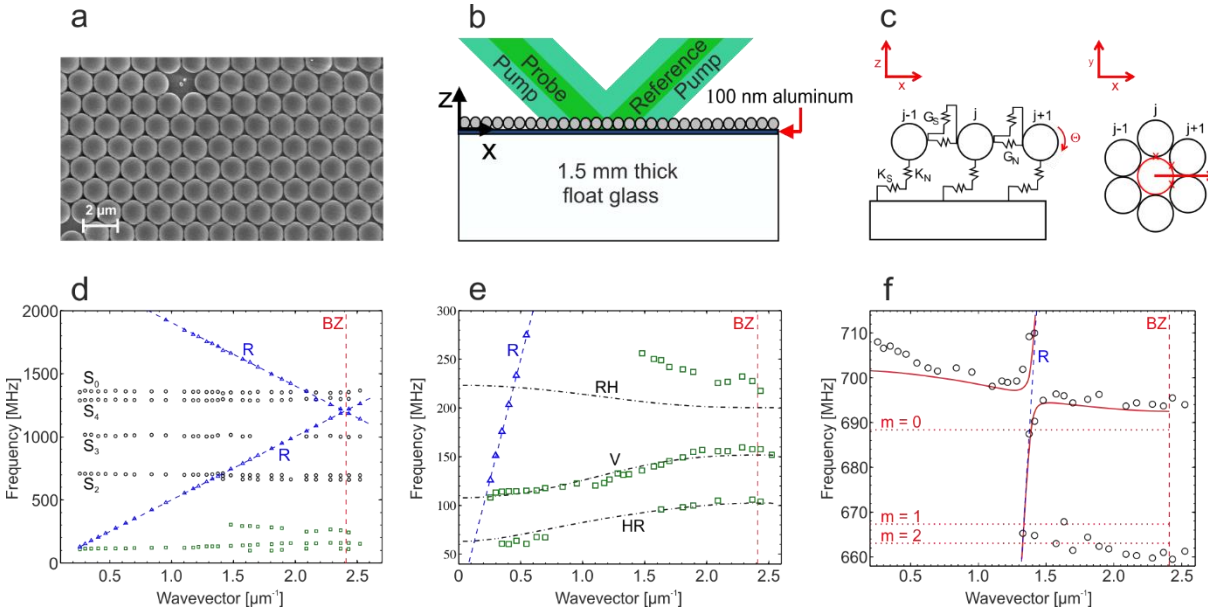


**Figure 2.3.** Vibrational dynamics of colloidal monolayers. (a) Scanning electron microscopy image of the polystyrene monolayer. (b) Scheme of the experimental setup. (c) Side-view and top-view scheme of the particle monolayer with particle-particle contacts  $G$  and particle-substrate contacts  $K$ . The red crosses indicate particle-particle contact springs, the red arrow denotes the wave propagation direction. (d) Measured dispersion diagram of a single crystalline particle monolayer. The dashed, blue line corresponds to the Rayleigh mode  $R$ , the dashed red line denotes the Brillouin zone boundary  $BZ$ . The spheroidal modes  $S_0$ ,  $S_2$ ,  $S_3$ ,  $S_4$  are labeled according to their angular number  $L$ . (e) Dispersion of the vertical  $V$  and horizontal contact-based modes  $RH$  and  $HR$ . The dash-dotted lines represent theoretical calculations. (f) Dispersion of the spheroidal mode  $S_2$ . The red dotted lines give the frequencies for an isolated sphere. The red solid line represents theoretical calculations. Reproduced from Physical Review B 96, 024303 (2017) with permission from American Physical Society.

Furthermore, the contact-based modes interact with the Rayleigh surface wave propagating in the substrate. While the avoided crossing of the vertical mode  $V$  and the Rayleigh surface wave is outside the measurement range, the interaction of the predominantly rotational ( $RH$ ) mode and the Rayleigh surface wave can be deduced from the peak width of the Rayleigh peak. Although the interaction cannot be observed directly, the broadened peak width at the expected intersection point is an evidence for a resonant attenuation of the Rayleigh peak.

At higher frequencies, four spheroidal modes  $S_L$  emerge, which can be characterized by a polar number  $L$ , an azimuthal number  $m$ , and a radial number  $n$ . In the absence of the substrate, the  $m = 2L + 1$  branches of the  $S_L$  modes degenerate. Due to the presence of the substrate, this

degeneracy is lifted for the intense  $S_2$  mode (Figure 2.3f). The dispersion of the branches of the  $S_2$  mode again indicates the influence of particle-particle interactions. Moreover, the  $S_L, m = 0$  branch distinctly shows a strong interaction with the Rayleigh surface wave yielding an avoided crossing behavior at 695 MHz.

Capitalizing on the high long-range order of the particle monolayer prepared by self-assembly, these new phenomena provide an insight into the interaction of acoustic waves with granular, periodic materials.

Additional to the particle size and the lattice period, the symmetry of the lattice crucially influences how waves interact with a colloidal crystal. Thus, controlling the symmetry is decisive to attain full control over the phononic and photonic properties of these assemblies, like the position of stop-bands. However, while the particle size and the lattice period are easily tunable using bottom-up approaches, the self-assembly of spherical particles nearly solely leads to the formation of hexagonal (two-dimensional) or face-centered-cubic (three-dimensional) arrangements. These structures present the thermodynamic minimum with a maximum of adjacent particle neighbors within the crystal. Different lattice symmetries are not readily accessible by colloidal assembly on a large scale. Therefore, a fabrication method was developed that allows for the preparation of particle monolayers with arbitrary lattice symmetry.

For this purpose, polymer particles with a diameter of 434 nm were assembled at the water/air interface giving hexagonal, close-packed particle monolayers. Subsequently, these floating monolayers were transferred onto hydrophobic substrates upon immersion of the substrate into the water sub-phase (Figure 2.4a). During this transfer step, the monolayer was stretched resulting in a change of the lattice symmetry. Nevertheless, when removing the particle-loaded substrate from the aqueous phase, the particle pattern was destroyed due to the capillary forces acting upon drying. This resulted in a loss of long-range order and clustered particles. To impede the capillary forces from distorting the structure during the drying step, the particles were fixed on the substrate. In this contribution, this was realized by heating the sample above the glass transition temperature of either the particles or a thin polymer coating on the substrate prior to the removal of the substrate.

The change of the lattice symmetry caused by the transfer onto hydrophobic substrates can be explained by a purely one-dimensional stretching of the originally hexagonal monolayer. This process can be described by the stretching vector  $\vec{S}$ , with the stretching factor  $S = |\vec{S}|$

determining the degree of stretching and the stretching angle  $\beta = \alpha - \delta$ . The stretching angle includes the orientation of the particle monolayer on the water/air interface  $\delta$  and the immersion direction of the substrate defined by the angle  $\alpha$  (Figure 2.4b).

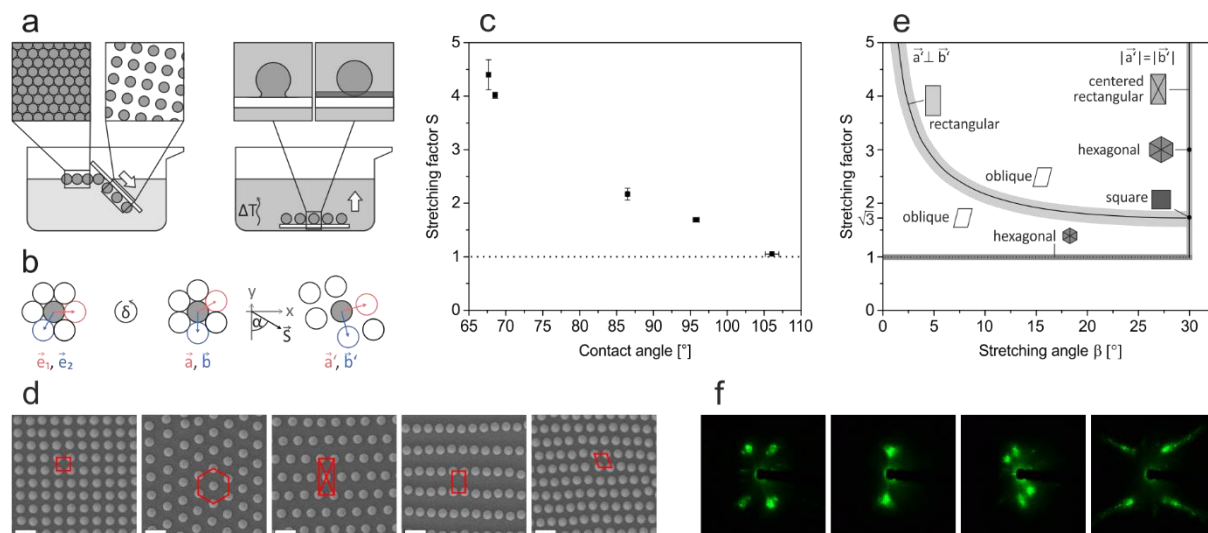


**Figure 2.4.** Non-hexagonal particle monolayers. (a) Scheme of the transfer process. (b) Scheme of the stretching parameters. (c) Stretching factor  $S$  as a function of the substrate contact angle. (d) Particle monolayers stretched into the five possible two-dimensional Bravais lattices. Scale bars are 1  $\mu\text{m}$ . (e) Phase diagram of stretched particle monolayers as a function of the stretching factor  $S$  and the stretching angle  $\beta$ . (f) Laser diffraction at distinct spots on one sample with  $S \sim 1.7$  show four different symmetries according to distinct stretching angles  $\beta$ . From left to right: Rectangular, close-packed particle lines, oblique and square. Reproduced from Langmuir 35, 973-979 (2019) with permission from American Chemical Society.

The stretching of the monolayer is a result of the hydrodynamic flow pattern of the liquid phase in proximity to a moving, hydrophobic substrate. It is known that for substrates with small contact angles, the water phase shows a split-injection streamline upon immersion of the substrate and the water/air interface moves away from the water/air/substrate contact line. Above a critical contact angle of the substrate, the water/air interface moves towards the substrate making a transfer of monolayers onto hydrophobic substrates possible. The velocity of the water interface approaching the contact line thereby is dependent on not only the immersion velocity of the substrate but also the contact angle of the substrate. The difference between the immersion velocity of the substrate and the velocity of the water interface thereby causes the stretching of the particle monolayer, with a stretching factor that is defined by the ratio of the two velocities. Accordingly, the stretching factor can be adjusted by tuning the water contact angle of the substrate (Figure 2.4c). While contact angles close to the critical angle

( $\sim 65^\circ$  in our case) yield extremely large stretching factors of  $S > 4$ , high contact angles of  $\theta = 106^\circ$  result in almost no stretching of the particle monolayer.

By tuning the stretching factor and the stretching angle, any of the possible two-dimensional Bravais lattices can be accessed: square, hexagonal, centered rectangular, rectangular and oblique (Figure 2.4d). The lattice symmetries obtained for given combinations of  $S$  and  $\beta$  can be extracted from the calculated phase diagram given in Figure 2.4e.

Although the particle monolayers prepared at the water/air interface are multi-crystalline, the size of the individual single-crystalline domains is large enough for diffraction experiments using a focused laser beam (Figure 2.4f). Due to the different orientation of the individual domains of the original, hexagonal monolayer, distinct lattice symmetries are attained within the same stretched monolayer. These lattice symmetries are defined by the same stretching factor but different stretching angles, which results in distinct scattering patterns for the individual domains of the stretched monolayer.

As the stretching takes place at the water/air/substrate contact line, the stretching mechanism is purely one-dimensional without the inherent transverse contraction when stretching particle monolayers on flexible substrates. Consequently, the stretching process is solely limited by the domain size of the original monolayer. This renders this process unique concerning the scalability and the large stretching factors accessible.

Manifold periodic structures can be replicated into different materials using colloidal lithography as described in chapter 1.2. The obtained surfaces offer structures in the colloidal size range and can, in turn, be used to direct the self-assembly of colloidal particles. Templated self-assembly strategies provide an additional tool for the fabrication of hierarchically structured materials with designed geometries. The concept of this contribution is based on the self-assembly of colloidal polystyrene particles into the holes of gold nanohole arrays solely by controlling the electrostatic interactions between the particles and the substrate (Figure 2.5a). The used gold nanomeshes feature hole diameters that are in the size range of the single particles. In order to realize a highly defined site-selective adsorption of the polymer particles, the electrostatic properties of the gold nanohole array and the underlying glass substrate were adjusted separately via chemical functionalization. To attract the negatively stabilized particles, a positive surface charge was created on the glass surface by covalently introducing an amino-terminated silane. Simultaneously, the gold surface was functionalized with a hydroxy-terminated thiol, which presents a negative charge in aqueous media and thus repels the

particles. The particles were then immobilized by immersing the functionalized substrate into the aqueous particle dispersion.

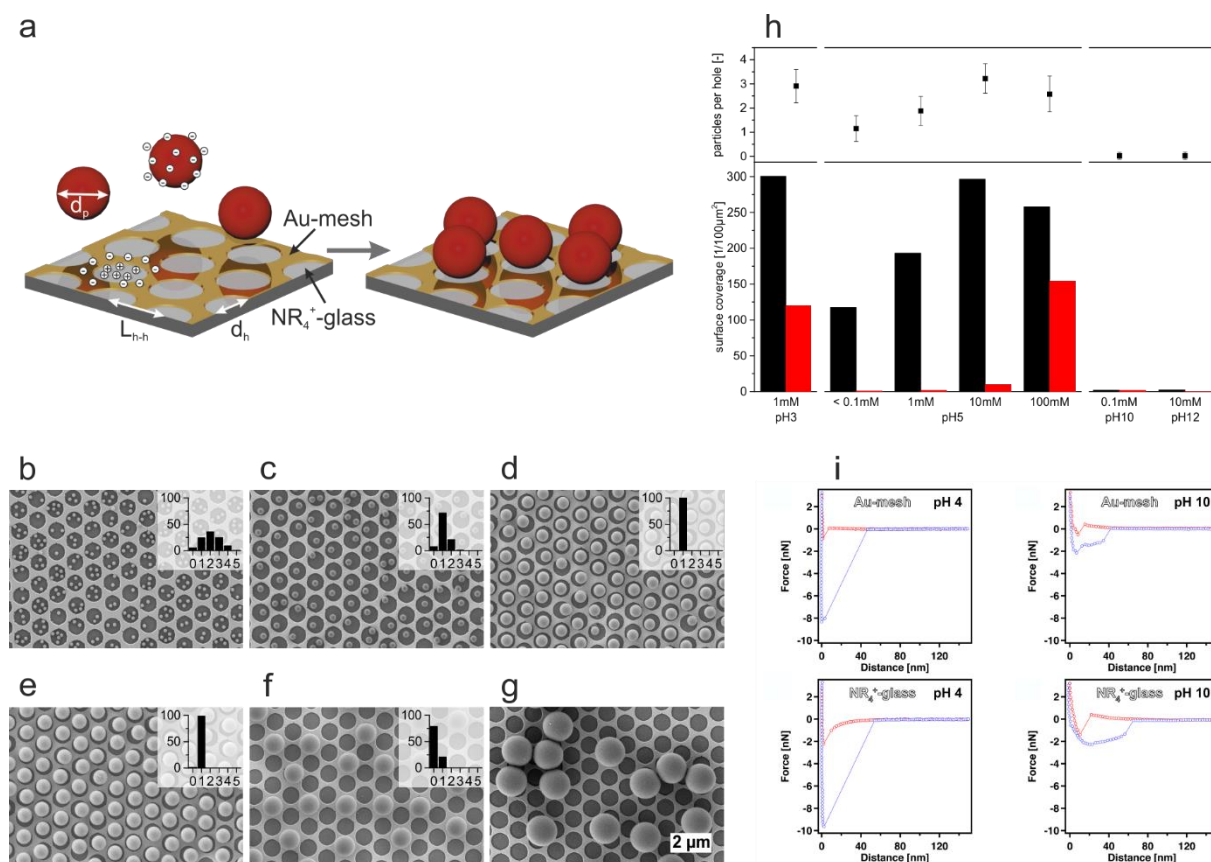


**Figure 2.5.** Particle assembly directed by gold nanohole arrays. (a) Schematic representation of the self-assembly process. Polystyrene particles with diameters of (b) 166 nm, (c) 320 nm, (d) 570 nm, (e) 740 nm, (f) 1040 nm and (g) 1500 nm assembled into a gold nanohole arrays with a period  $P = 1040$  nm and hole diameters of  $d = 870$  nm. The insets show the frequency distribution of the number of particles per hole in percent. (h) Average particles per hole and surface coverage as a function of pH and ionic strength for 320 nm particles assembled into a gold nanohole arrays with a period  $P = 1040$  nm and hole diameters of  $d = 870$  nm. Red: particles on gold, black: particles on glass. (i) Force *versus* distance profiles on the gold and glass surface at two different pH values measured in an AFM force experiment with a polystyrene colloidal probe. Red symbols depict the force during the approach, blue the force during the retraction of the colloidal probe. Reproduced from *Nanoscale* 8, 14556-14564 (2016) with permission from The Royal Society of Chemistry.

In Figure 2.5b-g the adsorption patterns of particles with distinct particle diameters in gold nanohole arrays with a lattice period of  $P = 1040$  nm and a hole diameter of  $d = 870$  nm are shown. As the assembly in nanohole arrays leads to non-close-packed particle arrangements, the assembled structures are very sensitive towards capillary forces upon drying, similar to the particle monolayers stretched into non-hexagonal symmetries. In this project, the capillary forces were minimized by exchanging the aqueous particle dispersion with ethanol and finally

hexane, which exhibits a considerably lower surface tension. The random sequential adsorption mechanism and the effective screening of the capillary forces resulted in the absence of direct particle-particle contacts even within one hole, which is not possible using convective assembly strategies. Because of the electrostatic repulsion between the particles, the self-assembly is limited to the first particle layer.

A highly selective adsorption was achieved for particles between 166 nm and 1040 nm. For particle diameters smaller than the hole radius, multiple particles are deposited in one hole (Figure 2.5b,c). Single particles are adsorbed for particle diameters between the hole radius and the hole diameter with more than 99 % of the holes being occupied (Figure 2.5d,e). Particles with a diameter equal to the lattice period cannot occupy adjacent holes due to the interparticle repulsion (Figure 2.5f). Even larger particles show no site-selective adsorption. As the particles are much larger than the surface structure, the particles only recognize an effective surface charge (Figure 2.5g).

Moreover, the influence of the ionic strength and the pH conditions were evaluated as depicted in Figure 2.5h. At constant pH conditions, the number of particles immobilized per hole can be controlled by varying the ionic strength of the particle dispersion. With increasing ionic strength the Debye length of the particles is more and more reduced. Thus, the average number of particles per hole is increased from 1.15 for an ionic strength of  $< 0.1$  mM NaCl to 3.22 for an ionic strength of 10 mM NaCl leading to a higher particle coverage on the glass surface (black bars in Figure 2.5h). Higher salt concentrations result in a high amount of particles adsorbed on the gold surface (red bars in Figure 2.5h) and, therefore, in a loss of selectivity. Furthermore, the assembly process is sensible towards the pH of the particle dispersion. While the particle adsorption is selective at neutral and slightly acidic pH conditions, the selectivity is lost at pH 3. In contrast, no particles are adsorbed at high pH values. The forces acting between the particles and the substrate surface were *in-situ* measured with spatial resolution using atomic force microscopy (AFM) with a polystyrene colloidal probe in slightly acidic (pH 4) and alkaline (pH 10) conditions at constant ionic strength (Figure 2.5i). At pH 4 a distinct long-range attractive force was observed on the glass surface in the approach profile. In contrast, a slight repulsion was measured on the gold surface. This contrast in electrostatic forces results in the directed adsorption of the particles on the glass surface. Once in contact with the surface, the particles show a strong, irreversible adhesion independent of the surface material in the retraction profile. Under alkaline conditions, repulsive interactions are dominant on both the gold and the glass surface. This repulsion is explained by the accumulation of hydroxyl ions at

the substrate surface, screening even the long-range attractive forces of the amino-terminated silane. Consequently, the adsorption of particles is impeded.

Altogether, using gold nanohole arrays, the particle-substrate interaction can be designed on a sub-micrometer size range facilitating the site-selective adsorption of colloidal particles with a high long-range order following the symmetry of the underlying template.

The last part of this thesis addresses the assembly of optical devices via colloidal lithography. For this purpose, the concept of colloidal lithography was expanded to enable the fabrication of gold nanohole arrays on arbitrary substrates. As colloidal lithography often applies harsh conditions such as plasma etching of the particles, the technique was hitherto confined to inert substrates such as glass or silicon. To enhance the variability of the structures accessible with colloidal lithography, a process for the transfer of metal nanohole arrays was established. The altered fabrication process is depicted in Figure 2.6a.

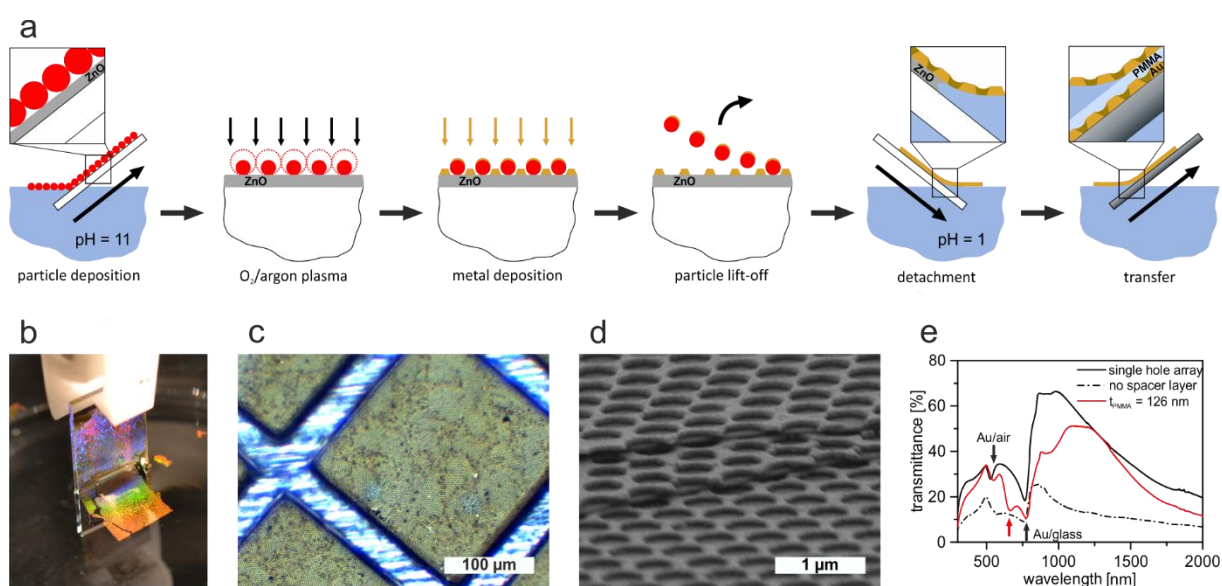


**Figure 2.6.** Interface mediated transfer of gold nanohole arrays. (a) Schematic representation of the preparation and transfer process. (b) Photograph of the detachment process. (c) Free-standing Au nanohole array with period  $P = 2560$  nm on a copper grid. (d) Side-view scanning electron microscopy image of a five-layer stack of alternating Au nanohole arrays and SiO<sub>2</sub> layers. (e) Transmittance spectrum of two Au nanohole arrays separated by 126 nm PMMA compared to a single nanohole array and two nanohole arrays stacked without spacer layer. The Au/glass and Au/air SPP resonances are highlighted by the black arrows, the metamaterial resonance of the stacked device is indicated by the red arrow. Reproduced from *Advanced Materials Interfaces* 5, 1800154 (2018) with permission from Wiley-VCH.

Prior to the assembly of the particles, a glass substrate was coated with a zinc oxide sacrificial layer. The particles were self-assembled into a hexagonal, close-packed monolayer at the

water/air interface and transferred onto the sacrificial layer under alkaline conditions. In contrast to organic sacrificial layers, zinc oxide is not degraded during the plasma etching step used for the size reduction of the particles. A gold layer was subsequently deposited by thermal evaporation followed by the removal of the particle template resulting in the gold nanohole array. In order to transfer the gold nanohole array onto the target substrate, the zinc oxide layer was dissolved by slowly immersing the support substrate into an acidic solution (Figure 2.6b). Due to the surface tension, the nanohole array was trapped at the water/air interface and subsequently deposited onto the target substrate.

In this way, nanohole arrays can be fabricated on surfaces that were not accessible before because of the aforementioned limitations such as flexible polymer materials. Likewise, transferring the detached nanohole arrays onto copper grids yielded free-standing nanohole arrays with self-supporting areas of  $204 \times 204 \mu\text{m}^2$  at a film thickness of only 100 nm (Figure 2.6c). Furthermore, by introducing a silica insulator layer directly on the sacrificial layer before the deposition of the particles, the combination of the insulator layer and the metal nanohole array was transferred. This allows for a very fast production of metal-insulator-metal (MIM) structures with high spatial uniformity and an arbitrary number of layers (Figure 2.6d). However, the transfer process does not permit the alignment of the nanohole patterns between individual layers. Together with the multi-crystalline nature of the nanohole arrays, this results in distinct Moiré patterns attributed to distinct in-plane rotational offsets of the nanohole arrays. Nevertheless, a three-layer stack comprising two gold nanohole arrays separated by a PMMA spacer layer features excellent optical properties (Figure 2.6e). Compared to a sample without the spacer layer, the transmittance is considerably enhanced. Besides, additional to the reflectance minima corresponding to the Au/glass and Au/air SPP resonances, which are also visible for a single nanohole array, a magnetic metamaterial resonance was identified. This metamaterial resonance originates from the coupling between the metal layers and is strongly dependent on the thickness of the spacer layer.

The developed transfer protocol for gold nanohole arrays was then applied to fabricate three-layered MIM structures consisting of a gold nanohole array, a polymeric insulator layer and a continuous gold back-reflector (Figure 2.7a,b). These structures exhibit pronounced plasmonic coupling effects, which were examined using angle-resolved UV-vis-NIR spectroscopy (Figure 2.7c). The spectral properties of the MIM structures drastically differ from the spectra of individual nanohole arrays. Narrow reflectance dips are observed and assigned to the resonant excitation of SPP modes of the MIM structures resulting in bright reflection colors of

the macroscopic samples. A high spatial homogeneity can be inferred from the uniformity of these reflection colors (insets in Figure 2.7c). For self-assembled materials, surprisingly high Q-factors of up to 14 for the strongest resonance were obtained in the visible wavelength range. This resonance was found to be strongly dependent on the lattice period of the nanohole array.

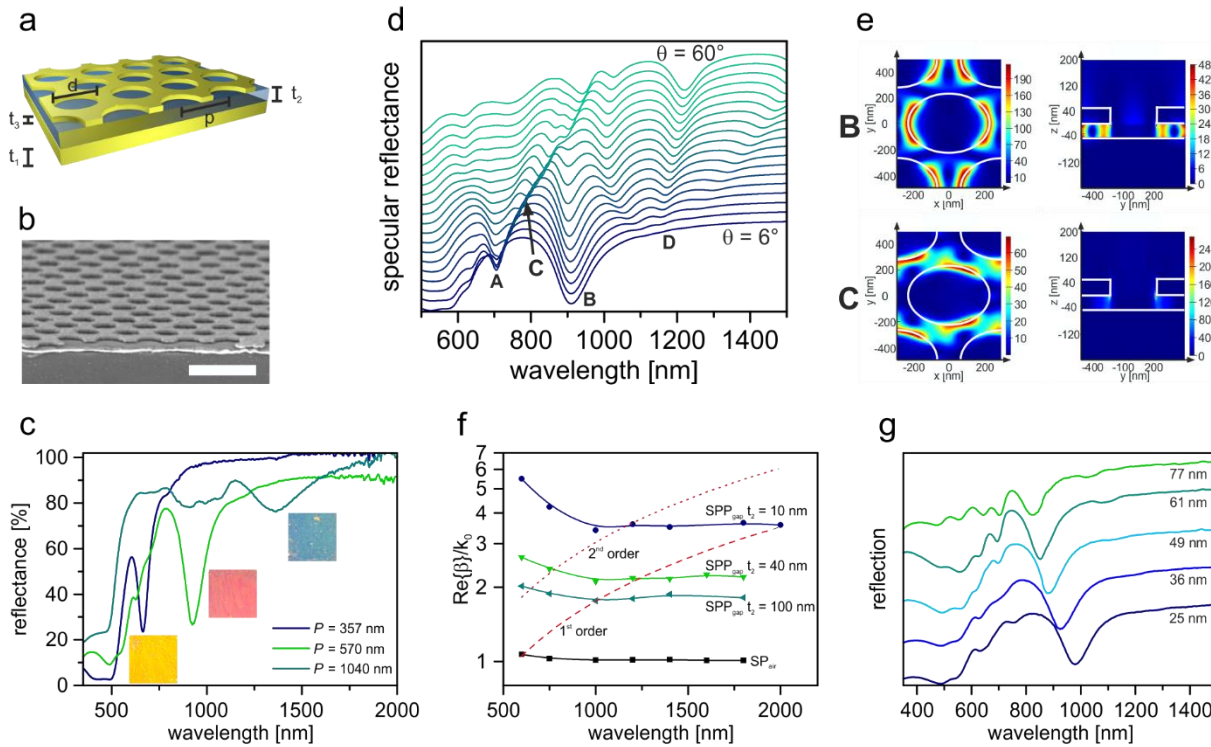


**Figure 2.7.** Optical properties of nanohole array MIM structures. (a) Schematic illustration of the MIM setup. (b) Side-view scanning electron microscopy image of a MIM structure. Scale bar is 1  $\mu\text{m}$ . (c) Total reflectance of MIM structures with different lattice periods measured with unpolarized light at an angle of incidence of  $\theta = 10^\circ$ . The insets are photographs and show the macroscopic reflectance colors of a  $5 \times 5 \text{ mm}^2$  sample area. (d) Angle-resolved specular reflectance of a MIM structure with  $P = 570 \text{ nm}$  and  $t_2 = 50 \text{ nm}$  measured in  $3^\circ$  steps between  $\theta = 6^\circ$  and  $\theta = 60^\circ$  with p-polarized light. (e) Electric field distributions normalized to the incident electric field evaluated for modes B and C along the horizontal and vertical cross-sections of the unit cell for light incident at an angle of  $\theta = 22^\circ$ . (f) Analytical derivation of the resonance wavelengths for distinct gap thicknesses. The dashed and dotted lines indicate the first and second order grating dispersion. The solid lines give the propagation constant  $\beta$  of the guided modes supported by the structure. Resonant excitation is possible where the dispersions of the guided modes and the grating intersect.  $k_0$  is the light wavenumber in vacuum. (g) Total reflection of MIM structures with different gap thicknesses measured with unpolarized light at an angle of incidence of  $\theta = 10^\circ$ . Reproduced from *Nanoscale* 10, 17983-17989 (2018) with permission from The Royal Society of Chemistry.

Finite-difference time domain (FDTD) simulations complemented by analytical calculations considering the diffraction phase-matching conditions of the SPP resonances were applied to analyze the rich plasmonic response revealed by angle-resolved UV-vis-NIR spectroscopy

(Figure 2.7d). All resonances can be ascribed to only two SPP modes localized at the Au/air interface ( $SPP_{\text{air}}$ ) and inside the insulator layer ( $SPP_{\text{gap}}$ ), respectively (Figure 2.7e). For a grating period of  $P = 570$  nm and small angles of incidence, the first and second order of the  $SPP_{\text{gap}}$  resonance are visible at approximately 900 nm (mode **B** in Figure 2.7d) and 700 nm (mode **A**). When increasing the angle of incidence the second order  $SPP_{\text{gap}}$  mode mixes with the  $SPP_{\text{air}}$  (mode **C**) resonance, which shows a strong dispersion in accordance with the diffraction coupling condition. Moreover, additional dispersive modes appear at 1200 nm (mode **D**), which were also attributed to the first order  $SPP_{\text{gap}}$  mode. Remarkably, the branch of the first order  $SPP_{\text{gap}}$  mode at 900 nm exhibits a non-dispersive behavior, which was explained by Bragg-scattering of the resonance.

The influence of the gap thickness was evaluated in experiment and simulation (Figure 2.7f,g). When decreasing the gap thickness, the  $SPP_{\text{gap}}$  modes strongly shift to longer wavelengths, and higher order  $SPP_{\text{gap}}$  modes appear at shorter wavelengths. In contrast, the  $SPP_{\text{air}}$  resonance is only marginally affected by the gap thickness. In a final series, the sensitivity of the MIM structures towards the refractive index environment was investigated. As expected, in contrast to the  $SPP_{\text{air}}$  resonance, the  $SPP_{\text{gap}}$  resonance is not sensitive to changes in the surrounding refractive index as its electric field is mainly confined inside the structure. Instead, the  $SPP_{\text{gap}}$  resonance can be affected by changing the refractive index in between the two gold layers. Accordingly, removing the polymer beneath the holes of the nanohole array by plasma etching leads to a shift of the  $SPP_{\text{gap}}$  resonance to shorter wavelengths.

After analyzing the plasmonic coupling effects in metal-insulator-metal stacks with non-absorbing insulator layers, plasmonic cavity modes were investigated in state-of-the-art organic solar cells. For this purpose, the transparent conducting indium tin oxide (ITO) electrode was replaced by gold nanohole arrays with distinct lattice periods. Together with the silver back-electrode, an optical cavity is formed, which supports SPP resonances. This contribution aimed to investigate the impact of these SPP resonances on the power conversion efficiency of the devices. For all periods, the hole diameter to period ratio was adjusted to  $d/P = 0.8$  to assure a constant area fraction to be covered by gold. Therefore, the transmittance was comparable for all samples in the visible range of approximately 40-60 %, which is considerably lower than for the reference ITO electrode exhibiting more than 80 %. When increasing the lattice period from 202 nm to 2560 nm, this loss in transmittance is more and more caused by a strong reflection of the metal layer, while the absorption dominates for small periods. As all nanohole arrays

exhibit an electrical conductivity comparable to ITO, all changes in the device performance are ascribed to the optical properties of the electrodes.

In a first series, bulk heterojunction solar cells were fabricated with the standard photoactive material P3HT:PC<sub>61</sub>BM (Figure 2.8a,b). Compared to the reference device comprising the ITO electrode, the power conversion efficiency is deteriorated for all devices based on a reduction of the short-circuit current ( $J_{SC}$ ). The efficiency increases with increasing grating period up to a period of  $P = 1040$  nm, which is explained with the decreasing parasitic absorption in the gold electrode. For larger periods, the efficiency was found to decline again caused by the increasing reflectance of the electrodes.

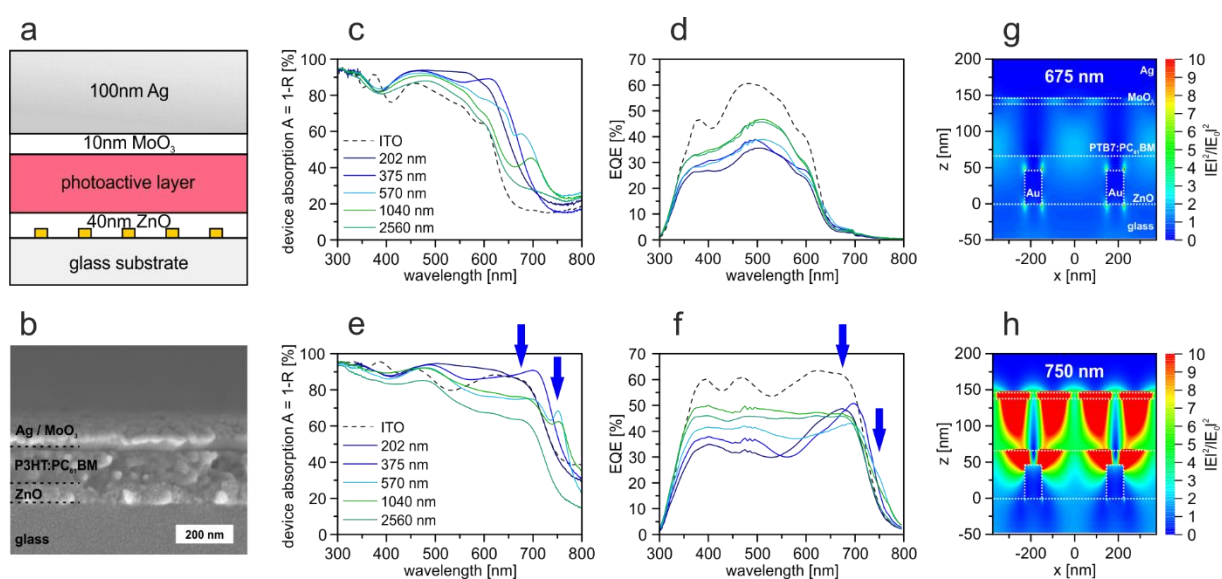


**Figure 2.8.** Au nanohole electrodes. (a) Schematic representation of the solar cell device structure. (b) Side-view scanning electron microscopy image of a P3HT:PC<sub>61</sub>BM device. (c) Measured device absorption and (d) external quantum efficiency of P3HT:PC<sub>61</sub>BM solar cells with gold nanohole electrodes with distinct lattice periods compared to a P3HT:PC<sub>61</sub>BM solar cell with ITO electrode (dashed lines). (e) Measured device absorption and (f) external quantum efficiency of PTB7:PC<sub>70</sub>BM solar cells with gold nanohole electrodes with distinct lattice periods compared to a PTB7:PC<sub>70</sub>BM solar cell with ITO electrode. (g) Electric field intensity distribution of a PTB7:PC<sub>70</sub>BM device with nanohole period  $P = 375$  nm at 675 nm and (h) 750 nm. The arrows in (e) and (f) indicate the wavelengths used for the calculation of the electric field intensity. Reproduced from Scientific Reports 7, 42530 (2017) with permission from Nature Publishing Group.

To correlate the device efficiency with the optical properties, UV-vis measurements of the assembled solar cells were performed (Figure 2.8c). Notably, the devices with the nanohole electrodes show an additional absorption peak, which is not present in the reference device. This absorption peak is located at the absorption edge of the photoactive layer and is only slightly shifting to longer wavelength for increasing periods. However, this additional

absorption does not contribute to the device efficiency, as no increased photocurrent generation was observed in the external quantum efficiency (EQE) (Figure 2.8d). Instead, the EQE is reduced throughout the whole absorption range of the photoactive layer.

In a second series, the photoactive layer was replaced by the low-bandgap polymer blend PTB7:PC<sub>71</sub>BM, which absorbs up to a wavelength of 750 nm. Surprisingly, the absorption peaks, attributed to an SPP resonance supported by the nanohole array structures, again become apparent at the absorption edge of the polymer (Figure 2.8e). Likewise, all nanohole array devices exhibit a reduced device performance compared to the reference device. The best performance is again found for the grating period of  $P = 1040$  nm. This trend is substantiated by a strong, uniform decrease in the EQE (Figure 2.8f). However, for small lattice periods, the EQE spectra displays an asymmetric line shape, which peaks at the spectral position of the SPP resonance. Additionally, for the period  $P = 375$  nm,  $P = 570$  nm and  $P = 1040$  nm, the EQE spectra of the nanohole devices even slightly exceed the EQE of the reference device at the absorption edge of the polymer.

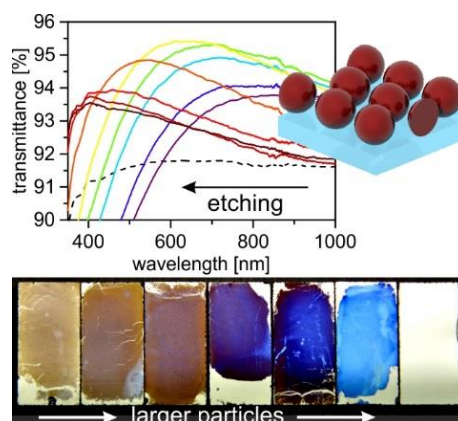
FDTD simulations were applied for a PTB7:PC<sub>71</sub>BM device with  $P = 375$  nm at the maximum EQE signal (Figure 2.8g) and the absorption edge of the polymer (Figure 2.8h) to identify the nature of the observed SPP resonances. At the lower wavelength, a dipolar plasmonic resonance is excited in the nanohole electrode and weakly couples to the silver back-electrode. The resonance is strongly damped by the absorption of the photoactive layer and, therefore, cannot contribute to the photocurrent generation of the device. In contrast, at the band edge of the polymer, a strong field enhancement is detected in the photoactive layer compared to the reference device, which elucidates the enhanced photocurrent generation at this wavelength. Thus, SPP resonances supported by structured metal electrodes actually can contribute to the device performance of organic solar cells. Nevertheless, this contribution is marginally small. Instead, the device performance is governed by the balance between reflectance and absorption losses caused by the nanohole electrode.

## 2.1 Graphical Table of Content

### Subwavelength Etched Colloidal Monolayers: A Model System for Tunable Antireflective Coatings

*Christian Stelling, Christoph Bernhardt, and Markus Retsch*

**The antireflective properties of well-defined colloidal monolayers** with sub-200 nm polystyrene particles are investigated. The key parameters, effective refractive index and layer thickness, can be adjusted precisely and independently to serve as single layer antireflection coating. This is realized by the fabrication of large area colloidal monolayers on glass substrates with ensuing plasma treatment.

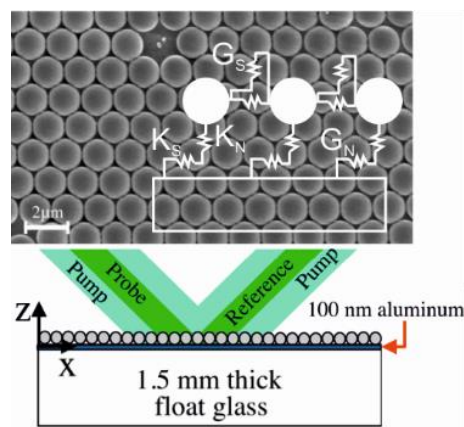


Page 93

### Vibrational Dynamics of a Two-Dimensional Microgranular Crystal

*Alejandro Vega-Flick, Ryan A. Duncan, Sam P. Wallen, Nicholas Boechler, Christian Stelling, Markus Retsch, Juan J. Alvarado-Gil, Keith A. Nelson, and Alexei A. Maznev*

**The acoustic dynamics of a hexagonal, close-packed monolayer of polystyrene microspheres** adhered to a solid substrate was studied using a laser-induced transient grating technique. Collective contact-based modes and spheroidal vibrations of the microspheres were identified across the entire Brillouin zone. Further, a resonance splitting of a spheroidal resonance and an avoided crossing between surface Rayleigh waves and a spheroidal mode were detected and described analytically.

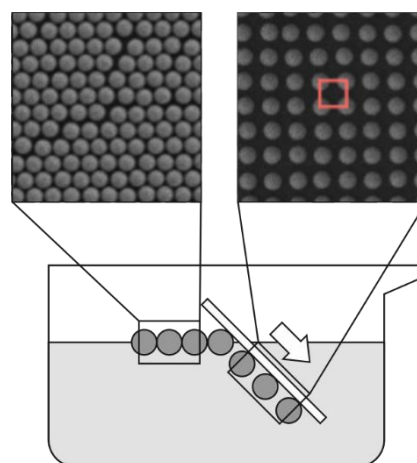


Page 113

### Ordered Particle Arrays via a Langmuir Transfer Process: Access to Any Two-Dimensional Bravais Lattice

*Miriam E.J. Hummel<sup>‡</sup>, Christian Stelling<sup>‡</sup>, Bernd A.F. Kopera, Fabian A. Nutz, Matthias Karg, Markus Retsch, and Stephan Förster*  
<sup>‡</sup> These authors contributed equally.

**Two-Dimensional, non-close-packed particle monolayers with all possible Bravais lattices** can be prepared by stretching hexagonal, close-packed particle arrays upon transfer from the water/air interface onto solid substrates. The symmetry of the lattice can be fully controlled by tuning the contact angle of the substrate and the monolayer orientation.

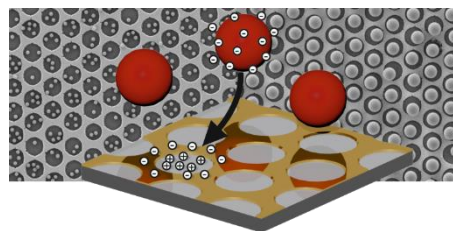


Page 131

## Showing Particles their Place: Deterministic Colloid Immobilization by Gold Nanomeshes

*Christian Stelling, Andreas Mark, Georg Papastavrou, and Markus Retsch*

**Deterministic particle immobilization** is a key technique for the fabrication of functional materials via directed self-assembly. Electrostatic interactions allow to selectively adsorb latex particles onto gold nanomesh arrays. Surface functionalization in combination with pH, ionic strength, and particle size allow for the preparation of non-close-packed monolayers with high surface coverage.

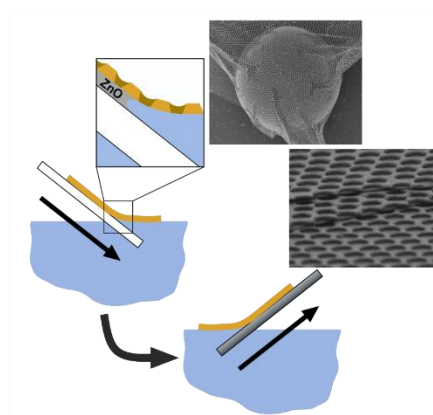


Page 151

## Nanomeshes at Liquid Interfaces: From Free-Standing Hole Arrays toward Metal-Insulator-Metal Architectures

*Christian Stelling and Markus Retsch*

**A bottom-up approach for the assembly of multilayer metal-insulator-metal structures based on metal nanohole arrays is demonstrated.** Gold nanohole arrays were prepared via nanosphere lithography on a zinc oxide sacrificial layer, which allows for an interface-mediated transfer of the nanohole arrays onto hydrophilic or hydrophobic substrates. The high mechanical stability of only 100 nm thick arrays is underlined by the preparation of free-standing nanomeshes.

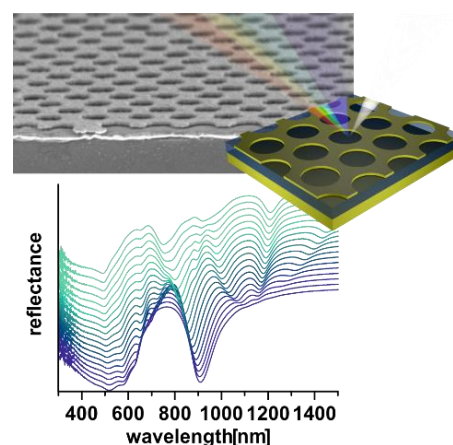


Page 183

## Surface Plasmon Modes of Nanomesh-on-Mirror Nanocavities Prepared by Nanosphere Lithography

*Christian Stelling, Stefan Fossati, Jakub Dostálek, and Markus Retsch*

**Metal-insulator-metal structures comprising gold nanohole arrays and opaque gold back-reflectors were prepared by colloidal lithography.** Unusually narrow gap plasmon modes were identified by angle-resolved UV-vis-NIR spectroscopy, FDTD simulation, and analytical theory. The spectral position of the gap mode can be controlled by tuning the grating period as well as the thickness and the refractive index of the dielectric spacer.

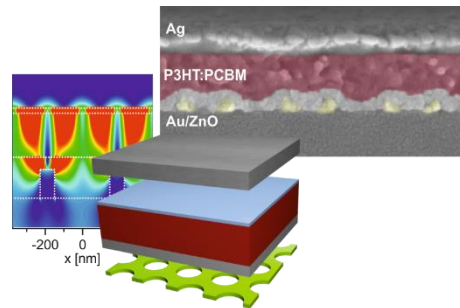


Page 199

## Plasmonic Nanomeshes: Their Ambivalent Role as Transparent Electrodes in Organic Solar Cells

*Christian Stelling, Chetan R. Singh, Matthias Karg, Tobias A. F. König, Mukundan Thelakkat, and Markus Retsch*

**Periodic nanomeshes are studied as transparent conducting electrodes in organic solar cells.** In the device, a cavity mode is excited, which contributes to the power conversion efficiency. However, as the mode is confined to the absorption edge of the active layer material for all periodicities, the plasmonic enhancement is negligible compared to the absorption losses in the nanomesh.



## 2.2 Contributions to Joint Publications

The publications presented in this thesis were prepared in collaboration with colleagues and other research groups. In the following, the individual contributions of all authors are specified in detail.

### **Chapter 3: Subwavelength Etched Colloidal Monolayers: A Model System for Tunable Antireflective Coatings**

by *Christian Stelling, Christoph Bernhardt and Markus Retsch*

I prepared the particle monolayers, characterized the samples by scanning electron microscopy, atomic force microscopy, UV-vis spectroscopy, and ellipsometry, carried out the data analysis, prepared the figures and corrected the manuscript.

Christoph Bernhardt helped with the preparation of particle monolayers.

Markus Retsch synthesized some of the particle dispersions, supervised the project and wrote the manuscript.

### **Chapter 4: Vibrational Dynamics of a Two-Dimensional Microgranular Crystal**

by *Alejandro Vega-Flick, Ryan A. Duncan, Sam P. Wallen, Nicholas Boechler, Christian Stelling, Markus Retsch, Juan J. Alvarado-Gil, Keith A. Nelson and Alexei A. Maznev*

Alejandro Vega-Flick conducted the measurement, evaluated the data, prepared the figures, and wrote the manuscript.

Ryan A. Duncan was involved in the measurement and the data evaluation and proofread the manuscript.

Sam P. Wallen developed the theoretical model, was involved in scientific discussions and proofread the manuscript.

Nicholas Boechler developed the theoretical model, was involved in scientific discussions and proofread the manuscript.

I prepared the particle monolayers, characterized the samples by scanning electron microscopy, wrote the sample preparation part of the manuscript, and proofread the manuscript.

Markus Retsch supervised the project, was involved in scientific discussions and proofread the manuscript.

Juan J. Alvarado-Gil was involved in scientific discussions and proofread the manuscript.

Keith A. Nelson, supervised the project, was involved in scientific discussions and proofread the manuscript.

Alexei A. Maznev supervised the project, was involved in scientific discussions and corrected the manuscript.

## **Chapter 5: Ordered Particle Arrays via a Langmuir Transfer Process: Access to Any Two-Dimensional Bravais Lattice**

*by Miriam E.J. Hummel<sup>‡</sup>, Christian Stelling<sup>‡</sup>, Bernd A.F. Kopera, Fabian A. Nutz, Matthias Karg, Markus Retsch and Stephan Förster*

*<sup>‡</sup> These authors contributed equally.*

Miriam E.J. Hummel contributed to the concept development, fabricated the monolayers, analyzed the samples with scanning electron and optical microscopy, was involved in scientific discussions, prepared the figures, and contributed to the manuscript.

I contributed to the concept development, fabricated the monolayers, analyzed the samples with scanning electron and optical microscopy, and contributed to the manuscript.

Bernd A.F. Kopera wrote a python script for the analysis of the lattice symmetry of the samples, analytically derived the phase diagram, and proofread the manuscript.

Fabian A. Nutz synthesized the particles and proofread the manuscript.

Matthias Karg was involved in scientific discussions and proofread the manuscript.

Markus Retsch was involved in scientific discussions, supervised the project, and corrected the manuscript.

Stephan Förster was involved in scientific discussions, supervised the project, and corrected the manuscript.

## **Chapter 6: Showing Particles their Place: Deterministic Colloid Immobilization by Gold Nanomeshes**

*by Christian Stelling, Andreas Mark, Georg Papastavrou and Markus Retsch*

I prepared the nanohole array substrates, performed the self-assembly experiments, characterized the particles via dynamic light scattering, characterized the samples via scanning electron microscopy, optical microscopy and confocal laser scanning microscopy, evaluated the data, prepared the figures, and wrote the manuscript.

Andreas Mark carried out the atomic force microscopy colloidal probe experiments, evaluated the associated data, was involved in scientific discussions, prepared a figure, and wrote a paragraph of the manuscript concerning the colloidal probe measurements.

Georg Papastavrou was involved in scientific discussions, supervised the project, and corrected the manuscript.

Markus Retsch was involved in scientific discussions, supervised the project, and corrected the manuscript.

## **Chapter 7: Nanomeshes at Liquid Interfaces: From Free-Standing Hole Arrays toward Metal-Insulator-Metal Architectures**

*by Christian Stelling and Markus Retsch*

I developed the concept, prepared the samples, performed the sample characterization with scanning electron microscopy, optical microscopy, atomic force microscopy and UV-vis spectroscopy, evaluated the data, prepared the figures, and wrote the manuscript.

Markus Retsch was involved in scientific discussions, supervised the project, and corrected the manuscript.

## **Chapter 8: Surface Plasmon Modes of Nanomesh-on-Mirror Nanocavities Prepared by Nanosphere Lithography**

*by Christian Stelling, Stefan Fossati, Jakub Dostalek and Markus Retsch*

I prepared the samples, carried out the sample characterization via scanning electron microscopy, atomic force microscopy, optical microscopy and UV-vis spectroscopy, evaluated the data, prepared the figures and wrote the manuscript.

Stefan Fossati performed the FDTD simulations, analyzed the associated data, was involved in scientific discussions and wrote the FDTD paragraph of the manuscript.

Jakub Dostalek was involved in scientific discussions, derived the analytical model, supervised the project, and corrected the manuscript.

Markus Retsch was involved in scientific discussions, supervised the project, and corrected the manuscript.

## **Chapter 9: Plasmonic Nanomeshes: Their Ambivalent Role as Transparent Electrodes in Organic Solar Cells**

*by Christian Stelling, Chetan R. Singh, Matthias Karg, Tobias A. F. König, Mukundan Thelakkat and Markus Retsch*

I prepared the nanohole electrodes, characterized the electrodes with scanning electron microscopy, characterized the neat electrodes as well as the full device stack with UV-vis spectroscopy, analyzed the data, prepared the figures and wrote the manuscript.

Chetan R. Singh fabricated and characterized the solar cell device performance, was involved in scientific discussions and wrote the device preparation and the device performance paragraph of the manuscript.

Matthias Karg was involved in scientific discussions.

Tobias A.F. König performed ellipsometry measurements, implemented the FDTD simulations, analyzed the associated data, was involved in scientific discussions, wrote the FDTD paragraph of the manuscript and supervised the project.

Mukundan Thelakkat was involved in scientific discussions, supervised the project, and corrected the manuscript.

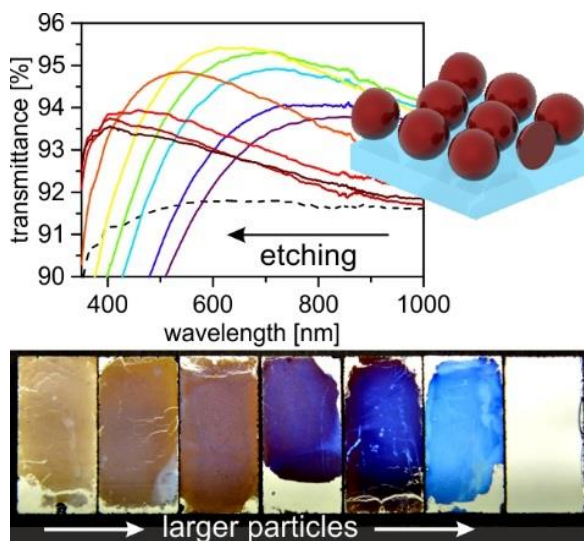
Markus Retsch was involved in scientific discussions, supervised the project, and corrected the manuscript.



### 3 Subwavelength Etched Colloidal Monolayers: A Model System for Tunable Antireflective Coatings

Christian Stelling, Christoph Bernhardt, and Markus Retsch\*

Physical Chemistry – Polymer Systems, University of Bayreuth, 95440 Bayreuth, Germany



Published in *Macromolecular Chemistry and Physics* 216, 1682-1688 (2015).

Reproduced with permission from Wiley-VCH.

### Abstract

Colloidal monolayers represent a versatile material class to fabricate nanostructures with high quality. The length scale of the nanostructured film is given by the size of the colloidal nanoparticles. Importantly, colloidal monolayers, though being of hexagonal, close-packed symmetry, still embody a high amount of free volume. This reduces the effective refractive index of thin colloidal monolayer films significantly. For particles and periodicities  $< 200$  nm the heterogeneous layer can be approximated by an effective medium theory. The amount of free volume can be further fine-tuned by a controlled size reduction of the constituting spheres, for instance by plasma etching. This can be utilized to realize an optimum refractive index for the application of colloidal monolayers as antireflective coatings. In contrast previously reported  $> 200$  nm monolayers demonstrate distinct extinction peaks due to grating diffraction. Rational design by the use of differently sized particles further allows shifting the best performance across the visible spectrum. Colloidal monolayers, though representing single layer antireflective coatings, exhibit broadband AR properties and are ideally suited to demonstrate the influence of refractive index and layer thickness, independently.

### 3.1 Introduction

Antireflective (AR) coatings are important and widespread components of optical devices. The key challenge in the fabrication of suitable antireflective coatings lies in the limited availability of low refractive index materials. This can be understood when looking at the Fresnel equation, which quantifies the amount of reflected light depending on the angle of incidence and the refractive index of the substrate ( $n_{glas}$ ) and surrounding medium ( $n_{air}$ ).

For the case of normal incidence the reflection  $R$  is given by the Fresnel equation

$$R = \left( \frac{n_c^2 - n_{glass}n_{air}}{n_c^2 + n_{glass}n_{air}} \right)^2 \quad 3.1$$

It yields a minimum in reflection for the case that the optical thickness of the antireflective coating layer with refractive index  $n_c$  amounts to a fourth of the wavelength  $\lambda$  of consideration. This resembles the case of destructive interference for reflection at the air-coating and coating-substrate interface. For the common case of AR coatings on glass substrates, the minimum in

reflectivity is obtained by  $n_c = \sqrt{n_{glass}n_{air}} = \sqrt{1.49 \cdot 1.00} = 1.23$ .<sup>1</sup> However, that low refractive indices are not known for dense materials.

A general approach to realize such low refractive indices is to utilize porous materials. Here, the low refractive index of air is introduced in such a way into the material that light scattering at these structures is suppressed, as the porosity is notably smaller than the wavelength of visible light.<sup>1,2</sup> Quite commonly, (meso)porous nanoparticles on the order of less than 200 nm in diameter are used, which can be applied via spin-coating to adjust a distinct layer thickness.<sup>1,3</sup> Other approaches comprise the fabrication of hollow nanoparticles with an even lower effective refractive index due to the air-filled core.<sup>4-7</sup> Colloidal assembly structures may further lower the effective refractive index of the layer by a considerable amount of free volume between the particles.

Colloidal monolayers represent a particularly well-defined particle superstructure, which is characterized by a highly ordered two-dimensional hexagonal lattice and layer thickness, both given by the constituting particle. A vast range of methods has been developed to access high quality colloidal monolayers, which are summarized in a recent review.<sup>8</sup> The optical properties of colloidal monolayers consisting of non-absorbing dielectric spheres such as polystyrene (PS) or silica have already been reported for particle sizes in the range of visible light.<sup>9,10</sup> In this case, a distinct (angle dependent) dip in the transmittance can be observed due to Bragg diffraction at the periodic grating. Going to sub-wavelength particle sizes and periodicities, the distinct diffraction peak vanishes and broad anti-reflective properties emerge.<sup>11,12</sup> However, in previous studies the lattice spacing still exceeded 200 nm<sup>12</sup> or limited control over the long range order and therefore the effective refractive index was reported.<sup>11</sup> Other reports have used silica particle monolayers to increase the overall transmission through a glass slide.<sup>13,14</sup> One should note that not only a reduced refractive index can lower the reflectivity, but that also the spherical topography and consequently the gradual variation of the refractive index can influence the refraction of light.<sup>14</sup> The particles were either be arranged on a regular hexagonal lattice<sup>13</sup> or can be electrostatically adsorbed in a random fashion.<sup>15</sup> The use of silica nanospheres, however, limits the possibility to precisely adjust the effective refractive index and the layer thickness on glass. This is due to the same chemical composition of the substrate (glass) and the SiO<sub>2</sub> particles. Etching of the SiO<sub>2</sub> spheres would simultaneously etch the supporting glass surface.

In order to complete the optical property characterization of simple dielectric colloidal monolayers we devote this study to sub-wavelength, highly ordered particle monolayers

consisting of polystyrene spheres. We demonstrate periodicities and layer thicknesses below 200 nm and can therefore treat the colloidal coating as an effective medium layer. We further investigate the intricate influence of the free volume between the constituting spheres on the antireflective properties of these monolayers. It shall be noted that the same type of colloidal monolayers can be used as template to fabricate even better antireflective coatings based on etched gradient structures. The interested reader for these kinds of moth-eye antireflective coatings is referred to recent reviews in this field.<sup>16,17</sup>

### 3.2 Results and Discussion

In this contribution we want to solely focus on the possibility to use the interstitial space of well-defined colloidal superstructures as a method to fabricate low refractive index, single-layer antireflective coatings. The use of polymer nanoparticle monolayers offers the possibility to tune the particle dimensions by plasma etching without harming the supporting glass substrate, due to their orthogonal chemical stability.<sup>10,18</sup> As reported by Vogel *et al.* the size reduction upon plasma etching leads to a shift of the Bragg refraction caused by interference and can be seen by a change of the colour of the coating layer.<sup>10</sup> However, they used colloidal particles of > 400 nm in diameter. Taking into account that the wavelength of the optimum performance  $\lambda_{max}$  of a single-layer coating can be calculated by

$$\lambda_{max} = 4 \cdot n_c \cdot d \quad 3.2$$

one notices, that an effective layer thickness  $d$  ranging from 80 – 160 nm should be realized to cover the visible regime on glass for the case of perpendicular illumination. Therefore, polymer particles in the range between 100 nm and 200 nm diameter should be used as starting material, as the particle size is reduced in the following procedure. This particle size is considerable smaller than the wavelength of visible light and thus diffuse scattering is minimized. A colloidal monolayer of such particles can therefore be approximated by an effective medium theory, where the interstitial space between the constituting spheres contributes to a reduced refractive index. This concept is outlined in Figure 3.1.

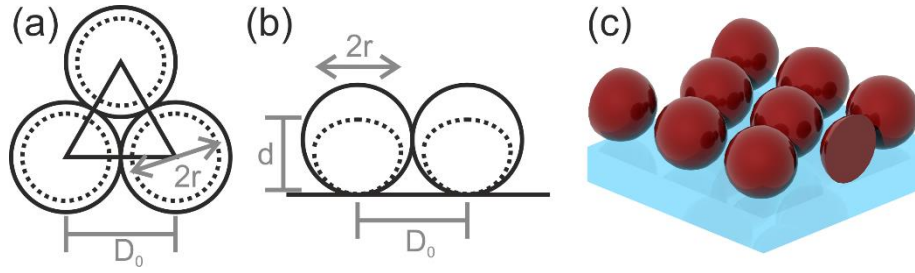


**Figure 3.1.** a) Top view and b) Side view of a colloidal monolayer. The interparticle spacing is given by the initial particle diameter  $D_0$  and remains constant during the size-reduction step. The layer thickness  $d$  depends on the size  $2r$  of the anisotropically etched particles. c) Three-dimensional model of an etched colloidal monolayer on a glass substrate.

By simple geometric considerations one can deduce that the area fraction  $\Theta$  of a colloidal monolayer is given by

$$\Theta = \frac{2 \cdot r^2 \cdot \pi}{D_0^2 \cdot \sqrt{3}} \quad 3.3$$

and the volume fraction  $\Phi$  is given by

$$\Phi = \frac{4 \cdot r^2 \cdot \pi}{3 \cdot D_0^2 \cdot \sqrt{3}} \quad 3.4$$

with  $r$  being the particle radius and  $D_0$  being the interparticle distance (see Figure 3.1), which is given by the initial particle diameter  $D_0$ .

For the case of unetched colloidal monolayers this becomes independent of the absolute particle size and leads to  $\Theta = 90.7 \%$  and  $\Phi = 60.5 \%$ , when taking the particle diameter  $2r$  as layer thickness. Using the Maxwell-Garnet effective medium approximation

$$n_{eff}^2 = n_{air}^2 \frac{2 \cdot (1 - \Phi) \cdot n_{air}^2 + (1 + 2\Phi) \cdot n_{PS}^2}{(2 + \Phi) \cdot n_{air}^2 + (1 - \Phi) \cdot n_{PS}^2} \quad 3.5$$

one notices that a perfect, defect-free colloidal monolayer will have an effective refractive index  $n_c = 1.33$ , when a refractive index of  $n_{PS} = 1.59$  is assumed for polystyrene. This is  $\Delta n = 0.1$  larger than the optimum  $n_c = 1.23$  required according to the Fresnel equation 3.1. Decreasing the volume fraction of the PS spheres will proportionally reduce the refractive index, which can be precisely achieved by plasma etching. Concomitantly, this will reduce the layer thickness, which will shift the optimum antireflective performance to lower wavelengths. When assuming a Maxwell-Garnett behavior, we expect to get an optimum performance at a volume fraction of  $\Phi = 43.3 \%$  (for the simplified case of isotropic particle etching). This corresponds to an area

fraction  $\Theta = 64.2\%$  and a reduction of the diameter of the initial polymer sphere to  $2r_{opt} = 0.84 \cdot D_0$ .

Plasma etching allows for a precise control in the fine-tuning of the size of polymer particles. By choosing the appropriate gas mixture and etching time combination one can reduce the diameter by a defined amount (Supporting information Figure S3.1)<sup>10</sup> and thereby adjust the effective refractive index accordingly. Figure 3.2 shows the evolution of the optical transmission through a colloidal monolayer with an initial particle diameter of 140 nm (PS140) with increasing etching time. (UV/VIS spectra covering a range from 350 nm to 2500 nm are displayed in Figure S3.2.)

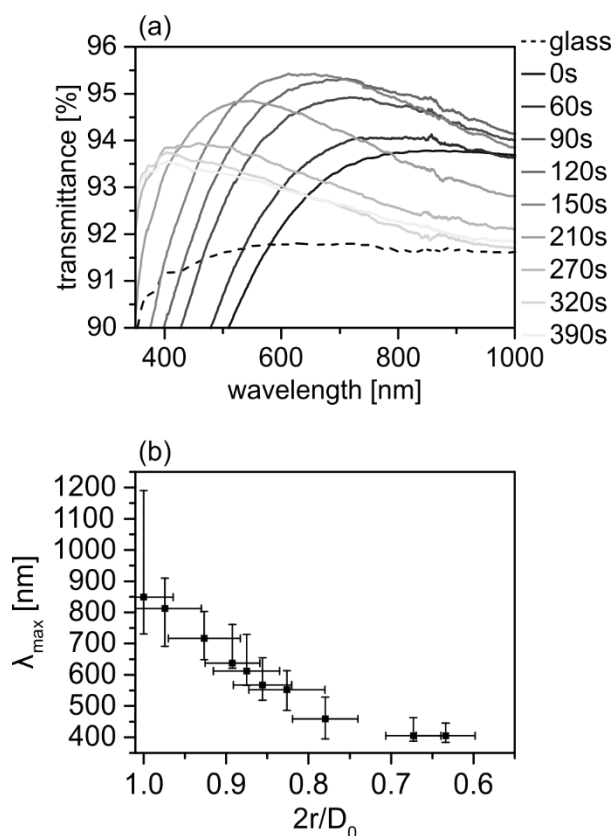


**Figure 3.2.** a) Transmission spectra of a colloidal PS monolayer with an initial particle diameter of 140 nm. Continued plasma etching leads to a size reduction of the PS spheres, which blue-shifts the maximum transmittance (dashed line: glass spectrum). b) The maximum transmittance  $\lambda_{max}$  monotonically shifts to lower wavelengths as the PS spheres are etched to 63 % of their initial size. The x-error bars indicate the standard deviation of the size of the etched particles, the y-error bars indicate the wavelength range at which the transmittance decreased by 0.2 % relative to the maximum position.

Two trends can be recognized, which follow the theoretical predictions. With increasing plasma etching time, the particle size decreases monotonically from initially 140 nm down to approx.

85 nm after 390 s. This results in a gradual blue-shift of the maximum light transmission from  $\lambda_{max} = 950$  nm to  $\lambda_{max} = 400$  nm (Figure 3.2b) as the effective layer thickness  $d$  is gradually decreasing, too. At the same time, the absolute transmission  $T_{max}$  at the optimum wavelength passes through a maximum, which is reached after 150 s etching at a value of  $T_{max} = 95.5$  %. This is very close to the theoretical transmission of  $T_{max} = 96$  % for an ideal, single sided AR coating on glass (the other 4 % are being lost at the second glass-air interface). The difference to the ideal value can be rationalized by a small amount of additional scattering at point- and line-defects, which are typically present in self-assembled colloidal monolayers or by a roughening of the particle surface during the etching process.

We further investigated the optical properties of the etched colloidal monolayers by ellipsometry (Figure 3.3). Using a Cauchy fit model, we fitted the layer thickness and the refractive index to the ellipsometric angles  $\Psi$  and  $\Delta$  (Figure S3.3). The ellipsometric data confirm the trend that has been observed in the spectroscopic transmission. The correlation between the covered area fraction and the refractive index measured by ellipsometry is depicted in Figure S3.4. The reduction of the particle diameter leads to a reduction in the optical layer thickness of the particle coating. However, one has to bear in mind that plasma etching of PS spheres typically leads to a slightly anisotropic etching, which results in spheroid-shaped objects rather than isotropically shrunk spheres.<sup>19</sup> This discrepancy becomes apparent, when comparing the diameter of the plasma-etched particles measured with scanning electron microscopy (SEM)  $2r$  (which resembles a top-view projection on the sample plane) to the layer thicknesses obtained from the ellipsometric fit and atomic force microscopy (AFM) measurements  $d$  (see Figure S3.7). As expected for spheroids, the actual layer thickness  $d$  is systematically less than the diameter of the projected PS particle  $2r$ . Nevertheless, the layer thicknesses from the ellipsometric fit and the AFM measurement agree very well with only a small deviation for the samples of the longest etching time. A potential reasons for this deviation could be an increase in surface roughness on the PS particles, which is often observed for longer etching times (Figure S3.1), which may lead to more scattering. Concomitant with the decrease in layer thickness is an increase in free volume between the nanoparticles. This results in a monotonic decrease of the effective refractive index of the colloidal monolayer (solid symbols in Figure 3.3a), which follows the Maxwell-Garnett plot.

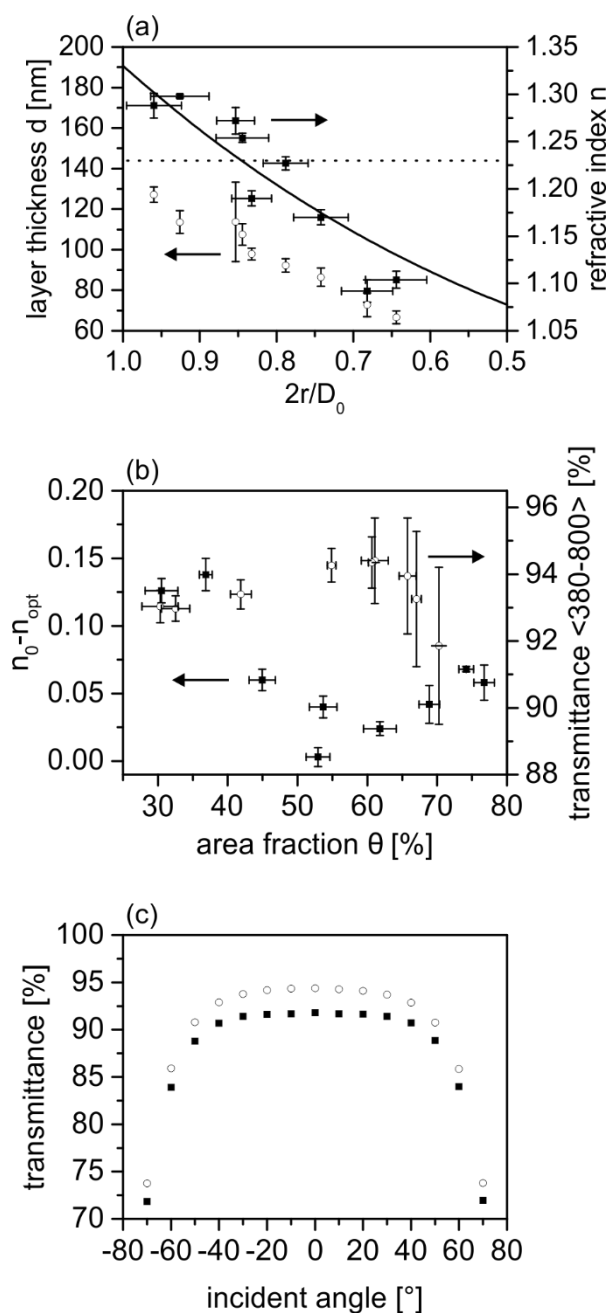


**Figure 3.3.** Ellipsometry data, Maxwell-Garnett plot and angle-dependent transmittance. a) ■ Refractive index and ○ layer thickness of PS140 with increasing etching time determined with the Cauchy model. The solid line represents the theoretically expected Maxwell-Garnett behavior of the effective refractive index. b) ■ deviation of the measured refractive index from the optimum refractive index ( $n = 1.23$ ), ○ averaged transmittance of PS140 series with increasing etching time as a function of the covered area fraction. c) Transmittance at 633 nm for ■ glass and ○ PS140 etched for 100 s in dependence of the incident angle.

The dashed line in Figure 3.3a marks the optimum refractive index, which indeed is realized by a size reduction of about 80 – 85 % of the initial particle diameter. Further etching leads to a refractive index  $< 1.23$ . As already discussed in Figure 3.2a, the absolute transmission therefore

runs through a maximum, which is quantitatively analyzed in Figure 3.3b. For this, we averaged the transmittance from  $\lambda = 380 - 800$  nm and related it to  $\Delta n = n_c - n_{opt}$ . The transmittance data exhibits a peak at an area fraction  $\Theta$  of about 60 %, which matches well to the theoretical optimum of 64 % as outlined above. This maximum coincides with a minimum in  $\square n$ . The standard deviation of the average transmittance is rather large for low etching times, which is indicative of a substantial amount of light being reflected for small wavelengths (compare Figure 3.2a). Upon reaching the optimum parameters, the transmittance features a broad maximum over a large wavelength range, resulting in a fairly broadband AR behavior and a small standard deviation. In Figure 3.3c the angle-dependency of the transmittance at 633 nm (wavelength of maximum transmittance at normal incidence) is shown for a monolayer of PS140 etched for 100 s (spectra are shown in Figure S3.2). The typical behavior of a single-layer AR coating is observed, where the transmittance exhibits a strong dependency on the angle of incidence. Nevertheless, the transmittance of the coated glass substrate is always higher than the untreated glass substrate even at large angles. However, compared to state-of-the-art gradient refractive index structures, the angle dependent AR performance of colloidal monolayers is inferior. Moth-eye AR coatings exhibit very low reflectivities up to angles of more than  $50^\circ$ .<sup>16</sup>

Colloidal monolayer AR coatings can be tuned to a desired optimum transmission wavelength by selecting the appropriate initial particle diameter. The optimum AR performance will always be reached after size-reducing the initial spheres to an area fraction of  $\Theta = 64$  % or  $2r = 0.84 D_0$ , which results in  $n_c = 1.23$ , whereas different layer thicknesses  $d$  will be obtained. The maximum transmittance is given by equation 3.2 and will therefore shift in accordance to the obtained layer thickness  $d$ . We demonstrate this influence with PS particles ranging from 102 nm to 181 nm (Figure 3.4a).

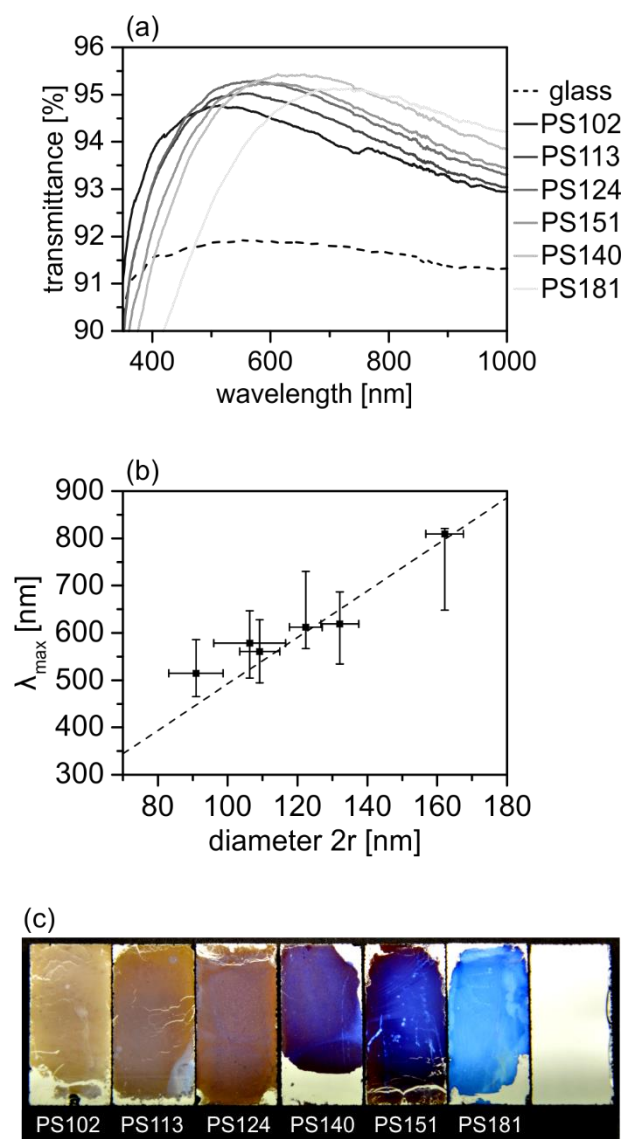


**Figure 3.4.** a) Spectra of monolayers with different initial particle diameter etched to a surface coverage of approximately 64%. b) Peak positions as a function of the etched particle diameter (including expected peak position as dashed line). c) Photograph of optimum monolayers with different particle sizes on black glass. Uncoated black glass under illumination to the right.

For all samples we achieved a transmittance of  $> 94.5\%$  at the optimum layer thickness. The transmittance peak, which always exhibits a broad maximum covering a few hundred nanometers, shifts along with the initial particle diameter (Figure 3.4a). Particles PS140 and PS151 mark an exception in this trend, which we relate to an inferior monolayer quality of the PS151 spheres. This leads to more defects and consequently free volume at the optimum etching conditions ( $2r/D_0 \approx 0.84$ ). With the samples under investigation here, we were able to cover a range from 800 nm to 500 nm in maximum transmittance. The experimental results follow the linear trend expected from equation 3.2 (dashed line in Figure 3.4b). A good quantitative

agreement is achieved, when using the particle diameter as layer thickness. Considering the anisotropic etching as discussed above, the maximum transmittance is slightly red-shifted compared to the actual layer thickness (see Figure S3.8). The efficiency of the colloidal monolayer AR coating can be inspected in Figure 3.4c, where we compare six monolayers of different particle sizes, i.e. layer thicknesses, to an uncoated black glass substrate. All monolayers have been plasma etched to  $\Theta = 64\%$ . A strong reduction in reflectivity can be observed for all samples.

However, the coating with the largest particles PS151 – PS181 feature a clear bluish hue, which originates from the inferior AR performance of these layers at small wavelengths ( $< 600$  nm). The best visual performance is obtained for the samples PS113 and PS124, which cover all parts of the visible regime. When using even smaller particles sizes (PS102) the AR performance in the red regime deteriorates leading to a bronze/brownish coloration.

### 3.3 Conclusion

In summary, we investigated the optical properties of colloidal monolayers in the subwavelength range. They can serve as model systems for single-layer antireflective coatings. The strength of this material class is its well-defined structure, which can be tuned to a specific refractive index and layer thickness. We were able to demonstrate two well-known properties of single-layer AR coatings with this widely available thin film coating. At first, the refractive index needs to be adjusted to the optimum value of  $n_c = 1.23$ . This can be achieved by controlled plasma etching, where the PS particles retain their periodicity and the interstitial space is increased. The highest transmittance is only observed at the optimum etching condition, which agrees well to the theoretically expected value of  $\Theta = 64\%$ . Further size reduction leads to even lower refractive indices, which will in turn increase the reflectivity. Additionally, the layer thickness of colloidal monolayer coatings can be tuned by varying the initial particle diameter. Single-layer AR coatings exhibit an optimum wavelength of transmission, where the criterion of destructive interference between the air-coating and coating-glass interface is fulfilled. Using particles ranging from 102 nm to 181 nm we were able to adjust the maximum transmittance over the entire visible regime. The best performance in terms of broadband reflection suppression was achieved for particles with a diameter of 113 nm and 124 nm. Polymeric colloidal monolayers will certainly not rival commercially established AR technologies in particular with respect to its durability, scratch-resistance, or angle-independence. However, it

allows valuable insight into the applicability of the Maxwell-Garnett effective medium theory of heterostructured materials and gives a thorough background on the most important design parameters for single-layer AR coatings. Furthermore, our study extends the optical properties characterization of colloidal monolayers to the  $< 200$  nm range, which are increasingly used as starting platform for other nanostructured materials and interfaces.

### 3.4 Experimental Section

The monomer styrene, the initiator potassium peroxydisulfate (KPS), and the comonomer sodium para-styrene sulfonate were purchased from *Sigma Aldrich* and used as received. Silicon wafers were obtained from (*Microchemicals*, Germany). As glass slides, standard microscopy slides (*Menzel, Braunschweig*, Germany) were used.

Monodisperse polystyrene nanospheres were synthesized using emulsifier free emulsion polymerization. The procedure was similar for all samples used. Styrene was dispersed in MilliQ water, degassed by bubbling with argon gas for 30 min, heated to 80°C and stirred at 850 rpm for 30 min. The comonomer (sodium styrene sulfonate or acrylic acid) was dissolved in 5 ml MilliQ water and added to the mixture. After 5min, the initiator, potassium peroxydisulfate (KPS), dissolved in 5 ml MilliQ water, was added to the mixture. After nucleation, the stirring speed was reduced to 550 rpm and the solution was refluxed for 24 h at 80 °C under argon atmosphere. After cooling to room temperature, the dispersion was filtered using a 125  $\mu\text{m}$  nylon filter sieve and dialyzed against MilliQ water.

Monolayers were prepared according to the procedure of *Vogel et al.*<sup>20</sup> Prior to the preparation of the monolayers the glass substrate was cleaned for 20 min in an ultrasonic bath with a 2 % aqueous *Hellmanex* (*Hellma GmbH*, Mühlheim, Germany) solution (in MilliQ water). The surfactant was extensively rinsed off with MilliQ water and the substrates were placed in the ultrasonic bath in ethanol for 10 minutes. Afterwards the substrate was dried with compressed air. A hydrophilic glass slide was partially immersed in a vessel filled with a 0.1 mM sodium dodecyl sulfate (SDS) solution in MilliQ water with a tilt angle of approximately 45 °. The aqueous colloidal dispersion was diluted with the same amount of ethanol and slowly dropped on the glass slide with a syringe trying to reach a constant flow of the particle dispersion. The formed monolayers were transferred to a silicon wafer or a hydrophilic glass substrate by immersing the substrate into the water phase below the monolayer and slowly withdrawing

under a sheer angle. The transferred monolayers were dried in air under an angle of approximately 30 °.

The prepared monolayers were etched in a plasma reactor *MiniFlecto* (*Plasma Technology GmbH, Herrenberg, Germany*) with an argon flow of 4 sccm and 100 % power at a pressure of ~0.2 mbar. The temperature of the bottom plate of the plasma chamber was controlled by an IR detector.

SEM images were taken on a *LEO 1530 Gemini Field Emission SEM* (*Carl Zeiss AG, Oberkochen, Germany*) at 3.00 kV. The images were evaluated with the software *ImageJ*.<sup>21</sup>

Atomic force microscopy was performed in tapping mode on a *Dimension 3100* microscope (*Veeco, USA*) with a *Nanoscope IV* controller and *Mikromasch* NSC15/AIBS cantilevers. The AFM images were analyzed with the software *Nanoscope Analysis*. To determine the film thickness at least two cross sections were measured for each sample (see Figure S3.5 and Figure S3.6). The local maxima were averaged to get the actual film thickness.

UV/VIS spectra were measured using a *V-670 Spectrophotometer* (*Jasco Germany GmbH, Gross-Umstadt, Germany*) between 350 and 2500 nm with an UV-bandgap of 1 nm, an IR-bandgap of 4 nm, a data interval of 0.5 nm and a scan speed of 1000 nm/min. The spectra were normalized to the lamp spectrum. Steps in the spectra deriving from the grating change at 850 nm were removed manually. Angle dependent spectra were conducted on a *Cary 5000 UV-Vis-NIR Spectrophotometer* (*Agilent Technologies*) with attached *Universal Measurement Accessory* between 300 and 2500 nm with an UV-bandgap of 1 nm, an IR-bandgap of 4 nm, a data interval of 1 nm, a UV/VIS scan speed of 120 nm/min and a NIR scan speed of 600 nm/min.

Ellipsometry was performed using a *SE850* spectrometric ellipsometer (*Sentech Instruments GmbH, Berlin, Germany*). For each sample three independent measurements at three individual spots were conducted between 360 and 680 nm at angles of 60, 65 and 70°. The data was fitted with the program *Spectraray* using a Cauchy model to determine the layer thickness as well as the refractive index and absorption coefficients. The Cauchy model consisted of a silicon 100 (Jellison) substrate, a 4 nm SiO<sub>2</sub> (Palik) layer, the undefined polymer layer and air.

## Acknowledgements

This work was funded by the German Research Foundation (DFG) by the SFB840. C.S. acknowledges support from the Elite Network Bavaria (ENB). M.R. acknowledges support by the VCI. The authors thank Fabian Nutz, Christian Kuttner and Pia Ruckdeschel for early

contributions to this project and Markus Hund for help with AFM measurements. We thank Dr. Beate Förster and Martina Heider from the Bayreuth Institute of Macromolecular Research for their support using the scanning electron microscopy facilities.

## References

1. Moghal, J., Kobler, J., Sauer, J., Best, J., Gardener, M., Watt, A. A. & Wakefield, G. High-Performance, Single-Layer Antireflective Optical Coatings Comprising Mesoporous Silica Nanoparticles. **4**, 854-859 (2011).
2. Yoldas, B. E. Investigations of porous oxides as an antireflective coating for glass surfaces. *Appl. Opt.* **19**, 1425-1429 (1980).
3. Cook, K. T., Tettey, K. E., Bunch, R. M., Lee, D. & Nolte, A. J. One-step index-tunable antireflection coatings from aggregated silica nanoparticles. *ACS Appl Mater Interfaces* **4**, 6426-6431 (2012).
4. Du, Y., Luna, L. E., Tan, W. S., Rubner, M. F. & Cohen, R. E. Hollow Silica Nanoparticles in UV– Visible Antireflection Coatings for Poly (methyl methacrylate) Substrates. *ACS nano* **4**, 4308-4316 (2010).
5. du Xin & He, J. Facile Fabrication of Hollow Mesoporous Silica Nanospheres for Superhydrophilic and Visible/Near-IR Antireflection Coatings. **17**, 8165-8174 (2011).
6. Sun, Z. J. & Luo, Y. W. Fabrication of non-collapsed hollow polymeric nanoparticles with shell thickness in the order of ten nanometres and anti-reflection coatings. **7**, 871-875 (2011).
7. Gao, T., Jelle, B. P. & Gustavsen, A. Antireflection properties of monodisperse hollow silica nanospheres. *Applied Physics A: Materials Science & Processing* **110**, 65-70 (2012).
8. Vogel, N., Retsch, M., Fustin, C. A., del Campo, A. & Jonas, U. Advances in Colloidal Assembly: The Design of Structure and Hierarchy in Two and Three Dimensions. (2015).
9. Farcau, C., Giloan, M., Vinteler, E. & Astilean, S. Understanding plasmon resonances of metal-coated colloidal crystal monolayers. *Appl. Phys. B* **106**, 849-856 (2012).
10. Vogel, N., Goerres, S., Landfester, K. & Weiss, C. K. A Convenient Method to Produce Close- and Non-close-Packed Monolayers using Direct Assembly at the Air-Water Interface and Subsequent Plasma-Induced Size Reduction. *Macromol. Chem. Phys.* **212**, 1719-1734 (2011).
11. Zhao, Y., Wang, J. & Mao, G. Colloidal subwavelength nanostructures for antireflection optical coatings. *Opt. Lett.* **30**, 1885 (2005).
12. Ray, M. A., Shewmon, N., Bhawalkar, S., Jia, L., Yang, Y. & Daniels, E. S. Submicrometer surface patterning using interfacial colloidal particle self-assembly. *Langmuir* **25**, 7265-7270 (2009).
13. Chan, C. H. *et al.* Anti-reflection layer formed by monolayer of microspheres. *Appl. Phys. B* **100**, 547-551 (2010).
14. Wang, Y., Chen, L., Yang, H., Guo, Q., Zhou, W. & Tao, M. Spherical antireflection coatings by large-area convective assembly of monolayer silica microspheres. *Sol. Energy Mater. Sol. Cells* **93**, 85-91 (2009).
15. Hattori, H. Anti-Reflection Surface with Particle Coating Deposited by Electrostatic Attraction. *Adv. Mater.* **13**, 51-54 (2001).

16. Chattopadhyay, S., Huang, Y. F., Jen, Y. J., Ganguly, A., Chen, K. H. & Chen, L. C. Anti-reflecting and photonic nanostructures. *Materials Science and Engineering: R: Reports* **69**, 1-35 (2010).
17. Askar, K., Phillips, B. M., Fang, Y., Choi, B., Gozubenli, N., Jiang, P. & Jiang, B. Self-assembled self-cleaning broadband anti-reflection coatings. *Colloids and Surfaces A: Physicochemical and Engineering Aspects* **439**, 84-100 (2013).
18. Haginoya, C., Ishibashi, M. & Koike, K. Nanostructure array fabrication with a size-controllable natural lithography. *Appl. Phys. Lett.* **71**, 2934-2936 (1997).
19. Akinoglu, E. M., Morfa, A. J. & Giersig, M. Understanding anisotropic plasma etching of two-dimensional polystyrene opals for advanced materials fabrication. *Langmuir* **30**, 12354-12361 (2014).
20. Vogel, N., Goerres, S., Landfester, K. & Weiss, C. K. A Convenient Method to Produce Close- and Non-close-Packed Monolayers using Direct Assembly at the Air-Water Interface and Subsequent Plasma-Induced Size Reduction. *Macromol. Chem. Phys.* **212**, 1719-1734 (2011).
21. Rasband, W. S. U. S. National Institutes of Health. *ImageJ*, <http://imagej.nih.gov/ij/> (1997-2014).

### 3.5 Supporting Information

#### Derivation of optimum etching parameter

Maxwell-Garnett:

$$n_{eff}^2 = n_{air}^2 \frac{2(1 - \Phi)n_{air}^2 + (1 + 2\Phi)n_{PS}^2}{(2 + \Phi)n_{air}^2 + (1 - \Phi)n_{PS}^2} \quad 3.6$$

Volume Fraction  $\Phi$  for  $n_{eff} = 1.23$  with PS ( $n_{PS} = 1.59$ ):

$$\begin{aligned} \Phi_{spheres} &= \frac{n_{eff}^2 - n_{air}^2}{n_{eff}^2 + 2n_{air}^2} * \frac{n_{PS}^2 + 2n_{air}^2}{n_{PS}^2 - n_{air}^2} = \frac{1.23^2 - 1.00}{1.23^2 + 2.00} * \frac{1.59^2 + 2.00}{1.59^2 - 1.00} \\ &= 0.433 \end{aligned} \quad 3.7$$

For optimum  $n_{eff}$ , new particle diameter  $d_{opt}$ , based on initial diameter  $D_0$ :

$$\frac{r^2}{D_0^2} = \frac{\Phi \cdot 3 \cdot \sqrt{3}}{4 \cdot \pi} \quad 3.8$$

$$\frac{r}{D_0} = \sqrt{\frac{0.433 \cdot 3 \cdot \sqrt{3}}{4 \cdot \pi}} = 0.421 \quad 3.9$$

$$d_{opt} = 0.842 \cdot D_0 \quad 3.10$$

This corresponds to an area fraction  $\Theta$ :

$$\Theta = \frac{0.5 \cdot r^2 \cdot \pi}{D_0^2 \cdot \sqrt{3}/4} = \frac{2 \cdot r^2 \cdot \pi}{D_0^2 \cdot \sqrt{3}} = \frac{2 \cdot (0.421 \cdot D_0)^2 \cdot \pi}{D_0^2 \cdot \sqrt{3}} = 0.642 \quad 3.11$$

Area fraction for unetched monolayers ( $D_0 = 2r$ ):

$$\Theta = \frac{0.5 \cdot r^2 \cdot \pi}{4r^2 \cdot \sqrt{3}/4} = \frac{\pi}{2 \cdot \sqrt{3}} = 0.907 \quad 3.12$$

Volume fraction for unetched monolayer ( $D_0 = 2r$ ):

$$\Phi = \frac{0.5 \cdot \frac{4}{3} \cdot r^3 \cdot \pi}{2r \cdot D_0^2 \cdot \sqrt{3}/4} = \frac{4 \cdot r^2 \cdot \pi}{3 \cdot D_0^2 \cdot \sqrt{3}} = \frac{\pi}{3 \cdot \sqrt{3}} = 0.605 \quad 3.13$$

Etching kinetics of PS140

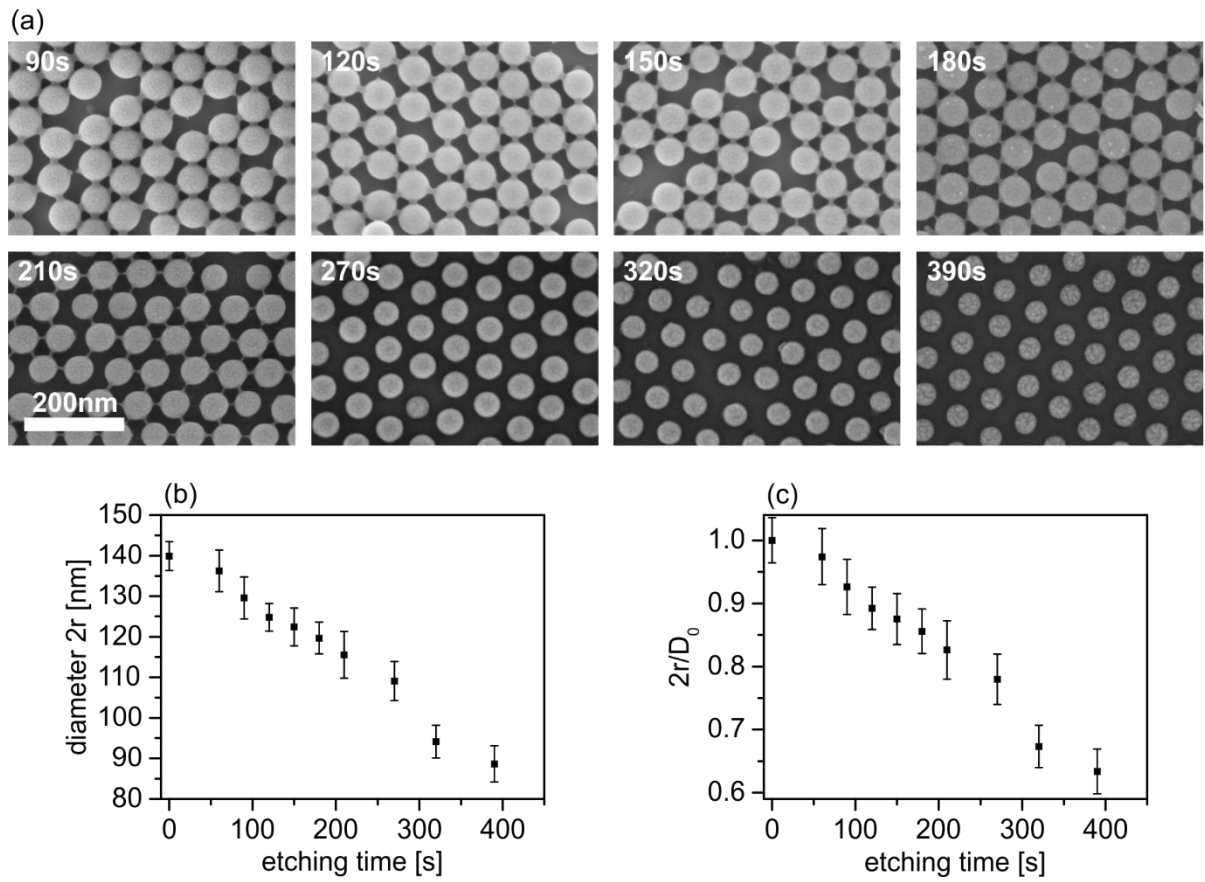


**Figure S3.1.** Etching kinetics of PS140. a) SEM images with increasing etching time. b) Diameter as a function of etching time. c) Ratio of diameter to initial diameter as a function of etching time.

### UV/VIS Spectra

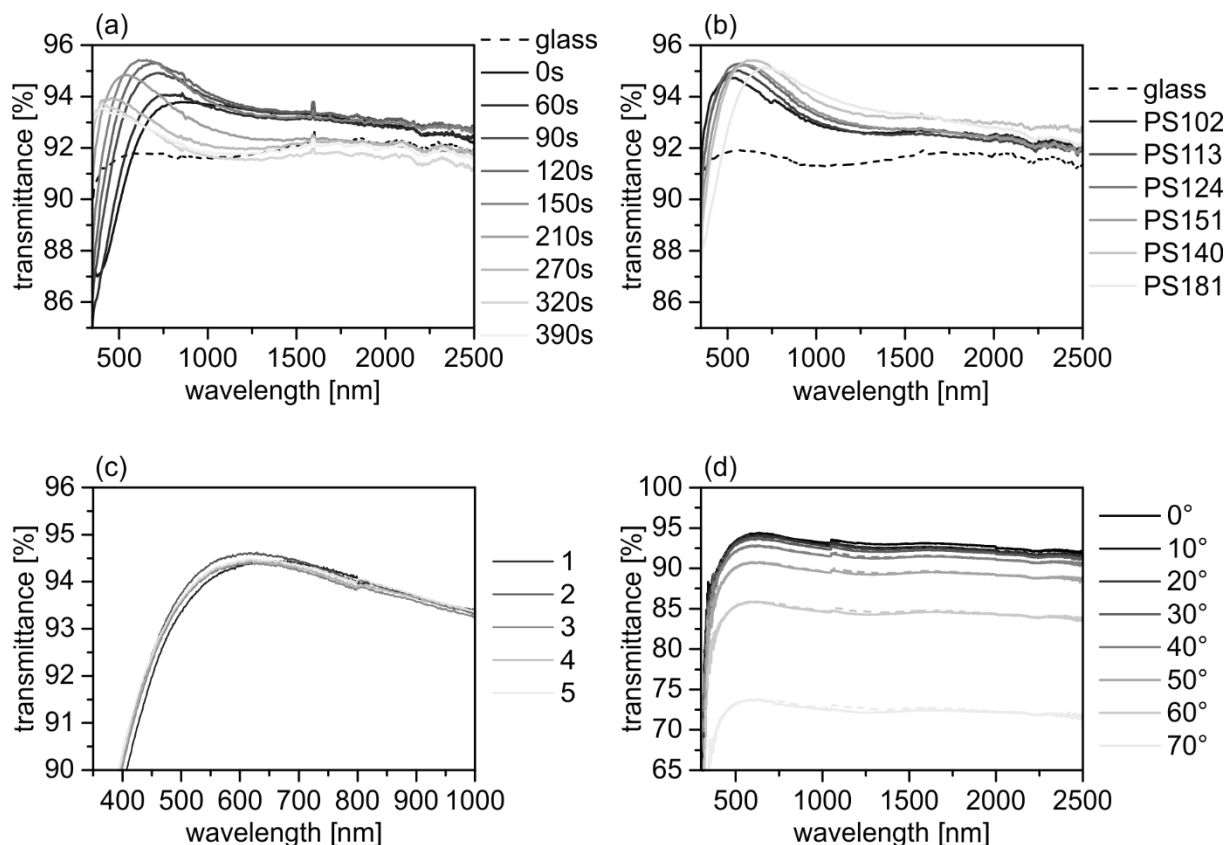


**Figure S3.2.** a) UV-VIS spectra of PS140 with increasing etching time. b) UV-VIS spectra of monolayers with different initial particle diameter etched to an area fraction of approximately 64%. c) UV-VIS spectra of PS140 etched for 100 s at five different positions. d) UV-VIS spectra of PS140 etched for 100 s at various angles of incidence. The dashed curves depict the spectra measured at negative angles.

### Exemplary ellipsometric fits using the Cauchy model

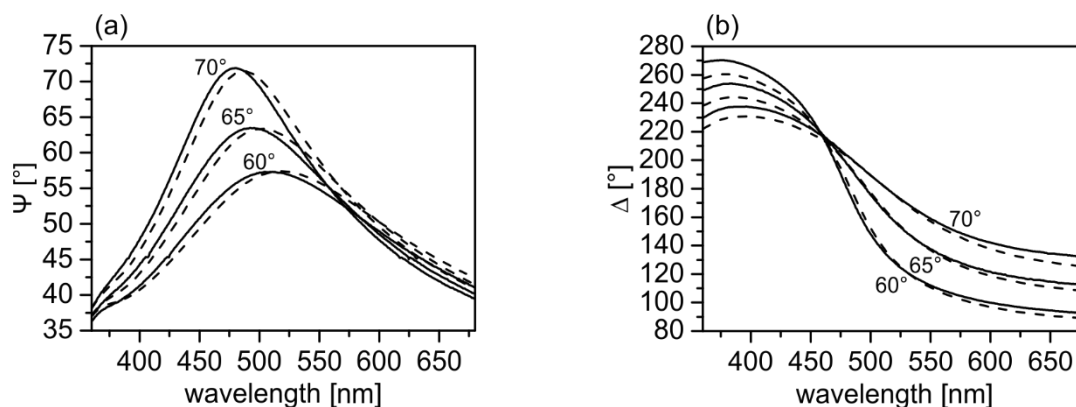


**Figure S3.3.** Wavelength dependence of  $\Psi$  (a) and  $\Delta$  (b) of PS140 (etched for 60s) measured at 60°, 65° and 70° including the fits using the Cauchy model as dashed lines.

### Correlation between area fraction and refractive index

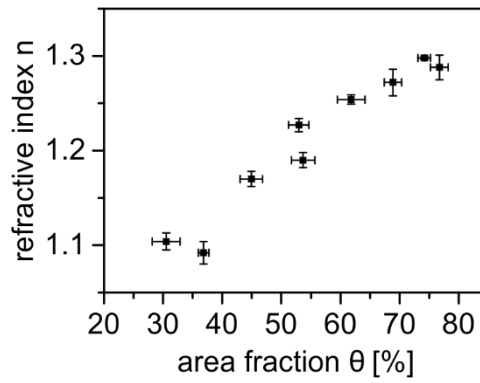


Figure S3.4. Dependence of refractive index on covered area fraction for PS140.

### AFM height evaluation

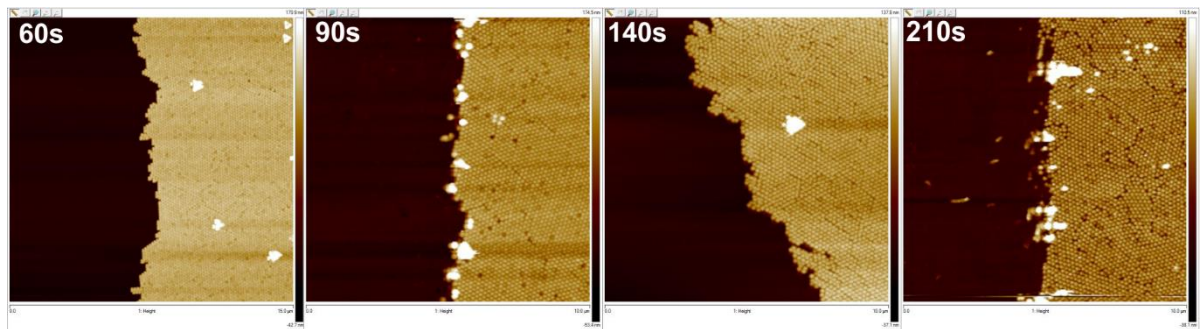


Figure S3.5. AFM micrographs of PS140 with increasing etching.

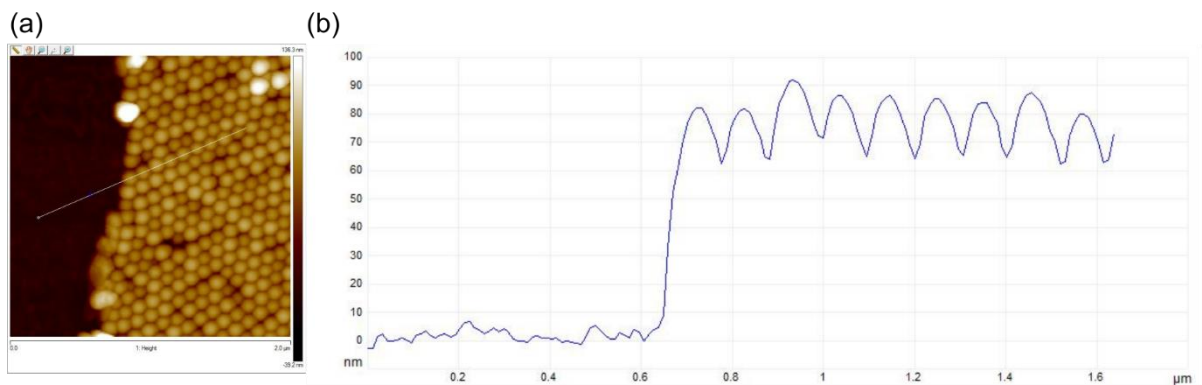
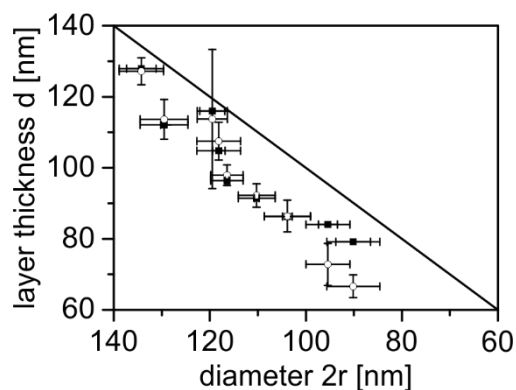


Figure S3.6. a) AFM micrograph of PS102 after 90s of plasma etching. b) Cross-section following the white line in a).

**Comparison between layer thickness (AFM and ellipsometry) and particle diameter (SEM)**



**Figure S3.7.** Relation of particle height (i.e. layer thickness) measured by AFM ( $\circ$ ) and layer thickness determined via ellipsometry ( $\blacksquare$ ) with respect to the particle diameter measured in SEM. The solid line represents perfectly round particles.

**Maximum transmittance in dependence of the layer thickness (AFM)**

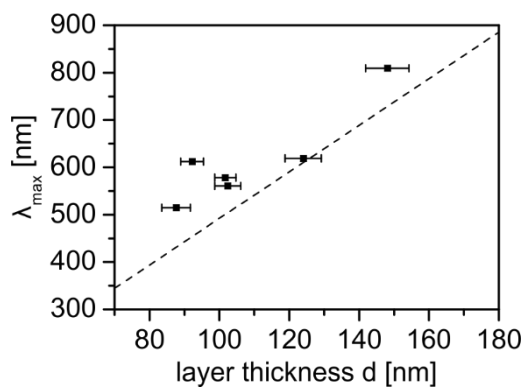


**Figure S3.8.** Maximum transmittance as a function of the actual layer thickness measured by AFM.

## 4 Vibrational Dynamics of a Two-Dimensional Microgranular Crystal

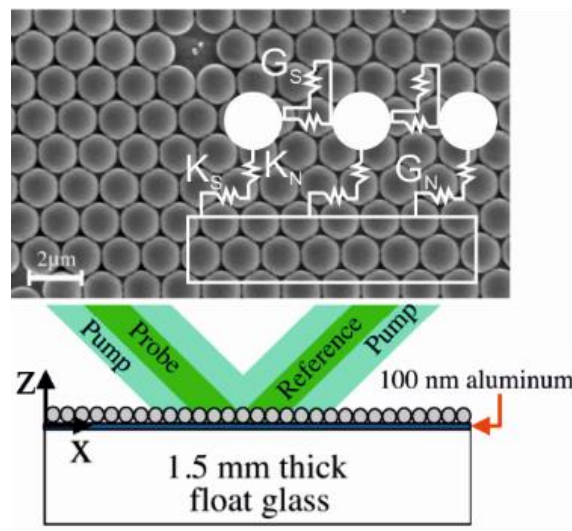
Alejandro Vega-Flick,<sup>1,2</sup> Ryan A. Duncan,<sup>1</sup> Sam P. Wallen,<sup>3</sup> Nicholas Boechler,<sup>3</sup> Christian Stelling,<sup>4</sup> Markus Retsch,<sup>4</sup> Juan J. Alvarado-Gil,<sup>2</sup> Keith A. Nelson,<sup>1</sup> and Alexei A. Maznev<sup>1\*</sup>

<sup>1</sup>Department of Chemistry, Massachusetts Institute of Technology, Cambridge, Massachusetts 02139, USA

<sup>2</sup>Applied Physics Department, CINVESTAV-Unidad Mérida, Carretera Antigua a Progreso Km 6, Cordemex, Mérida, Yucatán 97310, México

<sup>3</sup>Department of Mechanical Engineering, University of Washington, Seattle, Washington 98195, USA

<sup>4</sup>Physical Chemistry – Polymer Systems, University of Bayreuth, 95440 Bayreuth, Germany



Published in *Physical Review B* 96, 024303 (2017).

Reproduced with permission from American Physical Society.

## Abstract

We study the dynamics of an ordered hexagonal monolayer of polystyrene microspheres adhered to a glass substrate coated with a thin aluminum layer. A laser-induced transient grating technique is employed to generate and detect three types of acoustic modes across the entire Brillouin zone in the  $-K$  direction: low-frequency contact-based modes of the granular monolayer, high-frequency modes originating from spheroidal vibrations of the microspheres, and surface Rayleigh waves. The dispersion relation of contact-based and spheroidal modes indicates that they are collective modes of the microgranular crystal controlled by particle-particle contacts. We observe a spheroidal resonance splitting caused by the symmetry breaking due to the substrate, as well as an avoided crossing between the Rayleigh and spheroidal modes. The measurements are found to be in agreement with our analytical model.

## 4.1 Introduction

Vibrations of periodic arrays of spheres interacting via Hertzian contacts initially attracted attention following the discovery of solitary wave propagation in the "sonic vacuum" regime of a 1D chain of uncompressed spheres.<sup>1,2</sup> Subsequent studies were extended to 2D and 3D systems and yielded an array of novel acoustic phenomena.<sup>3</sup> Granular crystals, as these systems became known, can be considered a class of phononic crystal<sup>4</sup> with unique behavior specific to granular media. For instance, in addition to nonlinear effects such as solitons and discrete breathers<sup>2,3</sup>, unusual linear phenomena such as the existence of rotational acoustic modes have been revealed.<sup>5,6</sup> Due to the nonlinearity of Hertzian contacts, the acoustic properties of granular crystals can be easily tuned, for example by applying static compression, which makes them attractive for potential applications.<sup>3</sup>

Until very recently, granular crystal studies were conducted with macroscopic particles such as ball bearings. A new frontier was opened by laser-based experiments on 2D self-assembled monolayers of micron-sized particles on a solid substrate.<sup>7-11</sup> These experiments revealed the crucial role of adhesion, which is negligible for large particles but becomes an important factor in determining the contact stiffness at the microscale. The initial efforts focused on the vertical contact resonance of microspheres, arising due to contact with the substrate, and its interaction with surface acoustic waves (SAWs). In these initial studies, the observed phenomena, such as

an avoided crossing in the Rayleigh SAW dispersion<sup>7</sup> and the resonant attenuation of SAWs by microspheres,<sup>9</sup> could be well accounted for by a simple model where microspheres did not interact with each other.<sup>7</sup> Refined measurements of the resonant attenuation of SAWs revealed horizontal-rotational modes enabled by interparticle interactions.<sup>10</sup> However, none of the experiments performed on self-assembled microgranular monolayers were done on a “single crystal” sample with long-range order extending over distances comparable to the measurement spot size. The observed phenomena were limited to the regime in which the acoustic wavelength was much greater than the sphere size and the long-range periodic order was not essential. The purpose of this work is to study vibrational properties of a well-ordered “single crystal” lattice of microspheres, i.e., a true 2D microscale granular crystal.

An analogy can be drawn between a 2D granular crystal and a 2D lattice of atoms such as graphene. However, there is an important difference, as vibrations of a granular monolayer involve rotations of the spheres.<sup>10,12</sup> Spheres also have internal mechanical degrees of freedom; consequently, in addition to contact-based modes, one would expect to see collective modes originating from spheroidal vibrations of the spheres.<sup>13</sup> The presence of the substrate significantly alters the dispersion of contact-based modes<sup>14</sup> and adds Rayleigh SAWs in the substrate, which interact with the vibrational modes of the monolayer.<sup>10,14</sup> In this work, we characterize the dispersion of these three types of modes (contact-based, spheroidal, and Rayleigh) and their interaction across the entire Brillouin zone (BZ) for a chosen high symmetry direction of a 2D microgranular crystal.

## 4.2 Methodology

### Sample Description

Our sample is a 2D monolayer of  $(1.5 \pm 0.023)$ - $\mu\text{m}$ -diameter polystyrene spheres adhered to a float glass substrate coated with a 100-nm aluminum film. The microspheres are arranged in a highly ordered hexagonal lattice shown in Figure 4.1a. The sample preparation followed the approach described by Retsch et al.<sup>15</sup> Briefly, a 3 wt % dispersion of particles in ultrapure (MiliQ) water was spin-coated on a cationically functionalized glass slide at a speed of 4000 rpm. The particle-coated substrate was slowly immersed into a 0.1 mM SDS solution in MiliQ water, which was adjusted to pH 12 with aqueous ammonium hydroxide solution. The particles were assembled at the air/water interface into a freely floating monolayer, which was finally transferred to an aluminum coated glass substrate and dried in air.

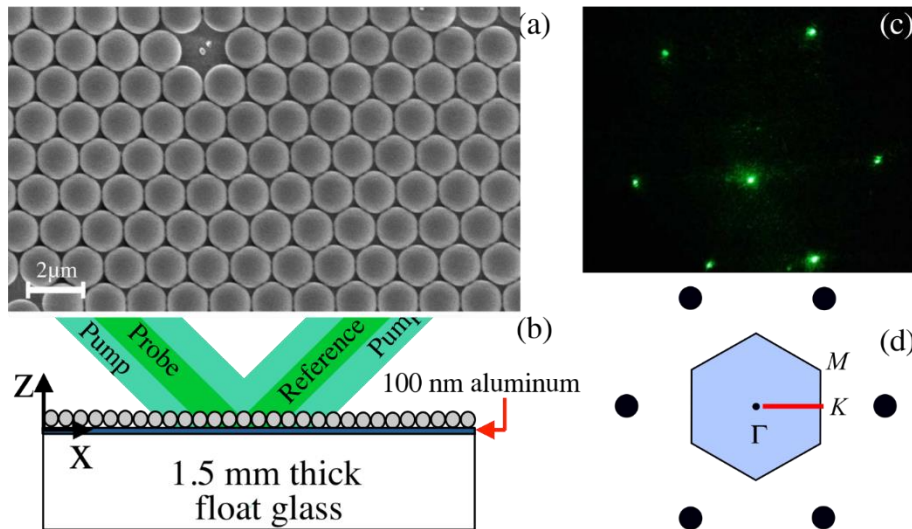


**Figure 4.1.** (a) Scanning electron microscope image of the microsphere monolayer. (b) Schematic of the experiment. (c) Diffraction pattern produced by the probe laser beam in reflection. (d) Reciprocal lattice and the first BZ of the microgranular crystal; red-line shows the wavevector range used in the experiment.

## Experiment

A laser-induced transient grating technique<sup>16,17</sup> was used to excite and probe acoustic modes of the structure. Two excitation pulses derived from the same laser source (515-nm wavelength, 60-ps pulse duration, 0.6- $\mu$ J total energy at the sample, 860- $\mu$ m spot diameter at  $1/e^2$  intensity level) were overlapped at the sample as shown in Figure 4.1b, forming an interference pattern of period  $\lambda$ . Absorption of the laser light by the aluminum film induced rapid thermal expansion, which generated counter-propagating acoustic modes with wavelength  $\lambda$ .<sup>17</sup> The wavelength can be varied by switching the diffraction grating pattern used to produce the excitation beams pair and fine-tuned by tilting it.<sup>18</sup> The detection of acoustic vibrations was accomplished via diffraction of a quasi-cw probe laser beam (532-nm wavelength, 200- $\mu$ m spot diameter, 160-mW power at the sample) with optical heterodyne detection.<sup>19,20</sup> The optical diffraction pattern from the microspheres was monitored, as shown in Figure 4.1c, to ensure that the laser spot was located in a highly ordered area, and to align the acoustic wavevector along the  $\Gamma$ -K direction of the reciprocal lattice as shown in Figure 4.1d.

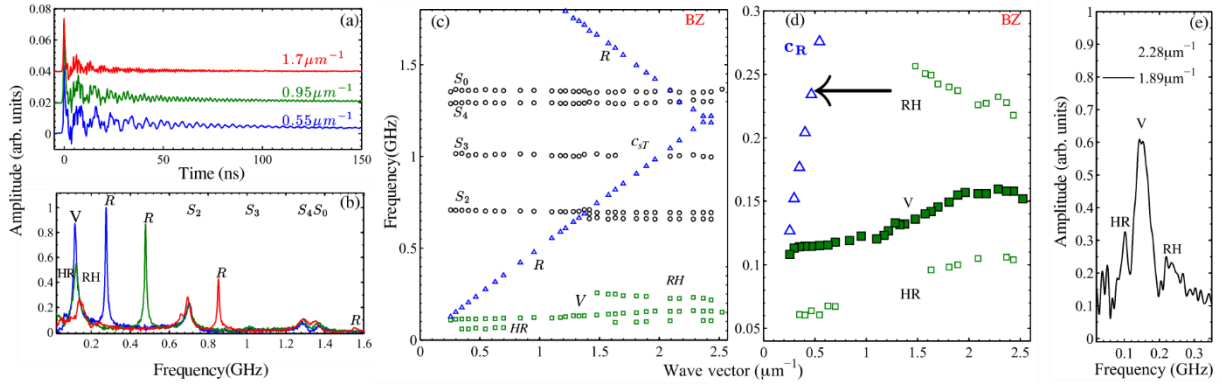


**Figure 4.2.** (a) Signal waveforms for three different wavevectors and (b) corresponding Fourier spectra. Peaks labeled V and R correspond to the vertical contact resonance mode and SAWs, respectively. Spheroidal modes are labeled  $S_0$ ,  $S_2$ ,  $S_3$ ,  $S_4$  according to their angular number  $L$ . (c) Measured dispersion of different modes labeled as in (b). Blue dashed line corresponds to SAW velocity for the substrate, red vertical dashed line corresponds to the BZ boundary. The dashed-dotted line corresponds to the transverse velocity of the substrate  $c_{ST}$ . (d) Dispersion in the range 0.05-0.3 GHz. Solid markers represent the predominantly vertical V mode, smaller hollow markers the horizontal-rotational HR and RH modes. Dashed-dotted lines are theoretical calculations. Horizontal arrow indicates the maximum SAW attenuation. (e) Fourier spectra for two representative wavevectors showing the HR and RH peaks.

Figure 4.2a shows typical signal waveforms measured at three different acoustic wavevectors. The corresponding Fourier spectra shown in Figure 4.2b reveal the presence of many acoustic modes. By plotting the identified frequencies for each wavevector,<sup>21</sup> we obtained the dispersion curves shown in Figure 4.2c. Three different types of acoustic modes can be identified: a mode labeled R with a nearly constant dispersion slope corresponding to the SAW velocity of the substrate; low frequency modes (HR, V, RH) with weaker frequency dependence, which we identify as contact-based modes<sup>14</sup> and high frequency nearly flat branches (S) corresponding to spheroidal vibrational modes of the spheres.

The Rayleigh mode dispersion is “zone-folded” at the BZ boundary (in Figure 4.2b this zone-folding is seen in the presence of two Rayleigh peaks at  $q = 1.7 \mu\text{m}^{-1}$ ). The zone-folding of the SAW dispersion at the expected location of the BZ boundary in the  $\Gamma$ -K direction confirms the “single crystal” structure of the sample and the correct orientation of the acoustic wavevector with respect to the microsphere lattice. Otherwise the SAW is virtually unaffected by the microspheres, with the exception of avoided crossings discussed below.

### 4.3 Contact-Based Modes

Figure 4.2d presents a more detailed view of the dispersion of low frequency contact-based modes. The mode labeled V corresponding to the most prominent peak in the spectra, as shown in Figure 4.2e, has been previously identified as the vertical contact resonance mode.<sup>7,9,10</sup> Figure 4.2e also shows small peaks to either side of the V mode peak which we assigned to horizontal-rotational modes labeled HR and RH following Ref.<sup>14</sup>. The avoided crossing between the vertical resonance mode and the SAW, studied in previous works,<sup>7,9</sup> is just outside the wavevector range of our measurements. In the absence of inter-particle interactions, the contact resonance frequency, past the avoided crossing with the SAW, is expected to be independent of the wavevector.<sup>7</sup> The interaction between microspheres should result in dispersion, predicted in Ref.<sup>14</sup> but not observed in previous studies due to the lack of long-range order in the samples. As can be seen in Figure 4.2d, our data clearly show the expected dispersion, indicating that we observe a collective mode of the microgranular crystal rather than vibrations of non-interacting particles.

A model describing vibrations of a monolayer of spheres on a substrate accounting for both sphere-substrate and sphere-sphere contacts has been developed for a square lattice<sup>14</sup> and subsequently modified for a hexagonal lattice.<sup>22</sup> The model yields three vibrational modes polarized in the sagittal plane;<sup>23</sup> one of them predominantly involves vertical displacements while the other two have primarily horizontal-rotational character. The diffraction of the probe beam is most sensitive to the vertical mode, which is the most prominent in the data.

The model treats the sphere-substrate and sphere-sphere contacts as normal and shear springs, with spring constants  $K_N$ ,  $K_S$  corresponding to sphere-substrate and  $G_N$ ,  $G_S$  to sphere-sphere contacts, where subscripts N and S refer to normal and shear, respectively. For a Hertz-Mindlin contact,<sup>24</sup> the ratio of normal and shear spring constants is determined by the elastic constants of the contacting materials.<sup>22</sup> Thus the model only has two independent parameters,  $K_N$  and  $G_N$ . We calculated the dispersion by fitting the experimental data of the V mode with the theoretical model,<sup>22</sup> using the contact stiffnesses  $K_N$  and  $G_N$  as fitting parameters. Since the HR and RH peaks are much smaller and noisier compared to the V mode, we felt that their assignment to the respective dispersion branches needs to be verified. Therefore we only used the V mode in the fitting procedure; small HR and RH peaks were not used. The calculated results are shown in Figure 4.2d as dashed-dotted curves.<sup>25</sup>

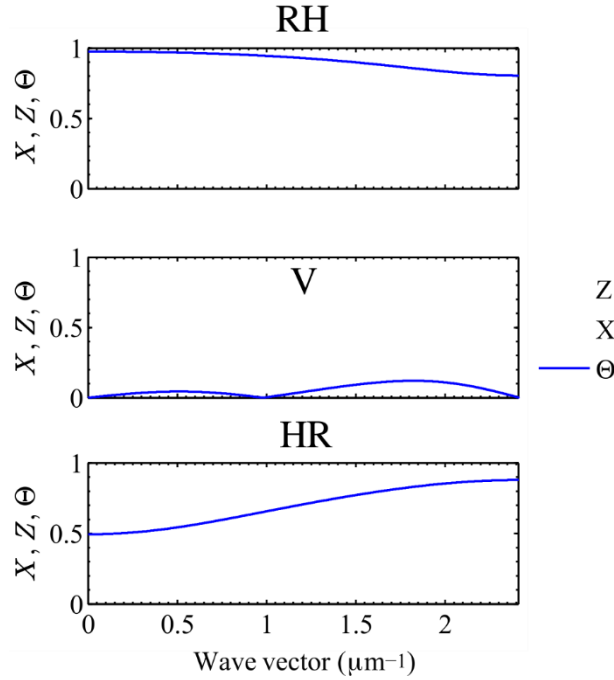


**Figure 4.3.** Relative amplitudes of the displacements and rotations for each contact-based vibrational mode.  $Z$  and  $X$  denote the amplitudes of the vertical and horizontal displacements of the spheres, while  $\Theta$  denotes the amplitude of the “rotational displacement”, i.e. the product of the rotation angle and the sphere radius. The amplitudes are normalized such that  $Z^2 + X^2 + \Theta^2 = 1$ .

The fitted values of the contact stiffnesses are  $K_N = 864$  N/m, and  $G_N = 135$  N/m. The corresponding shear stiffness values are  $K_S = 684$  N/m and  $G_S = 106$  N/m. As in prior studies,<sup>10</sup> the sphere-substrate contacts are found to be stiffer than the sphere-sphere contacts.

The calculated dispersion curves confirm the assignment of the HR and RH branches. In particular, the calculated HR branch is in good agreement with the measured peaks. The calculated RH branch, on the other hand, is lower than the measured values. As can be seen in Figure 4.2e, the RH peak is fairly broad; the discrepancy between the calculated and measured values is within the peak width, although the precision of the peak position measurement that can be assessed from the point-to-point scatter in the data is better than the peak width.

The discrepancy can be caused by inaccuracy of the Hertz-Mindlin contact model due to, for example, surface roughness or bending rigidity.

Figure 4.3 shows relative contributions of the sphere displacements and rotations for each contact-based mode across the BZ. These modes correspond to the calculated dispersion curves (V, HR, RH) shown in Figure 4.2d. It can be observed that the V mode involves predominantly vertical displacements while the HR and RH modes involve mainly horizontal and rotational motion of the spheres.

We also found indirect evidence of an intersection between the RH and SAW branches in the increased attenuation of the latter. As shown in Figure 4.4, the Rayleigh peak width in the Fourier spectrum has a distinct maximum at 235 MHz, while the model predicts the branch crossing at 223 MHz. We note that the presence of such resonant attenuation is consistent with previous observations.<sup>10</sup>

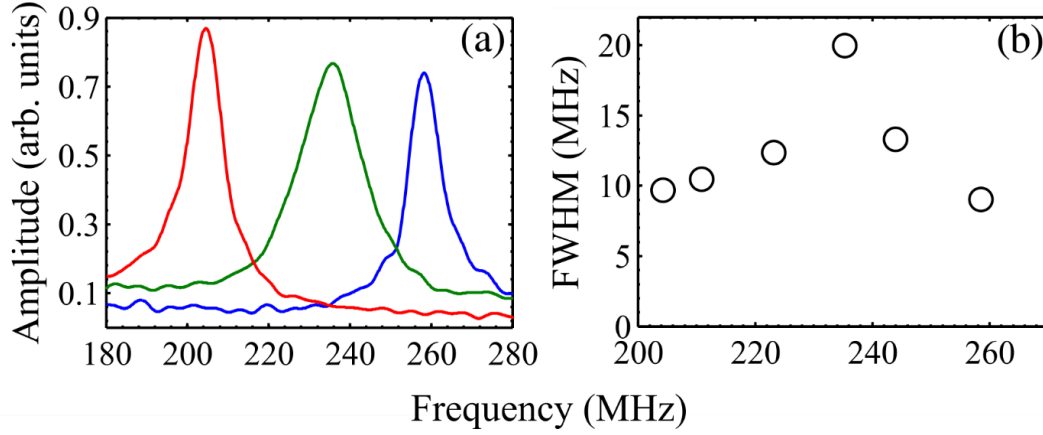


**Figure 4.4.** (a) SAW Fourier peaks in the frequency range 200-270 MHz. (b) FWHM of Fourier peaks versus SAW frequency. Peak broadening indicates resonant absorption of SAWs centered at 235 MHz.

Having determined the sphere-substrate contact stiffness, we estimate the width of the SAW bandgap at the BZ boundary. Treating contact springs as a periodic perturbation, we obtained the following expression for the width of the bandgap (see Appendix A),

$$\Delta = \frac{K_N - \chi^2 K_S}{2\omega_R M A_C} \quad 4.1$$

where  $A_C$  is the unit-cell area,  $\omega_R$  is the (unperturbed) SAW frequency at the BZ boundary,  $\chi$  is the ellipticity of the SAW and  $M$  is a constant defined in Ref.<sup>26</sup>. The calculated bandgap width is 1.85 MHz, which is much smaller than the Rayleigh peak width ( $\sim 16$  MHz) and hence cannot be resolved in our measurements; this explains why no bandgap in the SAW dispersion at the BZ boundary is visible in Figure 4.2c.

## 4.4 Spheroidal Vibrational Modes

### Sphere-substrate interaction

Turning our attention to the flat branches in the frequency range 600 – 1500 MHz, we attribute them to spheroidal vibrations of the microspheres,<sup>27-29</sup> corresponding to four spheroidal modes labeled  $S_L$  with angular numbers  $L = 0, 2, 3, 4$  and radial number  $n = 0$ . Table 4.1 shows measured and calculated frequencies of these modes averaged over the entire wavevector range. The calculations were done for an isolated sphere on a substrate: we start by calculating the spheroidal mode of a free-sphere,<sup>27,28</sup> then account for the contact with the substrate using a perturbation approach.<sup>22</sup> The calculations required the density and acoustic velocities (longitudinal and transverse) of polystyrene, as well as sphere-substrate spring constants  $K_N$  and  $K_S$ , previously obtained from the dispersion of the vertical contact mode. The density of polystyrene  $\rho = 1.04 \text{ g/cm}^3$  was provided by the particle supplier, but the precise values of acoustic velocities were unknown, as for a polymer these may depend on the manufacturing procedure. Therefore, we treated the acoustic velocities as fitting parameters. Our fitted values  $c_L = 2323 \text{ m/s}$  and  $c_T = 1174 \text{ m/s}$  are in agreement with previously reported values.<sup>29</sup>

**Table 4.1.** Measured frequencies (in MHz) for observed spheroidal modes and calculated frequencies for an isolated sphere with and without interaction with the substrate.

Mode	Measured frequency	Sphere/substrate	Free sphere
$S_0$	$1351 \pm 4$	1351	1347
$S_2^{m=0}$	$700 \pm 5$	689	660
$S_2^{m=1}$	$662 \pm 2$	667	660
$S_3$	$1007 \pm 5$	1020	983
$S_4$	$1295 \pm 4$	1305	1262

### Mode splitting

As shown in Table 4.1, the calculations including the substrate effect are quite close (within 1.5 %) to the measured values. Our calculations account for the splitting of the  $S_2$  mode seen at large wavevectors in Figure 4.2c and shown in detail in Figure 4.5. We ascribe this splitting to degeneracy lifting between modes with different azimuthal numbers  $m$  due to interaction with the substrate. In the case of free-sphere vibrations, a mode  $S_L$  has  $2L + 1$  fold degeneracy with an azimuthal number  $m = -L, \dots, L$  for each degenerate mode. The  $n = 0, S_2$  mode of the free-

sphere yields 5 degenerate modes with  $m = 0, \pm 1, \pm 2$ . For  $S_2^{m=0}$ , the sphere surface displacement at the contact point is vertical, for  $S_2^{m=1}$  (for the purpose of this discussion, we treat  $m = \pm 1$  modes as a single mode) the displacement is horizontal, and for  $S_2^{m=2}$  the displacement at the contact is zero, hence the latter mode is unaffected by the substrate. Since the spheres are optically transparent at the excitation wavelength, spheroidal vibrations can only be excited through the interaction with the substrate. The vertical motion of the substrate surface in the small wavevector limit can only excite the mode  $S_2^{m=0}$ . The substrate horizontal motion occurs on the time scale  $\lambda/c_R$ , where  $c_R$  is the Rayleigh velocity, and is too slow to excite the spheroidal mode at small wavevectors. Therefore, we expect the  $S_2^{m=1}$  mode to become observable only at higher wavevectors.

Thus, we identify the main  $S_2$  peak as the  $S_2^{m=0}$  mode whereas a smaller lower frequency peak emerging at high wavevectors is ascribed to the  $S_2^{m=1}$  mode; as seen in Table 4.1, this assignment agrees with the calculations. Such spheroidal mode splitting due to symmetry breaking by the substrate is not unexpected but has not been previously reported. Indeed, in a more typical measurement with the laser spot centered on an individual particle<sup>30-32</sup> only the  $S_L^{m=0}$  modes can be excited due to symmetry constraints. We expect similar mode splitting to take place for  $S_3$  and  $S_4$  modes; however, the signal from those modes is too weak to detect this phenomenon.

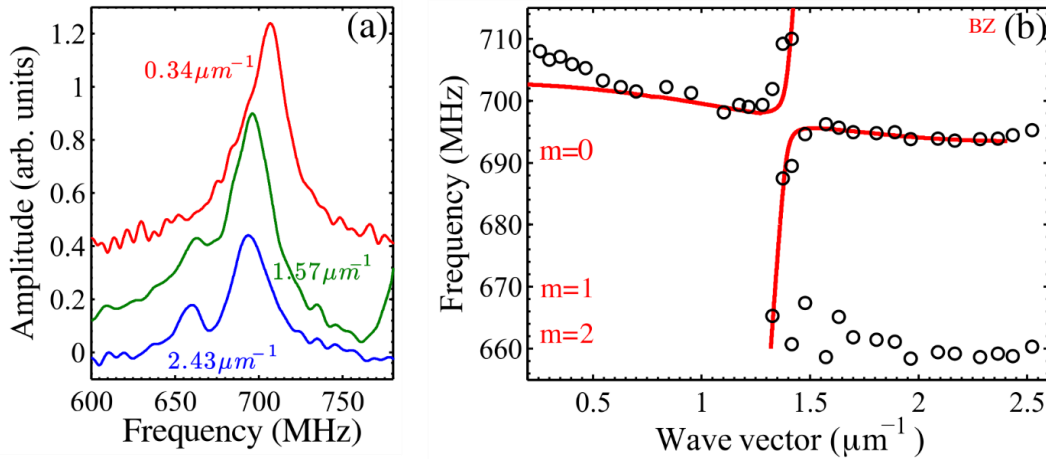


**Figure 4.5.** (a) Representative spectral peaks of the spheroidal mode  $S_2$  for three wavevectors, showing the mode splitting which becomes apparent at large wavevectors. (b) Dispersion of the  $S_2$  mode. Open circles show the measured frequencies. Blue dashed line corresponds to SAW velocity for the substrate, red solid lines corresponds to theoretical calculation for a monolayer of interacting spheres, red dashed lines show calculated frequencies for an isolated sphere.

### Spheroidal dispersion and interaction with surface Rayleigh waves

Further examination of the  $S_2^{m=0}$  mode data shown in Figure 4.5b reveals a small but appreciable dispersion across the BZ as well as a narrow avoided crossing with the SAW. The dispersion indicates that we are dealing with a collective mode of a microgranular crystal rather than vibrations of individual particles as was assumed in the calculations shown in Table 4.1. The particle-particle interaction can be taken into account using a perturbation approach<sup>22</sup> to obtain an equation relating the frequency  $\omega_1$  of the  $S_2^{m=0}$  mode to the wavevector  $q$ :

$$\omega_1^2 = \omega_0^2 + C_N \frac{K_N}{M_0} + S_N \frac{4G_N}{M_0} [2 + \cos(qD\sqrt{3}/2)], \quad 4.2$$

where  $\omega_0$  is the free-sphere frequency,  $D$  is the sphere diameter,  $M_0$  is the sphere mass,  $C_N$  and  $S_N$  are dimensionless constants calculated based on the displacement pattern in the free-sphere mode<sup>22</sup>:  $C_N = 3.32$ ,  $S_N = 0.83$ . The second term represents the frequency shift due to the sphere-substrate contact while the third describes the dispersion due to the sphere-sphere contact. Next we modified the effective medium model<sup>7</sup> to describe the interaction of spheroidal vibrations with the SAW in the substrate. This resulted in the following dispersion relation (see Appendix B):

$$\begin{aligned} (\omega_1^2 - \omega^2) & \left[ \left( 2 - \frac{\omega^2}{q^2 c_{ST}^2} \right) - 4 \sqrt{1 - \frac{\omega^2}{q^2 c_{ST}^2}} \sqrt{1 - \frac{\omega^2}{q^2 c_{SL}^2}} \right] \\ & = \frac{K_N \omega^2 \left( \omega_1^2 - C_N \frac{K_N}{M_0} - \omega^2 \right) \sqrt{1 - \frac{\omega^2}{q^2 c_{SL}^2}}}{q^3 A_c \rho_s c_{ST}^4} \end{aligned} \quad 4.3$$

where  $\rho_s = 2.44 \text{ g/cm}^3$ ,  $c_{ST} = 3438 \text{ m/s}$  and  $c_{SL} = 5711 \text{ m/s}$  are the density, transverse and longitudinal wave speeds of the substrate, respectively.  $\omega_1$  is the spheroidal mode frequency given by Eq. 4.2. The term in brackets in the left-hand side is the Rayleigh determinant yielding the frequency of the Rayleigh SAW.<sup>27</sup> The right side of Eq. 4.3 represents the coupling term between the Rayleigh wave and the spheroidal vibrations, effectively determining the width of the avoided crossing.

Figure 4.5b shows the calculated dispersion relation to be in good agreement with the experimental data. This is achieved without any fitting parameters, as the contact spring constants  $G_N$  and  $K_N$  used in Eqs. 4.2 and 4.3 were previously determined from the dispersion of the vertical contact mode.

### 4.5 Conclusion

In summary, we studied the linear dynamics of a fully ordered 2D microgranular crystal in the frequency range 0.05 - 2 GHz and investigated the behavior of three kinds of acoustic modes (contact-based, spheroidal, and Rayleigh) across the entire BZ. A range of previously unexplored phenomena have been revealed, including the dispersion of contact-based and spheroidal modes due to particle-particle interactions, the splitting of a spheroidal resonance due to symmetry breaking by the substrate, and the avoided crossing between a spheroidal mode and the SAW. The experimental results are well described by our analytical models. The two contact stiffnesses obtained from the vertical contact mode dispersion have been shown to describe the observations involving the spheroidal mode dispersion, the Rayleigh-spheroidal avoided crossing, and the absence of the Rayleigh bandgap at the BZ boundary.

We hope this report will stimulate further studies of wave phenomena in ordered microgranular lattices. Non-linear propagation of high-amplitude waves, 2D lattices with more complicated unit-cells and 3D lattices, dissipation in microgranular systems and thermal transport properties at low temperatures (when low-frequency vibrations control heat transport) present rich opportunities for exploration. The interaction of contact-based and spheroidal modes with SAWs may enable applications in SAW devices and sensors. Another avenue for future research is scaling the particle size down to nanometers, eventually leading to the borderline between granular and molecular crystals.

### Acknowledgments

The work performed at MIT was supported by the U.S. Department of Energy Grant DE-FG02-00ER15087 (experiment) and the National Science Foundation Grant CHE-1111557 (analysis). The work performed at the University of Washington was supported by the National Science Foundation (Grant CMMI-1333858). The work performed at University of Bayreuth was supported by the German Research Foundation SFB840. The work performed at CINVESTAV was partially supported by projects 192 (“Fronteras de la ciencia”), 251882 (“Investigacion Cientifica Basica 2015”), and the fund Conacyt-SENER-EnergySustainability (Grant 207450), within the Strategic Project CEMIESol-Cosolpi No. 10 (“Solar Fuels Industrial Processes”). A.V-F appreciates support from CINVESTAV and CONACYT through normal, mixed scholarships. C.S. acknowledges support from the Elite Network Bavaria (ENB).

## References

1. Lazaridi, A. N. & Nesterenko, V. F. Observation of a new type of solitary waves in a one-dimensional granular medium. *Journal of Applied Mechanics and Technical Physics* **26**, 405-408 (1985).
2. Nesterenko, V. *Dynamics of Heterogeneous Materials*. (Springer, New York, 2001).
3. Theocharis, G., Boechler, N. & Daraio, C. in *Acoustic Metamaterials and Phononic Crystals*. (ed Pierre Demier) Ch. 6, 95-156 (Springer, 2013).
4. Laude, V. *Phononic Crystals: Artificial Crystals for Sonic, Acoustic, and Elastic Waves*. Vol. 26, 2194-3532 (Walter De Gruyter, Berlin, 2015).
5. Merkel, A., Tournat, V. & Gusev, V. Experimental Evidence of Rotational Elastic Waves in Granular Phononic Crystals. *Phys. Rev. Lett.* **107**, 225502 (2011).
6. Allein, F., Tournat, V., Gusev, V. E. & Theocharis, G. Transversal-rotational and zero group velocity modes in tunable magneto-granular phononic crystals. *Extreme Mechanics Letters* **12**, 65-70 (2017).
7. Boechler, N., Eliason, J. K., Kumar, A., Maznev, A. A., Nelson, K. A. & Fang, N. Interaction of a Contact Resonance of Microspheres with Surface Acoustic Waves. *Phys. Rev. Lett.* **111**, 036103 (2013).
8. Khanolkar, A., Wallen, S., Ghanem, M. A., Jenks, J., Vogel, N. & Boechler, N. A self-assembled metamaterial for Lamb waves. *Appl. Phys. Lett.* **107**, 071903 (2015).
9. Eliason, J. K., Vega-Flick, A., Hiraiwa, M., Khanolkar, A., Gan, T., Boechler, N., Fang, N., Nelson, K. A. & Maznev, A. A. Resonant attenuation of surface acoustic waves by a disordered monolayer of microspheres. *Appl. Phys. Lett.* **108**, 061907 (2016).
10. Hiraiwa, M., Abi Ghanem, M., Wallen, S. P., Khanolkar, A., Maznev, A. A. & Boechler, N. Complex Contact-Based Dynamics of Microsphere Monolayers Revealed by Resonant Attenuation of Surface Acoustic Waves. *Phys. Rev. Lett.* **116**, 198001 (2016).
11. This approach was inspired by earlier experiments on self-assembled colloidal crystals; see Ref. [34].
12. Tournat, V., Pèrez-Arjona, I., Merkel, A., Sanchez-Morcillo, V. & Gusev, V. Elastic waves in phononic monolayer granular membranes. *New Journal of Physics* **13**, 073042 (2011).
13. Hladky-Hennion, A.-C., Cohen-Tenoudji, F., Devos, A. & Billy, M. d. On the existence of subresonance generated in a one-dimensional chain of identical spheres. *The Journal of the Acoustical Society of America* **112**, 850-855 (2002).
14. Wallen, S. P., Maznev, A. A. & Boechler, N. Dynamics of a monolayer of microspheres on an elastic substrate. *Phys. Rev. B* **92**, 174303 (2015).
15. Retsch, M., Zhou, Z., Rivera, S., Kappl, M., Zhao, X. S., Jonas, U. & Li, Q. Fabrication of Large-Area, Transferable Colloidal Monolayers Utilizing Self-Assembly at the Air/Water Interface. *Macromol. Chem. Phys.* **210**, 230-241 (2009).
16. Eichler, H. J., Günter, P. & Pohl, D. W. *Laser-Induced Dynamic Gratings*. Vol. 50, (Springer, Berlin, 1986).
17. Rogers, J. A., and, A. A. M., Banet, M. J. & Nelson, K. A. Optical Generation and Characterization of Acoustic Waves in Thin Films: Fundamentals and Applications. *Annu. Rev. Mater. Sci.* **30**, 117-157 (2000).
18. Vega-Flick, A., Eliason, J. K., Maznev, A. A., Khanolkar, A., Ghanem, M. A., Boechler, N., Alvarado-Gil, J. J. & Nelson, K. A. Laser-induced transient grating setup with continuously tunable period. *Rev. Sci. Instrum.* **86**, 123101 (2015).
19. Maznev, A. A., Nelson, K. A. & Rogers, J. A. Optical heterodyne detection of laser-induced gratings. *Opt. Lett.* **23**, 1319-1321 (1998).

20. Goodno, G. D., Dadusc, G. & Miller, R. J. D. Ultrafast heterodyne-detected transient-grating spectroscopy using diffractive optics. *J. Opt. Soc. Am. B* **15**, 1791-1794 (1998).
21. The data points shown in Figs. 4.2 and 4.2 were obtained by fitting the Fourier spectra peaks to a Lorentzian function. The window used for the Lorentzian fit was set by cutting the peak at 0.4 of its max value.
22. Vega-Flick, A., Duncan, R. A., Wallen, S. P., Boechler, N., Stelling, C., Retsch, M., Alvarado-Gil, J. J., Nelson, K. A. & Maznev, A. A. arXiv:1703.04784.
23. Generally, the lattice of spheres yields six contact-based vibrational modes corresponding to six degrees of freedom (three translations and three rotations). For a high-symmetry direction such as  $\Gamma$ - $\mathbf{K}$  there are three modes symmetric with respect to the sagittal plane. We are interested in only these symmetric sagittally polarized modes [14, 22] because antisymmetric ones cannot be excited or probed in our experiment.
24. Johnson, K. L. *Contact mechanics*. (Cambridge University Press, Cambridge, 1985).
25. The best-fit dispersion curves shown in Fig. 4.2 were found by minimizing the mean-square deviation between the calculated and measured frequencies using the Levenberg-Marquardt algorithm.
26. Maznev, A. A. & Every, A. G. Surface acoustic waves in a periodically patterned layered structure. *J. Appl. Phys.* **106**, 113531 (2009).
27. Camden, J. P., Dieringer, J. A., Zhao, J. & Van Duyne, R. P. Controlled Plasmonic Nanostructures for Surface-Enhanced Spectroscopy and Sensing. *Acc. Chem. Res.* **41**, 1653-1661 (2008).
28. Lamb, H. On the Vibrations of an Elastic Sphere. *Proceedings of the London Mathematical Society* **s1-13**, 189-212 (1881).
29. Cheng, W., Wang, J., Jonas, U., Fytas, G. & Stefanou, N. Observation and tuning of hypersonic bandgaps in colloidal crystals. *Nat. Mater.* **5**, 830 (2006).
30. Dehoux, T. *et al.* Vibrations of microspheres probed with ultrashort optical pulses. *Opt. Lett.* **34**, 3740-3742 (2009).
31. Guillet, Y., Audoin, B., Ferrié, M. & Ravaine, S. All-optical ultrafast spectroscopy of a single nanoparticle-substrate contact. *Phys. Rev. B* **86**, 035456 (2012).
32. Li, Y., Lim, H. S., Ng, S. C., Wang, Z. K., Kuok, M. H., Vekris, E., Kitaev, V., Peiris, F. C. & Ozin, G. A. Micro-Brillouin scattering from a single isolated nanosphere. *Appl. Phys. Lett.* **88**, 023112 (2006).

## 4.6 Appendices

### Appendix A: Bragg band gap of the Rayleigh mode

In order to find the frequencies of the Rayleigh mode at the BZ boundary, we followed the approach in Sec. IV of Ref.<sup>1</sup>. We treat the contact springs as a perturbation increasing the potential energy of the SAW. Since the SAW frequency at the BZ boundary is much larger than the contact resonance frequency, we disregard the center of mass motion of the spheres and assume that the deformation of the contact springs are determined by the SAW surface displacement.

For the even mode (all terms and notations as in Ref.<sup>1</sup>), the perturbation of the potential energy is given by

$$\Delta H_{even} = \frac{1}{2A_c} K_N u^2, \quad 4.4$$

where  $u$  is the vertical surface displacement amplitude and  $A_c$  is the area of the unit cell. For the odd mode, it is given by

$$\Delta H_{odd} = \frac{1}{2A_c} K_S \chi^2 u^2, \quad 4.5$$

where  $\chi$  is the ellipticity of the Rayleigh wave (see Eq. (24) of Ref.<sup>1</sup>). Consequently, the frequencies will be given by

$$\omega_{even} = \omega_R \left( 1 + \frac{K_N}{2KA_c} \right) \quad 4.6$$

$$\omega_{odd} = \omega_R \left( 1 + \frac{\chi^2 K_S}{2KA_c} \right) \quad 4.7$$

where  $\omega_R$  is the Rayleigh frequency and  $K = M\omega_R^2$ , where  $M$  is given by Eq. (23) of Ref.<sup>1</sup>. The bandgap width is given by

$$\Delta = \omega_{even} - \omega_{odd} = \omega_R \frac{K_N - \chi^2 K_S}{2KA_c} \quad 4.8$$

### Appendix B: Spheroidal-Rayleigh wave interaction

In order to calculate the spheroidal interaction with the SAW we consider a vertical force  $F$  acting on a single sphere at the contact point with the substrate. The equation of motion for the radial displacement  $u_{r,L,m}$  at the sphere-substrate contact can be expressed as

$$M_{L,m}\ddot{u}_{r,L,m} = -K_{L,m}u_{r,L,m} - F \quad 4.9$$

where  $M_{L,m}$  and  $K_{L,m}$  are constants defined in Ref.<sup>2</sup> and related by the expression  $K_{L,m} = \omega_0 M_{L,m}$ , where  $\omega_0$  is the free sphere vibration frequency. The force exerted by the contact spring is

$$F = K_N(u_{r,L,m} + u_z) \quad 4.10$$

where  $u_z$  is the vertical surface displacement due to elastic waves in the substrate. Applying a Fourier-transform in the time domain we obtain the following relationship for the Fourier-amplitudes of the sphere displacement

$$\tilde{u}_{r,L,m} = \frac{-K_N\tilde{u}_z}{K_{L,m} + K_N - M_{L,m}\omega^2} = \frac{-K_N\tilde{u}_z}{M_{L,m}\left(\omega_0^2 + C_N\frac{K_N}{M_0} - \omega^2\right)} \quad 4.11$$

where  $C_N = M_0/M_{L,m}$  is a dimensionless constant calculated based on the displacement pattern in the free sphere mode.<sup>2</sup> Using Eq. 4.11 we can determine the vertical force acting on a unit area of the substrate, leading to the following boundary conditions for the SAW at  $z = 0$ :

$$\sigma_{zz} = \frac{K_N(\tilde{u}_r + \tilde{u}_z)}{A_c} = \frac{K_N\tilde{u}_z(\omega_0^2 - \omega^2)}{A_c\left(\omega_0^2 + C_N\frac{K_N}{M_0} - \omega^2\right)}, \quad \sigma_{zx} = 0, \quad 4.12$$

where  $A_c = \sqrt{3}D^2/2$  is the area of the unit cell, and  $M_0$  is the mass of the sphere. We follow the standard procedure of deriving the Rayleigh wave dispersion,<sup>3</sup> substituting the stress-free boundary condition by Eq. 4.12 to obtain the following dispersion relation:

$$\begin{aligned} & \left[ \left( 2 - \frac{\omega^2}{q^2 c_{sT}^2} \right) - 4 \sqrt{1 - \frac{\omega^2}{q^2 c_{sT}^2}} \sqrt{1 - \frac{\omega^2}{q^2 c_{sL}^2}} \right] \\ & = \frac{K_N \omega^2 (\omega_0^2 - \omega^2) \sqrt{1 - \frac{\omega^2}{q^2 c_{sL}^2}}}{q^3 A_c \rho_s c_{sT}^4 \left( \omega_0^2 + C_N \frac{K_N}{M_0} - \omega^2 \right)} \end{aligned} \quad 4.13$$

where  $\rho_s$  is the substrate density and  $c_{sL}$  and  $c_{sT}$  are the longitudinal and transverse wave speeds of the substrate respectively. In the case of interacting spheres, we include the effect of the sphere-sphere interaction by substituting

$$\omega_0^2 \rightarrow \omega_0^2 + S_N \frac{4G_N}{M_0} [2 + \cos(qD\sqrt{3}/2)] \quad 4.14$$

into Eq. 4.13, where  $S_N$  is a dimensionless constant defined in Ref.<sup>2</sup> This leads to the following dispersion relation

$$\begin{aligned} (\omega_1^2 - \omega^2) & \left[ \left( 2 - \frac{\omega^2}{q^2 c_{sT}^2} \right) - 4 \sqrt{1 - \frac{\omega^2}{q^2 c_{sT}^2}} \sqrt{1 - \frac{\omega^2}{q^2 c_{sL}^2}} \right] \\ & = \frac{K_N \omega^2 \left( \omega_1^2 - C_N \frac{K_N}{M_0} - \omega^2 \right) \sqrt{1 - \frac{\omega^2}{q^2 c_{sL}^2}}}{q^3 A_c \rho_s c_{sT}^4} \end{aligned} \quad 4.15$$

where  $\omega_1$  is given by Eq. 4.2 of the main text. The effective medium approximation we used<sup>4</sup> requires the SAW wavelength to be much greater than the granular lattice constant. In our case, the SAW wavelength amounts to about four lattice constants.

## References

1. Maznev, A. A. & Every, A. G. Surface acoustic waves in a periodically patterned layered structure. *J. Appl. Phys.* **106**, 113531 (2009).
2. Vega-Flick, A., Duncan, R. A., Wallen, S. P., Boechler, N., Stelling, C., Retsch, M., Alvarado-Gil, J. J., Nelson, K. A. & Maznev, A. A. arXiv:1703.04784.
3. Ewing, W. M. & Jardetzky, W. S. *Elastic Waves in Layered Media*. (McGraw-Hill, New York, 1957).
4. Boechler, N., Eliason, J. K., Kumar, A., Maznev, A. A., Nelson, K. A. & Fang, N. Interaction of a Contact Resonance of Microspheres with Surface Acoustic Waves. *Phys. Rev. Lett.* **111**, 036103 (2013).



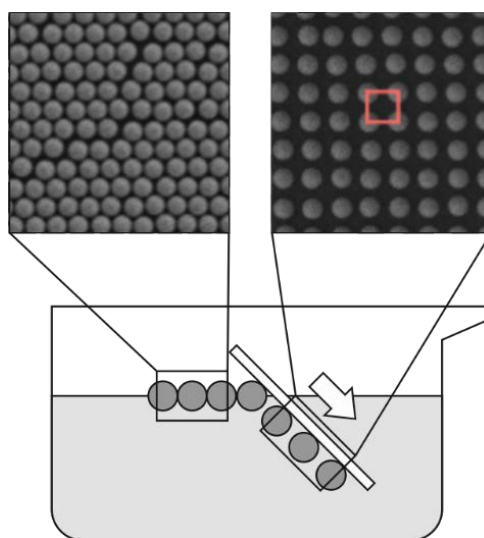
## 5 Ordered Particle Arrays via a Langmuir Transfer Process: Access to Any Two-Dimensional Bravais Lattice

Miriam E.J. Hummel,<sup>1</sup> Christian Stelling,<sup>1</sup> Bernd A.F. Kopera,<sup>1</sup> Fabian A. Nutz,<sup>1</sup> Matthias Karg,<sup>2</sup> Markus Retsch,<sup>1\*</sup> and Stephan Förster<sup>3\*</sup>

<sup>1</sup>Department of Physical Chemistry, University of Bayreuth, 95440 Bayreuth, Germany

<sup>2</sup>Physical Chemistry I, Heinrich-Heine-University, 40204 Düsseldorf, Germany

<sup>3</sup>Institute of Complex Systems (ICS-1), Forschungszentrum Jülich, 52425 Jülich, Germany



Published in *Langmuir* 35, 973-979 (2019).

Reproduced with permission from American Chemical Society.

## Abstract

We demonstrate how to directly transform a close-packed hexagonal colloidal monolayer into non-close-packed particle arrays of any two-dimensional symmetry at the air/water interface. This major advancement in the field of nanoparticle self-assembly is based on a simple one-dimensional stretching step in combination with the particle array orientation. Our method goes far beyond existing strategies and allows access to all possible two-dimensional Bravais lattices. A key element of our work is the possibility to macroscopically stretch a particle array in a truly one-dimensional manner, which has not been possible up to now. We achieve this by stretching the nanoparticle array at an air/water interface during the transfer process. The degree of stretching is simply controlled by the wettability of the transfer substrate. To retain the symmetry of the transferred structure, the capillary forces upon drying have to be circumvented. We demonstrate two concepts based on thermal fixation for this. It allows for the first time to fabricate non-close-packed, nonhexagonal colloidal monolayers on a macroscopic length scale.

## 5.1 Introduction

Solid substrates patterned with particle arrays are a key component for the fabrication of functional surfaces and thin film devices. They have applications in lithography,<sup>1-3</sup> optics,<sup>4</sup> photonics,<sup>5</sup> high-density data storage as well as adhesive/non-adhesive surfaces.<sup>6</sup> Established preparation methods are based on block copolymers,<sup>7,8</sup> direct assembly of colloidal particles on solid substrates,<sup>9</sup> or liquid interface-mediated assembly.<sup>10</sup> These techniques readily yield hexagonal, close-packed (*hcp*) particle arrays. For many applications, it is highly desirable to use non-close-packed particle arrays with tunable interparticle distances, and non-hexagonal symmetries to control optical, adhesive or magnetic surface properties, e.g., in the case of anti-reflective coatings<sup>11</sup> or photonic band gap devices.<sup>12</sup>

However, non-close-packed particle arrays are not readily accessible. One fabrication route is based on the assembly of colloidal particles at the oil/water interface. Here, attractive capillary forces, which lead to the formation of close-packed arrays, are screened, and repulsive electrostatic interactions become dominant. This method allows increasing the interparticle distances up to several times the particle diameter.<sup>13,14</sup> However, the colloidal monolayers lose

their non-close-packed character during transfer from the oil/water interface to a solid substrate due to the onset of attractive capillary forces.

A second fabrication method starts from *hcp* particle arrays on solid substrates. The monolayers are then transformed into non-close-packed arrays by plasma etching, which reduces the diameter of the colloids without affecting their position.<sup>10,15</sup> Here, the initial particle diameter predetermines the interparticle distance, and the particle size cannot be reduced indefinitely due to limitations of the etching process.<sup>16,17</sup> Further methods to prepare non-close-packed particle monolayers comprise spin-coating<sup>18</sup>, substrate swelling<sup>19</sup>, shrinking of close-packed particles<sup>20,21</sup> or degradation<sup>22,23</sup> of a polymer shell of core/shell particles. However, all these approaches merely produce hexagonal arrays.

Non-hexagonally ordered arrays are not accessible with standard self-assembly methods and usually require multiple step procedures. One approach to non-close-packed, non-hexagonal arrangements is based on a combination of isotropic swelling and anisotropic stretching of close-packed monolayers on elastomeric substrates. Depending on the individual stretching steps, the particles are separated along given directions yielding more complex arrays.<sup>24</sup> Besides, structured substrates have been used as templates to assemble colloidal particles in close-packed or non-close-packed arrays with various lattice geometries.<sup>25-27</sup> The combination of hard and soft colloidal particles alongside with a restriction of the available surface area has also been demonstrated to result in nonhexagonal and non-close-packed particle arrangements.<sup>28</sup> This experimental work is supported by modeling based on a hard core–soft shell interaction potential (Jagla potential).<sup>29</sup> Overall, there is currently no simple method available that could produce ordered non-close-packed arrays of any symmetry in a controlled manner.

Here, we report a straightforward fabrication method for non-close-packed particle arrays with any of the possible two-dimensional Bravais lattice symmetries. It starts from readily accessible *hcp*-monolayers, which are assembled at the water/air interface and collected on solid substrates. The transfer to the substrate induces a controlled, purely one-dimensional stretching of the *hcp*-array leading to a variety of symmetries depending on the transfer angle and degree of stretching. This method can be applied to colloidal particles of various composition and yields nanostructured areas of macroscopic size.

## 5.2 Results and Discussion

We prepared the particle monolayers at the water/air interface via an established method.<sup>30</sup> As model particles, we chose spherical polymer colloids (poly(*n*-butyl acrylate-*co*-methyl methacrylate) (P(*n*BA-*co*-MMA)) with a diameter of  $434 \pm 12$  nm. The monolayers consist of large single-crystalline domains, resulting in intense iridescent colors. These monolayers were subsequently transferred onto solid substrates to fabricate the desired non-close-packed and non-hexagonal particle arrays (Figure 5.1).

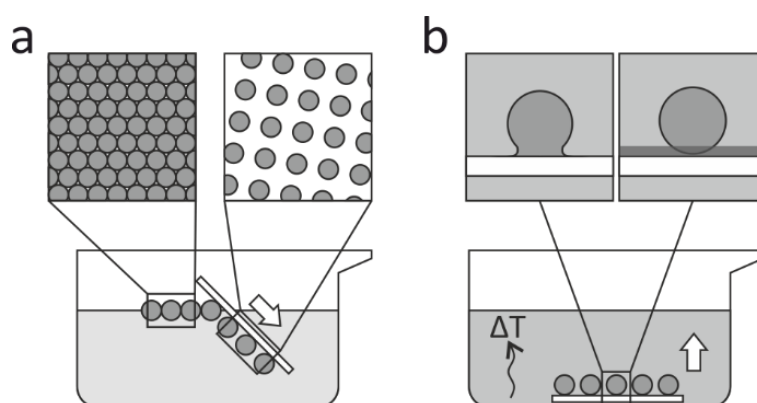


**Figure 5.1.** Fabrication of non-close-packed monolayers. (a) A *hcp* monolayer from the water/air interface is transferred to the lower side of a hydrophobic substrate by submerging the substrate through the monolayer into the subphase. Thereby the particle monolayer is stretched into a non-close-packed array. (b) The particles are immobilized on the substrate via thermal fixation near the glass transition temperature ( $T_g$ ) of the particles or the substrate. In the final step, the substrate with the monolayer can be recovered from the solution while the structure is preserved.

We first tested the conventional transfer of a monolayer onto a *hydrophilic* substrate, which is withdrawn from the water (*Z*-type deposition<sup>31</sup>). As expected, this leads to the formation of ordered *hcp* particle arrays (Figure S5.1a).<sup>30</sup> The preparation of non-close-packed arrays requires transferring the monolayer onto a *hydrophobic* substrate by immersion into water (*X*-type deposition). This is possible if the contact angle of the substrate is larger than a critical angle, in our case  $\theta_c \sim 65^\circ$ . The monolayer is then deposited on the lower side of the substrate. We hypothesized, that during the transfer of the monolayer to the substrate, the monolayer would align and stretch into the transfer direction, such that non-close-packed ordered arrays are accessible (Figure 5.1a). Unfortunately, the subsequent removal of the substrate from the aqueous solution resulted in the formation of a collapsed particle assembly (Figure S5.1b). This is a consequence of attractive capillary forces acting during the removal and drying.

Nevertheless, a closer inspection of the SEM images revealed that the particles were not completely disordered, but showed a preferential alignment along the diagonals of the image. This indicated that the particles have indeed become aligned into non-close-packed arrays, but then rearranged into close-packed structures and lost their order during removal of the substrate from the aqueous solution.

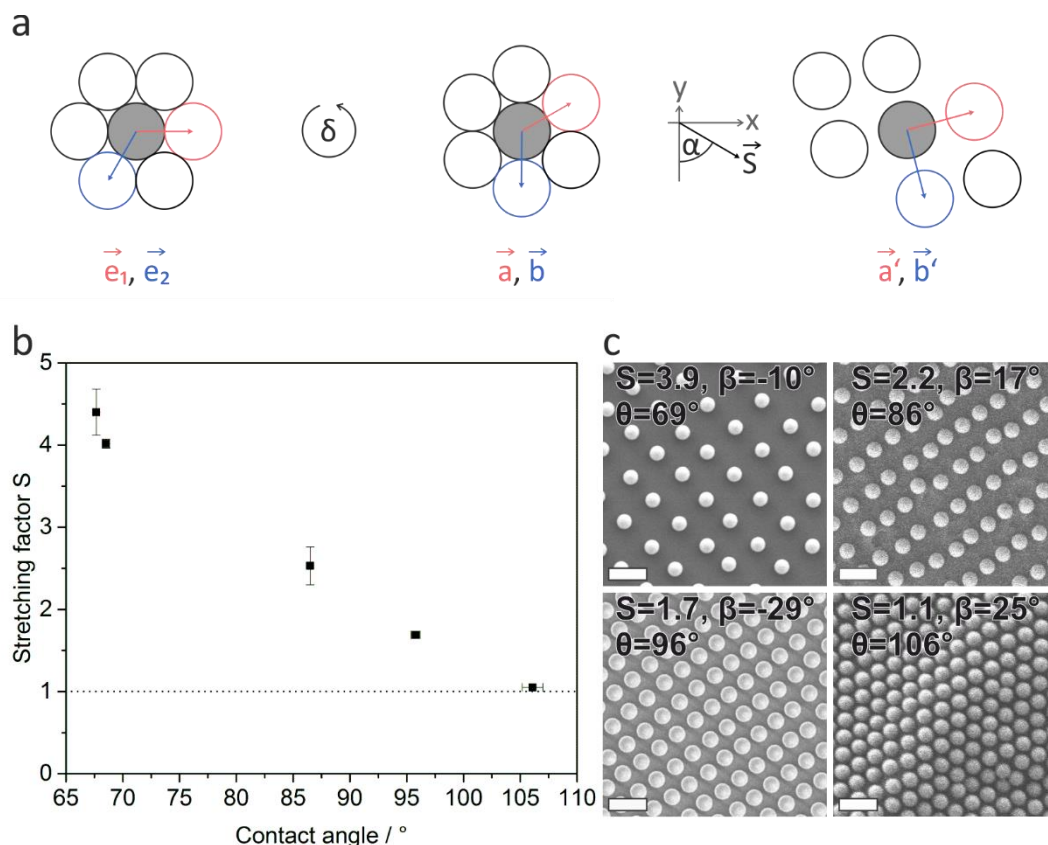


**Figure 5.2.** Stretched particle arrays. (a) Definition of the initial *hcp*-domain orientation angle  $\delta$ , stretching angle  $\alpha$  and stretching vector  $\vec{S}$ . (b) Dependence of the stretching factor  $S$  on the contact angle  $\theta$  of the substrates. (c) Polymer particles on substrates with different contact angles: SU-8 ( $\theta = 69^\circ$ ), P(S-co-nBA) ( $\theta = 86^\circ$ ), PS ( $\theta = 96^\circ$ ), PTFE film ( $\theta = 106^\circ$ ). The stretching factor  $S$  decreases with increasing contact angle with at a constant stretching direction  $\beta$ . Scale bars are 1  $\mu\text{m}$ .

To suppress the rearrangement, we immobilized the particle arrays prior to the removal from the aqueous solution by increasing their adhesive contact area on the substrate (Figure S5.2). For polymer particles with moderate glass transition temperatures ( $T_g$ ), this can be conveniently done by thermal fixation near the  $T_g$  of the particles (Figure 5.1b). We also provide an alternative concept for arbitrary particles. These can be thermally immobilized on substrates coated with a thin polymer interlayer with adequately low glass transition temperature (Figure S5.3). One can imagine further fixation strategies such as chemical crosslinking or an

exchange of the solvent.<sup>13</sup> After this fixation step, we were able to recover the substrate from the aqueous solution without affecting the particle positions (Figure S5.1c). An example for a successful immobilization of a non-close-packed particle array with non-hexagonal order covering the entire substrate (1 x 1 cm<sup>2</sup>) is shown in Figure S5.4. This demonstrates that the transfer onto hydrophobic substrates can generate large-area, non-close-packed particles arrays, and that a fixation step is crucial to maintaining the structure.

The broad implication of this transfer method bases on the fact that the obtained type of particle array is completely defined by the transfer direction and the stretching factor and can be theoretically predicted as shown in Figure 5.2a. We derive this mathematically, starting from the base vectors  $\vec{e}_1$  and  $\vec{e}_2$  of the hexagonal unit cell of the *hcp*-layer which are given as

$$\vec{e}_1 = \begin{pmatrix} 1 \\ 0 \end{pmatrix}; \vec{e}_2 = \begin{pmatrix} -0.5 \\ -0.5\sqrt{3} \end{pmatrix} \quad 5.1$$

The orientation of the *hcp*-domain at the water/air interface before it is transferred to the substrate is specified by the rotation angle  $\delta$ .

The base vectors  $\vec{a}, \vec{b}$  for the oriented *hcp*-domain prior to transfer can be calculated using a rotation matrix

$$\vec{a} = \begin{bmatrix} \cos \delta & -\sin \delta \\ \sin \delta & \cos \delta \end{bmatrix} \circ \vec{e}_1 \quad 5.2$$

$$\vec{b} = \begin{bmatrix} \cos \delta & -\sin \delta \\ \sin \delta & \cos \delta \end{bmatrix} \circ \vec{e}_2 \quad 5.3$$

The stretching vector  $\vec{S}$  with a stretching factor  $S = |\vec{S}|$  determines the degree of stretching upon transfer of the *hcp*-domain to the substrate. Additionally, the direction is defined by the angle  $\alpha$  between the stretching vector  $\vec{S}$  and the y-axis. (Figure 5.2a). Mathematically, the stretching process can be described by a sequence of a rotation by an angle  $-\alpha$  ( $M_{-\alpha}$ ), followed by an uniaxial stretching along the y-axis ( $M_S$ ), and finally a back rotation ( $M_\alpha$ ) with the matrices

$$M_\alpha = \begin{bmatrix} \cos \alpha & -\sin \alpha \\ \sin \alpha & \cos \alpha \end{bmatrix} \quad 5.4$$

$$M_S = \begin{bmatrix} 1 & 0 \\ 0 & S \end{bmatrix} \quad 5.5$$

This results in the following stretching matrix ( $M = M_\alpha \circ M_S \circ M_{-\alpha}$ ) and the stretched vectors  $\vec{a}'$  and  $\vec{b}'$  of the final particle array

$$M = \begin{bmatrix} \cos^2 \alpha + \sin^2 \alpha \cdot S & \sin \alpha \cdot \cos \alpha \cdot (1 - S) \\ \sin \alpha \cdot \cos \alpha \cdot (1 - S) & \cos^2 \alpha \cdot S + \sin^2 \alpha \end{bmatrix} \quad 5.6$$

$$\vec{a}' = M \circ \vec{a} \quad 5.7$$

$$\vec{b}' = M \circ \vec{b} \quad 5.8$$

With this calculation, we show that the obtained two-dimensional arrays, characterized by the base vectors  $\vec{a}'$  and  $\vec{b}'$ , are completely determined by the parameters  $\delta$ ,  $\alpha$  and  $S$ .

In the reversed case where the stretching factor and direction need to be determined from the observed array, the equations to calculate  $\delta$ ,  $\alpha$  and  $S$  are given in the SI (Equation 5.10 and 5.11) The two orientation angles  $\delta$  and  $\alpha$  are fully determined by the domain orientation and immersion direction and can be reduced to an angle  $\beta = \alpha - \delta$ , which describes the effective stretching direction with respect to the direction of the *hcp*-array at the water/air interface. Due to its 6-fold rotational symmetry it is sufficient to consider an angular range  $0^\circ \leq |\beta| \leq 30^\circ$ . The same structures evolve for all angles  $|\beta \pm n * 60^\circ|$ , when keeping  $S$  constant, with  $n$  being an integer.

We further demonstrate that also the stretching factor  $S$  can be well controlled experimentally. This is possible by adjusting the substrate contact angle  $\theta$  as shown in Figure 5.2b.<sup>31</sup> A wide range of contact angles was realized by spin-coating glass substrates with different polymers or directly using a polytetrafluoroethylene (PTFE) film. We thus covered a range of contact angles from PTFE ( $\theta = 106^\circ$ ), polystyrene (PS) ( $\theta = 96^\circ$ ), poly(*n*-butyl acrylate-*co*-styrene) (P(*n*BA-*co*-S)) ( $\theta = 86^\circ$ ), SU-8 photoresist ( $\theta = 69^\circ$ ) to poly(methyl methacrylate) ( $\theta = 68^\circ$ ). Using the different substrates leads to a large variation of the stretching parameter  $S$ , starting from the same floating *hcp*-monolayer (Figure 5.2c). Substrates with a very high contact angle ( $\theta = 106^\circ$ ) exhibit almost no stretching and the observed structures usually show a hexagonal, close-packed arrangement. Lowering the contact angle leads to increasing stretching factors of the original monolayer. Contact angles near the critical angle ( $\theta = 69^\circ$ ) result in remarkably large stretching factors, which promote the formation of particle lines and large tetragons. We want to stress two important properties of this interfacial stretching concept: (1) Since we work at the air-water interface, a truly one-dimensional stretching is accessible. Lateral shear forces are negligible, which is in contrast to previous stretching strategies employing elastomeric substrates.<sup>19,32</sup> This strongly increases the macroscopic homogeneity of

the transferred structure. (2) High stretching factors up to 400 % can be realized, simply by adjusting the hydrophobicity of the target substrate.

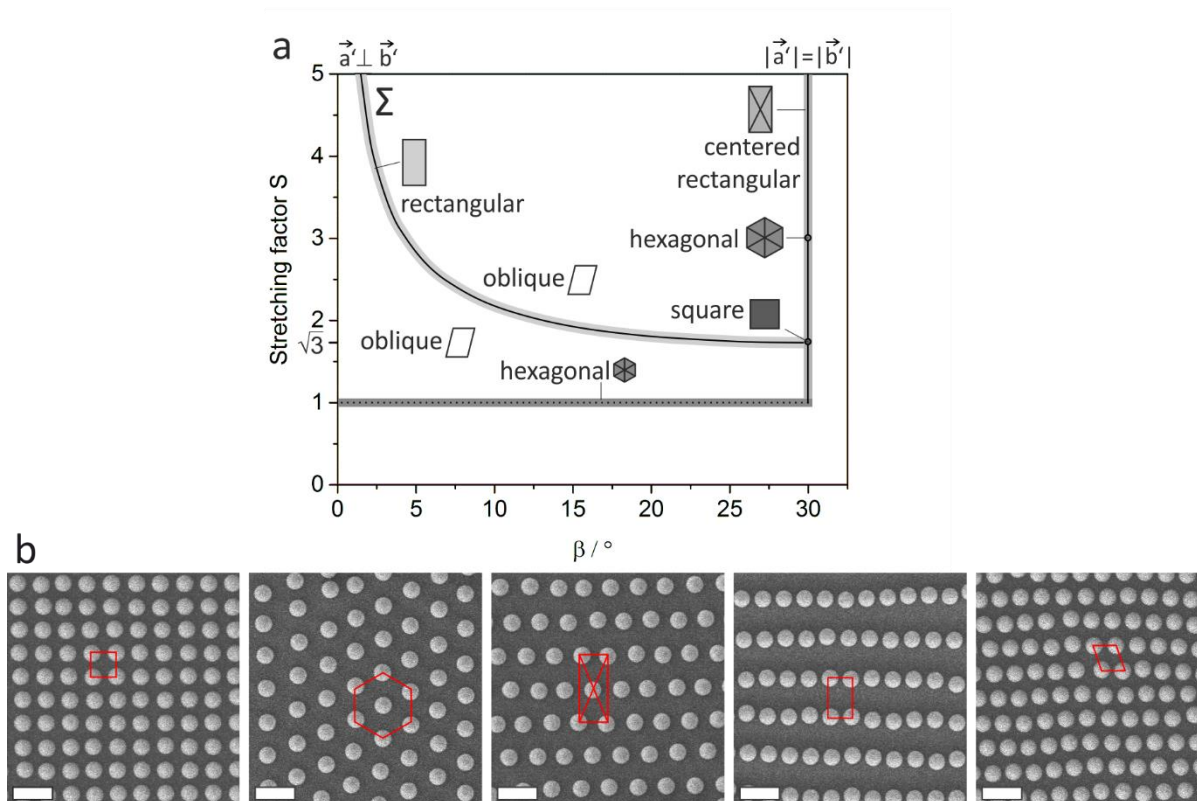
The observed dependence of the stretching factor  $S$  on the substrate contact angle  $\theta$  can be well rationalized in terms of the flow pattern in the water subphase during immersion of the substrate (Figure S5.5). This has been described in detail in literature.<sup>31</sup> For contact angles smaller than  $\theta_c \sim 65^\circ$  the subphase shows a split-injection streamline such that the monolayer moves away from the contact line. Thus X-type monolayer transfer is impossible. For slightly larger contact angles the monolayer starts to flow towards the contact line, but at a velocity smaller than the immersion velocity of the substrate. This leads to a large ratio between immersed substrate area  $A_{sub}$  and transferred monolayer area  $A_{mon}$ , which determines the stretching factor  $S = A_{sub}/A_{mon}$ . Increasing the contact angle beyond  $\theta_c$  increases the flow velocity of the monolayer towards the substrate, thus decreasing the stretching factor. At high contact angles, as e.g. for PTFE, the monolayer transfer and substrate immersion velocity eventually become equal. This results in a transfer ratio close to unity, so that the stretching factors approach  $S \sim 1$ . With this, we show that the stretching factor can also be well controlled experimentally over a large range (between  $S \sim 1$  and  $S \sim 4$ ) via the substrate contact angle.

Figure 5.3a demonstrates the full potential of this simple approach. All possible two-dimensional Bravais lattices symmetries are accessible by tuning both the stretching factor  $S$  and the effective stretching direction  $\beta$ . A square array of particles is obtained by stretching with a factor of  $S = \sqrt{3} \approx 1.73$  and a stretching direction along one of the vectors defining the initial hexagonal unit cell ( $\beta = 30^\circ$ ). An ideal non-close-packed hexagonal array can be realized by stretching with a factor of  $S = 3$  along one of the initial vectors ( $\beta = 30^\circ$ ), whereas a centered rectangular array is the result for  $S \neq 1.73$  and  $S \neq 3$  at  $\beta = 30^\circ$ . For rectangular arrays, there exist various discrete combinations of stretching factors and directions that fulfill the following equation

$$S = \frac{1}{\sqrt{\frac{\sin \beta \cdot (\sqrt{3} - \tan \beta)}{\sqrt{3} \cdot \sin \beta + \cos \beta}}} \quad 5.9$$

which is indicated by the branch  $\Sigma$ . For all other parameter combinations and  $\beta \neq 30^\circ$  and  $\beta \neq 0^\circ$  oblique lattices are obtained. Close-packed particle lines, corresponding to highly extended oblique lattices, can be fabricated by choosing  $\beta = 0^\circ$ . Thus, non-close-packed particle arrays for any of the five two-dimensional Bravais lattices (square, hexagon, rectangular, centered

rectangular, oblique) can be realized by a suitable combination of domain orientation and stretching factor.



**Figure 5.3.** Particle array symmetries determined by  $\beta$  and  $S$ . (a) Phase diagram for Bravais lattice structures as a function of the stretching factor  $S$  and stretching angle  $\beta$ . (b) Particle monolayers are stretched to yield the five possible Bravais lattices in the two-dimensional space. (from left to right) Square, hexagonal, centered rectangular, rectangular, oblique. Scale bars are 1  $\mu\text{m}$ .

Our findings have broad implications for the fabrication of ordered particle arrays, as the method should generally apply to all nano- and microscale particles that can be assembled at the water/air interface and transferred to a hydrophobic substrate. A crucial step is the immobilization of the particles on the substrate. For this purpose, we thermally fixated the monolayers to increase adhesive contact to the substrate, but also covalent or other non-covalent binding strategies are well conceivable. The fixation chemistry may thereby originate from the particle itself (e.g. its  $T_g$ ), or the target substrate (e.g. spin-coated interlayer with appropriate  $T_g$ ). We note that the immersion velocity of the substrate (1 mm/min – 1 cm/s) has no significant influence on the resulting particle arrays. At these time scales the advancing contact angle can be assumed constant, which completely defines the magnitude of stretching.<sup>31</sup> Moreover, the immersion angle ( $30^\circ - 90^\circ$ ) can also be neglected as only the local contact angle has to be considered.

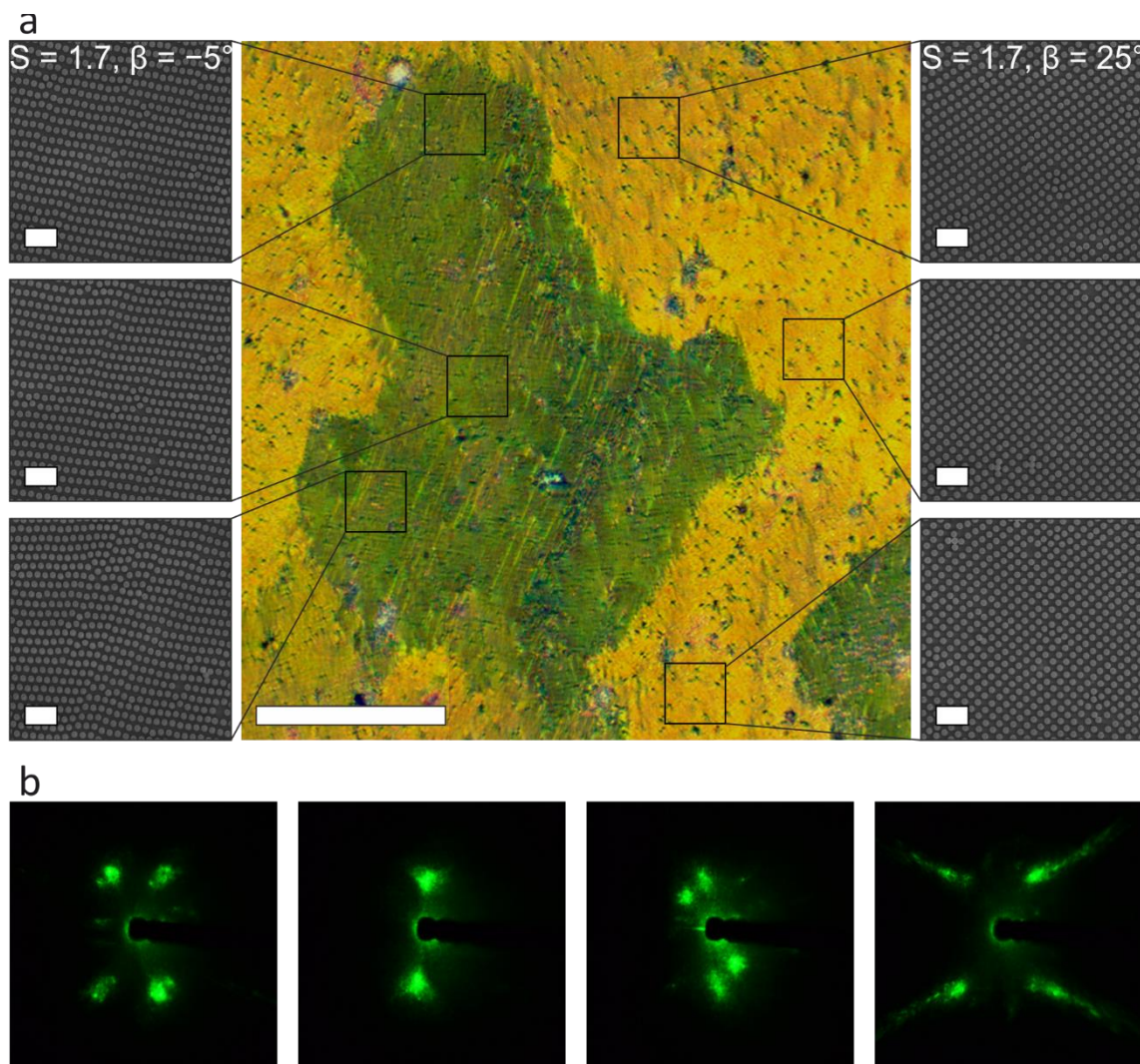


**Figure 5.4.** Uniform stretching of multi-crystalline monolayers. (a) Optical microscopy image of large area, single-crystalline domains and correlative electron microscopy on a sample with  $S \sim 1.7$  (PS). Scale bars are  $50 \mu\text{m}$  (optical microscopy) and  $2 \mu\text{m}$  (electron microscopy). (b) Laser diffraction at various spots on one sample with  $S \sim 1.7$ . Four distinct array symmetries can be found when scanning across the substrate: (from left to right) Rectangular, close-packed particle lines, oblique, and square.

In contrast to the stretching of monolayers on rubber substrates, which inherently show a contraction in the direction perpendicular to the strain direction, our method yields a uniform and purely one-dimensional stretching across the whole substrate. In Figure 5.4a, an optical microscopy image is shown of a monolayer transferred to a PS substrate. Two extended single-crystalline domains can be discerned from the distinct scattering colors corresponding to different domain orientations. We demonstrate that these distinct lattices are well-explained by the same degree of stretching; solely their initial orientation to the stretching direction differs.

The absolute stretching value is constant across the whole image ( $S \sim 1.7$ ) and identical structures are found within the whole single-crystalline areas.

A possible limitation for the preparation of large-area arrays could be the size limitation of the monocrystalline *hcp*-domains. However, the area of monocrystalline domains formed by the method outlined above<sup>30</sup> is already sufficiently large for micro-optical applications.<sup>33</sup> A series of diffraction measurements on our samples, using a focused laser beam shows distinct scattering patterns, which can be attributed to monocrystalline areas with a specific symmetry (Figure 5.4b).

Finally, excellent techniques have been reported to reach uniform domain orientation of even larger size.<sup>34,35</sup> The combination of such improved methods for monocrystalline colloidal monolayer formation with in situ techniques to assess the monolayer lattice orientation will finally allow to fix the stretching direction  $\beta$  and consequently to deterministically fabricate a specific pre-defined Bravais lattice. Depending on the particle size (length scale) and composition (contrast), different methods can be envisioned for this task. Most straightforward will be laser diffraction experiments or direct optical microscopy at the air/water interface. More challenging will be grazing-angle X-ray scattering methods, which, however, will be able to address the sub-100 nm length scale as well.

### 5.3 Conclusion

In conclusion, we demonstrated a convenient and versatile method for the preparation of ordered non-close-packed particle arrays with symmetries of any of the two-dimensional Bravais lattices. We are able to predict and experimentally realize a variety of ordered particle arrays by tuning only two parameters, the contact angle of the substrate and the stretching direction relative to the monolayer orientation. Compared to existing routes to non-close-packed colloidal crystals, our approach is superior with respect to its simplicity, variability, and scalability. Up to now many of the fabricated array symmetries that we show have not been accessible by other self-assembly methods.

The presented technique offers a new approach to enable the preparation of a large variety of defined ordered particle arrays to tune their optical, photonic and wetting properties to specific applications. Furthermore, the method is compatible with batch and continuous solution surface processing methods with immediate implications for the generation of ordered particle arrays on a variety of solid and flexible substrates.

## 5.4 Experimental Section

**Synthesis of P(nBA-co-MMA) particles:** Monodisperse P(nBA-co-MMA) particles were prepared by emulsifier-free emulsion polymerization. 450 mL milliQ water were mixed with 35 mL MMA and 15 mL nBA, respectively. The mixture was equilibrated at 75 °C under a slight argon flow for 15 minutes. Subsequently, 2 mL of acrylic acid were added to the mixture followed by a further equilibration step for 5 min. The polymerization was started by a rapid injection of 150 mg potassium peroxydisulfate dissolved in 5 mL milliQ water. The reaction was carried out overnight. The polymerization was quenched by exposure to air. Residual educts were removed by dialysis against water for five days, changing water twice a day. Particles with a mean diameter of  $434 \pm 12$  nm and with a glass transition temperature of 61 °C were obtained.

**Preparation of hydrophobic substrates:** Hydrophobic substrates were prepared by spin-coating glass slides with either PS, P(nBA co S) or PMMA and subsequent annealing at 200 °C for 5 min. SU 8 substrates were obtained by spin-coating SU 8 2050. After soft bake at 65 °C for 1 min and 95 °C for 7 min, the substrate was exposed to UV light 2 x 4 s. A post exposure bake was carried out at 65 °C for 1 min and 95 °C for 6 min. PTFE films were used as received.

**Preparation of colloidal crystals:** The preparation of hcp monolayers is described in detail in reference 25. Aqueous particle dispersions with a concentration of 2.5 wt% were spin-coated on cationically functionalized glass slides at a speed of 4000 rpm. Freely floating monolayers were assembled at the water/air interface by slow immersion of the particle coated glass substrate into a 0.1 mM SDS solution in milliQ water. The aqueous phase was adjusted to pH 12 by adding 30 % aqueous NH<sub>3</sub>. A hydrophobic substrate was immersed through the floating monolayer at an angle of 45 ° relative to the water surface and was left at the bottom of the beaker with the monolayer facing upwards. After heating the water near the glass transition temperature of the particles for 5 min on a hotplate, the monolayers were removed from the solution and dried at ambient conditions.

**Characterization:** SEM images were taken on a LEO 1530 Gemini Field Emission SEM (Carl Zeiss AG, Oberkochen, Germany) at 3.00 kV. Particle positions and diameters were determined from the SEM images using MATLAB's circle detection function (Figure S5.6). From the particle positions, the average stretched basis vectors  $(a')^{\rightarrow}$  and  $(b')^{\rightarrow}$  were then determined by averaging all interparticle vectors with a Python script (Figure S5.7). Contact angle measurements were performed on an OCA 20 (DataPhysics Instruments GmbH, Filderstadt, Germany).

## Acknowledgements

This work was funded by the German Research Foundation (DFG) by the SFB840. M.E.J.H., C.S. and B.A.F.K. acknowledge support from the Elite Network of Bavaria (ENB). The authors thank Dr. Beate Förster and Martina Heider from the Bavarian Polymer Institute (BPI) for their support using the scanning electron microscopy facilities. M.E.J.H. and C.S. contributed equally to this work.

## References

1. Nemiroski, A., Gonidec, M., Fox, J. M., Jean-Remy, P., Turnage, E. & Whitesides, G. M. Engineering shadows to fabricate optical metasurfaces. *ACS Nano* **8**, 11061-11070 (2014).
2. Vogel, N., Weiss, C. K. & Landfester, K. From soft to hard: the generation of functional and complex colloidal monolayers for nanolithography. *Soft Matter* **8**, 4044-4061 (2012).
3. Yang, S. M., Jang, S. G., Choi, D. G., Kim, S. & Yu, H. K. Nanomachining by colloidal lithography. *Small* **2**, 458-475 (2006).
4. Romanov, S. G. *et al.* Probing guided modes in a monolayer colloidal crystal on a flat metal film. *Phys. Rev. B* **86**, 195145 (2012).
5. Ai, B., Yu, Y., Möhwald, H., Zhang, G. & Yang, B. Plasmonic films based on colloidal lithography. *Adv. Colloid Interface Sci.* **206**, 5-16 (2014).
6. Drotlef, D.-M., Stepien, L., Kappl, M., Barnes, W. J. P., Butt, H.-J. & del Campo, A. Insights into the Adhesive Mechanisms of Tree Frogs using Artificial Mimics. *Adv. Funct. Mater.* **23**, 1137-1146 (2013).
7. Möller, M., Spatz, J. P. & Roescher, A. Gold nanoparticles in micellar poly(styrene)-b-poly(ethylene oxide) films—size and interparticle distance control in monoparticulate films. *Adv. Mater.* **8**, 337-340 (1996).
8. Glass, R., Möller, M. & Spatz, J. P. Block copolymer micelle nanolithography. *Nanotechnology* **14**, 1153-1160 (2003).
9. Denkov, N. D., Velev, O. D., Kralchevsky, P. A., Ivanov, I. B., Yoshimura, H. & Nagayama, K. Two-dimensional crystallization. *Nature* **361**, 26-26 (1993).
10. Vogel, N., Retsch, M., Fustin, C. A., Del Campo, A. & Jonas, U. Advances in colloidal assembly: the design of structure and hierarchy in two and three dimensions. *Chem. Rev.* **115**, 6265-6311 (2015).
11. Stelling, C., Bernhardt, C. & Retsch, M. Subwavelength Etched Colloidal Monolayers: A Model System for Tunable Antireflective Coatings. *Macromol. Chem. Phys.* **216**, 1682-1688 (2015).
12. Fenollosa, R. & Meseguer, F. Non-Close-Packed Artificial Opals. *Adv. Mater.* **15**, 1282-1285 (2003).
13. Isa, L., Kumar, K., Müller, M., Grolig, J., Textor, M. & Reimhult, E. Particle lithography from colloidal self-assembly at liquid-liquid interfaces. *ACS Nano* **4**, 5665-5670 (2010).
14. Law, A. D., Buzza, D. M. & Horozov, T. S. Two-dimensional colloidal alloys. *Phys. Rev. Lett.* **106**, 128302 (2011).
15. Vogel, N., Goerres, S., Landfester, K. & Weiss, C. K. A Convenient Method to Produce Close- and Non-close-Packed Monolayers using Direct Assembly at the Air-

- Water Interface and Subsequent Plasma-Induced Size Reduction. *Macromol. Chem. Phys.* **212**, 1719-1734 (2011).
16. Akinoglu, E. M., Morfa, A. J. & Giersig, M. Understanding anisotropic plasma etching of two-dimensional polystyrene opals for advanced materials fabrication. *Langmuir* **30**, 12354-12361 (2014).
  17. Plettl, A., Enderle, F., Saitner, M., Manzke, A., Pfahler, C., Wiedemann, S. & Ziemann, P. Non-Close-Packed Crystals from Self-Assembled Polystyrene Spheres by Isotropic Plasma Etching: Adding Flexibility to Colloid Lithography. *Adv. Funct. Mater.* **19**, 3279-3284 (2009).
  18. Jiang, P., Prasad, T., McFarland, M. J. & Colvin, V. L. Two-dimensional nonclose-packed colloidal crystals formed by spincoating. *Appl. Phys. Lett.* **89**, 011908 (2006).
  19. Yan, X., Yao, J., Lu, G., Li, X., Zhang, J., Han, K. & Yang, B. Fabrication of non-close-packed arrays of colloidal spheres by soft lithography. *J. Am. Chem. Soc.* **127**, 7688-7689 (2005).
  20. Volk, K., Fitzgerald, J. P., Retsch, M. & Karg, M. Time-Controlled Colloidal Superstructures: Long-Range Plasmon Resonance Coupling in Particle Monolayers. *Adv. Mater.* **27**, 7332-7337 (2015).
  21. Quint, S. B. & Pacholski, C. Extraordinary long range order in self-healing non-close packed 2D arrays. *Soft Matter* **7**, 3735-3738 (2011).
  22. Vogel, N., Fernandez-Lopez, C., Perez-Juste, J., Liz-Marzan, L. M., Landfester, K. & Weiss, C. K. Ordered arrays of gold nanostructures from interfacially assembled Au@PNIPAM hybrid nanoparticles. *Langmuir* **28**, 8985-8993 (2012).
  23. Spatz, J. P., Mössmer, S., Hartmann, C., Möller, M., Herzog, T., Krieger, M., Boyen, H.-G., Ziemann, P. & Kabius, B. Ordered Deposition of Inorganic Clusters from Micellar Block Copolymer Films. *Langmuir* **16**, 407-415 (2000).
  24. Li, X., Wang, T., Zhang, J., Yan, X., Zhang, X., Zhu, D., Li, W., Zhang, X. & Yang, B. Modulating two-dimensional non-close-packed colloidal crystal arrays by deformable soft lithography. *Langmuir* **26**, 2930-2936 (2010).
  25. Malaquin, L., Kraus, T., Schmid, H., Delamarche, E. & Wolf, H. Controlled particle placement through convective and capillary assembly. *Langmuir* **23**, 11513-11521 (2007).
  26. Khanh, N. N. & Yoon, K. B. Facile organization of colloidal particles into large, perfect one- and two-dimensional arrays by dry manual assembly on patterned substrates. *J. Am. Chem. Soc.* **131**, 14228-14230 (2009).
  27. Stelling, C., Mark, A., Papastavrou, G. & Retsch, M. Showing particles their place: deterministic colloid immobilization by gold nanomeshes. *Nanoscale* **8**, 14556-14564 (2016).
  28. Rey, M., Law, A. D., Buzza, D. M. A., & Vogel, N. Anisotropic Self-Assembly from Isotropic Colloidal Building Blocks. *J. Am. Chem. Soc.* **139**, 17464-17473 (2017).
  29. Jagla, E. A. Phase behavior of a system of particles with core collapse. *Phys. Rev. E* **58**, 1478-1486 (1998).
  30. Retsch, M., Zhou, Z., Rivera, S., Kappl, M., Zhao, X. S., Jonas, U. & Li, Q. Fabrication of Large-Area, Transferable Colloidal Monolayers Utilizing Self-Assembly at the Air/Water Interface. *Macromol. Chem. Phys.* **210**, 230-241 (2009).
  31. Cerro, R. L. Moving contact lines and Langmuir-Blodgett film deposition. *J. Colloid Interface Sci.* **257**, 276-283 (2003).
  32. Choi, H. K., Im, S. H. & Park, O. O. Shape and feature size control of colloidal crystal-based patterns using stretched polydimethylsiloxane replica molds. *Langmuir* **25**, 12011-12014 (2009).

33. Vega-Flick, A., Duncan, R. A., Wallen, S. P., Boechler, N., Stelling, C., Retsch, M., Alvarado-Gil, J. J., Nelson, K. A. & Maznev, A. A. Vibrational dynamics of a two-dimensional microgranular crystal. *Phys. Rev. B* **96**, 024303 (2017).
34. Shinotsuka, K., Kajita, Y., Hongo, K. & Hatta, Y. Crystal Perfection of Particle Monolayer at the Air-Water Interface. *Langmuir* **31**, 11452-11457 (2015).
35. Meng, X. & Qiu, D. Gas-flow-induced reorientation to centimeter-sized two-dimensional colloidal single crystal of polystyrene particle. *Langmuir* **30**, 3019-3023 (2014).

## 5.5 Supporting Information

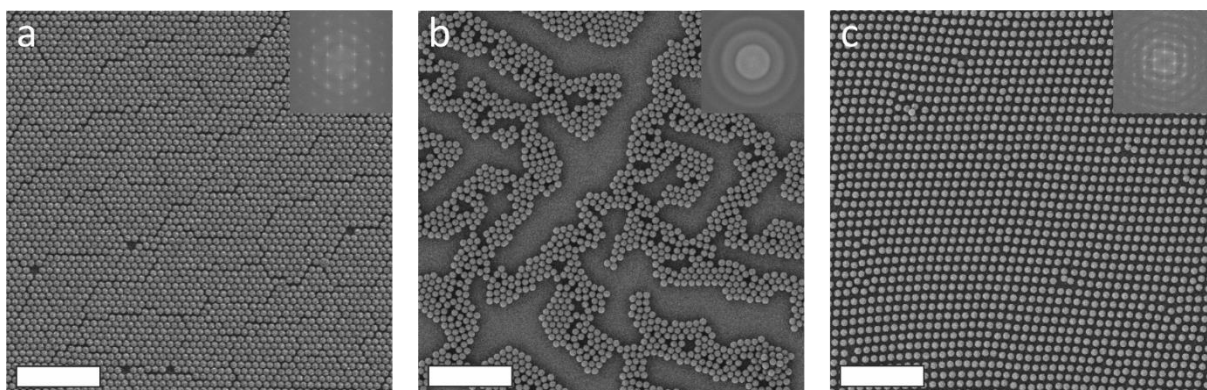


**Figure S5.1.** SEM images of particle monolayers on hydrophilic and hydrophobic substrates. The insets show the corresponding fast Fourier transform (FFT). (a) Particles on a hydrophilic glass substrate (*hcp* structure). (b) Particles on a hydrophobic substrate without thermal fixation (collapsed line structure). (c) Particles on a hydrophobic substrate with thermal fixation (non-close-packed oblique structure). Scale bars are 5  $\mu\text{m}$ .

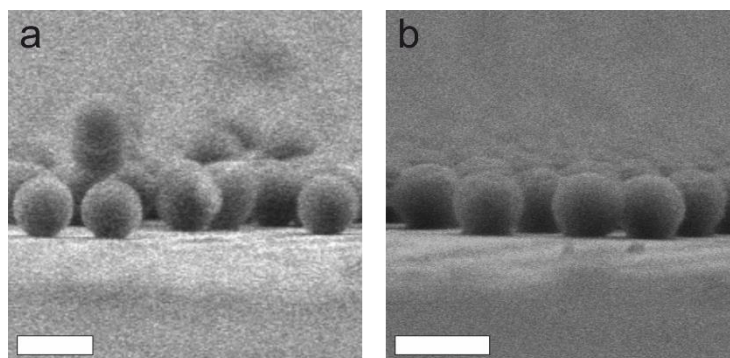


**Figure S5.2.** Side view SEM images of (a) non-immobilized and (b) immobilized particles. Without thermal annealing, the particles can be viewed as hard spheres which feature a minimum contact area on the substrate. Upon drying of the monolayer, these particles are subject to capillary forces that lead to a shift to new particle positions. Thermal annealing of the particles above their glass transition temperature  $T_g$  leads to an increase of the contact area on the substrate. In the viscous state, the particles fuse onto the substrate and become immobilized at their positions even under capillary stress. Scale bars are 500 nm.

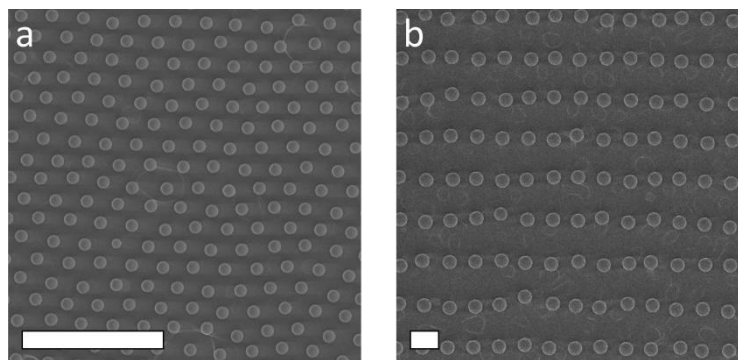


**Figure S5.3.** SEM images of particle monolayers immobilized on hydrophobic substrates with moderate glass transition temperature. PS Particles ( $T_g \approx 105$  °C) with a diameter of (a) 453 nm and (b) 2560 nm thermally fixated on spin-coated *P(nBA-co-MMA)* layer ( $T_g \approx 55$  °C). Scale bars are 5  $\mu$ m.

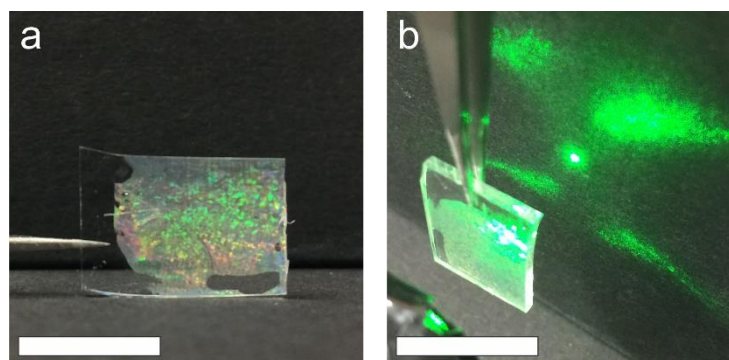


**Figure S5.4.** Immobilized particle monolayer. (a) Photograph of an immobilized particle monolayer on a hydrophobic substrate. The iridescent color preserved after drying of the monolayer indicate an intact positional arrangement of the particles. (b) Laser diffraction of an immobilized particle monolayer. The sharp peaks confirm the high order of the particles in the monolayer. Scale bars are 1 cm.

### Calculation of $\delta$ , $\alpha$ and $S$

Experimentally found structures can be assigned to specific stretching parameters  $\delta$ ,  $\alpha$  and  $S$ . For this the stretched vectors  $\vec{a}'$  and  $\vec{b}'$  with the coordinates  $x_a', y_a'$  and  $x_b', y_b'$  have to be extracted from SEM images. The coordinates are inserted into the following two equations to calculate  $\alpha$  and  $S$ . In order to determine the right parameters, the results of both  $\vec{a}'$  and  $\vec{b}'$  have to be screened with respect to  $\delta$ .

$$\alpha = \operatorname{arccot} \frac{y' - y(\delta)}{x' - x(\delta)} \quad 5.10$$

$$S = \frac{x' - x(\delta) \cdot \cos^2 \alpha + y(\delta) \cdot \sin \alpha \cdot \cos \alpha}{x(\delta) \cdot \sin^2 \alpha + y(\delta) \cdot \sin \alpha \cdot \cos \alpha} \quad 5.11$$

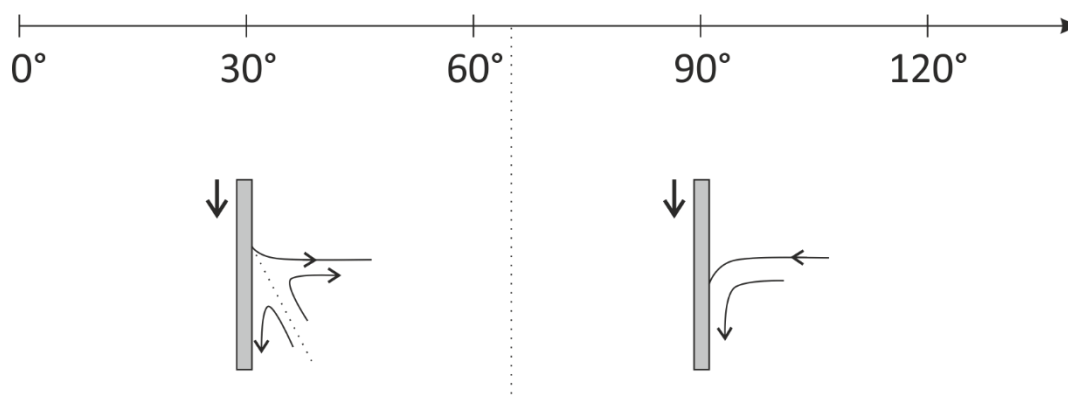


**Figure S5.5.** Streamline profiles upon immersion of a solid substrate at different contact angles.<sup>[1]</sup> The dotted line indicates the critical angle  $\theta_c$  below which an X-type is impossible.

[1] R. L. Cerro, *J. Colloid Interface Sci.* **2003**, 257, 276.

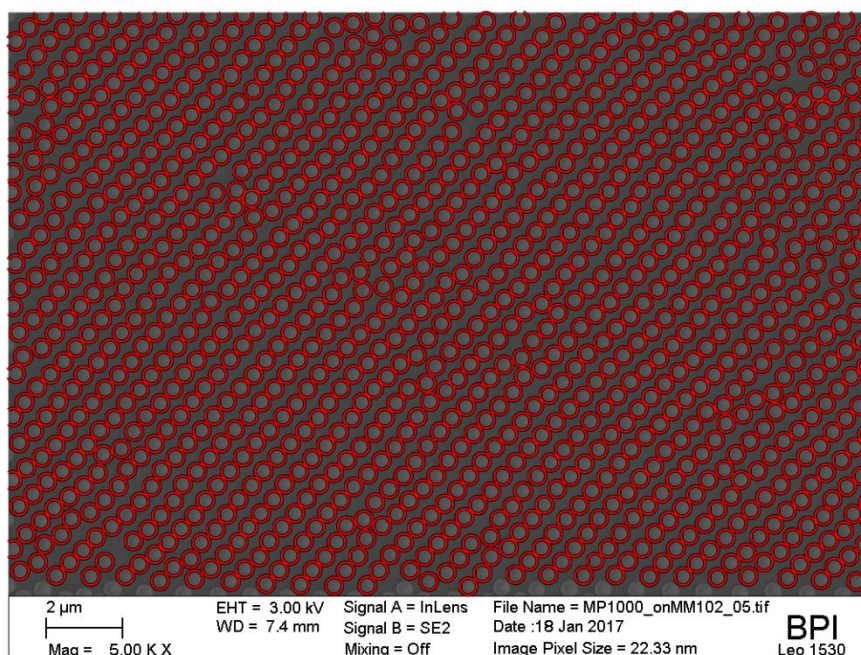


**Figure S5.6.** SEM image of a stretched monodomain. The red circles indicate the particles found by MATLAB's circle detection function after optimizing the search parameters manually.

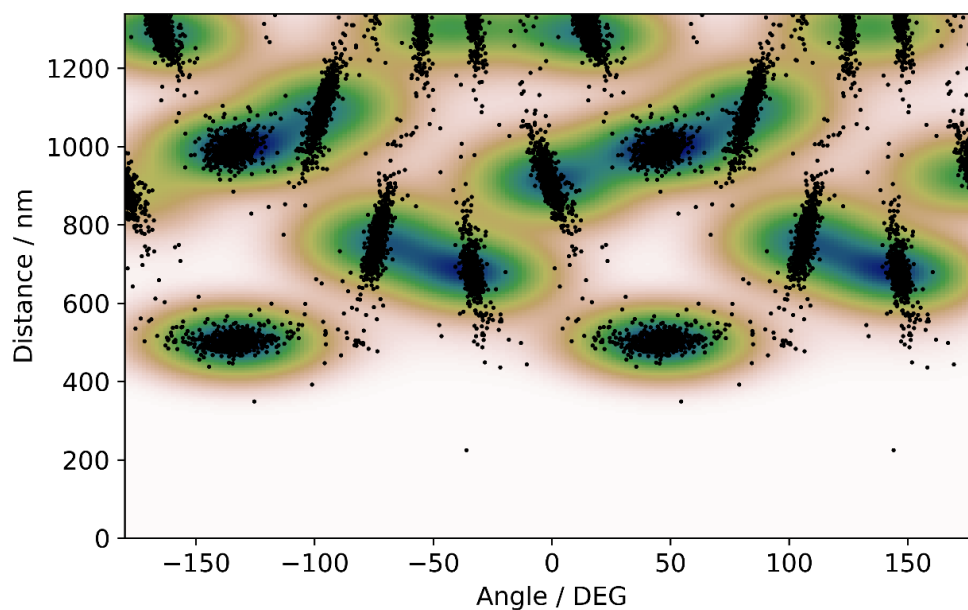


**Figure S5.7.** 2D Histogram of the distance between particle pairs and the corresponding angle with the x-axis for the SEM image in Figure S5.7. Each black dot represents an inter-particle connection. A Gaussian kernel density estimator is used to calculate the smooth distribution function (color). Local maxima in the distribution, with small interparticle distances, represent possible candidates for the stretched basis vectors  $\vec{a}'$  and  $\vec{b}'$  in polar coordinates.

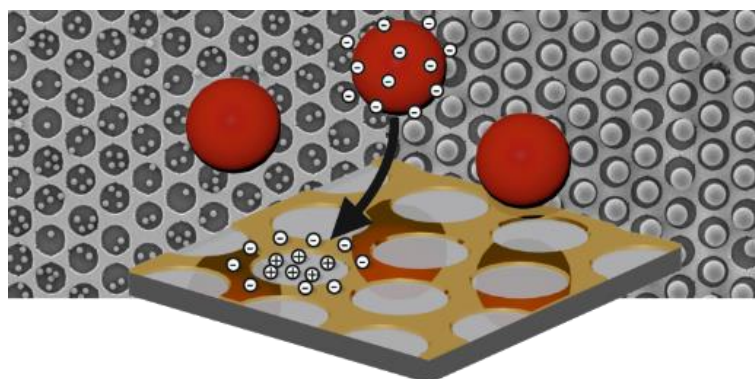


## 6 Showing Particles their Place: Deterministic Colloid Immobilization by Gold Nanomeshes

Christian Stelling,<sup>1</sup> Andreas Mark,<sup>2</sup> Georg Papastavrou,<sup>2\*</sup> and Markus Retsch<sup>1\*</sup>

<sup>1</sup>Physical Chemistry – Polymer Systems, University of Bayreuth, 95440 Bayreuth, Germany

<sup>2</sup>Physical Chemistry – Physics of Polymers, University of Bayreuth, 95440 Bayreuth,  
Germany



Published in *Nanoscale* 8, 14556-14564 (2016).

Reproduced with permission from The Royal Society of Chemistry.

## Abstract

The defined immobilization of colloidal particles on a non-close-packed lattice on solid substrates is a challenging task in the field of directed colloidal self-assembly. In this contribution the controlled self-assembly of polystyrene beads into chemically modified nanomeshes with a high particle surface coverage is demonstrated. For this, solely electrostatic interaction forces **were** exploited by the use of topographically shallow gold nanomeshes. Employing orthogonal functionalization, an electrostatic contrast between the glass surface and the gold nanomesh **was** introduced on a sub-micron scale. This surface charge contrast promotes a highly site-selective trapping of the negatively charged polystyrene particles from the liquid phase. AFM force spectroscopy with a polystyrene colloidal probe **was** used to rationalize this electrostatic focusing effect. It provides quantitative access to the occurring interaction forces between the particle and substrate surface and clarifies the role of the pH during the immobilization process. Furthermore, the structure of the non-close-packed colloidal monolayers can be finely tuned by varying the ionic strength and geometric parameters between colloidal particles and nanomesh. Therefore one is able to specifically and selectively adsorb one or several particles into one individual nanohole.

## 6.1 Introduction

Colloidally assembled structures have been widely applied over the past years to prepare a broad range of functional nano- and mesostructured materials.<sup>1</sup> Despite the fact that complex two- and three-dimensional ensembles can be fabricated by fairly simple methods, this research field is still very active due to the many degrees of freedom inherent in colloidal assemblies, such as packing geometry, inter-particle spacing, or particle material.<sup>2,3</sup> In any preparation method under consideration, the tight control over the mutual colloidal interaction forces, the adsorption kinetics, and the drying conditions is of paramount importance in order to obtain the desired colloidal superstructure in two or three dimensions. These assemblies show many new properties in terms of their optical appearance,<sup>4,5</sup> thermal conductance,<sup>6</sup> or reflection properties,<sup>7,8</sup> which can be tuned by varying the colloidal dimensions and order parameters. While these structures can extend in all three dimensions, it is often the first layer on the substrate that crucially defines the growing conditions of the following layers.<sup>9,10</sup>

In order to build 2-dimensional colloidal structures with maximal degrees of freedom, the underlying interactions governing the assembly of colloidal structures have to be finely controlled. Previous wet-chemical approaches can be classified as either convective or electrostatic assembly.<sup>2</sup> In topographically controlled assembly structures a particular substrate pattern, which is commensurate or larger than the colloidal particle under consideration, is fabricated with a distinct height. Suitable patterns of various symmetry and periodicity have been produced for example by e-beam lithography or photolithography. The colloidal order is driven by capillary forces, which take place at the liquid-gas interfaces and drive the particle in the topographically lower regions of the pattern. Consequently, a dry colloidal monolayer or crystal is obtained at the end of the assembly process. The topographic template substrates provide access to hierarchical two-dimensional colloidal arrays,<sup>11-13</sup> non-close-packed ensembles,<sup>14,15</sup> larger mono-crystalline domains,<sup>16,17</sup> and predefined lattice symmetries.<sup>9,18,19</sup> Additionally, very precise particle positioning on sparsely distributed topographic features has been demonstrated, which allows to prepare few oriented particle clusters on a flat substrate.<sup>20</sup> Capillary forces commonly dominate electrostatic interaction between the particles during the drying procedure.<sup>21</sup> However, in the absence of such capillary forces, e.g. by transfer to a solvent with a lower surface tension<sup>22</sup> the original structure remains intact. If the particle-substrate interaction is sufficient to prevent rearrangement of adsorbed particles, one finds the so-called extended random-sequential adsorption,<sup>23,24</sup> which includes the inter-particle forces due to diffuse layer overlap. However, the single particle positions are stochastically distributed despite the presence of characteristic separation distance between the particles.

The electrostatic immobilization of colloidal particles on chemically modified patches, which are considerably larger than the particle itself is a commonly utilized strategy to obtain a deterministic placement of particles at defined places.<sup>21,25-27</sup> The necessary surface modification has been achieved by molecular self-assembled monolayers,<sup>25</sup> polyelectrolytes,<sup>26</sup> microcontact printing,<sup>21</sup> or functional silanes.<sup>27</sup> Nevertheless, the mutual order within these large area patches is still governed by random sequential adsorption or hexagonal packing in the case that capillary forces dominate.

In order to implement inter-particle spacing that show well-defined order parameters extending over nearest neighbors, different strategies have to be followed. One possibility is defined chemical modification in combination with highly specific interactions, such as receptor-ligand pairs or DNA-hybridization.<sup>28,29</sup> However, these preparation techniques require sophisticated equipment in order to prepare samples with sub-micron features.

Here, we present a more elegant method that is based on nano-mesh structures, which are obtained by evaporation of noble metals on pre-adsorbed and etched colloidal monolayers. This so-called nanosphere lithography is well-established and has been described previously by various research groups.<sup>30-34</sup> Subsequently, we orthogonally modify the two different surface materials (*i.e.* gold and glass) with thiols and silanes, respectively, in order to obtain highly defined surface areas of opposite charge. The term orthogonally expresses that this independent functionalizing can provide surface areas with opposite characteristics, such as sign of surface charge. During particle deposition these surface charges on the structured collector surface lead to a defined adsorption of the particles that depends solely on the particle-surface interaction and not on inter-particle interaction. Hence, particle spacing superior to the ones obtainable by inter-particle forces can be achieved – yet at a high surface coverage. We demonstrate that one can obtain a highly selective process by which a defined number of small particles can be assembled in defined sub-micron surface areas. The required tuning of the particle/substrate and particle/particle interaction parameters can be achieved by adjustment of the ionic strength and the pH. We investigate the self-assembly process for pattern patches, which are larger, equal or smaller than the colloid size under investigation. The underlying interaction mechanisms during the particle deposition process have been quantified by direct force measurement based on the colloidal probe technique.<sup>35</sup> In particular, direct force measurements demonstrate that the surface charge and not topographic features are responsible for the observed, irreversible adsorption process.

## 6.2 Results and Discussion

In Figure 6.1 the concept of selective particle deposition into the nanomesh is outlined. The different materials of the nanohole array allow an orthogonal functionalization of glass and gold. The glass holes are selectively functionalized with an aminosilane to obtain positively charged holes in acidic and neutral pH conditions, thus attracting the negatively charged polystyrene particles. In contrast, the Au-mesh is treated with OH-terminated thiol, which has been found to be negatively charged at pH 4.<sup>36</sup> This modification introduces a repulsive potential while being hydrophilic and thus resulting in good wetting properties of the entire surface.

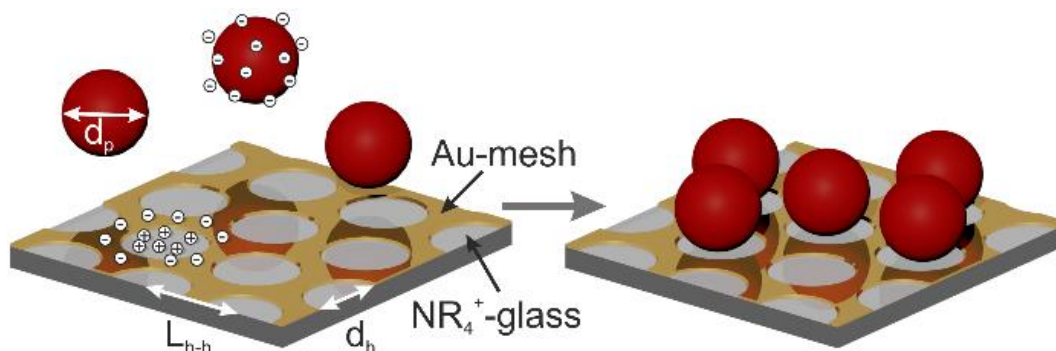


**Figure 6.1.** Schematic representation of self-assembly of polystyrene particles on a nanohole array.

Although directed electrostatic adsorption of nanoparticles by chemically patterned surfaces has been shown before for 40 nm Au colloids,<sup>29</sup> a quantitative investigation of the underlying mechanism is still missing. For the first time, we directly determined the forces responsible for the particle adsorption by colloidal probe AFM measurements and studied the influence particle size, pH and ionic strength in detail. Furthermore we extended the size range applicable to colloidal particles between 150 nm and 1500 nm. Atomic force microscopy is utilized to study the long-range interactions on the orthogonally functionalized Au-nanohole arrays in order to understand particle immobilization on these substrates. By using a polystyrene bead as colloidal probe static force measurements can be performed to directly reveal the interaction behaviour between the particles and the sample. This allows a direct comparison of AFM measurements and macroscopic particle immobilization experiments. Exemplary force versus distance profiles on both the Au-mesh and the NR<sub>4</sub><sup>+</sup>-modified glass are shown in Figure 6.2 for measurements in pH 4 and pH 10 solution. When using HCl and NaOH to adjust the pH value, for pH 4 and pH 10 the ionic strength of the solution equals 0.1 mM. Thus, differences in the adsorption process can be directly referred to the pH value. All AFM measurements were conducted in aqueous solutions with a low total ionic strength of 0.2 mM to achieve sufficiently large Debye lengths.

At pH 4 (Figure 6.2b,d) the force profiles on the approach part (red curve) significantly differ between the Au-mesh and the NR<sub>4</sub><sup>+</sup>-glass, whereas the retraction parts (blue curve) show comparable trends for the adhesion once the particles are in contact with the surface. On the NR<sub>4</sub><sup>+</sup>-modified glass a distinct long-range attraction for the polystyrene particles used as probe particles is observed. For the thiol-modified Au-surface, however, an absence of long-range attractive forces and a slight repulsion is observed. Particles adhere strongly at this pH to both surface types, suggesting an irreversible adsorption of particles once they are in contact with the surface.

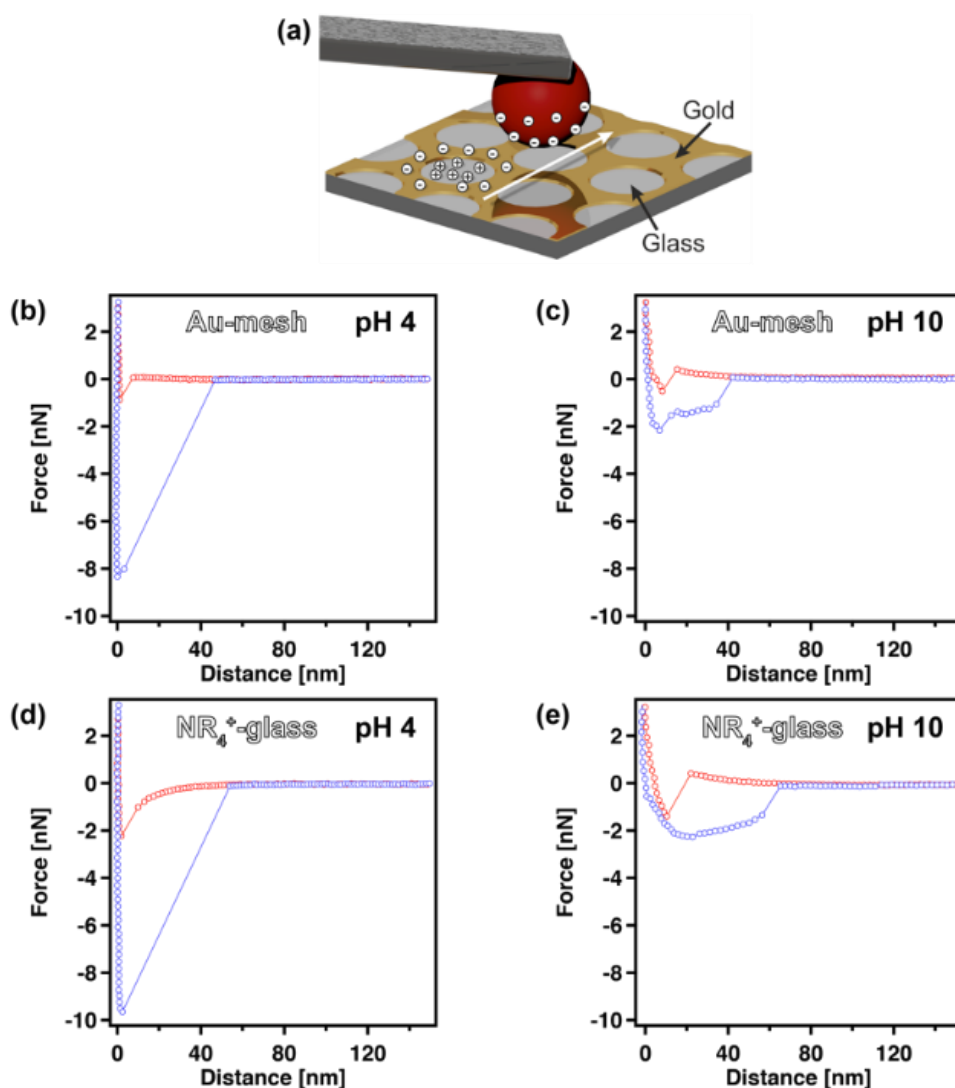


**Figure 6.2.** (a) Schematic illustration of an AFM force experiment with a polystyrene colloidal probe on an Au-nanohole array. (b-e) Resulting force versus distance profiles for measurements in an aqueous solution at pH 4 and pH 10. Depiction of the approach (red) and retraction (blue) part of force versus distance profiles on the Au-mesh (b,c) and NR<sub>4</sub><sup>+</sup>-glass (d,e).

At pH 10 (Figure 6.2c,e) the long-range attraction forces between the cationic glass surface and the polystyrene probe vanish and instead a repulsive interaction is observed. Additionally, the repulsive interactions on the Au-surface areas increase. The combination of both effects leads to an effectively repulsive substrate for the negatively charged PS particles for pH 10. However, the retraction curves show again adhesion, albeit lower than for pH 4. Monolayers of hydroxy-terminated thiols are known to have a negative surface potential even in slightly acidic environment due to preferential accumulation of anions at the monolayer surface, while at pH 10 an increased adsorption of hydroxyl ions and thus a more negative surface charge.<sup>36-38</sup> The weak repulsive forces at pH 10 for the aminosilane-modified glass can be attributed to

hydroxyl-ion adsorption as well as an incomplete silane layer with an underlying highly negatively charged glass substrate.

Due to sulfate moieties, the particles are negatively charged over the whole pH-range as confirmed by zeta potential measurements for three different particle sizes (Figure S6.11). Nevertheless, the magnitude of the zeta potential increases in alkaline conditions due to a higher dissociation of the sulfate moieties, leading stronger substrate-particle repulsion.

The adhesion forces have found to be almost independent of the position on the nanohole array. Once a particle is in contact with the surface it adsorbs irreversibly. Based on these interaction profiles, we expect the long-range interaction forces to be the crucial key for a selective guidance of the particles into the holes.

A more detailed study of the local interaction forces is important for the rational understanding of the process of electrostatic focusing. Figure 6.3a shows a topography image resulting from a force mapping experiment.

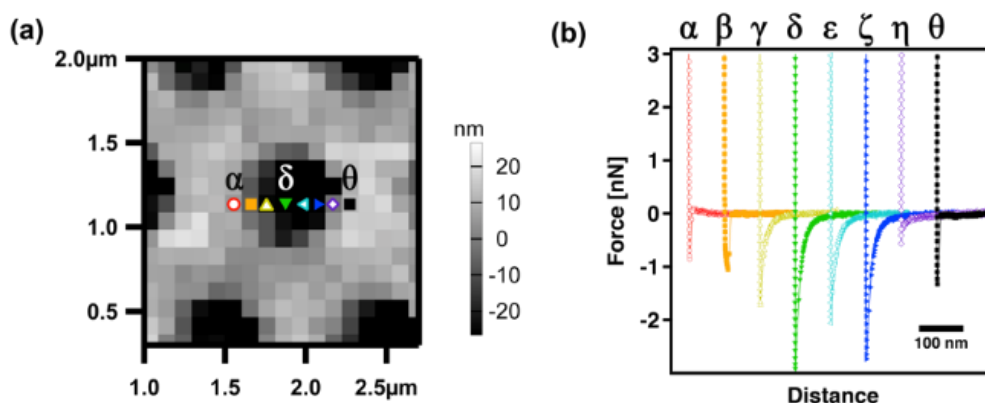


**Figure 6.3.** (a) Topography image resulting from the force mapping experiment at pH 4. The symbols indicate the positions of a line scan of force profiles across one hole. (b) Approaching force versus distance profiles corresponding to the symbols in (a).

The hexagonally patterned Au-mesh can be inferred from the topographic image with the black areas marking the glass surface. The thickness of the gold-mesh amounts to  $\sim 45$  nm. The different symbols mark the position of individual force profiles resulting in a cross-section over one nanohole. The corresponding approach part of the force profiles is depicted in Figure 6.3b. A clear trend of increasing attractive forces towards the center of the hole is observable. The attractive forces vanish at the edges and even turn repulsive on the Au-mesh. Since the effective apex diameter of the probe is comparable to the hole dimensions, the gradual transition of the interaction forces may be the result of mixed contributions from both the Au-mesh and the  $\text{NR}_4^+$ -glass. Minor deviations from the trend may be attributed to a certain sample roughness.

This line scan demonstrates that the particles will be exclusively attracted towards the glass surface, caused by the electrostatic interaction, which we refer to as electrostatic focusing. We want to stress that these experiments have been carried out on completely water-submersed substrates. Therefore, contributions from capillary or convective forces can be ruled out. Also hydrophobic contributions will not play a role due to the hydrophilic moieties on the Au-mesh (hydroxyl-terminated) and glass surface (quarternary-amine terminated).

Based on the AFM force mapping experiments, we can now predict the macroscopic adsorption behavior of negatively charged PS beads. In the following we will demonstrate that the particle immobilization can be tuned by pH and ionic strength, as well as the respective size ratios between particle, hole diameter, and lattice periodicity. Furthermore, we established a protocol allowing us to transfer this fully immersed system into the dry state.

### **Tuning by pH**

In Figure 6.4 the adsorption of PS spheres on functionalized Au nanomeshes is depicted in dependence of the pH value of the particle dispersion. The pH was adjusted to pH 5 and pH 10 with HCl and NaOH, respectively. For all experiments nanomeshes with a center-to-center distance of  $L_{h-h} = 1.04 \mu\text{m}$  and a hole diameter of  $d_h = 0.87 \mu\text{m}$  were used. The *in-situ* assembly dynamics of commercial fluorescent 606 nm PS particles into the nanomeshes can be monitored using confocal laser scanning microscopy. No further functionalization of the PS particles is necessary. A video showing the first 10 min of the assembly process for both pH values is shown in the SI. Figure 6.4a and b display off-equilibrium snapshots of the adsorbed particles (green) 10 min after the addition of the particle dispersion on the nanomesh at pH 5 and pH 10, respectively. A clear correlation between the pH value of the particle dispersion and the particle adsorption can be recognized. At pH 5 a fast adsorption of the negatively charged particles predominantly on the  $\text{NR}_4^+$ -functionalized glass surface can be observed with 26 % of the holes being occupied after 10 min. Due to the electrostatic repulsion of the like-charged particles in solution, no particle agglomeration is observed and further particles are repelled once a hole is occupied. Moreover, the irreversible nature of the adsorption onto the glass areas is visible in the video, which supports the mechanistic results of the colloidal probe measurements. In contrast, at pH 10 hardly any particle adsorption can be found, with less than 6 % occupied holes after 10 min. The few particles on the surface show a rather undefined adsorption behavior and no clear tendency towards the glass surface.

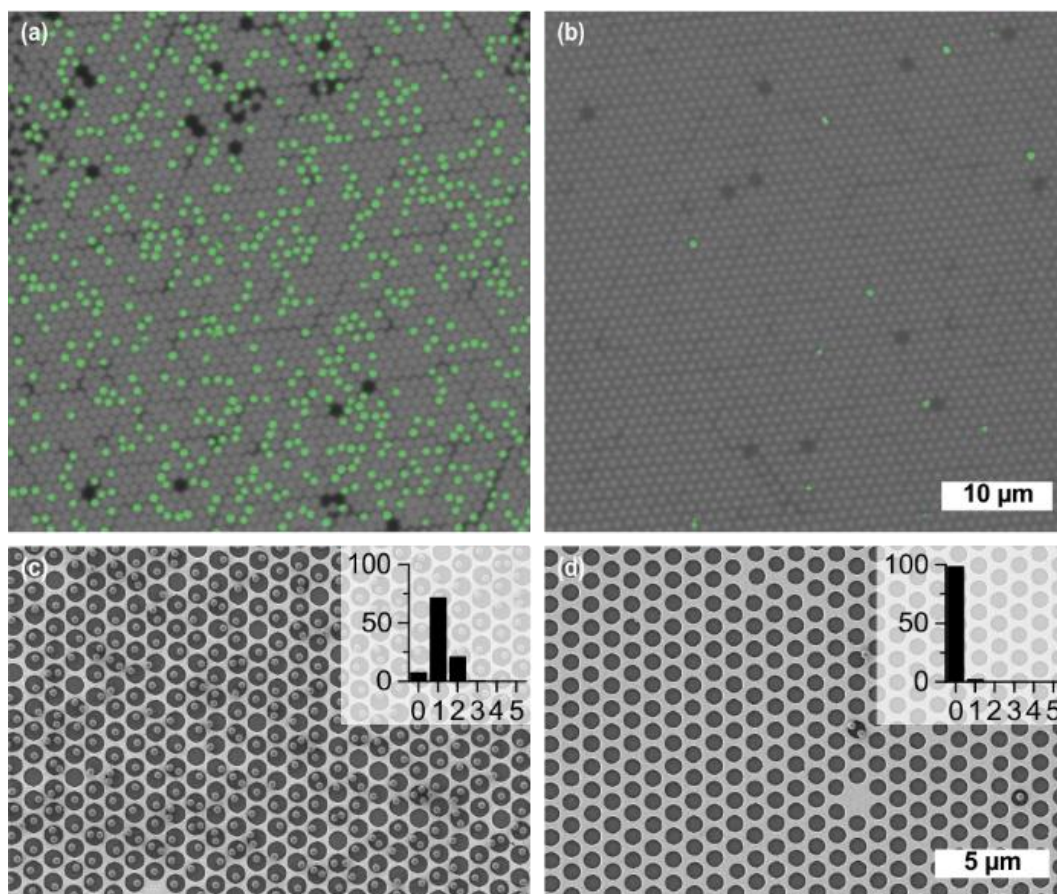


**Figure 6.4.** Dependence of particle adsorption on pH dependence. Top row: in-situ confocal laser scanning microscopy of fluorescent polystyrene spheres (green) with a diameter of 606 nm at pH 5 (a) and pH 10 (b) after 10 min. Bottom row: SEM micrographs of 320 nm negatively charged PS particles on Au nanomeshes at pH 5 (c) and pH 10 (d). Insets in (c) and (d) show the frequency distribution of the number of particles per hole in percent. Both experiments were carried out with  $1.04 \mu\text{m}$   $L_{h-h}$  and a hole diameter of  $\sim 0.87 \mu\text{m}$ .

This trend is consistent with the predictions from the force-distance measurements, which showed a repulsive force for both, the  $\text{NR}_4^+$ -functionalized glass and the hydroxy-functionalized Au surface at pH 10 resulting in no particle immobilization. At pH 4, however, the extraordinary long-ranged electrostatic attraction of the glass surface drives the particles into the nanomesh holes. The same behavior can be seen in SEM images of nanomeshes after 15 h immersion in a dispersion of monodisperse 320 nm PS particles at pH 5 (Figure 6.4c) and pH 10 (Figure 6.4d) and subsequent drying. After 15 h a plateau in the particle coverage is reached due to the particle-particle repulsion. Whereas the pH 5 sample is almost fully covered with selectively immobilized particles, practically no electrostatic adsorption takes place at pH 10. The sample prepared at pH 5 exhibits a high occupation rate with more than 92 % of the holes being occupied by one or more particles. Additionally, a high selectivity is discernible. Approximately 99 % of the immobilized particles are trapped on the glass

surface, which covers about 51.6 % of the surface. Since high concentrations of colloidal dispersions (6 wt%) were used for the colloidal assembly, this implies a self-quenching behavior of the particle adsorption process after the first particle layer. For pH 10 the repulsive surface potential results in a very low surface coverage of less than 3.3 particles per 100  $\mu\text{m}^2$ , which corresponds to only 2 % occupied holes.

The transfer of the assembled particle structure into the dry state requires tight control on the capillary forces during the transfer process. Otherwise, the colloidal pattern formed in the wet state can be disrupted by strong capillary forces acting on liquid bridges between adjacent particles. Therefore, the solvent is systematically exchanged to first ethanol and then hexane prior to the drying step.<sup>22,39</sup>

The spatial uniformity of the dried samples can be seen in Figure S6.1. Moreover, correlative optical microscopy and electron microscopy images of the 320 nm particles assembled at pH 5 are shown in Figure S6.2. The samples are uniformly covered on a macroscopic scale on the range of several  $\text{mm}^2$  without drying effects and particle clusters. The good control of the capillary forces during the drying procedure can be inferred from the spatially separated beads, even within one mesh in the Au grid. Many of such particle pairs are separated by less than 100 nm, yet, the strong adsorption to the glass surface prevented them from aggregating during drying. Thus, using an electrostatic adsorption mechanism instead of convective assembly,<sup>20</sup> a particle monolayer without direct interparticle contact even within the nanoholes is attained. The number of particles per hole for the corresponding sample is evaluated in the insets in Figure 6.4c and d. To check the reproducibility of our method, two samples were prepared separately at equal conditions and compared in Figure S6.3. Both, the variation of the average number of particles per hole at different spots on one sample as well as the variation on different samples lies within the standard deviation of one particular spot.

To expand the influence of the pH, additional samples were prepared at pH 3 (Figure S6.4a) and pH 12 (Figure S6.4b). pH 3 yields a nonselective adsorption of the particles onto the substrate. At this pH the repulsion of the Au surface is strongly reduced while the glass surface remains highly attractive. Therefore, the PS particles are strongly attracted towards the surface with approximately 36 % becoming immobilized on the Au surface. Concomitant with the reduced pH is a reduction of the Debye screening length of the particles, which results in a higher loading of the particles on the surface and a decreased interparticle distance compared to pH 5 (see Figure S6.5). Nevertheless, despite the high surface coverage no particle agglomeration but clearly separated spheres are noticeable. At pH 12 no significant difference can be seen compared to pH 10, with no adsorption being observable.

Overall, the choice of the pH of the particle dispersion is critical for the controlled immobilization. Weak acidic conditions are favorable to achieve high selectivity at a concomitantly high surface coverage.

### Tuning by ionic strength

To separately investigate the contribution of the Debye length without the influence of the pH, the ionic strength was varied by adding NaCl while pH 5 was kept constant. In Figure 6.5 the adsorption of 320 nm PS particles into the Au nanomeshes is displayed for NaCl concentrations of 1 mM (a), 10 mM (b) and 100 mM (c) and a constant assembly time of 15 h. Low magnification SEM images are depicted in Figure S6.6.

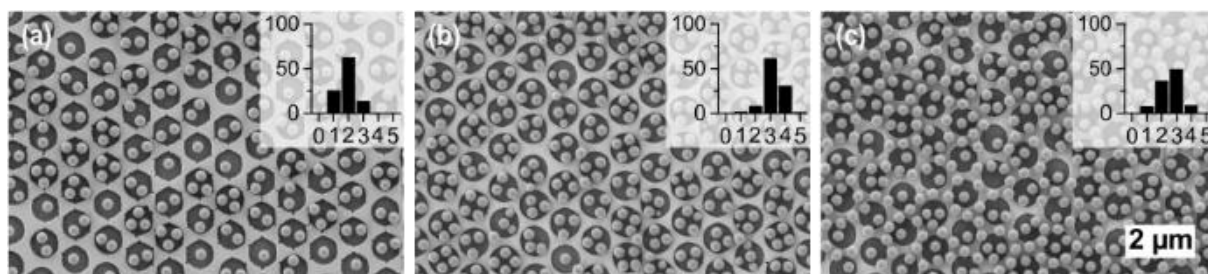


**Figure 6.5.** Dependence of the adsorption of 320 nm negatively charged PS particles on the NaCl salt concentration on Au nanomeshes with  $1.04 \mu\text{m}$   $L_{h-h}$  and a hole diameter of  $0.87 \mu\text{m}$ . NaCl concentrations of 1 mM (a), 10 mM (b) and 100 mM (c) were used. Insets show the frequency distribution of the number of particles per hole in percent.

For an ionic strength of 1 mM, the average number of trapped particles is increased to 1.88 particles per hole compared to 1.15 particles per hole for the sample with an ionic strength of  $< 0.1$  mM (Figure 6.4c). Nonetheless, a high selectivity is preserved with 99 % of the particles being adsorbed on the glass surface. Increasing the ionic strength to 10 mM, even 3.22 particles per hole can be reached, while the selectivity suffers only by 3 %. Further increasing the ionic strength to 100 mM, however, results in a complete loss of selectivity (55 % of particles adsorbed on glass) and a random sequential adsorption of the PS particles is obtained. This trend can be corroborated with the nearest neighbor distance ( $I_{\text{NND}}$ ) determined by the radial distribution functions, which correlates to the mutual distance between all trapped particles (Figure S6.7). Due to the increasing Debye screening, the  $I_{\text{NND}}$  slightly decreases for higher ionic strength from 447 nm for a salt concentration of less than 0.1 mM to 382 nm for 100 mM. Yet, the particles are clearly separated and no agglomeration is visible even for high ionic strengths. One can also infer the selectivity of the adsorption process from the RDF profiles by the presence of clear correlation peaks at the positions corresponding to the hexagonally ordered

nanomesh indicated by the vertical lines. The peaks are being smeared out with increasing ionic strength.

A summary regarding the selectivity and surface coverage of the particle adsorption for the case of 320 nm particles in 0.87  $\mu\text{m}$  holes at various pH values and salt concentrations is given in Figure 6.6.

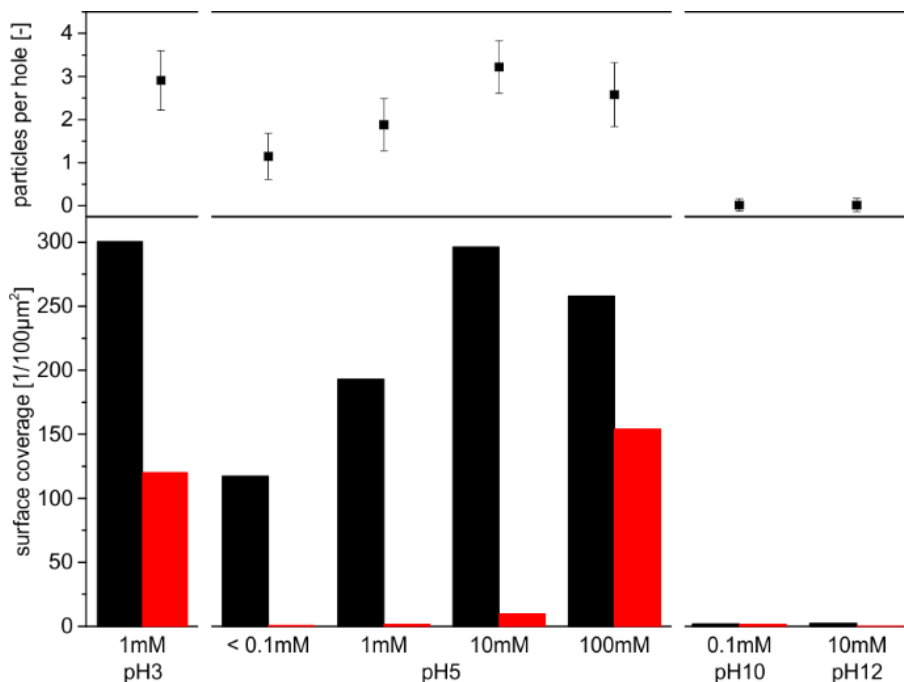


**Figure 6.6.** Summary of the controlled deposition of 320 nm negatively charged PS particles on Au nanomeshes with 1.04  $\mu\text{m}$   $L_{h-h}$  and a hole diameter of 0.87  $\mu\text{m}$ . The area fraction of glass is 51.6 %. Average number of particles per hole (top) and surface coverage (bottom) of the samples in dependence of the different pH values and the overall ionic strengths. Red: particles on Au, black: particles on glass.

Increasing the ionic strength decreases the Debye screening length, and consequently leads to a higher amount of particles, which can be fitted into one single glass mesh. However, the selectivity is destroyed by too high salt concentrations (100 mM). Meanwhile, changing the pH drastically reduces the mutual electrostatic interaction. The selectivity is already lost at an HCl concentration of 1 mM (pH3). Higher pH leads to strong repulsive forces on Au and glass resulting in almost no particle deposition.

### Tuning by geometry

As the underlying nanomesh and the adsorbed particles are prepared independently, both the size of the particles and the geometry of the hole array can be tuned individually. Nevertheless, the size of the particles relative to the geometrical parameters of the nanomesh has a significant

influence on the adsorption process. In this case, we kept  $L_{h-h} = 1.04 \mu\text{m}$  and  $d_h = 0.87 \mu\text{m}$  of the nanomesh constant and varied the particle diameter from 170 nm up to 1500 nm (see Figure S6.9 for nanomeshes with different  $L_{h-h}$  and  $d_h$ ). pH 5 was used for the assembly as the particle dispersions in MilliQ water lead to pH 5 without the addition of HCl or NaOH. Thus the Debye lengths are not reduced by any electrolyte. All particles under investigation exhibited similar surface chemistry (see Table 6.1 for zeta potential measurements). SEM images of the obtained structures are depicted in Figure 6.7. Overview SEM images are depicted in Figure S6.8.

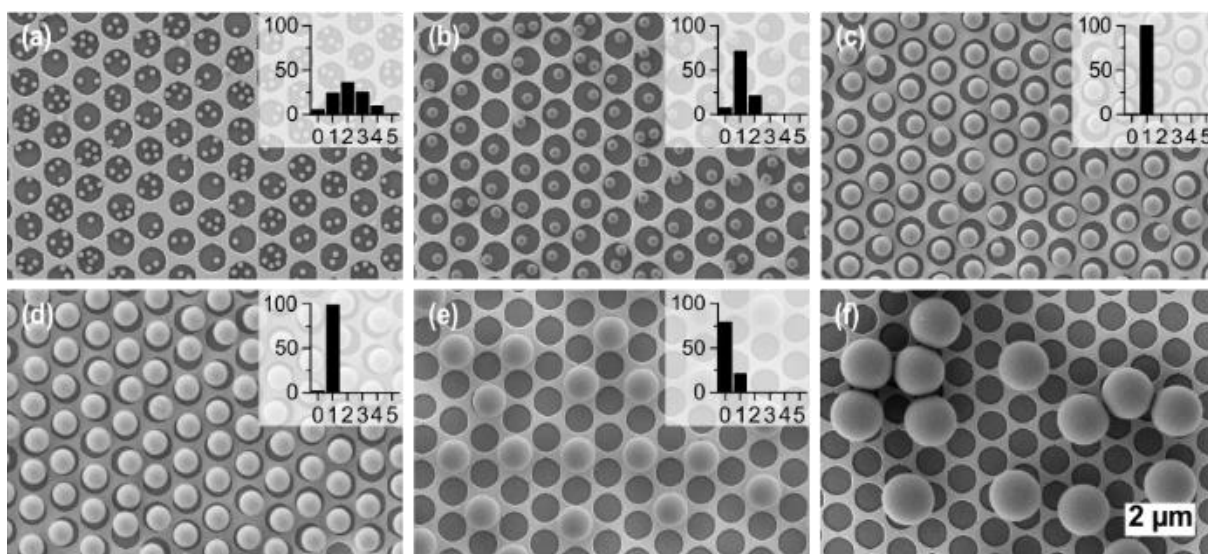


**Figure 6.7.** PS particles of different diameter immobilized in nanohole arrays with  $d_h = 0.87 \mu\text{m}$  and  $L_{h-h} = 1.04 \mu\text{m}$ . PS particles have a diameter of (a) 166 nm (b) 320 nm (c) 570 nm (d) 740 nm (e) 1040 nm, and (f) 1500 nm. Insets show the frequency distribution of the number of particles per hole in percent.

A highly controlled adsorption is feasible over a wide range of particle diameters with high regioregularity up to a particle diameter of 1040 nm. As the topographical contribution of the nanomesh can be neglected with respect to  $d_h$ , a highly selective adsorption of nearly 100 % is possible even for particle diameters that exceed  $d_h$  (Figure 6.7e). Nonetheless, for particles with a diameter much larger than  $d_h$  (Figure 6.7f) a loss of regularity is observed. This can be due to gravitational forces, which are more critical for larger particles. Moreover, as the particle dimensions are much greater than the surface structure, the particles may not recognize a strong chemical contrast between the  $\text{NR}_4^+$ -functionalized glass surface and the hydroxy-functionalized Au surface, reducing the possibility for electrostatic focusing.

The number of particles immobilized per hole is evaluated in the insets of Figure 6.7. In Figure 6.8a the average number of particles per hole is given as a function of the particle diameter.

Apparently, single loading of the holes is only possible in a small size range between  $0.5 d_h$  and  $d_h$ . Accordingly, for the particles with 570 nm (Figure 6.7c) and 740 nm (Figure 6.7d) excellent hole occupation with single spheres surpassing 99 % is achieved. In contrast to previous works,<sup>27</sup> we constricted the pattern size to the sub micrometer dimension allowing the production of non-close-packed particle arrays with interparticle distances controlled by the template. Below the threshold of  $0.5 d_h$  multiple deposition of particles per hole is noticeable, with 1.15 particles per hole for a particle diameter of 320 nm and 2.11 particles per hole for a particle diameter of 166 nm. Furthermore, particles below this threshold will always exhibit a more or less broad distribution of particles trapped per hole, depending on the ionic strength of the particle dispersion as discussed above.

When the particle diameter exceeds  $d_h$  and is in the range of the lattice parameter of the nanomesh, the adsorption process is constricted by the interparticle electrostatic repulsion. Particles with a diameter of 1040 nm (Figure 6.7e), which is equal to  $L_{h-h}$ , do not occupy adjacent holes as this would imply unfavorable direct contact of the particles. This results in a theoretical maximum of 0.25 particles per hole assuming that particles cannot be trapped in adjacent spots once a particle is immobilized in one hole. In practice, a number of approximately 0.21 particles per hole is reached as the random fashion of the adsorption process is taken into account. To accomplish an occupation rate approaching 100 % with these large spheres, however,  $L_{h-h}$  has to be increased (Figure S6.9c).

For a quantitative analysis of the obtained, two-dimensional colloidal patterns, the center-of-mass coordinates of the adsorbed particles were determined in ImageJ and used to calculate the radial distribution function  $g(r)$  (Figure 6.8b-g). This function displays the frequency of the occurring particle-particle distances. The presence of defined peaks up to high distances corresponding to the most likely distances occurring in the pattern indicates a system with good long-range order. Assumptions about the short-range order can be made by evaluating the position and width of the first peak ( $l_{\text{NND}}$ ). The solid ticks indicate the peak positions of the given ideal hexagonal structure of the underlying nanomesh with the first tick representing  $L_{h-h}$ . For all particles up to a diameter of 1040 nm short-range order is detectable, with a well-defined  $l_{\text{NND}}$  and a low value of  $g(r)$  at  $d_p$  (dashed line) indicating the absence of particle agglomeration. Moreover, long-range order is visible for all particles except the 1500 nm particles. The predominant occupation of the glass surface results in clear peaks occurring at the distances corresponding to the hexagonal lattice of the hole array.

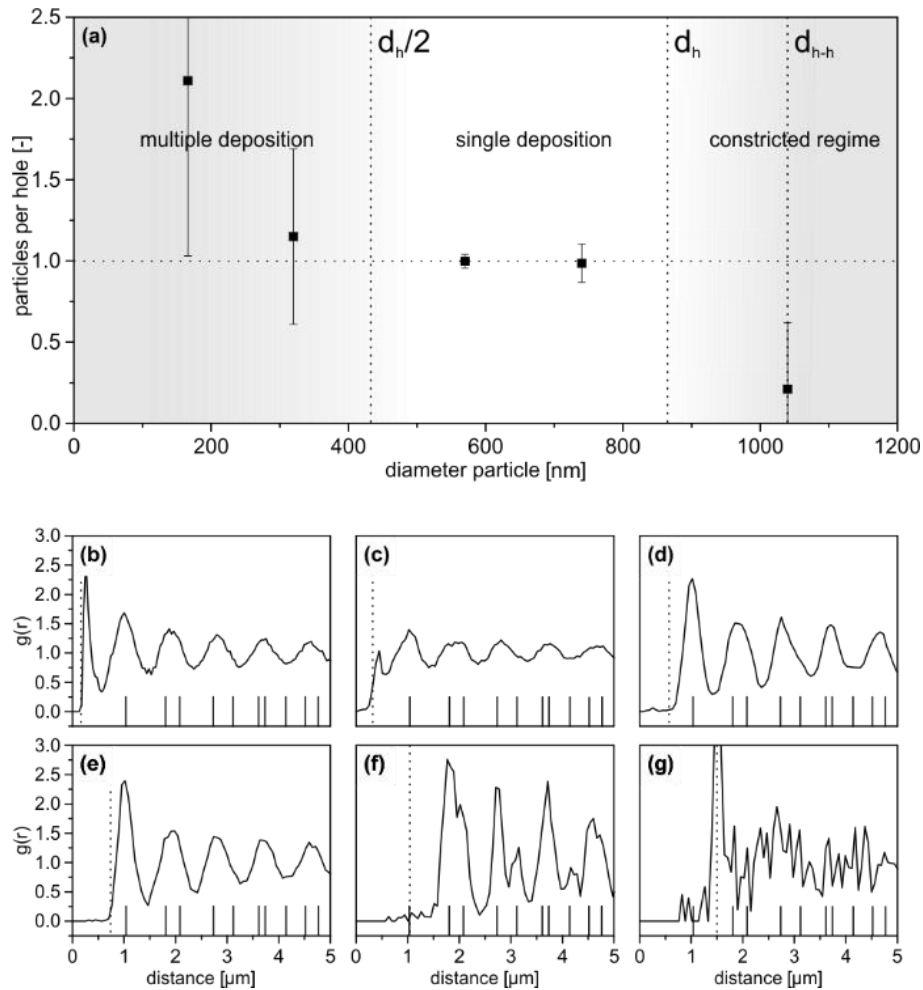


**Figure 6.8.** a) Particle coverage as a function of particle diameter. Vertical dashed lines mark important geometric transition regions. Radial distribution functions  $g(r)$  for various particles immobilized in a nanomesh with  $1.04 \mu\text{m}$   $L_{h-h}$  and hole diameter  $d_h = 0.87 \mu\text{m}$ : b) 166 nm c) 320 nm d) 570 nm e) 740 nm f) 1040 nm g) 1500 nm. The dotted lines indicate the particle diameter, the solid ticks indicate the  $g(r)$  of the underlying Au-nanomesh.

The particles with a diameter of 166 nm (Figure 6.8b) and 320 nm (Figure 6.8c) exhibit an  $l_{\text{NND}}$  of 270 nm and 447 nm, respectively, which is smaller than  $L_{h-h}$  but greater than  $d_p$  as multiple particles are trapped per hole. For the particles diameters of 570 nm (Figure 6.8d) and 740 nm (Figure 6.8e)  $g(r)$  is congruent with the  $g(r)$  of the hole array with the  $l_{\text{NND}}$  equal  $L_{h-h}$ . The relatively high standard deviation of the peaks despite of the single loading of the holes is given by the random, non-centrosymmetric position of the immobilized spheres.

No occupation of  $L_{h-h}$  is noticeable for a particle diameter of 1040 nm (Figure 6.8f). Instead,  $l_{\text{NND}}$  of the particles is present at the preferred second distance of the nanomesh lattice. However, a particular well-defined long-range order is observed at higher distances due to the uniformly centered position of the particles.

A different case is discernible for the particle diameter of 1500 nm (Figure 6.8g). The maximum of  $g(r)$  at  $d_p$  correlates to the presence of direct interparticle contacts. Furthermore, no long-range order is inferable, which associates with random sequential adsorption.

Finally, the adsorption process is highly reproducible not only for a broad range of particle diameters but universally applicable for negatively charged polymer colloids. This generality of the method is depicted in Figure S6.10 for colloidal PMMA particles with a diameter of 260 nm. As the self-assembly process simply relies on electrostatic interactions, the concept can be readily conveyed to arbitrary negatively stabilized colloids. Therefore, a sophisticated surface functionalization of the particles is not necessary.

### 6.3 Conclusion

In summary, we investigated the controlled placement of polystyrene particles into Au nanohole arrays by electrostatic modelling of the substrate. An orthogonal functionalization of gold and glass is exploited to introduce a selective electrostatic attraction of the particles towards the glass surface. In this study, we demonstrate the highly reproducible immobilization of polystyrene particles over a broad range of particle diameters ranging from 170 nm to 1040 nm. Tailoring the ratio of the diameter of the particles and the geometric parameter of the nanohole arrays enables one to switch between different adsorption regimes, with multiple particles per hole or highly defined single particle adsorption.

Furthermore, we found that the tuning of the experimental parameters such as pH and ionic strength during the assembly process is important to control the adsorption pattern. Colloidal probe atomic force microscopy revealed a high sensitivity of the effective interaction potentials towards the pH. The attractive potential of the  $\text{NR}_4^+$ -functionalized glass can be switched off when increasing the pH from pH 3 to pH 10 giving a uniform repulsive potential and an impeded particle adsorption. In addition, the ionic strength of the particle dispersion determines the Debye lengths of the electrostatic forces deriving from the nanomesh and the particles. Thus, the average number of particles in one hole can be controlled by ionic strength maintaining a good selectivity up to 10 mM NaCl. Higher salt concentrations result in random adsorption of the particles. By adjusting an ionic strength of 10 mM the number of particles per hole was nearly tripled.

This selective particle deposition occurs foremost in the dispersed liquid state without the aid of topography, convective or capillary forces. Confocal microscopy hints towards an

irreversible adsorption of the particles onto the glass surface, which is supported by adhesive profiles in the retracting curves of colloidal probe force measurements. We could successfully transfer this immersed structure into the dry state by exchanging the dispersion medium and thereby controlling the capillary forces. Finally, this structuring concept works universally for polymer particles with a negative surface charge.

To our knowledge, this is the first paper, in which the immobilization of particles is shown in nanohole arrays made by bottom-up nanosphere lithography. The electrostatic adsorption allows to direct particles into hole arrays with very shallow topographic contrast, which are not accessible with convective or capillary particle assembly. This represents a simple and versatile route for the assembly of particles on optically active metal substrates, which might be utilized to create complex plasmonic waveguide structures or sensing devices in the future.

#### 6.4 Experimental Section

**Materials:** Polystyrene particles were purchased at *Microparticles GmbH* (Berlin) or synthesized using emulsifier free emulsion polymerization. N-Trimethoxysilylpropyl-N,N,N-trimethylammonium chloride (*ABCR GmbH*, Karlsruhe, Germany, 50% in methanol), 3-Mercapto-1-propanol (*ABCR GmbH*, Karlsruhe, Germany, > 96%), Sodium Dodecyl Sulfate (*Serva Electrophoresis GmbH*, Heidelberg, Germany), Hellmanex III (*Hellma GmbH*, Müllheim, Germany), ethanol (*Sigma-Aldrich GmbH*, Munich, Germany,  $\geq 99.8\%$ ), *n*-hexane (*VWR International GmbH*, Darmstadt, Germany, > 98%), NaCl (*Sigma-Aldrich GmbH*, Munich, Germany,  $\geq 99.0\%$ ), NaOH (*Sigma-Aldrich GmbH*, Munich, Germany,  $\geq 98\%$ ), ammonium hydroxide solution (*Sigma-Aldrich GmbH*, Munich, Germany, 28.0-30.0%), HCl (*Grüssing GmbH*, Filsum, Germany, 1 M) were used as received. Standard microscopy slides (*Menzel*, Braunschweig, Germany) were used.

**Fabrication of Au nanomeshes:** Monolayers were prepared according to the procedure of Retsch et al.<sup>40</sup> In brief cationically functionalized glass slides were spin-cast with a 3 wt% particle dispersion ( $1.04 \pm 0.04 \mu\text{m}$  diameter) at a speed of 4000 rpm. Freely floating monolayers were assembled at an air/water interface by slow immersion of the particle coated glass substrate into a 0.1 mM SDS solution in MilliQ water. The aqueous phase was adjusted to pH 12 by adding a few drops of  $\text{NH}_3$ . The floating monolayer was finally transferred to a glass substrate and dried in air. The prepared monolayers were etched in a plasma reactor MiniFlecto (Plasma Technology GmbH, Herrenberg, Germany) with 75 % argon and 25 %

oxygen at 80 W power at a pressure of 0.14 mbar. Etching was conducted for 20 min in order to obtain non-close-packed monolayers with particles of 870nm diameter. A 3 nm chromium layer and 50 nm Au were deposited using a Balzers BA360 thermal evaporation chamber. The layer thickness was monitored via a SQM 160 microbalance (Sigma Instruments, Schaefer Technologie GmbH). The particles were removed using Scotch® tape (3M) giving the nanohole arrays. The Au substrates were cleaned for 10 min in an ultrasonic bath with a 2 % aqueous Hellmanex (Hellma GmbH, Mühlheim, Germany) solution in MilliQ water. The surfactant was extensively rinsed off with MilliQ water and the substrates were placed in the ultrasonic bath in ethanol for 10 minutes and dried with compressed air.

**Chemical functionalization of Au nanomeshes:** After hydrophilization in 100 % oxygen plasma at 0.2 mbar for 30 s the nanohole arrays were immersed in a 1 vol% solution of N-Trimethoxysilylpropyl-N,N,N-trimethylammonium chloride in MilliQ water for 1 hour. Excess silane was rinsed off with MilliQ water and the substrates were placed in a 1 vol% solution of 3-Mercapto-1-propanol in ethanol for 2 hours. After rinsing with ethanol the substrates were dried at 90 °C for 1 hour.

**Particle immobilization on nanomeshes:** The nanohole arrays were placed in the particle dispersion for at least 2 hours. The pH was adjusted with HCl and NaOH, respectively. To remove excess particles, the supernatant was repeatedly diluted with MilliQ water. Care was taken that the substrates do not run dry during this rinsing procedure. Finally, the solvent was exchanged consecutively with ethanol and hexane and the sample was dried in air.

**Characterization:** Confocal Laser Scanning Microscopy was performed on a TSC SP8 STED 3x (Leica) using an oil immersion objective (63x augmentation), a 514 nm laser for excitation and 4 frames per second. SEM images were taken on a LEO 1530 Gemini Field Emission SEM (Carl Zeiss AG, Oberkochen, Germany) at 3.00 kV. The images were evaluated with the software ImageJ.<sup>41</sup> Particle positions were extracted using the “Find Maxima” tool and the radial distribution functions were calculated using a self-written software (details are given in the supporting information). For the statistical analysis the occupation of at least 450 holes was evaluated for each sample, i.e. 1000 – 2000 particles were analyzed for the 151 nm – 1040 nm particles. 406 particles were analyzed for the particles with a diameter of 1500 nm (random adsorption). For the particles assembled at pH 10 and pH 12, 85 and 53 particles were counted, respectively.

The preparation of colloidal probes used here, has been described previously.<sup>38,42</sup> Tipless AFM cantilevers (NSC-12, MikroMasch, Tallinn, Estonia) were cleaned with a series of solvents (ethanol, water, acetone) directly before preparation. A single polystyrene particle with an

average diameter of 3.00  $\mu\text{m}$  (micro particles, Berlin, Germany) was attached to the end of a tipless cantilever by means of a micromanipulator (STM3, Märzhäuser, Wetzlar, Germany), which was mounted next to a fixed stage optical microscope (Axio Examiner D1, Zeiss, Jena, Germany). The particle was immobilized by UV-curable glue (Norland Optical Adhesive 63, Norland Products, Cranbury, NJ) that was cured directly on the microscope stage by means of the mercury lamp illumination. The spring constants of the cantilevers has been determined previously by the thermal noise method,<sup>43</sup> i.e. before gluing the colloidal particles onto the lever. Measurements of interaction forces were performed with an AFM equipped with a closed-loop scanner for all three axes (MFP-3D, Asylum Research, Santa Barbara, CA). The AFM was placed in an acoustic shielding. Force curves were acquired with a cantilever velocity of about 200 nm/s and a maximum loading force of about 5 nN. The surface topography was calculated from the set of consecutive force curves acquired on a grid with 3x3  $\mu\text{m}$  size consisting of 30x30 points, which results in a surface map where the single data points have a separation of 100 nm. The measured deflection versus displacement curves were converted to force versus distance curves by means of a set of custom evaluation procedure written in IGOR PRO (Wavemetrics, Portland, OR).<sup>42,44</sup> The direct force measurements were performed in aqueous solution at pH 4 and 10 and a total ionic strength of 0.2 mM.e.

### **Acknowledgements**

This work was funded by the German Research Foundation (DFG) by the SFB840. C.S. acknowledges support from the Elite Network Bavaria (ENB). The experimental support by Tanja Feller is appreciated. M.R. acknowledges support by the VCI. The authors thank Fabian Nutz for the particle synthesis, Pia Ruckdeschel for correlative SEM measurements, Dr. Martin Dulle for help with the  $g(r)$  calculations and Dr. Beate Förster and Martina Heider from the Bayreuth Institute of Macromolecular Research (BIMF) for their support using the scanning electron microscopy facilities. Prof. Stephan Förster is acknowledged for providing access to the confocal laser scanning microscope. Microparticles GmbH is acknowledged for providing special PS microbeads for the colloidal probe preparation.

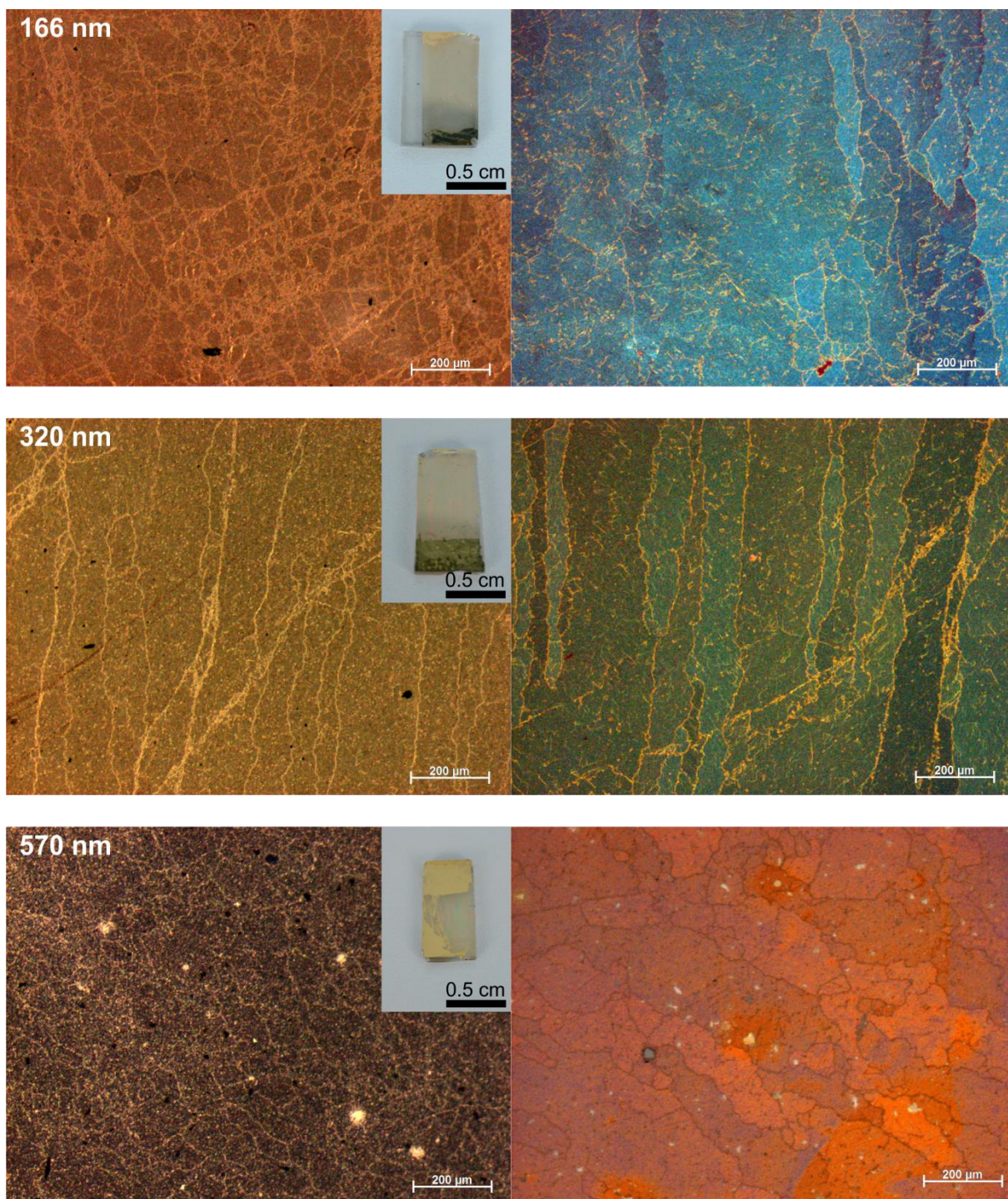
**References**

1. Velev, O. D. & Gupta, S. Materials Fabricated by Micro- and Nanoparticle Assembly – The Challenging Path from Science to Engineering. *Adv. Mater.* **21**, 1897-1905 (2009).
2. Vogel, N., Retsch, M., Fustin, C. A., Del Campo, A. & Jonas, U. Advances in Colloidal Assembly: The Design of Structure and Hierarchy in Two and Three Dimensions. *Chem. Rev.* **115**, 6265-6311 (2015).
3. Zhang, J., Li, Y., Zhang, X. & Yang, B. Colloidal Self-Assembly Meets Nanofabrication: From Two-Dimensional Colloidal Crystals to Nanostructure Arrays. *Adv. Mater.* **22**, 4249-4269 (2010).
4. Harun-Ur-Rashid, M., Bin Imran, A., Seki, T., Ishii, M., Nakamura, H. & Takeoka, Y. Angle-Independent Structural Color in Colloidal Amorphous Arrays. *Chemphyschem* **11**, 579-583 (2010).
5. Vogel, N. *et al.* Color from hierarchy: Diverse optical properties of micron-sized spherical colloidal assemblies. *Proc Natl Acad Sci U S A* (2015).
6. Nutz, F. A., Ruckdeschel, P. & Retsch, M. Polystyrene Colloidal Crystals: Interface Controlled Thermal Conductivity in an Open-Porous Mesoparticle Superstructure. *J. Colloid Interface Sci.* **457**, 96-101 (2015).
7. Stelling, C., Bernhardt, C. & Retsch, M. Subwavelength Etched Colloidal Monolayers: A Model System for Tunable Antireflective Coatings. *Macromol. Chem. Phys.* **216**, 1682-1688 (2015).
8. Vogel, N., Goerres, S., Landfester, K. & Weiss, C. K. A Convenient Method to Produce Close- and Non-close-Packed Monolayers using Direct Assembly at the Air-Water Interface and Subsequent Plasma-Induced Size Reduction. *Macromol. Chem. Phys.* **212**, 1719-1734 (2011).
9. vanBlaaderen, A., Ruel, R. & Wiltzius, P. Template-directed colloidal crystallization. *Nature* **385**, 321-324 (1997).
10. Zhang, J., Alsayed, A., Lin, K. H., Sanyal, S., Zhang, F., Pao, W.-J., Balagurusamy, S. K., Heiney, P. A. & Yodh, A. G. Template-directed convective assembly of three-dimensional face-centered-cubic colloidal crystals. *Appl. Phys. Lett.* **81**, 3176-3178 (2002).
11. Yin, Y. D., Lu, Y., Gates, B. & Xia, Y. N. Template-assisted self-assembly: A practical route to complex aggregates of monodispersed colloids with well-defined sizes, shapes, and structures. *J. Am. Chem. Soc.* **123**, 8718-8729 (2001).
12. Müller, M., Karg, M., Fortini, A., Hellweg, T. & Fery, A. Wrinkle-assisted linear assembly of hard-core/soft-shell particles: impact of the soft shell on the local structure. *Nanoscale* **4**, 2491-2499 (2012).
13. Li, X., Wu, Y., Hang, L., Men, D., Cai, W. & Li, Y. Aligned gold nanobowl arrays: their fabrication, anisotropic optical response and optical grating applications. *J. Mater. Chem. C* **3**, 51-57 (2015).
14. Allard, M., Sargent, E. H., Lewis, P. C. & Kumacheva, E. Colloidal Crystals Grown on Patterned Surfaces. *Adv. Mater.* **16**, 1360-1364 (2004).
15. Sharma, V., Xia, D., Wong, C. C., Carter, W. C. & Chiang, Y.-M. Templated self-assembly of non-close-packed colloidal crystals: Toward diamond cubic and novel heterostructures. *J. Mater. Res.* **26**, 247-253 (2011).
16. Mishchenko, L., Hatton, B., Kolle, M. & Aizenberg, J. Patterning Hierarchy in Direct and Inverse Opal Crystals. *Small* **8**, 1904-1911 (2012).
17. Bitai, I., Yang, J. K., Jung, Y. S., Ross, C. A., Thomas, E. L. & Berggren, K. K. Graphoepitaxy of self-assembled block copolymers on two-dimensional periodic patterned templates. *Science* **321**, 939-943 (2008).

18. Ozin, G. A. & Yang, S. M. The race for the photonic chip: Colloidal crystal assembly in silicon wafers. *Adv. Funct. Mater.* **11**, 95-104 (2001).
19. Hoogenboom, J., van Langen-Suurling, A., Romijn, J. & van Blaaderen, A. Hard-Sphere Crystals with hcp and Non-Close-Packed Structure Grown by Colloidal Epitaxy. *Phys. Rev. Lett.* **90** (2003).
20. Malaquin, L., Kraus, T., Schmid, H., Delamarche, E. & Wolf, H. Controlled particle placement through convective and capillary assembly. *Langmuir* **23**, 11513-11521 (2007).
21. Aizenberg, J., Braun, P. V. & Wiltzius, P. Patterned colloidal deposition controlled by electrostatic and capillary forces. *Phys. Rev. Lett.* **84**, 2997-3000 (2000).
22. Isa, L., Kumar, K., Müller, M., Grolig, J., Textor, M. & Reimhult, E. Particle lithography from colloidal self-assembly at liquid-liquid interfaces. *ACS Nano* **4**, 5665-5670 (2010).
23. Adamczyk, Z. & Warszyński, P. Role of electrostatic interactions in particle adsorption. *Adv. Colloid Interface Sci.* **63**, 41-149 (1996).
24. Semmler, M., Mann, E. K., Rička, J. & Borkovec, M. Diffusional Deposition of Charged Latex Particles on Water–Solid Interfaces at Low Ionic Strength. *Langmuir* **14**, 5127-5132 (1998).
25. Tien, J., Terfort, A. & Whitesides, G. M. Microfabrication through Electrostatic Self-Assembly. *Langmuir* **13**, 5349-5355 (1997).
26. Chen, K. M., Jiang, X., Kimerling, L. C. & Hammond, P. T. Selective Self-Organization of Colloids on Patterned Polyelectrolyte Templates. *Langmuir* **16**, 7825-7834 (2000).
27. Jonas, U., del Campo, A., Krüger, C., Glasser, G. & Boos, D. Colloidal assemblies on patterned silane layers. *Proc. Natl. Acad. Sci. U.S.A.* **99**, 5034-5039 (2002).
28. Lalander, C. H., Zheng, Y., Dhuey, S., Cabrini, S. & Bach, U. DNA-directed self-assembly of gold nanoparticles onto nanopatterned surfaces: controlled placement of individual nanoparticles into regular arrays. *ACS Nano* **4**, 6153-6161 (2010).
29. Zheng, Y., Lalander, C. H., Thai, T., Dhuey, S., Cabrini, S. & Bach, U. Gutenberg-style printing of self-assembled nanoparticle arrays: electrostatic nanoparticle immobilization and DNA-mediated transfer. *Angew. Chem. Int. Ed. Engl.* **50**, 4398-4402 (2011).
30. Yang, S.-M., Jang, S. G., Choi, D.-G., Kim, S. & Yu, H. K. Nanomachining by colloidal lithography. *Small* **2**, 458-475 (2006).
31. Morfa, A. J., Akinoglu, E. M., Subbiah, J., Giersig, M. & Mulvaney, P. Transparent metal electrodes from ordered nanosphere arrays. *J. Appl. Phys.* **114**, 054502 (2013).
32. Yu, Y. & Zhang, G. in *Updates in Advanced Lithography*. (ed Sumio Hosaka) Ch. 1, 3-34 (InTech, 2013).
33. Burmeister, F., Schäfle, C., Matthes, T., Böhmisch, M., Boneberg, J. & Leiderer, P. Colloid monolayers as versatile lithographic masks. *Langmuir* **13**, 2983-2987 (1997).
34. Xia, Y. N., Rogers, J. A., Paul, K. E. & Whitesides, G. M. Unconventional methods for fabricating and patterning nanostructures. *Chem. Rev.* **99**, 1823-1848 (1999).
35. Kappl, M. & Butt, H.-J. The Colloidal Probe Technique and its Application to Adhesion Force Measurements. *Part. Part. Syst. Char.* **19**, 129 (2002).
36. Maroni, P., Ruiz-Cabello, F. J. & Tiraferri, A. Studying the role of surface chemistry on polyelectrolyte adsorption using gold-thiol self-assembled monolayer with optical reflectivity. *Soft Matter* **10**, 9220-9225 (2014).
37. Kreuzer, H. J., Wang, R. L. & Grunze, M. Hydroxide ion adsorption on self-assembled monolayers. *J. Am. Chem. Soc.* **125**, 8384-8389 (2003).

38. Kuznetsov, V. & Papastavrou, G. Ion Adsorption on Modified Electrodes as Determined by Direct Force Measurements under Potentiostatic Control. *The Journal of Physical Chemistry C* **118**, 2673-2685 (2014).
39. Ray, M. A. & Jia, L. Micropatterning by Non-Densely Packed Interfacial Colloidal Crystals. *Adv. Mater.* **19**, 2020-2022 (2007).
40. Retsch, M., Zhou, Z., Rivera, S., Kappl, M., Zhao, X. S., Jonas, U. & Li, Q. Fabrication of Large-Area, Transferable Colloidal Monolayers Utilizing Self-Assembly at the Air/Water Interface. *Macromol. Chem. Phys.* **210**, 230-241 (2009).
41. Rasband, W. S. U. S. National Institutes of Health. *ImageJ*, <http://imagej.nih.gov/ij/> (1997-2015).
42. Rentsch, S., Pericet-Camara, R., Papastavrou, G. & Borkovec, M. Probing the validity of the Derjaguin approximation for heterogeneous colloidal particles. *Phys. Chem. Chem. Phys.* **8**, 2531-2538 (2006).
43. Hutter, J. L. & Bechhoefer, J. Calibration of atomic-force microscope tips. *Rev. Sci. Instrum.* **64**, 1868 (1993).
44. Pericet-Camara, R., Papastavrou, G., Behrens, S. H. & Borkovec, M. Interaction between Charged Surfaces on the Poisson–Boltzmann Level: The Constant Regulation Approximation. *J. Phys. Chem. B* **108**, 19467-19475 (2004).

## 6.5 Supporting Information



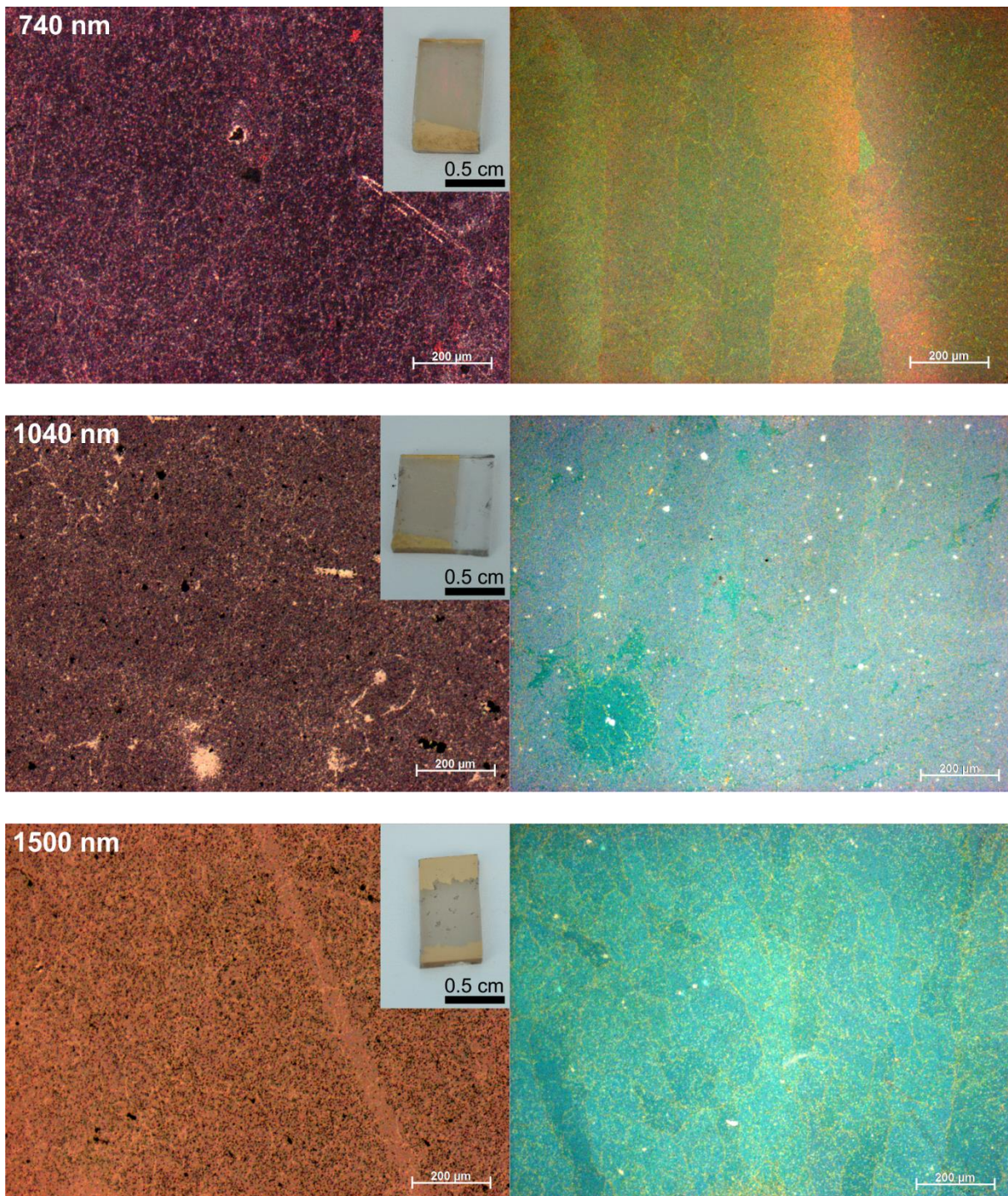


**Figure S6.1.** Optical microscopy. Bright field (left) and dark field (right) images of PS particles of different diameter immobilized in nanohole arrays with  $d_h = 0.87 \mu\text{m}$  and  $L_{h-h} = 1.04 \mu\text{m}$ . The diameter of the PS particles is indicated at the top left. Insets show a photograph of the samples.

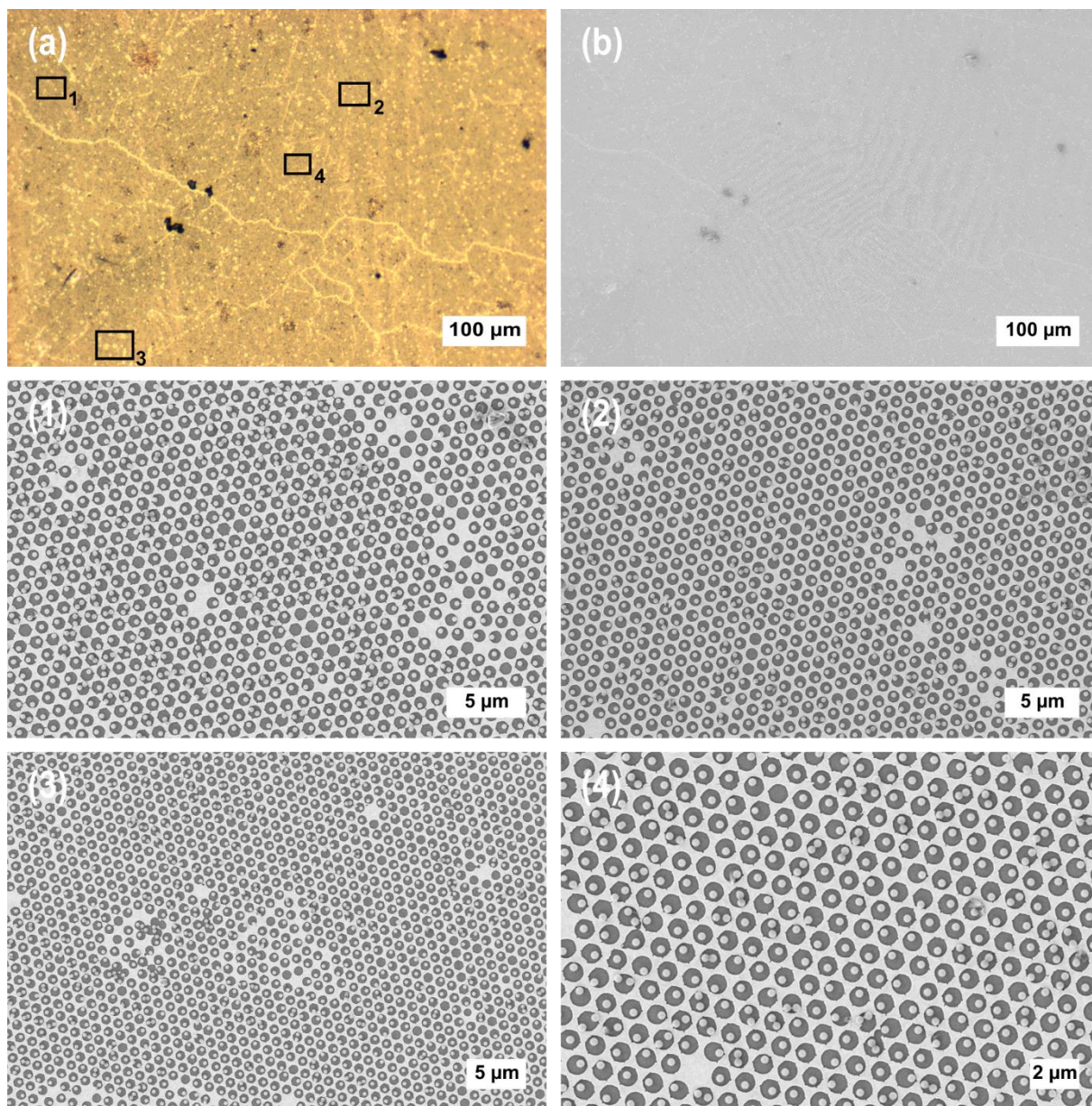


**Figure S6.2.** Correlative optical and electron microscopy of 320nm particles adsorbed at pH 5 in a nanohole array with  $d_h = 0.87 \mu\text{m}$  and  $L_{h-h} = 1.04 \mu\text{m}$ . (a) Optical microscopy and (b) electron microscopy showing the same sample section. (1) – (4) Higher magnification images of the sample spots marked in (a).

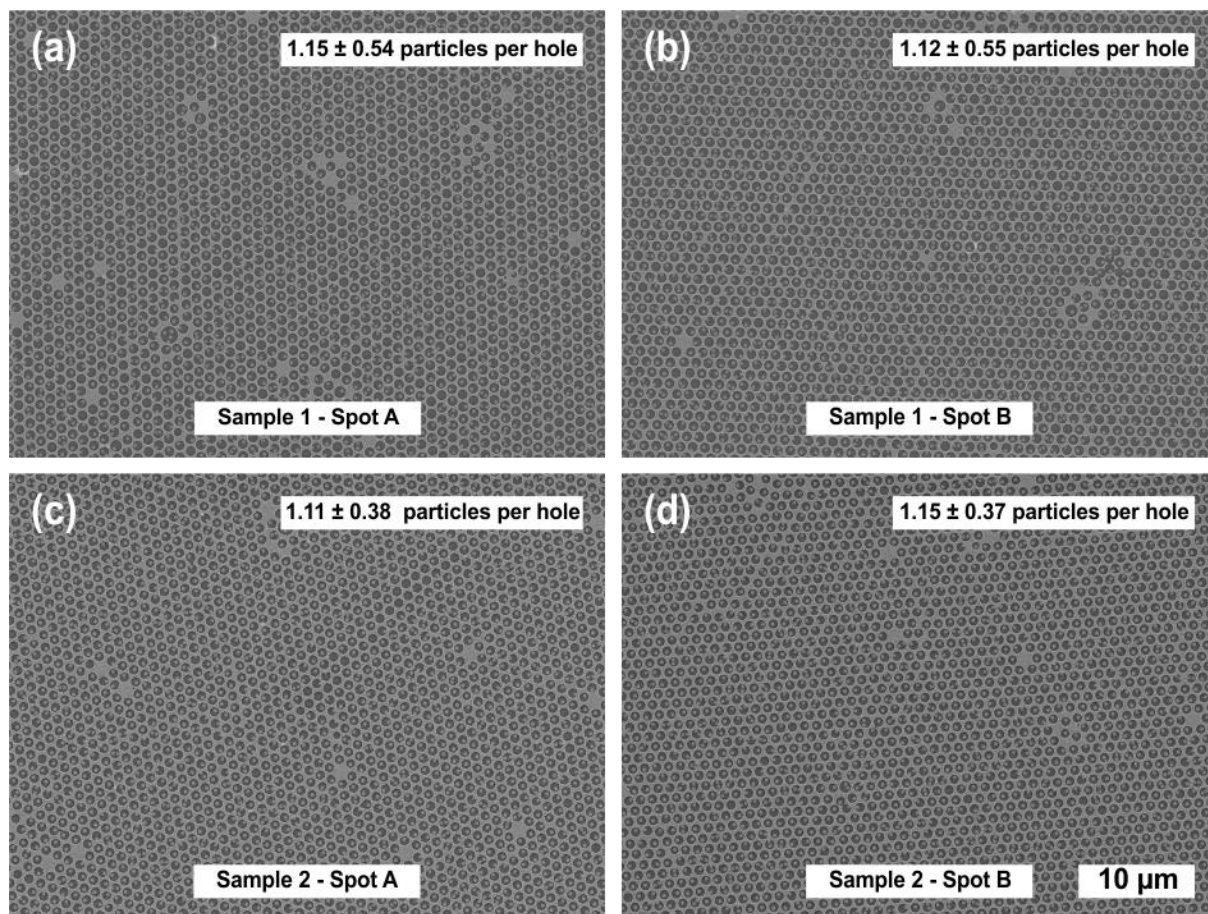


**Figure S6.3.** SEM images of 320 nm PS particles assembled on two independent nanohole arrays with  $d_h = 0.87 \mu\text{m}$  and  $L_{h-h} = 1.04 \mu\text{m}$  at equal conditions. (a) and (b) are different spots on sample 1, (c) and (d) show independent spots on sample 2.

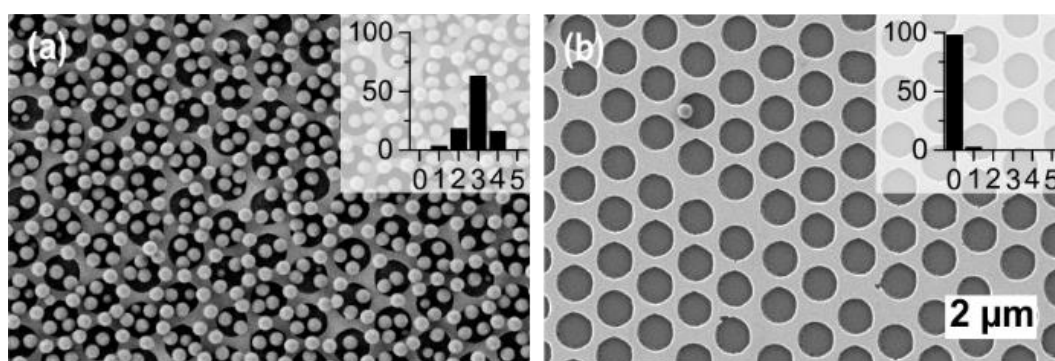


**Figure S6.4.** SEM images of 320 nm PS particles adsorbed at (a) pH 3 and (b) pH 12 in nanohole arrays with  $d_h = 0.87 \mu\text{m}$  and  $L_{h-h} = 1.04 \mu\text{m}$ . Insets show the frequency distribution of the number of particles per hole in percent.

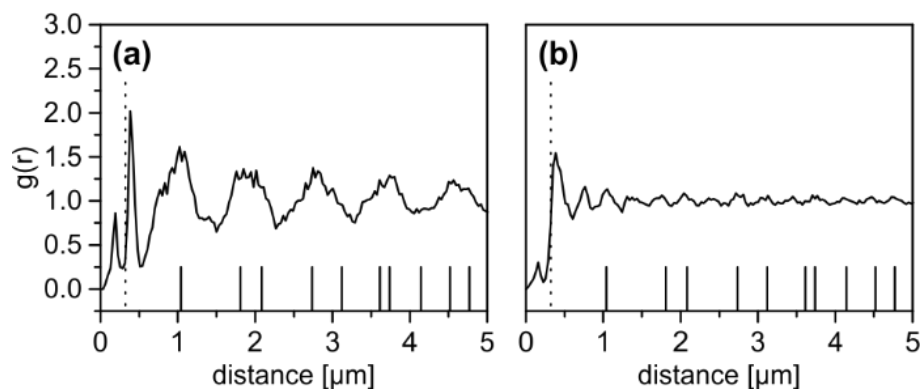


**Figure S6.5.** Radial distribution functions  $g(r)$  for 320 nm particles immobilized in nanomeshes with  $d_h = 0.87 \mu\text{m}$  and  $L_{h-h} = 1.04 \mu\text{m}$  at (a) pH 5 and 1 mM NaCl (b) pH 3 (1 mM HCl). The dotted lines indicate the particle diameter, the solid ticks indicate the  $g(r)$  of the underlying Au-nanomesh.

Particle positions were extracted using the “Find Maxima” tool in ImageJ. The radial distribution functions  $g(r)$  were calculated using a self-written software. The  $g(r)$  was calculated by determining all distances  $r$  within the extracted coordinates. These distances were binned to give a histogram of 600 different distance values with a fixed spacing of  $dr$ . Then in order to calculate the  $g(r)$  from this histogram the area of the circle with a thickness of  $dr$  is calculated at every of the 600 bins. The number of particles that are to be expected on average on this area is calculated by multiplying the circle area with the number density. This value is the average number of particles on this area. Then the histogram value that belongs to that  $dr$  (or circle area) is divided by this average and the result is the value for the  $g(r)$  at  $rdr$ .

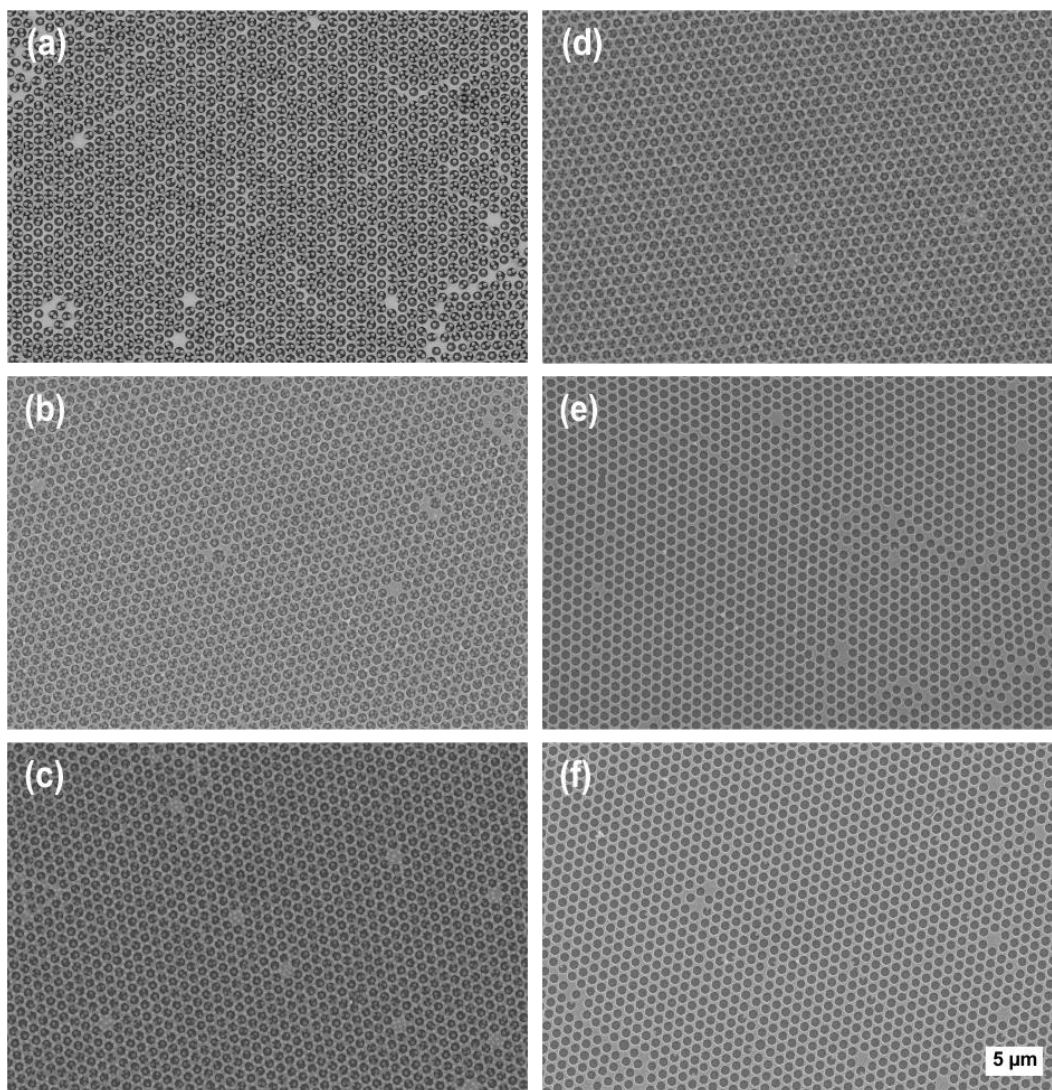


**Figure S6.6.** Overview SEM images of 320 nm particles immobilized in nanomeshes with  $d_h = 0.87 \mu\text{m}$  and  $L_{h-h} = 1.04 \mu\text{m}$  at (a) pH 5 and 1 mM NaCl, (b) pH 5 and 10 mM NaCl, (c) pH 5 and 100mM NaCl, (d) pH 3, (e) pH 10 and (f) pH 12.

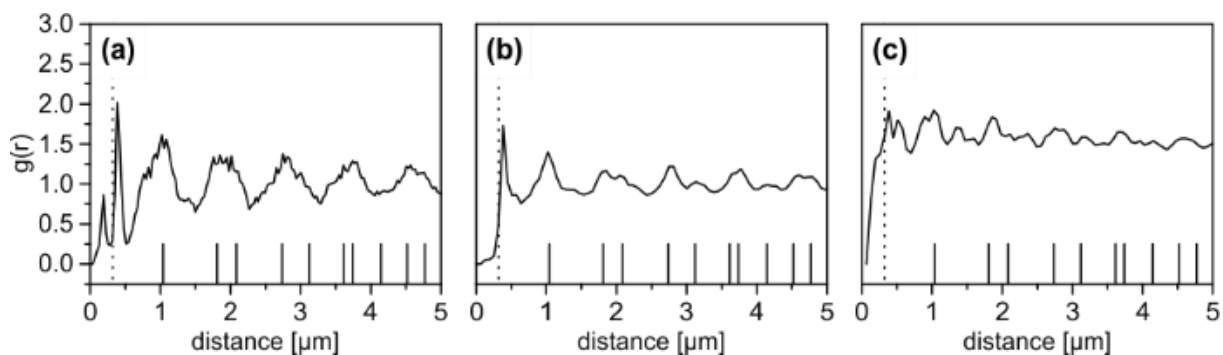


**Figure S6.7.** Radial distribution functions  $g(r)$  for 320 nm particles immobilized in a nanomesh with  $d_h = 0.87 \mu\text{m}$  and  $L_{h-h} = 1.04 \mu\text{m}$  at (a) 1 mM NaCl (b) 10 mM NaCl and (c) 100 mM NaCl. The dotted lines indicate the particle diameter, the solid ticks indicate the  $g(r)$  of the underlying Au-nanomesh.

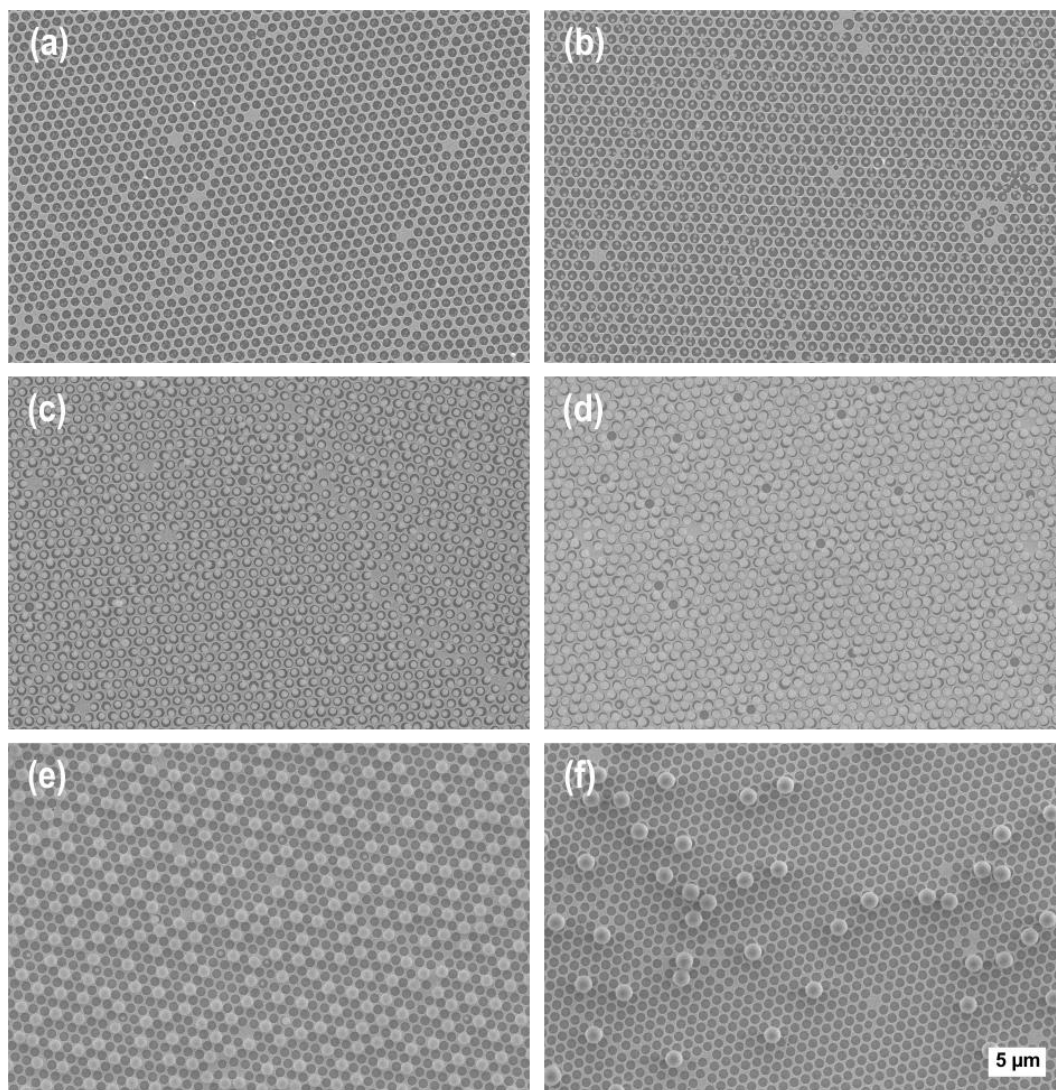


**Figure S6.8.** Overview SEM images of PS particles immobilized in nanomeshes with  $d_h = 0.87 \mu\text{m}$  and  $L_{h-h} = 1.04 \mu\text{m}$ . (a) 166 nm (b) 320 nm (c) 570 nm (d) 740 nm (e) 1040 nm, and (f) 1500 nm.

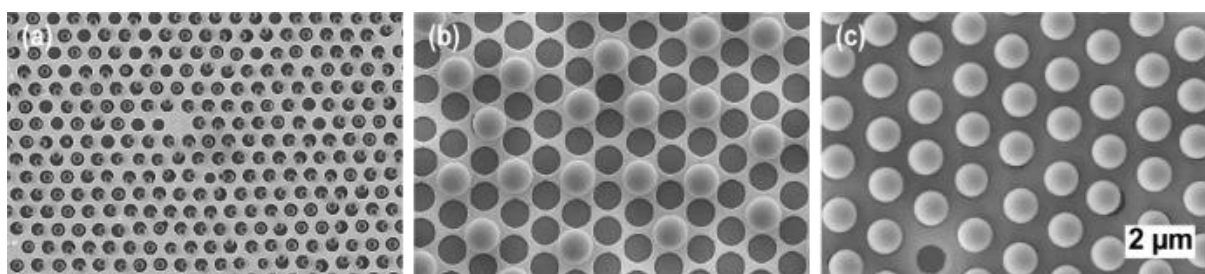


**Figure S6.9.** PS particles immobilized in nanohole arrays with variable  $L_{h-h}$ . (a) 258 nm particles on a nanomesh with  $d_h = 0.41 \mu\text{m}$  and  $L_{h-h} = 0.57 \mu\text{m}$  (b) 1040 nm particles on a nanomesh with  $d_h = 0.87 \mu\text{m}$  and  $L_{h-h} = 1.04 \mu\text{m}$  (c) 1040 nm particles on a nanomesh with  $d_h = 0.83 \mu\text{m}$  and  $L_{h-h} = 1.50 \mu\text{m}$ .

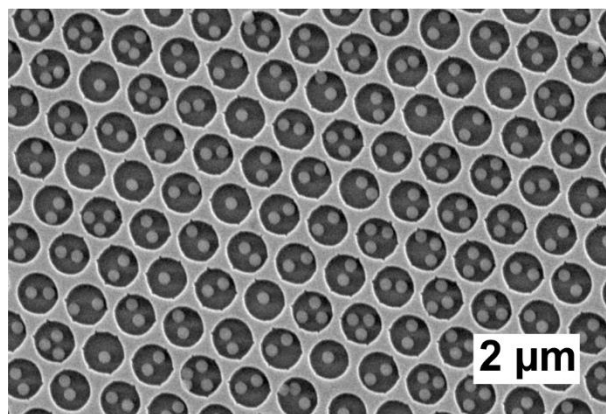


**Figure S6.10.** SEM micrograph of 238 nm PMMA particles in a nanohole array with  $d_h = 0.87 \mu\text{m}$  and  $L_{h-h} = 1.04 \mu\text{m}$ .

**Table 6.1.** Zeta potential of the used PS particles at pH 4.

Partikel	Zetapotential [mV]
166nm	-54
320nm	-39
570nm	-42
740nm	-42
1040nm	-47
1500nm	-51

The zeta potential was measured using a *Zetasizer Nano ZS (Malvern)* at 25 °C, a total ionic strength of 10 mM adjusted with NaCl and a particle concentration of 0.001 wt%. The pH was adjusted with HCl and NaOH, respectively.

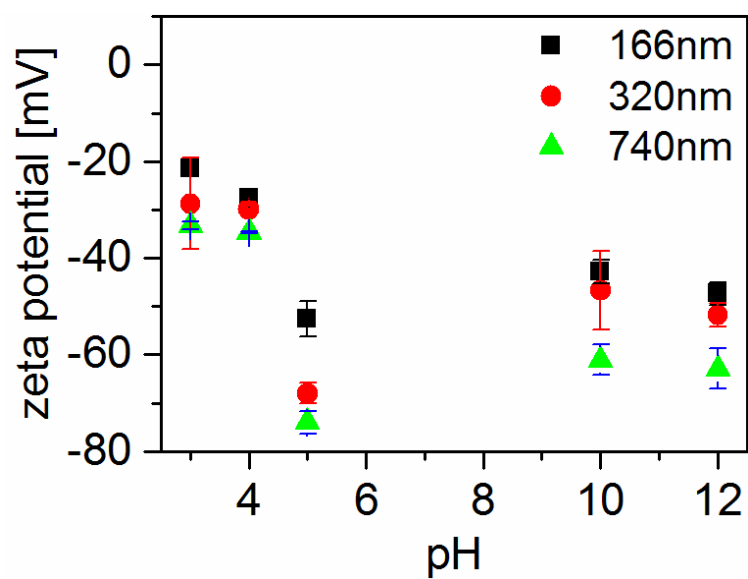


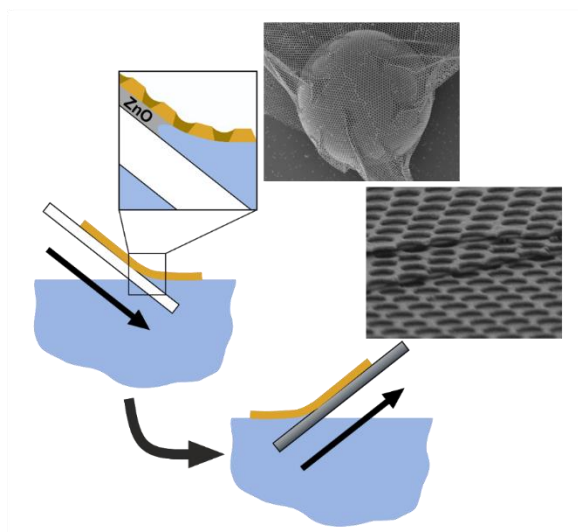
**Figure S6.11.** Zeta potential of the PS particles with 166 nm, 320 nm and 740 nm in dependence of the pH.



## 7 Nanomeshes at Liquid Interfaces: From Free-Standing Hole Arrays toward Metal-Insulator-Metal Architectures

Christian Stelling and Markus Retsch\*

Physical Chemistry – Polymer Systems, University of Bayreuth, 95440 Bayreuth, Germany



Published in *Advanced Materials Interfaces* 5, 1800154 (2018).

Reproduced with permission from Wiley-VCH.

## Abstract

The superior optical properties of metamaterials often rely on hierarchical structures in the sub-wavelength regime comprising stacks of individually patterned layers. For the fabrication of metamaterials in the visible regime, specific top-down lithographic methods have been developed. These techniques, however, have several inherent drawbacks such as the lack of scalability and low production speeds. Here, a simple and modular approach for the construction of multilayer metal-insulator-metal structures based on the transfer of metal nanohole arrays via liquid interfaces is demonstrated. Gold nanohole arrays are used as model systems that are prepared via nanosphere lithography on a zinc oxide sacrificial layer. Exploiting an interface mediated method, the prepared nanohole arrays are subsequently transferred onto arbitrary hydrophilic or hydrophobic substrates without compromising the high quality of the nanomeshes. Two approaches to stack such nanostructured layers with nanometer precision in a rapid way are demonstrated. Finally, the high mechanical stability of only 100 nm thick gold nanohole arrays allows for the preparation of free-standing nanomeshes in the order of several hundreds of square-micrometers.

## 7.1 Introduction

Metallic nanohole arrays present an attractive building block for optical metasurfaces as well as 3D metamaterials. Since the discovery of extraordinary optical transmission by Ebbesen *et al.*, metal nanohole arrays have been extensively studied.<sup>1</sup> Due to the periodic perforation, metal nanohole arrays exhibit surface plasmon polaritons, which can be easily tuned by varying the period, diameter or shape of the hole structure.<sup>2,3</sup> Nanohole arrays have been used for surface-enhanced spectroscopy, as optical sensors, color filters or transparent conducting electrodes.<sup>4-9</sup> Recently, multilayer structures consisting of two or more layers of metal nanohole arrays have been explored. Tang *et al.* observed a new resonance and increasingly high quality factors for silver nanohole array/dielectric multilayers due to the coupling of the hole arrays.<sup>10</sup> Moreover, stacked nanohole arrays, sometimes also referred to as double fishnet structures, give rise to negative refraction.<sup>11-17</sup>

However, the majority of these metal-insulator-metal (MIM) structures are fabricated using top-down methods like e-beam lithography or focused-ion-beam milling. These techniques not only

are very time-consuming but also need sophisticated equipment making the production process expensive and hardly applicable to large areas. Especially, multilayer structures are difficult to access using classical top-down methods. Consequently, fabrication techniques suitable for the fast and cost-effective production of MIM structures still remain a challenge. Bottom-up approaches could overcome these problems by capitalizing on self-assembly strategies in the colloidal regime.<sup>18</sup> Tagliabue *et al.* prepared periodic MIM arrays with a perforated metal structure and an (unperforated) metal back reflector employing nanosphere lithography (NSL) without a transfer step.<sup>19,20</sup> For this purpose, successive e-beam evaporation of a silver or gold layer and an insulating silica layer was followed by the deposition of a gold layer through a particle template. A similar approach was used by Zhou *et al.* to prepare MIM structures with two perfectly aligned silver nanohole arrays, which supported magnetic cavity modes in the visible and NIR range.<sup>21</sup> As multiple layers are deposited onto the same particle monolayer, the number of layers in the MIM structure is limited by the height of the templating structure.

Gong *et al.* reported a self-assembled MIM structure consisting of two stacked silver nanohole arrays. The hole arrays were consecutively prepared by NSL combined with electrochemical metal deposition. Although the self-assembly process inherently yielded misaligned hole arrays, the structures showed a negative index of refraction in the visible regime.<sup>22</sup> Misaligned, stacked nanohole arrays even exhibit interesting chiroptical effects, which depend on the in-plane rotational offset of the nanohole arrays.<sup>23</sup>

To further facilitate the production of MIM structures, the direct transfer of readily prepared hole arrays is highly desirable. The transfer procedures currently available usually rely on the dissolution of thick silicon, aluminum or copper substrates or the chromium adhesive layer under harsh conditions.<sup>23-27</sup> Alternatively, silver or polymer sacrificial layers have been used, which limits the freedom of fabrication regarding the nanohole array materials.<sup>28,29</sup> Nanoimprint lithography can be used to transfer nanohole arrays prepared by top-down lithographic techniques, but is not compatible with NSL due to the high adhesion of the metal layer on the substrate.<sup>30,31</sup> Furthermore, free-standing nanomeshes are not accessible by nanoimprint lithography.

Employing NSL directly at the liquid/gas interface is a promising alternative to attain free-standing hole arrays, which can then be transferred to solid substrates.<sup>32</sup> However, this technique is limited to nanomesh materials such as Ag<sub>2</sub>S that can be synthesized in liquid/gas interface reactions. Thus, there is a need for readily accessible methods that can transfer individual metal nanohole arrays onto arbitrary substrates.

## 7.2 Results and Discussion

In this work, we present a simple protocol for the transfer of gold nanohole arrays based on a ZnO sacrificial layer approach. The choice of ZnO as a sacrificial layer is essential as it possesses several unique properties, which are critical for the fabrication procedure. Previously, ZnO has been used to epitaxially grow and transfer GaN and metal oxide films due to the matching crystal structures.<sup>33-35</sup> Here, we make use of the possibility to trigger the solubility of ZnO by changing the pH value, while staying in an aqueous environment. Whereas ZnO dissolves in acidic solutions allowing the detachment of the nanohole array, its stability at high pH values is crucial for the transfer of the particle monolayers.<sup>36</sup> This method is easily scalable and can be extended to rapidly construct multilayer MIM architectures. The fabrication of the gold nanohole arrays via NSL starts with the preparation of close-packed monolayers of spherical polystyrene particles at the water/air interface. Here, we used an established procedure, which yields large single-crystalline domains.<sup>36</sup>

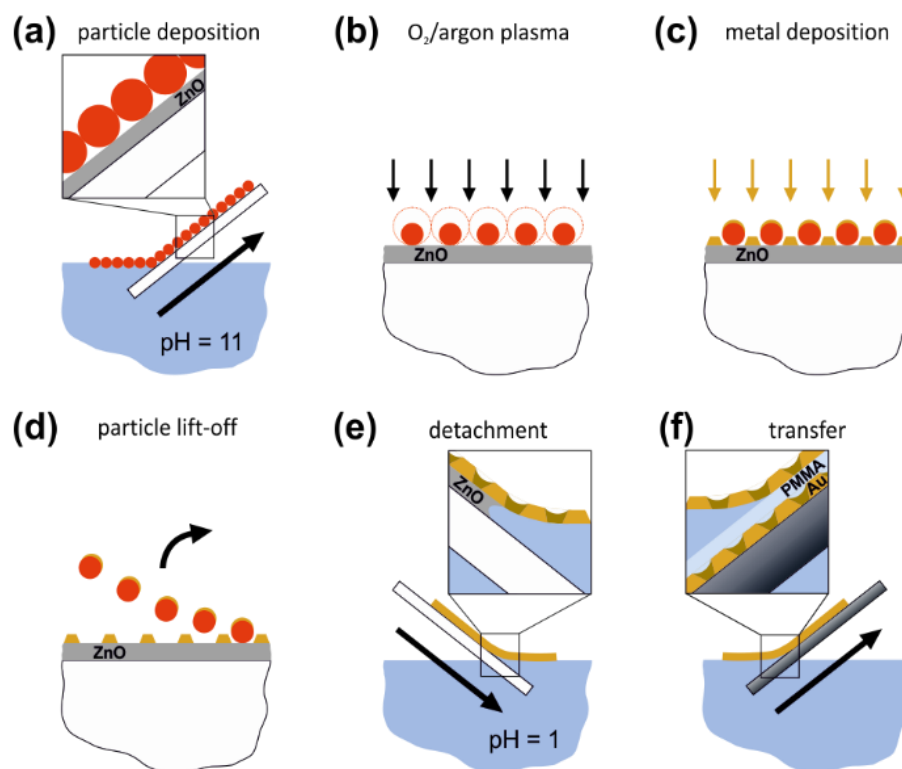


**Figure 7.1.** Fabrication and transfer of gold nanohole arrays. (a) Transfer of a hexagonal, close-packed particle monolayer onto the parental substrate. (b) Preparation of a non-close-packed particle monolayer by reactive ion etching. (c) Gold deposition. (d) Removal of the particle template. (e) Detachment of the hole array from the parental substrate. (f) Transfer of a hole array to a solid substrate.

The particle monolayers are then transferred to the parental glass substrate coated with a thin ( $\sim 40$  nm) ZnO layer (Figure 7.1a). Subsequently, the particle diameter is reduced by plasma etching to obtain non-close-packed particle monolayers (Figure 7.1b).

Unlike organic sacrificial layers, ZnO is not degraded by the O<sub>2</sub>/argon plasma used to etch the particles. Gold nanohole arrays are then received by sequential deposition of gold via thermal evaporation (Figure 7.1c) and removal of the templating particles (Figure 7.1d). Finally, the parental substrate is slowly immersed into an acidic aqueous solution. Thereby, the ZnO sacrificial layer is dissolved, and the nanohole array is detached from the parental substrate (Figure 7.1e). The detached nanohole array remains trapped at the water/air interface and can finally be picked up by an arbitrary substrate (Figure 7.1f).

The periodicity  $d_{h-h}$  of the gold nanohole arrays is determined by the initial diameter of the polystyrene spheres. The hole diameter  $d_h$  can be tuned by the diameter of the spheres after plasma etching. If not stated otherwise the nanohole arrays used here exhibit a thickness of  $t_{\text{Au}} = 50$  nm, a periodicity of  $d_{h-h} = 570$  nm and a hole diameter of approximately  $d_h = 430$  nm. In Figure 7.2a, the detachment of a  $10 \times 25$  mm<sup>2</sup> gold nanohole array is shown. The immersion of the parental substrate is performed at pH 1 using a dip-coater system at a constant speed of 1 mm/min. The immersion speed and the pH of the aqueous phase have to be carefully tuned to achieve a uniform detachment of the nanohole array. Both, too fast and too slow immersion result in crack-formation. For too low immersion speeds the dissolution of the ZnO layer progresses faster than the nanohole array reaches the three-phase-contact-line. In contrast, if the substrate is immersed too quickly, the hole array is not trapped at the interface and forced into the aqueous subphase. An immersion angle of approximately  $45^\circ$  with respect to the water surface was applied to minimize bending tensions in the metal film, which can also result in crack-formation.<sup>37</sup> The interface assisted lift-off of the nanohole arrays leads to higher ZnO dissolution rates compared to the complete immersion of the sample, as the metal layer is simultaneously separated from the substrate. This facilitates the diffusion of the etchant to the etching front and allows for the large scale fabrication.<sup>38,39</sup>

After detachment, the floating nanohole array can be transferred to a broad range of substrates. Both, hydrophilic and hydrophobic substrates can be used. Consequently, nanohole arrays can be prepared on substrates that were inapplicable beforehand. For example, large-area nanohole arrays can be fabricated on flexible PDMS substrates employing the transfer method as shown in Figure 7.2b. Thereby, despite its limited thickness of only 50 nm, the structure of the nanohole arrays remains intact on a macroscopic and microscopic level as depicted in Figure 7.2c.

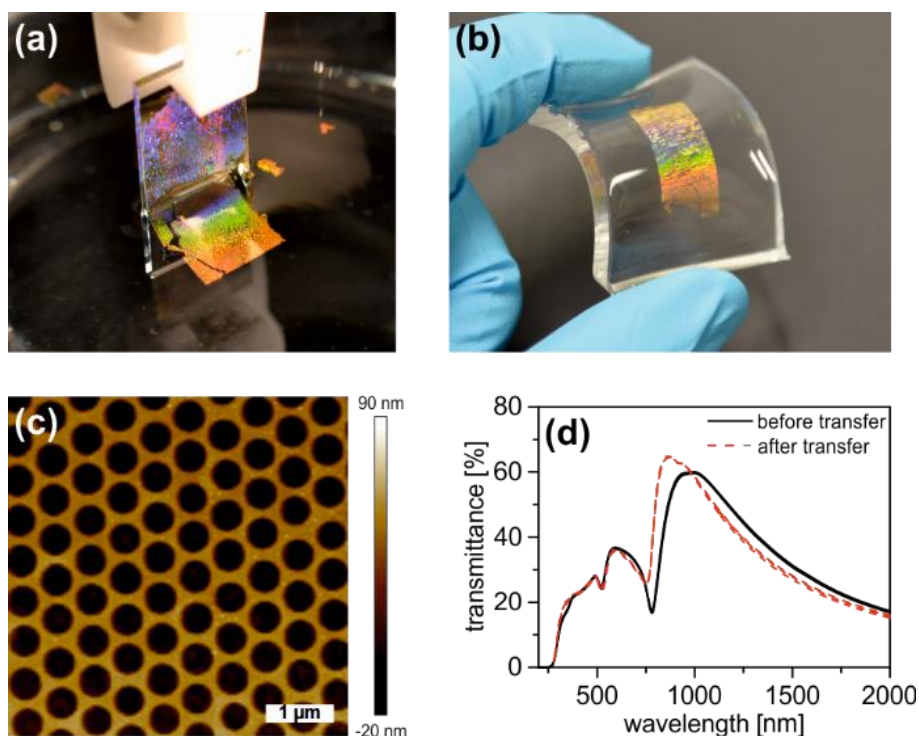


**Figure 7.2.** Transferred gold nanohole arrays. (a) Transfer setup. (b) Gold nanohole array transferred onto a PDMS substrate. (c) Atomic force microscopy image of a nanohole array after transfer to PDMS. (d) Transmittance spectra before and after transfer to glass.

Care must be taken concerning the roughness of the ZnO layer.<sup>40</sup> Under usual conditions, the roughness of the ZnO did not exceed the roughness of the evaporated gold layer. The topography of the ZnO layer is fully replicated into the gold coating. This roughness, in turn, will then limit the precise distance tuning in MIM structures in the low (< 20 nm) nanometer range. An example for the replication of a rather rough ZnO layer is given in Figure S7.1, where the top and bottom surface are imaged by atomic force microscopy. For a higher degree of precision (< 5 nm range), one needs to resort to well-known template-stripping methods, which have been established for ultra-smooth gold surfaces.<sup>41</sup>

The extraordinary stability of the nanomeshes upon transfer is also verified by the optical properties of the transferred nanohole arrays. In Figure 7.2d, far-field transmittance measurements of the same nanohole array before and after the transfer to glass are shown. Spectra of three different sample spots are depicted for both cases. In the spectra of the nanohole array before the transfer, two distinct minima can be observed at wavelengths of 780 nm and 520 nm, which correspond to the propagating surface plasmons located at the Au/ZnO and Au/air interface according to equation 7.1.<sup>42,43</sup> The minimum at 720 nm is shifted towards a shorter wavelength after the transfer. As this minimum corresponds to the surface plasmon

propagating at the bottom Au interface, this can be simply explained by the lower refractive index of the receiving glass substrate ( $n = 1.54$ ) compared to ZnO ( $n > 1.9$ ). The transmittance minimum at 520 nm (Au/air plasmon), however, does not change regarding the resonance wavelength or the intensity. Together with the low spatial variation of the optical spectra, this demonstrates the high reproducibility of the transfer process.

The mechanical stability of the nanohole arrays was further examined by transferring the metallic structure onto curved substrates and free-standing grids. For this, nanohole arrays with periods of 570 nm and 1040 nm were deposited on polystyrene microspheres with a diameter of 52  $\mu\text{m}$  (Figure 7.3a and b). The nanomeshes tightly wrap around the microspheres without ripping. In Figure 7.3c, a nanomesh was deposited on a trimeric structure of microspheres.

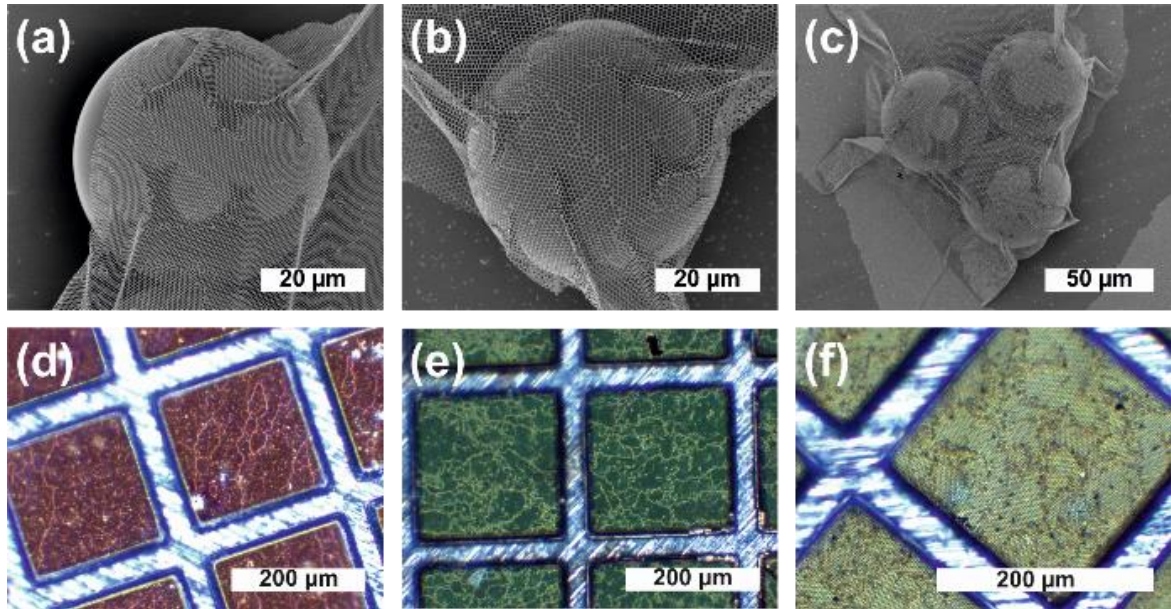


**Figure 7.3.** Free-standing nanohole arrays. Nanohole arrays with periods of (a)  $d_{h-h} = 570 \text{ nm}$  and (b)  $d_{h-h} = 1040 \text{ nm}$  transferred onto microspheres with a particle diameter of 52  $\mu\text{m}$ . (c) Free-standing nanohole array with a period of  $d_{h-h} = 570 \text{ nm}$  between three microspheres. Free-standing nanohole arrays with periods of (d)  $d_{h-h} = 570 \text{ nm}$ , (e)  $d_{h-h} = 1040 \text{ nm}$ , and (f)  $d_{h-h} = 2560 \text{ nm}$  on copper grids.

Thereby, the nanomesh is spanned between the three particles giving a free-standing nanohole array over several hundreds of square-micrometers. This underlines the exceptional flexibility as well as the mechanical stability of the perforated metal films despite a thickness of only 50 nm. To approach truly macroscopic, free-standing films, the gold layer thickness was increased to 100 nm. Nanohole arrays with 570 nm, 1040 nm, and 2560 nm periodicity were then transferred onto copper grids with hole widths of 204 x 204  $\mu\text{m}^2$ . Figure 7.3d-e demonstrate that these areas can be fully covered with intact nanomeshes. Nevertheless, owing

to the strong capillary forces during the drying process from water also some ruptured parts were obtained. These defects can be certainly mitigated either by even thicker gold layers ( $> 100$  nm) or by a solvent exchange to liquids with a much lower interfacial tension.<sup>44,45</sup>

Having verified the stability of the nanomeshes upon transfer, we now focus on the assembly of MIM structures. First, we used poly(methyl methacrylate) (PMMA) as spacer material, which can be easily deposited onto a glass supported nanohole array by spin-coating. Subsequently, a second nanohole array with a thickness of 50 nm was placed on top of the PMMA layer using the interfacial transfer introduced above (Figure 7.4a).

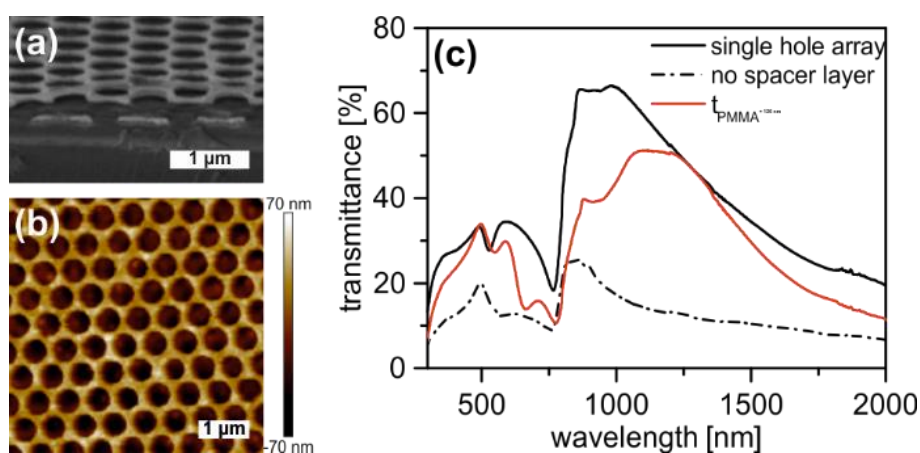


**Figure 7.4.** Stacked nanohole arrays with PMMA spacer. (a) Side-view electron microscopy image and (b) AFM height image of the Au/PMMA/Au structure. (c) Transmittance spectrum of Au/PMMA/Au structure compared to spectra of a single nanohole array and two nanohole arrays stacked without spacer layer.

For a 126 nm thick PMMA spacer layer the nanohole array uniformly covers the PMMA surface. An influence of the bottom nanohole array topography on the top layer is not discernible (Figure 7.4b). In Figure 7.4c, the transmittance spectrum of the Au/PMMA/Au structure is compared to the spectra of a single Au nanohole array and two stacked nanohole arrays without the PMMA layer. Without the dielectric spacer, the peaks corresponding to the Au/glass and Au/air interface are only slightly red-shifted compared to the single nanohole array due to the increased effective refractive index environment. Concomitantly, the transmittance intensity is strongly reduced throughout the whole spectrum. Interestingly, when introducing the PMMA spacer layer, the loss in transmittance is strongly reduced or even comparable to the single nanomesh layer ( $\sim 1250$  nm). Additionally, a new peak appears at a wavelength of 663 nm, which can be assigned to a magnetic metamaterial resonance.<sup>21</sup> This resonance is confined to the gap between the metal layers and thus exhibits a strong dependence on the thickness of the PMMA spacer layer (Figure S7.2). Thus, this simple spectroscopic

analysis demonstrates that indeed, interesting coupling effects comparable to perfectly registered nanohole array MIM stacks can be found in these misaligned structures based on NSL and interfacial transfer. However, for very thin insulating layers polymer coatings are only partially suitable for the preparation of highly defined MIM materials. When the PMMA layer thickness is commensurate with the Au thickness, the PMMA conformally coats the bottom nanohole array, filling the holes of the structure. Consequently, the distance between the two gold layers spatially varies, impeding the precise tuning the spacer thickness when depositing the upper nanohole array.

Therefore, we introduced the dielectric spacer directly into the fabrication process of the nanohole array. For this, a silica layer was sputtered on top of the ZnO sacrificial layer before immobilizing the particle monolayer. Thus, the nanohole array is fabricated directly on the insulator layer, and the combination of both layers can be deposited in the transfer process (Figure 7.5a). This parallel deposition allows for a very fast production of multilayer MIM stacks. The silica interlayers, in contrast to polymer interlayers, do not adapt to the topography of underlying hole arrays and thus are highly uniform in thickness (Figure 7.5b). Moreover, due to the higher mechanical stability of the double layer and the good adhesion of the gold layer on the silica, the formation of defects upon transfer is further reduced. Therefore, a higher number of layers can be stacked without affecting the uniformity of the sample, which is a major advantage of this extension of our technique. It is furthermore readily conceivable to use any other spacer layer instead of  $\text{SiO}_2$ , as long as it withstands  $\text{O}_2$  plasma treatment and the basic and acidic aqueous transfer process.

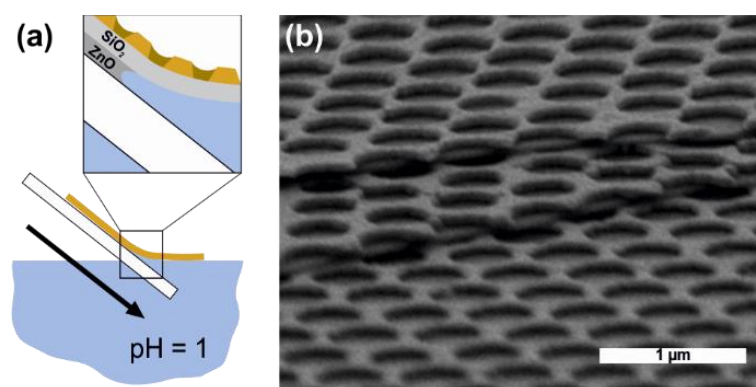


**Figure 7.5.** Nanohole array multilayer structures. (a) Scheme of the transfer process of  $\text{SiO}_2/\text{Au}$  double layer. (b) Side-view electron microscopy image of a five-layer stack of alternating Au and  $\text{SiO}_2$  layers.

The method used here for the production of the particle monolayers yields polycrystalline monolayers with a decent grain size, owing to the NSL process. Therefore, multiple orientations of the hexagonal, close-packed monolayer can be found on one sample. Thus, the sequential stacking of such two-dimensional multi-grain materials does not allow for a registration between the individual layers. Figure 7.6a-d show scanning electron microscopy (SEM) images of different sample spots on a double-layer MIM stack. Using a suitably high accelerating voltage, the top and bottom nanohole array can be imaged at the same time. We find distinct Moiré patterns on the same sample corresponding to different mutual orientations of the nanohole arrays.

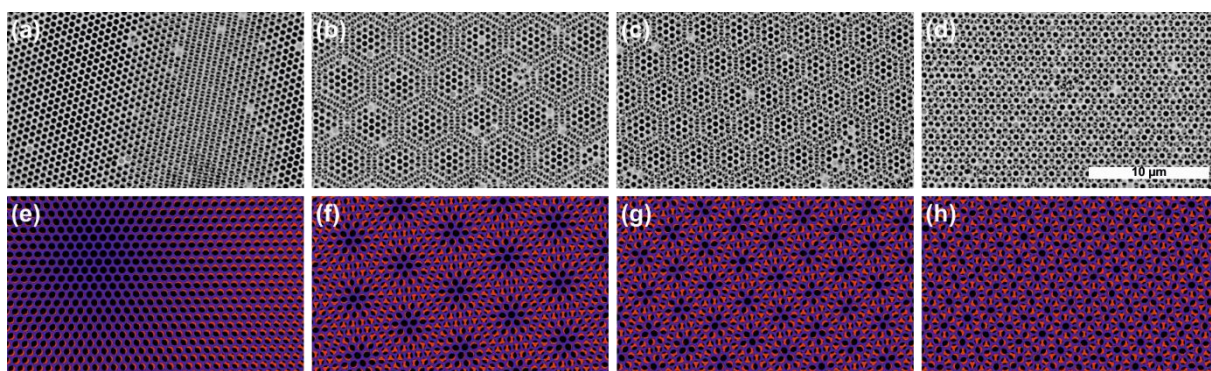


**Figure 7.6.** Top-view electron microscopy images of double layer nanohole array (a)-(d) and reconstructed Moiré patterns by rotation of the blue nanohole array by (e)  $1^\circ$ , (f)  $9^\circ$ , (g)  $14^\circ$ , (h)  $24^\circ$ .

In general, the superposition of two identical patterns can result in a Moiré effect, when the two patterns are slightly rotated or displaced with respect to each other. The Moiré patterns visible in Figure 7.6 can be reproduced by merely rotating the top (blue) nanohole array versus the bottom (red) pattern as shown in Figure 7.6e-h. Due to the 6-fold symmetry, all patterns can be found using rotation angles between  $0^\circ$  and  $30^\circ$ . Thereby, the larger the rotation angle, the smaller is the repetition unit of the Moiré pattern.

Currently, the evolution of these Moiré patterns is inevitable for this sort of fabrication process and can be regarded as the major limiting factor towards high-quality metamaterials. Nevertheless, to further optimize the structural uniformity of the stacks, techniques are already accessible in literature, which yield large-scale, nearly single crystalline particle monolayers.<sup>46,47</sup> Applying light scattering, this would also permit determine the orientation of the nanohole pattern in the nanohole arrays floating at the water/air interface during the transfer step. Consequently, one could control the in-plane rotational offset of the nanohole arrays.

Moreover, it was reported that a small degree of misalignment does not affect the optical properties of the MIM structure.<sup>22</sup>

### 7.3 Conclusion

In summary, we developed a convenient method for the production of MIM multilayer structures, based on the transfer of metal nanohole arrays. Via the detachment at the water/air interface, the nanohole arrays can be easily transferred to arbitrary organic or inorganic solid substrates, independent of the substrate wetting behavior. Even macroscopically free-standing nanohole arrays can be obtained by the transfer to grid substrates. Decoupling the preparation of the individual nanohole arrays and the stacking of the multilayer structure presents a versatile and modular approach for the rational fabrication of optical metamaterials. Compared to classical top-down lithographic methods, our technique capitalizes on NSL and offers high fabrication speeds, low costs, and compatibility with many materials as well as scalability.

### 7.4 Experimental Section

**Materials:** Polystyrene particles were purchased from Microparticles GmbH (Berlin).

**Substrates:** The ZnO layers were prepared using a sol-gel method. For this, glass slides were cleaned for 10 min by ultrasonication in 2 % aqueous Hellmanex (Hellma GmbH, Mühlheim, Germany) solution in MilliQ water. After rinsing off the surfactant with MilliQ water, the substrates were further sonicated for 10 minutes in ethanol and finally dried with compressed air. Subsequently, the ZnO films were formed by spin-coating a zinc acetate solution (110 mg zinc acetate in 30  $\mu$ l 2-aminoethanol and 1 ml 2-methoxyethanol) at 2000 rpm for 50 s and subsequent baking at 150 °C for 5 min. The poly(methyl methacrylate) spacer layers were prepared by spin-coating.

**Fabrication of Au nanomeshes:** Monolayers of polystyrene particles were prepared according to the procedure of Retsch *et al.*<sup>36</sup> Cationically functionalized glass slides were spin-coated with a 3 wt% particle dispersion at 4000 rpm. Subsequently, the coated glass substrates were immersed in a 0.1 mM sodium dodecyl sulfate solution in MilliQ. The aqueous phase was adjusted to pH 12 by adding a few drops of NH<sub>3</sub>. A monolayer was formed at the liquid/air interface by the self-assembly of the detaching particles. The monolayer was transferred to the

ZnO coated glass substrates and dried in air. The monolayers were etched in a plasma reactor MiniFlecto (Plasma Technology GmbH, Herrenberg, Germany) with 75 % argon and 25 % oxygen at 80 W at a pressure of 0.14 mbar to obtain non-close-packed monolayers. A 3 nm chromium layer and the respective layer thickness of gold were deposited using a Balzers BA360 thermal evaporation chamber. The layer thickness was monitored via an SQM 160 microbalance (Sigma Instruments, Schaefer Technologie GmbH). SiO<sub>2</sub> was deposited by sputtering. Afterwards, the particles were removed using Scotch® tape (3M) giving the nanohole arrays. The Au substrates were cleaned by ultrasonication for 10 min in tetrahydrofuran and dried with compressed air. All samples were stored under inert gas.

**Transfer of Au nanomeshes:** The Au nanohole arrays were detached from their parental substrate by immersion into an aqueous hydrochloric acid solution (pH 1) with a speed of 1 mm/min and an immersion angle of 45 ° using a home built dip-coater system. After complete detachment of the gold film, the nanohole array is transferred when lifting the (hydrophilic) receiving substrate out of the water phase or immersing a (hydrophobic) substrate into the water phase.

**Characterization:** UV/VIS spectra were measured using a Cary 5000 UV-Vis-NIR Spectrophotometer (Agilent Technologies). SEM images were taken on a LEO 1530 Gemini Field Emission SEM (Carl Zeiss AG, Oberkochen, Germany). The images were evaluated with the software ImageJ.<sup>48</sup> Atomic force microscopy was performed in tapping mode on a Dimension 3100 microscope (Veeco, USA) with a Nanoscope IV controller and OTESPA-R3 cantilevers (Bruker). The AFM images were analyzed with the software Nanoscope Analysis.

## Acknowledgements

This work was funded by the German Research Foundation (DFG) by the SFB840. C.S. acknowledges support from the Elite Network of Bavaria (ENB). The authors thank Dr. Beate Förster and Martina Heider from the Bavarian Polymer Institute (BPI) for their support using the scanning electron microscopy facilities.

## References

1. Ebbesen, T. W., Lezec, H. J., Ghaemi, H. F., Thio, T. & Wolff, P. A. Extraordinary optical transmission through sub-wavelength hole arrays. *Nature* **391**, 667-669 (1998).
2. Wu, W. & Tassi, N. G. A broadband plasmonic enhanced transparent conductor. *Nanoscale* **6**, 7811-7816 (2014).

3. Inoue, D., Miura, A., Nomura, T., Fujikawa, H., Sato, K., Ikeda, N., Tsuya, D., Sugimoto, Y. & Koide, Y. Polarization independent visible color filter comprising an aluminum film with surface-plasmon enhanced transmission through a subwavelength array of holes. *Appl. Phys. Lett.* **98**, 093113 (2011).
4. Sannomiya, T., Scholder, O., Jefimovs, K., Hafner, C. & Dahlin, A. B. Investigation of plasmon resonances in metal films with nanohole arrays for biosensing applications. *Small* **7**, 1653-1663 (2011).
5. Cetin, A. E., Etezadi, D., Galarreta, B. C., Busson, M. P., Eksioglu, Y. & Altug, H. Plasmonic Nanohole Arrays on a Robust Hybrid Substrate for Highly Sensitive Label-Free Biosensing. *ACS Photonics* **2**, 1167-1174 (2015).
6. Lu, B. R., Xu, C., Liao, J., Liu, J. & Chen, Y. High-resolution plasmonic structural colors from nanohole arrays with bottom metal disks. *Opt. Lett.* **41**, 1400-1403 (2016).
7. Cheng, F., Yang, X., Rosenmann, D., Stan, L., Czuplewski, D. & Gao, J. Enhanced structural color generation in aluminum metamaterials coated with a thin polymer layer. *Opt. Express* **23**, 25329-25339 (2015).
8. Morfa, A. J., Akinoglu, E. M., Subbiah, J., Giersig, M. & Mulvaney, P. Transparent metal electrodes from ordered nanosphere arrays. *J. Appl. Phys.* **114**, 054502 (2013).
9. Ai, B., Basnet, P., Larson, S., Ingram, W. & Zhao, Y. Plasmonic sensor with high figure of merit based on differential polarization spectra of elliptical nanohole array. *Nanoscale* **9**, 14710-14721 (2017).
10. Tang, Z. H., Peng, R. W., Wang, Z., Wu, X., Bao, Y. J., Wang, Q. J., Zhang, Z. J., Sun, W. H. & Wang, M. Coupling of surface plasmons in nanostructured metal/dielectric multilayers with subwavelength hole arrays. *Phys. Rev. B* **76**, 195405 (2007).
11. Parsons, J., Hendry, E., Sambles, J. R. & Barnes, W. L. Localized surface-plasmon resonances and negative refractive index in nanostructured electromagnetic metamaterials. *Phys. Rev. B* **80**, 245117 (2009).
12. Zhang, S., Fan, W., Panoiu, N. C., Malloy, K. J., Osgood, R. M. & Brueck, S. R. Experimental demonstration of near-infrared negative-index metamaterials. *Phys. Rev. Lett.* **95**, 137404 (2005).
13. Dolling, G., Wegener, M., Soukoulis, C. M. & Linden, S. Negative-index metamaterial at 780 nm wavelength. *Opt. Lett.* **32**, 53-55 (2007).
14. Mary, A., Rodrigo, S. G., Garcia-Vidal, F. J. & Martin-Moreno, L. Theory of negative-refractive-index response of double-fishnet structures. *Phys. Rev. Lett.* **101**, 103902 (2008).
15. Valentine, J., Zhang, S., Zentgraf, T., Ulin-Avila, E., Genov, D. A., Bartal, G. & Zhang, X. Three-dimensional optical metamaterial with a negative refractive index. *Nature* **455**, 376-379 (2008).
16. Yang, J., Sauvan, C., Liu, H. T. & Lalanne, P. Theory of fishnet negative-index optical metamaterials. *Phys. Rev. Lett.* **107**, 043903 (2011).
17. Garcia-Meca, C., Hurtado, J., Marti, J., Martinez, A., Dickson, W. & Zayats, A. V. Low-loss multilayered metamaterial exhibiting a negative index of refraction at visible wavelengths. *Phys. Rev. Lett.* **106**, 067402 (2011).
18. Lodewijks, K., Verellen, N., Van Roy, W., Moshchalkov, V., Borghs, G. & Van Dorpe, P. Self-assembled hexagonal double fishnets as negative index materials. *Appl. Phys. Lett.* **98**, 091101 (2011).
19. Tagliabue, G., Eghlidi, H. & Poulidakos, D. Facile multifunctional plasmonic sunlight harvesting with tapered triangle nanopatterning of thin films. *Nanoscale* **5**, 9957-9962 (2013).

20. Tagliabue, G., Höller, C., Eghlidi, H. & Poulidakos, D. Proximal gap-plasmon nanoresonators in the limit of vanishing inter-cavity separation. *Nanoscale* **6**, 10274-10280 (2014).
21. Zhou, Z. *et al.* Broad-Range Electrically Tunable Plasmonic Resonances of a Multilayer Coaxial Nanohole Array with an Electroactive Polymer Wrapper. *ACS Appl Mater Interfaces* **9**, 35244-35252 (2017).
22. Gong, B., Zhao, X., Pan, Z., Li, S., Wang, X., Zhao, Y. & Luo, C. A visible metamaterial fabricated by self-assembly method. *Sci. Rep.* **4**, 4713 (2014).
23. Wu, Z. & Zheng, Y. Moiré Chiral Metamaterials. *Advanced Optical Materials* **5**, 1700034 (2017).
24. Jeon, S., Jeong, J. H., Song, Y. S., Jeong, W. I., Kim, J. J. & Youn, J. R. Vacuum nano-hole array embedded organic light emitting diodes. *Nanoscale* **6**, 2642-2648 (2014).
25. Zhao, Z., Zhou, Z., Zhang, G. & Chiechi, R. C. Transfer and control of the orientation of 3D nanostructures fabricated by nanoskiving. *Nanoscale Horiz.* **1**, 473-479 (2016).
26. Kwak, E. S., Henzie, J., Chang, S. H., Gray, S. K., Schatz, G. C. & Odom, T. W. Surface plasmon standing waves in large-area subwavelength hole arrays. *Nano Lett.* **5**, 1963-1967 (2005).
27. Jones, D., Liu, N., Corbett, B., Lovera, P., Quinn, A. J. & O'Riordan, A. Surface Plasmon assisted extraordinary transmission in metallic nanohole arrays and its suitability as a bio-sensor. *Journal of Physics: Conference Series* **307**, 012005 (2011).
28. Min Huang, F., Sinha, J. K., Gibbons, N., Bartlett, P. N. & Baumberg, J. J. Direct assembly of three-dimensional mesh plasmonic rolls. *Appl. Phys. Lett.* **100**, 193107 (2012).
29. Acikgoz, C., Ling, X. Y., Phang, I. Y., Hempenius, M. A., Reinhoudt, D. N., Huskens, J. & Vancso, G. J. Fabrication of Freestanding Nanoporous Polyethersulfone Membranes Using Organometallic Polymer Resists Patterned by Nanosphere Lithography. *Adv. Mater.* **21**, 2064-2067 (2009).
30. Yoo, D., Johnson, T. W., Cherukulappurath, S., Norris, D. J. & Oh, S. H. Template-Stripped Tunable Plasmonic Devices on Stretchable and Rollable Substrates. *ACS Nano* **9**, 10647-10654 (2015).
31. Sharma, N., Keshmiri, H., Zhou, X., Wong, T. I., Petri, C., Jonas, U., Liedberg, B. & Dostalek, J. Tunable Plasmonic Nanohole Arrays Actuated by a Thermoresponsive Hydrogel Cushion. *J. Phys. Chem. C* **120**, 561-568 (2016).
32. Li, C., Hong, G. & Qi, L. Nanosphere Lithography at the Gas/Liquid Interface: A General Approach toward Free-Standing High-Quality Nanonets. *Chem. Mater.* **22**, 476-481 (2010).
33. Rogers, D. J. *et al.* Use of ZnO thin films as sacrificial templates for metal organic vapor phase epitaxy and chemical lift-off of GaN. *Appl. Phys. Lett.* **91**, 071120 (2007).
34. Rajan, A. *et al.* Wafer-scale epitaxial lift-off of optoelectronic grade GaN from a GaN substrate using a sacrificial ZnO interlayer. *Journal of Physics D: Applied Physics* **49**, 315105 (2016).
35. Dral, A. P., Nijland, M., Koster, G. & ten Elshof, J. E. Film transfer enabled by nanosheet seed layers on arbitrary sacrificial substrates. *APL Materials* **3**, 056102 (2015).
36. Retsch, M., Zhou, Z., Rivera, S., Kappl, M., Zhao, X. S., Jonas, U. & Li, Q. Fabrication of Large-Area, Transferable Colloidal Monolayers Utilizing Self-Assembly at the Air/Water Interface. *Macromol. Chem. Phys.* **210**, 230-241 (2009).

37. Harrison, K. L., Biedermann, L. B. & Zavadil, K. R. Mechanical Properties of Water-Assembled Graphene Oxide Langmuir Monolayers: Guiding Controlled Transfer. *Langmuir* **31**, 9825-9832 (2015).
38. Cheng, C. W., Shiu, K. T., Li, N., Han, S. J., Shi, L. & Sadana, D. K. Epitaxial lift-off process for gallium arsenide substrate reuse and flexible electronics. *Nat Commun* **4**, 1577 (2013).
39. Parchine, M., McGrath, J., Bardosova, M. & Pemble, M. E. Large Area 2D and 3D Colloidal Photonic Crystals Fabricated by a Roll-to-Roll Langmuir-Blodgett Method. *Langmuir* **32**, 5862-5869 (2016).
40. Znaidi, L. Sol-gel-deposited ZnO thin films: A review. *Materials Science and Engineering: B* **174**, 18-30 (2010).
41. Hegner, M., Wagner, P. & Semenza, G. Ultralarge Atomically Flat Template-Stripped Au Surfaces for Scanning Probe Microscopy. *Surf. Sci.* **291**, 39-46 (1993).
42. Lin, E.-H., Tsai, W.-S., Lee, K.-L., Lee, M.-C. M. & Wei, P.-K. Enhancing angular sensitivity of plasmonic nanostructures using mode transition in hexagonal gold nanohole arrays. *Sensors and Actuators B: Chemical* **241**, 800-805 (2017).
43. Couture, M., Liang, Y., Poirier Richard, H. P., Faid, R., Peng, W. & Masson, J. F. Tuning the 3D plasmon field of nanohole arrays. *Nanoscale* **5**, 12399-12408 (2013).
44. Stelling, C., Mark, A., Papastavrou, G. & Retsch, M. Showing particles their place: deterministic colloid immobilization by gold nanomeshes. *Nanoscale* **8**, 14556-14564 (2016).
45. Isa, L., Kumar, K., Müller, M., Grolig, J., Textor, M. & Reimhult, E. Particle lithography from colloidal self-assembly at liquid-liquid interfaces. *ACS Nano* **4**, 5665-5670 (2010).
46. Shinotsuka, K., Kajita, Y., Hongo, K. & Hatta, Y. Crystal Perfection of Particle Monolayer at the Air-Water Interface. *Langmuir* **31**, 11452-11457 (2015).
47. Meng, X. & Qiu, D. Gas-flow-induced reorientation to centimeter-sized two-dimensional colloidal single crystal of polystyrene particle. *Langmuir* **30**, 3019-3023 (2014).
48. Rasband, W. S. *ImageJ*, U. S. National Institutes of Health, Bethesda, Maryland, USA, <http://imagej.nih.gov/ij> (1997-2016).

## 7.5 Supporting Information

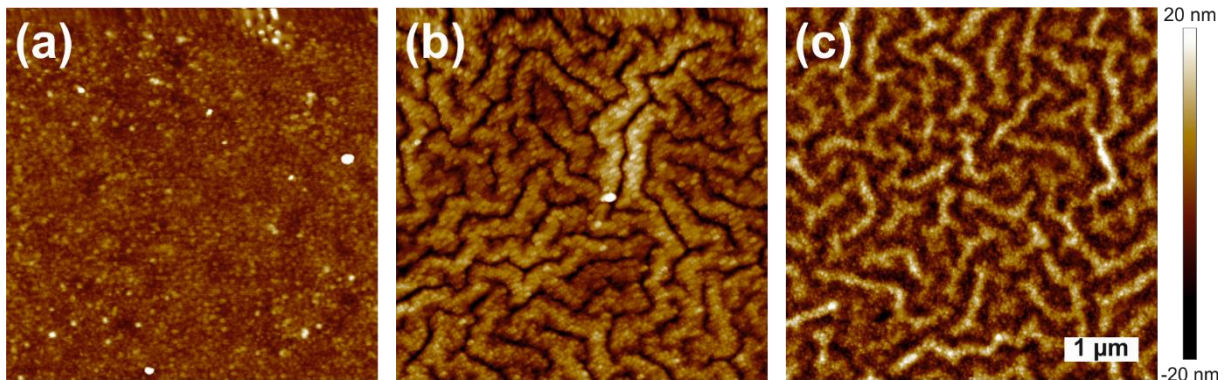


**Figure S7.1.** AFM micrographs of (a) a reference gold layer (b) bottom side and (c) top side of a transferred gold film with a thickness of 50 nm.

For normal incidence the plasmon equation for hexagonal nanohole arrays is given by

$$\lambda_0 = \frac{P}{\sqrt{\frac{4}{3}(i^2 + ij + j^2)}} * \sqrt{\frac{\epsilon_1 \epsilon_2}{\epsilon_1 + \epsilon_2}} \quad 7.1$$

The root mean square averaged roughness of the gold films equals to 2.4 nm for the reference film, 5.01 nm for the bottom interface and 5.87 nm for the top interface of the gold film transferred from ZnO.

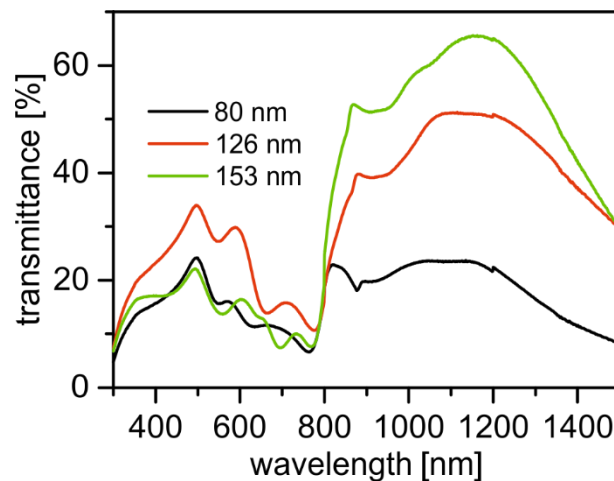


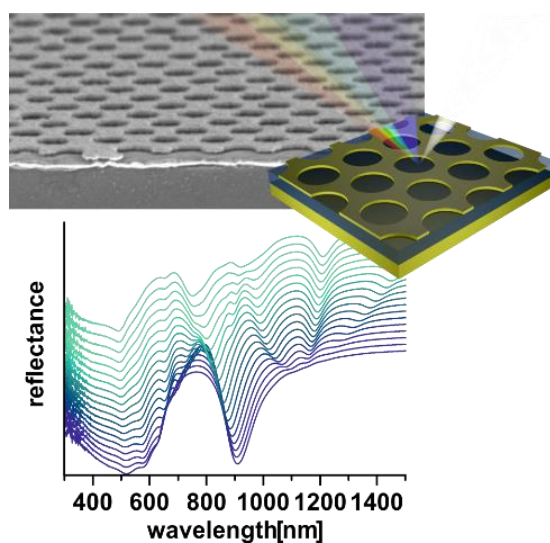
**Figure S7.2.** Transmittance spectra of Au/PMMA/Au structures with distinct PMMA layer thicknesses.

## 8 Surface Plasmon Modes of Nanomesh-on-Mirror Nanocavities Prepared by Nanosphere Lithography

Christian Stelling,<sup>1</sup> Stefan Fossati,<sup>2</sup> Jakub Dostálek,<sup>2\*</sup> and Markus Retsch<sup>1\*</sup>

<sup>1</sup>Physical Chemistry – Polymer Systems, University of Bayreuth, 95440 Bayreuth, Germany

<sup>2</sup>Biosensor Technologies, Austrian Institute of Technology, 3430 Tulln, Austria



Published in *Nanoscale* 10, 17983-17989 (2018).

Reproduced with permission from The Royal Society of Chemistry.

## Abstract

Metal-insulator-metal (MIM) structures show great potential for numerous photonic applications due to their ability to confine light energy to volumes with deeply sub-wavelength dimensions. Here, MIM structures comprising hexagonal gold nanohole arrays were prepared by nanosphere lithography. Angle-resolved UV-vis-NIR spectroscopy revealed a series of narrow, dispersive and non-dispersive modes, which were attributed to the excitation of surface plasmon polariton (SPP) modes. Applying finite-difference time-domain (FDTD) simulations and analytical diffraction phase-matching theory all resonances can be ascribed to only two SPP modes traveling at the outer gold surface and in the gap layer sandwiched between two metal films. Metamaterial resonances, as reported in literature for similar structures, are not needed to fully explain the reflectance spectra. Bragg scattering of the symmetric gap SPP mode results in a gap resonance, which is insensitive to the angle of incidence over a broad angular range. The spectral position of this flat band can be controlled by tuning the grating period of the nanohole array as well as the thickness and the refractive index of the dielectric gap.

## 8.1 Introduction

Metallic nanohole arrays have been subject to extensive research after the seminal discovery of their extraordinary optical transmission.<sup>1</sup> They exhibit exceptional optical properties that are associated with the excitation of surface plasmon polariton (SPP) as well as localized surface plasmon (LSP) modes. As a consequence, metal nanohole arrays have been implemented into optical devices that serve as optical sensors<sup>2</sup>, color filters<sup>3</sup> or transparent conducting electrodes.<sup>4-6</sup>

When placed near an unperforated metal film, the arrays of nanoholes allows for the coupling of light to a metal-insulator-metal (MIM) structure. Such architecture exhibits rich characteristics including near perfect absorption<sup>7-9</sup> and coupling to magnetic resonances, similar to that found for nanoparticle arrays.<sup>10,11</sup> Near perfect absorbers were realized at visible frequencies<sup>7,8</sup> and for the near infrared part of the spectrum.<sup>9</sup> The optical response of perforated MIM structure is often assigned to the excitation of Fabry-Pérot resonances in the trilayer structures<sup>12,13</sup> as well as to the resonant excitation of coupled SPP modes located at the opposite metal/dielectric interfaces.<sup>14</sup>

Due to their relatively simple structure, perforated MIM-type metasurfaces can be readily prepared via lithographic methods.<sup>8,10</sup> Thereby, the optical properties are mainly defined by the precisely tuned structure of the material. Top-down lithographic processes such as e-beam lithography or focused-ion-beam milling give structural control on the nanometer range, thus being capable of fabricating metamaterials for wavelengths down to the visible spectrum.<sup>14</sup> Nevertheless, for the sake of large-scale production, much effort is put into the development of solution-processed techniques, which capitalize on self-assembly methods.<sup>15</sup> Nanohole arrays coupled to thin metal films were, therefore, prepared using nanosphere lithography (NSL).<sup>16</sup> The wavelength of the primary resonance satisfied both the grating equation of the nanohole array and the Fabry-Pérot condition, thus showing a strong dependence on the distance between the nanohole array and the metal film.<sup>13</sup> Closely connected are nanohole-dielectric-nanohole structures, which equally show the existence of gap modes.<sup>17-19</sup>

Here we present a full and comprehensive understanding of a MIM structure, which is prepared by a facile and scalable implementation of NSL. The MIM architecture comprises a highly ordered nanohole arrays separated from a continuous gold film by a thin polymer layer. Using angle-resolved UV-vis-NIR spectroscopy, we were able to fully assign the rich plasmonic response of the resulting nanocavity arrays to diffraction coupling to only two SPP modes. We explored the structure-property relationship concerning the gap size and period of the nanohole arrays in detail and identified rules to prepare structures with remarkably narrow resonances exhibiting high absorption efficiency.

## 8.2 Results and Discussion

The preparation of the MIM structures starts with the fabrication of gold nanohole arrays on a sacrificial layer via NSL (Figure 8.1a). Subsequently, the nanohole arrays were transferred onto the target substrate comprising the readily prepared spacer layer (poly(methyl methacrylate) (PMMA)) on top of a continuous gold film, following the recently published, interface-mediated method.<sup>17</sup> This transfer process allowed for a fast and modular production of metasurface areas at square centimeter scale with highly uniform and reproducible optical properties. In Figure 8.1b the geometrical parameters of the assembled structures are displayed. The lattice period  $p$  and the hole diameter  $d$  of the gold nanohole arrays are determined by the initial particle diameter and the particle diameter after plasma etching, respectively. An SEM image of a typical sample is shown in Figure 8.1c.

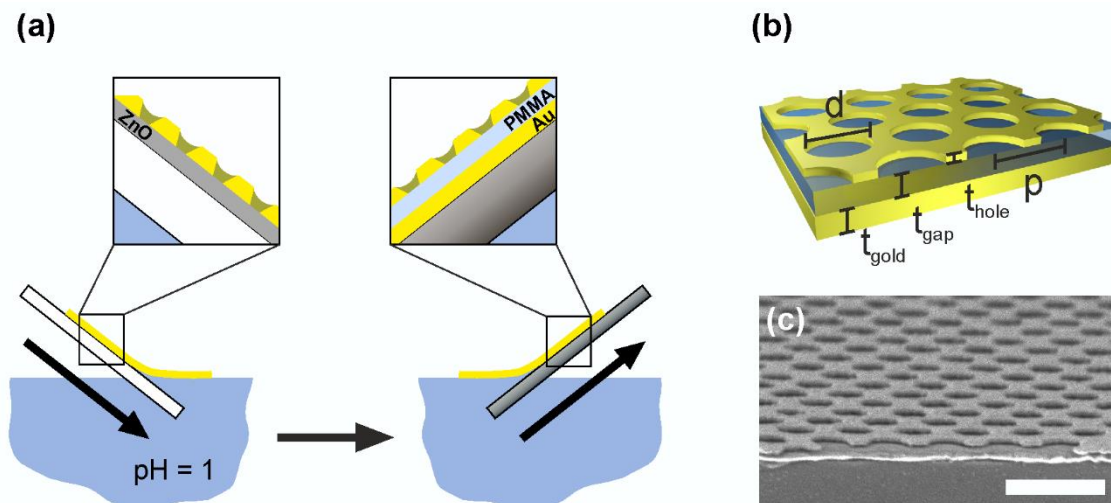


**Figure 8.1.** Metal-insulator-metal structures. (a) Scheme of transfer of gold nanohole arrays via the water/air interface. (b) Schematic illustration of the MIM geometry. (c) Side-view scanning electron microscopy image of a prepared MIM structure. Scale bar is 1  $\mu\text{m}$ .

In order to characterize the optical properties of the prepared MIM nanostructures, series of reflectance measurements were carried out for varied angles of incidence and wavelengths in the visible and near-infrared part of the optical spectrum. Firstly, the reflectance measurements were performed at an angle of incidence fixed at  $\theta = 10^\circ$  for samples with different lattice period  $p$ . We chose periods of  $p = 375 \text{ nm}$ ,  $p = 570 \text{ nm}$  and  $p = 1040 \text{ nm}$  while keeping the  $d/p$  ratio constant at 0.75. The thickness of the PMMA gap layer and the perforated metallic film was adjusted to  $t_{\text{gap}} = 40 \text{ nm}$  and  $t_{\text{hole}} = 90 \text{ nm}$ , respectively. As the thickness of the bottom gold layer was set to  $t_{\text{gold}} = 100 \text{ nm}$ , the transmittance through the structure is negligible. As seen in the photographs in the inset of Figure 8.2 and the optical microscopy images (Figure S8.1), the samples with varied geometry exhibit distinct colors. The uniformity of these colors suggests an excellent spatial homogeneity over a sample area of  $> 1 \text{ cm}^2$  that can be fabricated on very short timescales. As can be seen in Figure 8.2, the perceived color of the gold MIM nanostructures is due to a series of narrow dips in the reflectivity spectrum, which occur in the visible and NIR part of the spectrum.

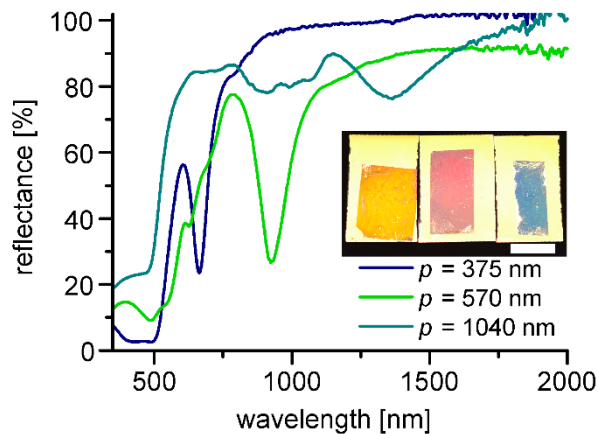


**Figure 8.2.** Influence of the lattice period. Total reflectance of MIM structures with distinct lattice periods of the nanohole arrays measured at an angle of incidence of  $\theta = 10^\circ$  with unpolarized light. The inset shows a photograph of the macroscopic samples with  $p = 375$  nm,  $p = 570$  nm and  $p = 1040$  nm (from left to right). Scale bar is 10 mm.

In general, by increasing the lattice period  $p$  the spectral position of the reflectance dips shifts to longer wavelengths. For example, the MIM nanostructure with  $p = 375$  nm exhibits the most prominent reflectivity dip at a wavelength of 665 nm, while it is strongly redshifted to 926 nm for  $p = 570$  nm and further to 1363 nm for  $p = 1040$  nm. These resonances exhibit extraordinarily high Q-factors compared to other self-assembled materials.<sup>23</sup> The corresponding Q-factors (calculated by dividing the resonance wavelength by the full width at half minimum of the resonance) are equal to 14, 8 and 6 for the samples with periods of 375 nm, 570 nm, and 1040 nm, respectively. These high values are surprising considering the defects that are inevitable when using a bottom-up approach and support the robustness of our method. The dependence of the determined Q factors on the wavelength can be attributed to varied coupling strength for the chosen  $d/p$  ratio (which may cause over-coupling of the longer wavelength resonances) and higher sensitivity to defects of the lattice that is attributed to the increasing propagation length of SPPs with the wavelength. Additionally, a broad absorption band is visible below 500 nm which does not change with the period  $p$  and which originate from the decreased reflectivity from gold above its plasma frequency. The narrow dips occurring in the red and NIR part of the spectrum are attributed to the resonant excitation of SPP modes supported by the MIM structure with a dielectric gap layer sandwiched between the flat bottom gold layer and the gold film with the nanohole arrays. These resonances are not visible for nanohole arrays without the bottom gold layer (Figure S8.2) and rapidly vanish when reducing the thickness of the bottom gold layer to a thickness comparable to the skin depth of gold

(~ 20 -45 nm) (Figure S8.3). As soon as the bottom gold film exceeds the skin depth of gold, however, the optical properties are hardly affected by the film thickness.<sup>24</sup>

To clarify the nature of the observed resonances, we performed reflectance measurements with incident angles between  $\theta = 6^\circ$  and  $\theta = 60^\circ$ . Figure 8.3a shows an example of the measured spectra for a structure with  $p = 570$  nm and  $t_{\text{gap}} = 50$  nm. These results show a rich set of spectral features that shift with the angle of incidence, particularly at around 700 nm, and which appear non-dispersive for the resonance close to 900 nm. Additional reflectance dips are observed at longer wavelengths of around 1160 nm for non-normal angles of incidence, and they split into three branches for increasing angles of incidence. All these resonances depend on the grating period  $p$  of the nanohole array (Figures S8.5 and S8.6).

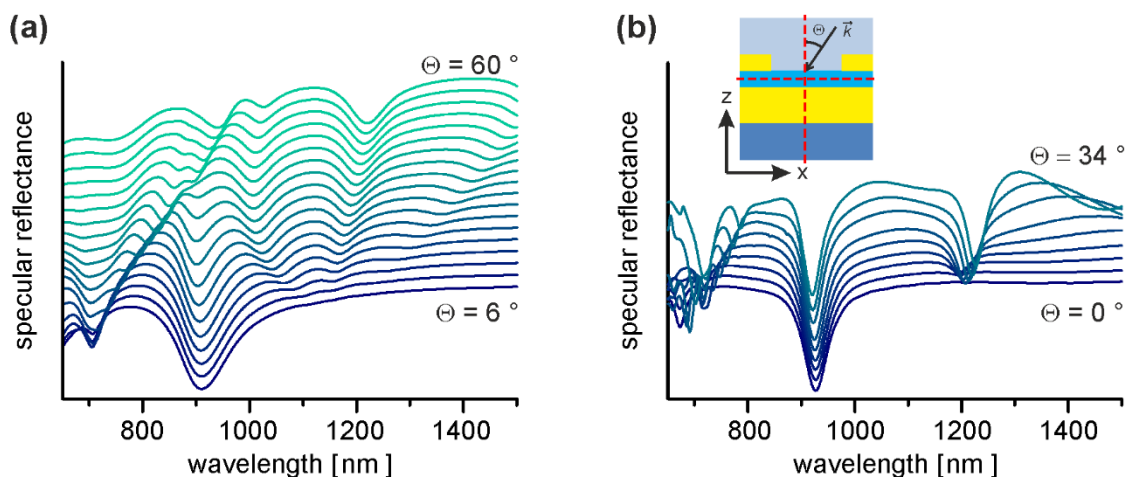


**Figure 8.3.** Influence of angle of incidence. Angle-resolved reflectance measurements (a) and FDTD simulations (b) for a sample with  $p = 570$  nm and  $t_{\text{gap}} = 50$  nm and p-polarized light. The measurements in (a) were conducted in  $3^\circ$  steps. Spectra in (b) were calculated at  $\theta = 0^\circ, 4^\circ, 8^\circ, 14^\circ, 18^\circ, 22^\circ, 26^\circ, 30^\circ, 34^\circ$ . The angle of incidence is defined in the inset of (b).

Interestingly, the observed optical properties of MIM nanostructures are in stark contrast to that of nanohole arrays without the bottom gold film, which represents a well-characterized system (Figure S8.4). In order to elucidate the nature of the observed resonances at perforated MIM structures, finite-difference time-domain (FDTD) simulations were employed, and these results were complemented by an analytical theory based on diffraction phase-matching to surface plasmon waves. The modal analysis was performed for non-perforated top gold films, and it revealed that only two surface plasmon modes with transverse magnetic (p) polarization are supported by the MIM structure. The first surface plasmon mode,  $\text{SP}_{\text{air}}$ , propagates at the top Au/air interface. The second gap surface plasmon,  $\text{SP}_{\text{gap}}$ , confines its energy in the PMMA layer sandwiched between two metallic films. This mode exhibits a symmetric profile of the electric

field. Moreover, additional anti-symmetric gap surface plasmon can occur but the investigated thicknesses of the PMMA gap  $t_{\text{gap}} < 100$  nm are below its cutoff, and therefore this mode is not present.<sup>25</sup>

The light incident at the periodically perforated MIM structure can couple to  $\text{SP}_{\text{air}}$  and  $\text{SP}_{\text{gap}}$  by diffraction. The resonant excitation of these modes occurs when the phase-matching condition is fulfilled, and the real part of the mode propagation constant  $\text{Re}\{\beta\}$  is matched to that of the parallel component of incident light  $k_0 \sin(\theta)$  by the grating momentum  $2\pi/p$ . In general, the diffraction coupling to surface plasmon modes on a grating with hexagonal symmetry depends on the orientation of the lattice with respect to the incident plane and can occur via different diffraction orders (Figure S8.7). It is worth noting that the measurements were performed on areas of several  $\text{mm}^2$ , which is much larger than the single crystalline domain size of the prepared MIM 2D crystal structures. Therefore, the measured resonances due to the diffraction coupling become averaged over different orientations of the lattice.

Figure 8.3b compares the simulated reflectance spectra with those experimentally measured, which are presented in Figure 8.3a. Due to the angular dispersion of the plane wave source, the angular range for which the simulation can be carried out is limited. For the smallest angle of incidence  $\theta = 6^\circ$ , two resonances are observed in the measured data at a wavelength of about 690 nm, and 910 nm and simulations predict almost identical results with two resonance dips located at 700 and 900 nm (field distributions are discussed in Figure 8.4). According to the analytical theory, these two modes are associated with the first and second order diffraction coupling to  $\text{SP}_{\text{gap}}$  and first diffraction order coupling to  $\text{SP}_{\text{air}}$  on a hexagonal grating with  $p = 570$  nm. As can be seen in Figure S8.7a, analytical phase matching-based model predicts the appearance of these modes at longer wavelengths of 770 nm and 1200 nm. This discrepancy can be attributed to changes in the propagation constant  $\beta$  due to the perforation, which is not taken into account by the analytical model. When increasing the angle of incidence  $\theta$ , the experimentally observed short wavelength resonance splits into two branches, which indicates diffraction coupling. In addition, one can see a spectrally broad decrease in the reflectivity in between these two measured branches. However, the simulations indicate richer spectrum of modes appearing in the same spectral window when increasing the angle of incidence  $\theta$ , which can be attributed to the mixing of the second order excitation of  $\text{SP}_{\text{gap}}$  with the first order excitation of  $\text{SP}_{\text{air}}$ . This discrepancy can be attributed to the potential smearing of these features in the measured reflectivity spectrum that can be ascribed to the averaging over differently oriented lattices occurring in the colloidal crystal. In contrast to shorter wavelength resonances, the first order  $\text{SP}_{\text{gap}}$  resonance located at about 900 nm does not shift with the angle of incidence

$\theta$  as observed experimentally as well as captured by simulations. Instead, a series of dispersive bands appears at longer wavelengths around 1200 nm and 1400 nm when increasing the angle of incidence  $\theta$ . The fact that these modes disappear at normal incidence and that the  $SP_{\text{gap}}$  mode at 900 nm is non-dispersive qualitatively agrees with the simulations and can be explained by strong Bragg-scattering of the  $SP_{\text{gap}}$  modes, which is known to flatten the dispersion relation of propagating surface plasmons.<sup>26</sup>

Following this, we simulated the near-field distribution of the electromagnetic field for specific reflectivity dips at normal ( $\theta = 0^\circ$ ) and tilted ( $\theta = 22^\circ$ ) illumination of the structure with the period of  $p=570$  nm (Figure 8.4a). The spatial distribution of the electric field intensity  $|E|^2$  was normalized with that of the incident light beam  $|E_0|^2$  and showed as a cross-section parallel and perpendicular to the structure (indicated as a dashed line in the inset of Figure 8.3b). At normal incidence, only two resonances are distinctively visible in the simulated spectra at 923 nm and 670 nm. The corresponding near-field distributions predict an extreme electric field intensity confinement within the gap between the two metal films, indicating a gap-like nature of the resonances (Figure 8.4c). A dipolar characteristic is clearly apparent for the longer wavelength resonance (B) reaching an enhancement factor  $|E|^2/|E_0|^2$  of approximately 25. The resonance at 670 nm (A) shows a higher order field distribution and the field is partially confined outside the structure at the air interface. Thus, these observations agree with the hypothesis of 1<sup>st</sup> and 2<sup>nd</sup> order diffraction coupling to  $SP_{\text{gap}}$  and partial mixing with the excitation of  $SP_{\text{air}}$  at the outer interface.

Tilting the angle of incidence  $\theta$  leads to the splitting of the resonances for different diffraction orders, which are otherwise degenerated and excited simultaneously at normal incidence.<sup>27,28</sup> Therefore, new resonances are observed in the numerically simulated data between 650 nm and 780 nm and at 1194 nm (Figure 8.4b). The near-field distribution of the series of resonances noted as I - VI (as indicated in Figure 8.4b) is presented in Figure 8.4c. Interestingly, the field distribution of the strongest non-dispersive resonance (V) is not altered by changing the angle of incidence  $\theta$ . The electric field maps of the short wavelength modes I – IV show a mixed nature due to the overlap of the  $SP_{\text{gap}}$ , and the  $SP_{\text{air}}$  and particularly resonance II exhibits substantial field confinement at the outer interface. When compared with the experiments, probably only mode IV is visible, and the other resonances are smeared by averaging over lattice orientations. The longer wavelength resonances such as VI exhibit solely the  $SP_{\text{gap}}$  nature as seen in the respective near-field plots. Thus, all resonances, including the non-dispersive modes, can be attributed to either  $SP_{\text{air}}$  or  $SP_{\text{gap}}$ . This highlights the simplicity of the given

description which provides an alternative view to previous interpretations using magnetic, localized hole plasmons or Fabry-Pérot resonances.<sup>9,10,13</sup>

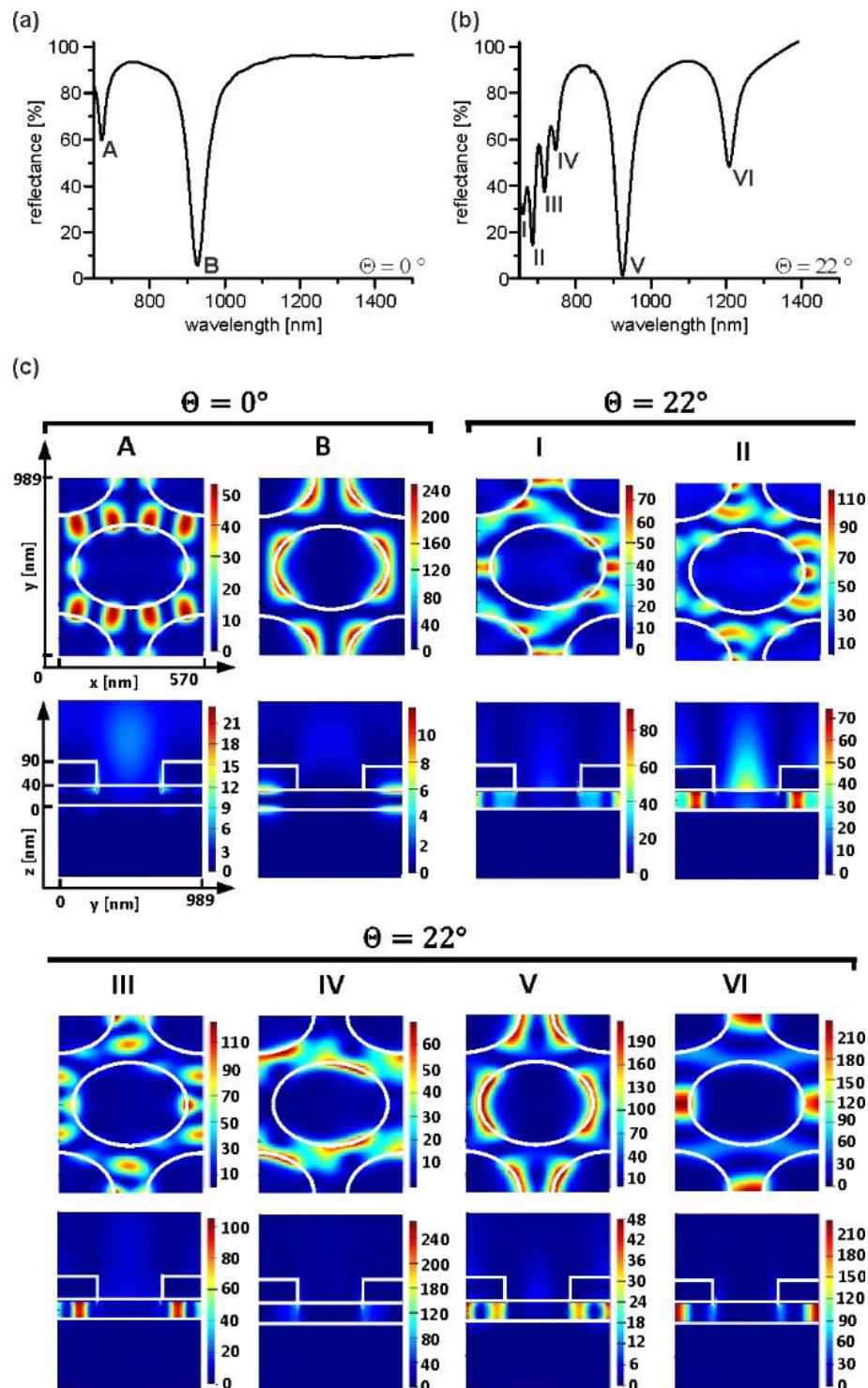


**Figure 8.4.** Simulation of the electric near-field distribution. (a) Simulated reflectance spectrum at normal incidence. (b) Simulated reflectance spectrum at  $\theta = 22^\circ$ . (c) Electric field intensity  $|E|^2$  distributions normalized to the incident electric field intensity  $|E_0|^2$  for the resonance wavelengths assigned in (a) and (b). The electric field enhancement was evaluated along the horizontal and vertical cross-sections shown in the inset of Figure 8.3b.

The influence of the gap layer thickness was examined experimentally as well as theoretically (Figure 8.5). In the experiments, the gap PMMA film thickness  $t_{\text{gap}}$  was controlled between 25 nm and 77 nm by adjusting the spin-coating parameters, and layers with a smaller thickness between 1 nm and 15 nm were prepared using a layer-by-layer approach. When decreasing the thickness  $t_{\text{gap}}$  from 77 nm to 1 nm, the strongest  $\text{SP}_{\text{gap}}$  resonance drastically shifts from 826 nm to 1417 nm. This observation is confirmed by numerical simulations (see Figure 8.5c), and the same trend is predicted by the phase-matching model due to the increased propagation constant of  $\text{SP}_{\text{gap}}$  when decreasing the gap thickness  $t_{\text{gap}}$  (see Figure S8.7c). Concomitantly, the higher order  $\text{SP}_{\text{gap}}$  resonances become strongly apparent at shorter wavelength, and they shift towards longer wavelengths when decreasing  $t_{\text{gap}}$ . In contrast, the resonance below 600 nm that is ascribed to the excitation of  $\text{SP}_{\text{air}}$  is weakly affected by changing the gap thickness  $t_{\text{gap}}$  as only a small portion of its electric field intensity is confined in the gap. For narrow gaps, gap resonances can be observed even for high angles of incidence (Figure S8.8 and Figure S8.9). In contrast, for thick gap layers, all resonances appear in a narrow wavelength range leading to strong coupling between  $\text{SP}_{\text{gap}}$  and  $\text{SP}_{\text{air}}$  modes at larger angles of incidence (Figure S8.10 and Figure S8.11). This results in a mixed nature of the resonance at large angles of incidence showing a dispersive behavior.

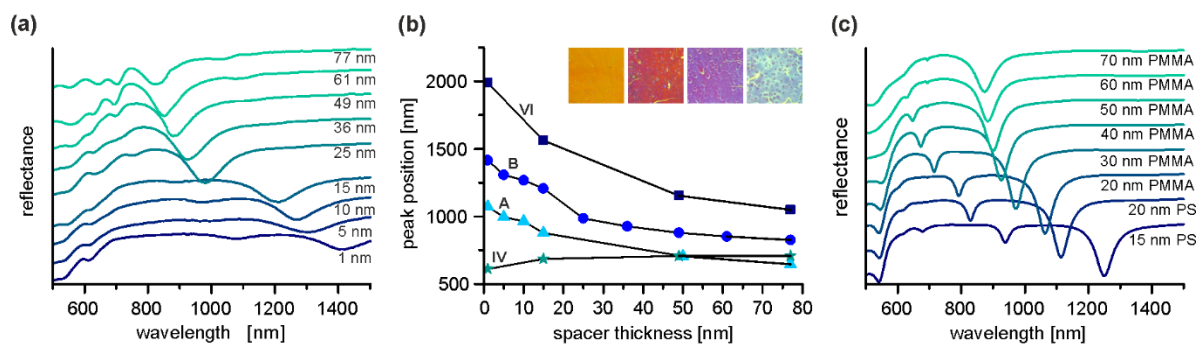


**Figure 8.5.** Influence of gap thickness. (a) Reflectance of MIM structures with distinct gap thickness measured at  $\theta = 10^\circ$  with unpolarized light. Gap layers with a thickness of  $t_{\text{gap}} < 20$  nm were prepared using a layer-by-layer approach. Layer thicknesses with  $t_{\text{gap}} > 20$  nm were prepared by spin-coating of PMMA. (b) Peak positions in dependence of the gap thickness obtained from reflectance measurements. Modes IV and VI were extracted from angle-resolved measurements. The inset shows macroscopic photographs of  $7 \times 7$  mm<sup>2</sup> MIM structures with gap thickness  $t_{\text{gap}} = 32$  nm, 40 nm, 61 nm and 77 nm. (c) Simulated reflectance of MIM structures with distinct gap thickness for normal incident light.

A complementary approach to shed light on the observed resonances was performed based on examining the influence of the refractive index environment. For this purpose, the samples were immersed in glycerine-water mixtures with different compositions. Thereby, the refractive

index above the structure can be tuned between 1.33 (pure water) and 1.47 (pure glycerine). At first, the effect of the surrounding medium was analyzed using the as-prepared MIM structure ( $p = 570$  and  $t_{\text{gap}} = 50$  nm). When increasing the surrounding refractive index from 1.33 to 1.47, the SPP confined to the outer Au interface ( $\text{SP}_{\text{air}}$ ) shifts to longer wavelengths by approximately 53 nm (Figure 8.6a). In accordance with the field profiles predicted by numerical simulations, the resonances occurring at longer wavelengths ( $\text{SP}_{\text{gap}}$ ) are not sensitive to changes in the refractive index as their electric field is mainly confined inside the structure.

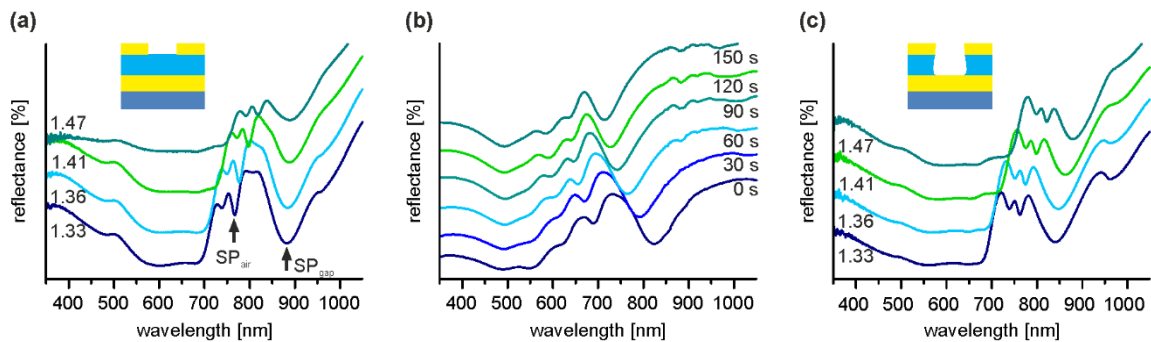


**Figure 8.6.** Refractive index sensitivity. (a) Reflectance of the as-prepared MIM structure immersed in glycerine-water mixtures with distinct refractive indices. (b) Reflectance of the MIM structures in air after different times of plasma etching. (c) Reflectance of the MIM structure etched for 150 s, immersed in glycerine-water mixtures with distinct refractive indices.

Next, capitalizing on the organic gap layer, we varied the refractive index of the dielectric gap layer with an initial thickness of  $t_{\text{gap}} = 51$  nm by plasma etching (Figure 8.6b). In consecutive etching steps, the PMMA within the holes of the nanohole array is gradually removed until the bottom gold layer is reached after 120 s. This can be inferred from the increasing depth of the holes measured by atomic force microscopy (see Figure S8.12). Nevertheless, the distance between the metal films and the homogeneity of the sample are not affected. Due to the strongly decreasing refractive index environment in the gap, all resonances (including  $\text{SP}_{\text{gap}}$ ) are shifting to shorter wavelengths. Further etching results in an ongoing shift of the resonance wavelength as now the gold-covered PMMA between the holes is removed (underetching). Thus, a quasi-free-standing nanohole array is produced. The smallest shift of 54 nm after 150 s is observed for the mode confined to the Au/air interface ( $\text{SP}_{\text{air}}$ ). A higher sensitivity to a change in the refractive index was expected for the gap modes because of the high electric field intensities within the dielectric gap. Indeed, a strong spectral shift from 824 nm to 714 nm is seen for  $\text{SP}_{\text{gap}}$  resonance. We then immersed the MIM sample with a quasi-freestanding nanohole array into glycerine-water mixtures (Figure 8.6c). Thus, the liquid medium can penetrate the nanohole

arrays and change the refractive index between the two gold films. As expected, with a spectral shift of 60 nm, the sensitivity of the  $SP_{\text{air}}$  resonance in the etched sample is comparable to the non-etched sample. At the same time, the resonance wavelength of the  $SP_{\text{gap}}$  mode is now influenced. A shift of 39 nm can be observed when increasing the surrounding refractive index from 1.33 to 1.47. Altogether, the sensitivity of the MIM-stack results in 379 nm/RIU and 429 nm/RIU for the  $SP_{\text{air}}$  mode in the unetched and etched sample and 279 nm/RIU for the  $SP_{\text{gap}}$  mode.

### 8.3 Conclusion

In summary, we demonstrated the production of trilayer MIM cavities via a simple bottom-up approach. By using an interface-mediated transfer of gold nanohole arrays prepared via nanosphere lithography, high-quality metamaterials were fabricated on a substrate with square centimeter area. We thoroughly characterized the optical properties of the resulting MIM stacks composed of an opaque gold film, a polymer gap layer and a second gold film comprising the nanohole array. The rich plasmonic response can be assigned to the coupling to only two propagating surface plasmon modes, which is strongly dependent on the grating period of the nanohole array and the thickness of the dielectric gap. The resonant excitation of the symmetric  $SP_{\text{gap}}$  resonance is insensitive to the angle of incidence and shows an unusually high Q-factor for self-assembled materials comparable to those prepared by top-down lithography techniques. The detailed understanding of the presented phenomena in combination with absorbing layers is of great importance for light harvesting devices.<sup>4,29,30</sup>

### 8.4 Experimental Section

**Materials:** Polystyrene particles were purchased at Microparticles GmbH (Berlin).

**Fabrication of ZnO coated substrates:** The ZnO layers were prepared using a sol-gel method. For this, glass slides were cleaned for 10 min by ultrasonication in 2 % aqueous Hellmanex (Hellma GmbH, Mühlheim, Germany) solution in MilliQ water. After rinsing off the surfactant with MilliQ water, the substrates were further sonicated for 10 minutes in ethanol and finally dried with compressed air. Subsequently, the ZnO films were formed by spin coating a zinc

acetate solution (110 mg zinc acetate in 30  $\mu$ l 2-aminoethanol and 1 ml 2-methoxyethanol) at 2000 rpm for 50 s and subsequent baking at 150 °C for 5 min.

**Fabrication of Au nanomeshes:** Monolayers of polystyrene particles were prepared according to the procedure of Retsch *et al.*<sup>20</sup> Cationically functionalized glass slides were spin-coated with a 3 wt% particle dispersion at 4000 rpm. Subsequently, the coated glass substrates were immersed into a 0.1 mM SDS solution in MilliQ. The aqueous phase was adjusted to pH 12 by adding a few drops of NH<sub>3</sub>. A monolayer was formed at the liquid/air interface by self-assembly of the detaching particles. The monolayer was transferred to the ZnO coated glass substrates and dried in air. The monolayers were etched in a plasma reactor MiniFlecto (Plasma Technology GmbH, Herrenberg, Germany) with 75 % argon and 25 % oxygen at 80 W at a pressure of 0.14 mbar to obtain non-close packed monolayers. A 3 nm chromium layer and 50 nm gold were deposited using a Balzers BA360 thermal evaporation chamber. The layer thickness was monitored via an SQM 160 microbalance (Sigma Instruments, Schaefer Technologie GmbH). Afterwards, the particles were removed using Scotch® tape (3M) giving the nanohole arrays. The Au substrates were cleaned by ultrasonication for 10 min in THF and dried with compressed air. All samples were stored under inert gas.

**Fabrication of MIM structures:** 100 nm thick gold film was deposited on cleaned microscopy slides. Subsequently, the gap layer was prepared by spin-coating commercially available poly(methyl methacrylate) (PMMA). Thin gap layers (1 nm – 15 nm) were made via a layer-by-layer approach. For this, one layer of polyethylenimine followed by alternating layers of poly(styrene sulfonate) and poly(allylamine hydrochloride) were applied by spray-coating. The Au nanohole arrays were detached from their parental substrate by immersion into an aqueous hydrochloric acid solution (pH 1) with a speed of 1 mm/min and an immersion angle of 45 ° using a home built dip-coater system. After complete detachment of the gold film, the nanohole array is transferred when lifting the receiving substrate out of the water phase.

**Characterization:** UV-vis-NIR spectra were measured using the Diffuse Reflectance Accessory of a Cary 5000 UV-vis-NIR Spectrophotometer (Agilent Technologies) at 10 ° angle of incidence with unpolarized light. Angle-resolved UV-vis-NIR spectroscopy was conducted with the Universal Measurement Accessory of the same spectrometer with 3 ° increment with p- and s-polarized light. To examine the effect of the refractive index environment the samples were immersed in glycerine/water mixtures with refractive indices of 1.33 (pure water), 1.36 (20 % glycerine), 1.41 (60 % glycerine) and 1.47 (pure glycerine).

SEM images were taken on a LEO 1530 Gemini Field Emission SEM (Carl Zeiss AG, Oberkochen, Germany). The images were evaluated with the software ImageJ.<sup>31</sup>

Atomic force microscopy was performed in tapping mode on a Dimension 3100 microscope (Veeco, USA) with a Nanoscope IV controller and OTESPA-R3 (Bruker) cantilevers. The AFM images were analyzed with the software Nanoscope Analysis.

**FDTD simulations:** A commercial package by Lumerical that relies on the finite-difference time-domain method was used to simulate optical properties of gold nanomeshes.<sup>32</sup> As shown in Figure S8.13, a rectangular unit cell with the hexagonal arrays of holes was used. Bloch boundary conditions were applied at the interfaces of the unit cell that are perpendicular to the structure surface while perfectly matched layers were used on its top and bottom. The investigated structure was approximated by a stack of a perforated gold layer with the thickness of  $t_{\text{hole}} = 50$  nm, an intermediate layer of PMMA with a thickness of  $t_{\text{gap}}$  and a flat gold layer with a thickness of  $t_{\text{gold}} = 100$  nm. Refractive index of PMMA of  $n_{\text{PMMA}} = 1.4848$  was used in the whole spectral range, and the refractive index of gold was determined by fitting to CRC data.<sup>33</sup> BK7 glass substrate with  $n_{\text{substrate}} = 1.52$  was assumed below the plasmonic stack of layers. The excitation light beam was generated with a plane wave source in air above the structure, and it was made incident on the perforated gold film. In the used version of FDTD solutions, planar sources exhibit angular dispersion if the beam does not propagate normal to the source. To minimize the angular dispersion, simulations were carried out for wavelength range 550 nm to 900 nm and 900 nm to 1500 nm separately, and the spectra were subsequently stitched. Field intensity and power monitors were placed above or below the unit cell in order to obtain reflectivity and transmission spectra. Electric near-field intensity profiles were calculated by using monitors placed inside the structure. Convergence of the simulation results was confirmed by variation of mesh size and comparison of reflectance results (Figure S8.14).

### Acknowledgements

The work in Bayreuth was funded by the German Research Foundation (DFG) by the SFB840. C.S. acknowledges support from the Elite Network of Bavaria (ENB). The authors thank Dr. Beate Förster and Martina Heider from the Bavarian Polymer Institute (BPI) for their support using the scanning electron microscopy facilities. J.D. and S.F. was supported by European Union's Horizon 2020 research and innovation programme under grant agreement no 633937, project ULTRAPLACAD.

## References

1. Ebbesen, T. W., Lezec, H. J., Ghaemi, H. F., Thio, T. & Wolff, P. A. Extraordinary optical transmission through sub-wavelength hole arrays. *Nature* **391**, 667-669 (1998).
2. Sharma, N., Keshmiri, H., Zhou, X., Wong, T. I., Petri, C., Jonas, U., Liedberg, B. & Dostalek, J. Tunable Plasmonic Nanohole Arrays Actuated by a Thermoresponsive Hydrogel Cushion. *J. Phys. Chem. C* **120**, 561-568 (2016).
3. Inoue, D., Miura, A., Nomura, T., Fujikawa, H., Sato, K., Ikeda, N., Tsuya, D., Sugimoto, Y. & Koide, Y. Polarization independent visible color filter comprising an aluminum film with surface-plasmon enhanced transmission through a subwavelength array of holes. *Appl. Phys. Lett.* **98**, 093113 (2011).
4. Stelling, C., Singh, C. R., Karg, M., König, T. A. F., Thelakkat, M. & Retsch, M. Plasmonic nanomeshes: their ambivalent role as transparent electrodes in organic solar cells. *Sci. Rep.* **7**, 42530 (2017).
5. Zhu, J., Zhu, X., Hoekstra, R., Li, L., Xiu, F., Xue, M., Zeng, B. & Wang, K. L. Metallic nanomesh electrodes with controllable optical properties for organic solar cells. *Appl. Phys. Lett.* **100**, 143109 (2012).
6. Morfa, A. J., Akinoglu, E. M., Subbiah, J., Giersig, M. & Mulvaney, P. Transparent metal electrodes from ordered nanosphere arrays. *J. Appl. Phys.* **114**, 054502 (2013).
7. Hu, C., Zhao, Z., Chen, X. & Luo, X. Realizing near-perfect absorption at visible frequencies. *Opt. Express* **17**, 11039 (2009).
8. Cheng, F., Yang, X., Rosenmann, D., Stan, L., Czaplewski, D. & Gao, J. Enhanced structural color generation in aluminum metamaterials coated with a thin polymer layer. *Opt. Express* **23**, 25329-25339 (2015).
9. Pitchappa, P., Ho, C. P., Kropelnicki, P., Singh, N., Kwong, D.-L. & Lee, C. Dual band complementary metamaterial absorber in near infrared region. *J. Appl. Phys.* **115**, 193109 (2014).
10. Behera, G. & Ramakrishna, S. A. Tri-layered composite plasmonic structure with a nanohole array for multiband enhanced absorption at visible to NIR frequencies: plasmonic and metamaterial resonances. *J. Phys. D-Appl. Phys.* **49**, 075103 (2016).
11. Maurer, T., Adam, P.-M. & Lévêque, G. Coupling between plasmonic films and nanostructures: from basics to applications. *Nanophotonics* **4**, 363-382 (2015).
12. Shu, S. & Li, Y. Y. Triple-layer Fabry-Perot/SPP aluminum absorber in the visible and near-infrared region. *Opt. Lett.* **40**, 934-937 (2015).
13. Tagliabue, G., Höller, C., Eghlidi, H. & Poulidakos, D. Proximal gap-plasmon nanoresonators in the limit of vanishing inter-cavity separation. *Nanoscale* **6**, 10274-10280 (2014).
14. Fang, Z., Zhen, Y.-R., Fan, L., Zhu, X. & Nordlander, P. Tunable wide-angle plasmonic perfect absorber at visible frequencies. *Phys. Rev. B: Condens. Matter* **85** (2012).
15. Mayer, M., Tebbe, M., Kuttner, C., Schnepf, M. J., König, T. A. & Fery, A. Template-assisted colloidal self-assembly of macroscopic magnetic metasurfaces. *Faraday Discuss.* **191**, 159-176 (2016).
16. Vogel, N., Weiss, C. K. & Landfester, K. From soft to hard: the generation of functional and complex colloidal monolayers for nanolithography. *Soft Matter* **8**, 4044-4061 (2012).
17. Wu, Z., Chen, X., Wang, M., Dong, J. & Zheng, Y. High-Performance Ultrathin Active Chiral Metamaterials. *ACS Nano* **12**, 5030-5041 (2018).
18. Ortuño, R., García-Meca, C., Rodríguez-Fortuño, F. J., Martí, J. & Martínez, A. Role of surface plasmon polaritons on optical transmission through double layer metallic hole arrays. *Phys. Rev. B* **79** (2009).

19. Stelling, C. & Retsch, M. Nanomeshes at Liquid Interfaces: From Free-Standing Hole Arrays toward Metal-Insulator-Metal Architectures. *Adv. Mater. Interfaces* **5**, 1800154 (2018).
20. Retsch, M., Zhou, Z., Rivera, S., Kappl, M., Zhao, X. S., Jonas, U. & Li, Q. Fabrication of Large-Area, Transferable Colloidal Monolayers Utilizing Self-Assembly at the Air/Water Interface. *Macromol. Chem. Phys.* **210**, 230-241 (2009).
21. Vogel, N., Goerres, S., Landfester, K. & Weiss, C. K. A Convenient Method to Produce Close- and Non-close-Packed Monolayers using Direct Assembly at the Air-Water Interface and Subsequent Plasma-Induced Size Reduction. *Macromol. Chem. Phys.* **212**, 1719-1734 (2011).
22. Parchine, M., McGrath, J., Bardosova, M. & Pemble, M. E. Large Area 2D and 3D Colloidal Photonic Crystals Fabricated by a Roll-to-Roll Langmuir-Blodgett Method. *Langmuir* **32**, 5862-5869 (2016).
23. Volk, K., Fitzgerald, J. P. S., Ruckdeschel, P., Retsch, M., König, T. A. F. & Karg, M. Reversible Tuning of Visible Wavelength Surface Lattice Resonances in Self-Assembled Hybrid Monolayers. *Advanced Optical Materials* **5**, 1600971 (2017).
24. Christ, A., Leveque, G., Martin, O. J., Zentgraf, T., Kuhl, J., Bauer, C., Giessen, H. & Tikhodeev, S. G. Near-field-induced tunability of surface plasmon polaritons in composite metallic nanostructures. *J. Microsc.* **229**, 344-353 (2008).
25. Dionne, J. A., Sweatlock, L. A., Atwater, H. A. & Polman, A. Plasmon slot waveguides: Towards chip-scale propagation with subwavelength-scale localization. *Phys. Rev. B: Condens. Matter* **73**, 035407 (2006).
26. Barnes, W. L., Preist, T. W., Kitson, S. C. & Sambles, J. R. Physical origin of photonic energy gaps in the propagation of surface plasmons on gratings. *Phys. Rev. B: Condens. Matter* **54**, 6227-6244 (1996).
27. Ghaemi, H., Thio, T., Grupp, D., Ebbesen, T. & Lezec, H. Surface plasmons enhance optical transmission through subwavelength holes. *Phys. Rev. B: Condens. Matter* **58**, 6779-6782 (1998).
28. Couture, M., Liang, Y., Poirier Richard, H. P., Faid, R., Peng, W. & Masson, J. F. Tuning the 3D plasmon field of nanohole arrays. *Nanoscale* **5**, 12399-12408 (2013).
29. Diukman, I., Tzabari, L., Berkovitch, N., Tessler, N. & Orenstein, M. Controlling absorption enhancement in organic photovoltaic cells by patterning Au nano disks within the active layer. *Opt. Express* **19 Suppl 1**, A64-71 (2011).
30. Fei Guo, C., Sun, T., Cao, F., Liu, Q. & Ren, Z. Metallic nanostructures for light trapping in energy-harvesting devices. *Light-Sci. Appl.* **3**, e161 (2014).
31. Rasband, W. S. *ImageJ*, U. S. National Institutes of Health, Bethesda, Maryland, USA, <http://imagej.nih.gov/ij> (1997-2018).
32. Lumerical Inc. *Lumerical Inc.*, <http://www.lumerical.com/tcad-products/fdtd/>
33. Weaver, J. H. & Frederikse, H. P. R. in *CRC Handbook of Chemistry and Physics*. (ed David R. Lide) Ch. 12, 33-156 (CRC Press, 2005).

## 8.5 Supporting Information

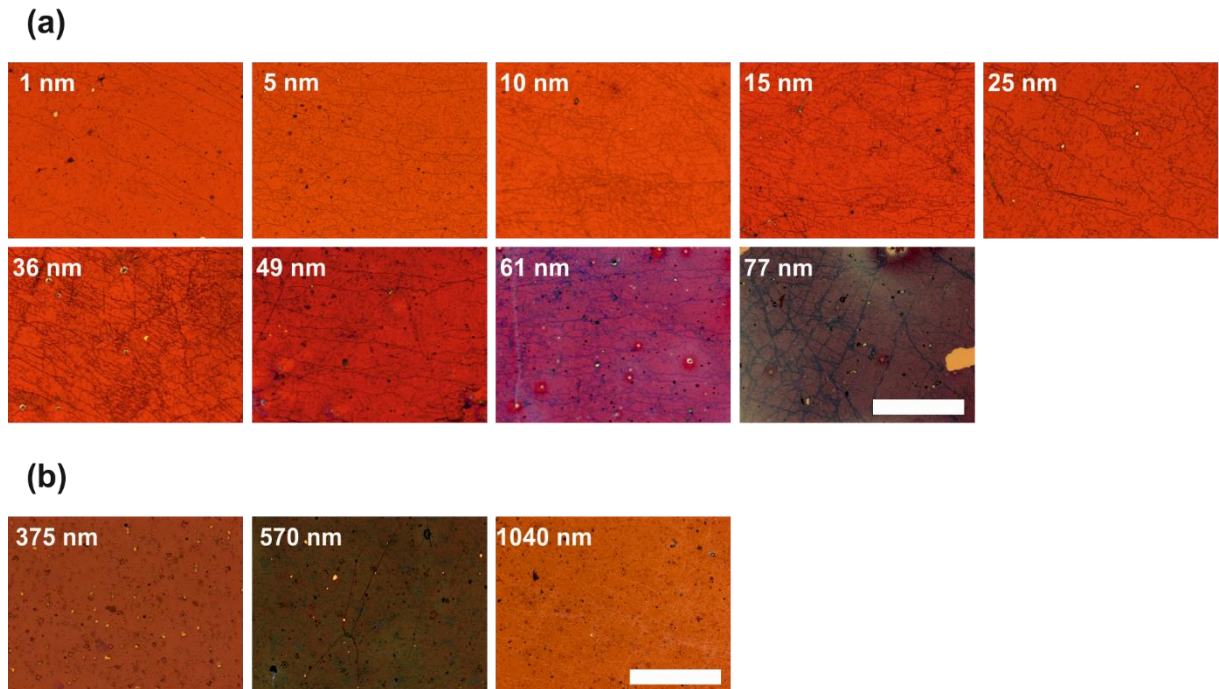


**Figure S8.1.** Optical microscopy images of MIM structures with (a) distinct spacer thicknesses and (b) distinct lattice periods. Scale bars are 500  $\mu\text{m}$ .

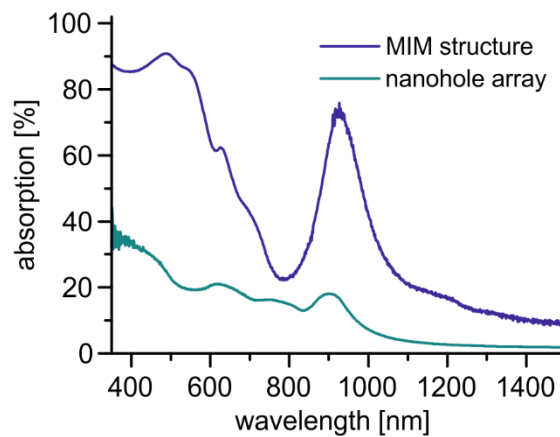


**Figure S8.2.** Measured absorption (1-reflectance) of a MIM structure with  $p = 570$  nm,  $t_1 = 100$  nm,  $t_2 = 50$  nm and  $t_3 = 90$  nm compared to an isolated gold nanohole array with  $p = 570$  nm.

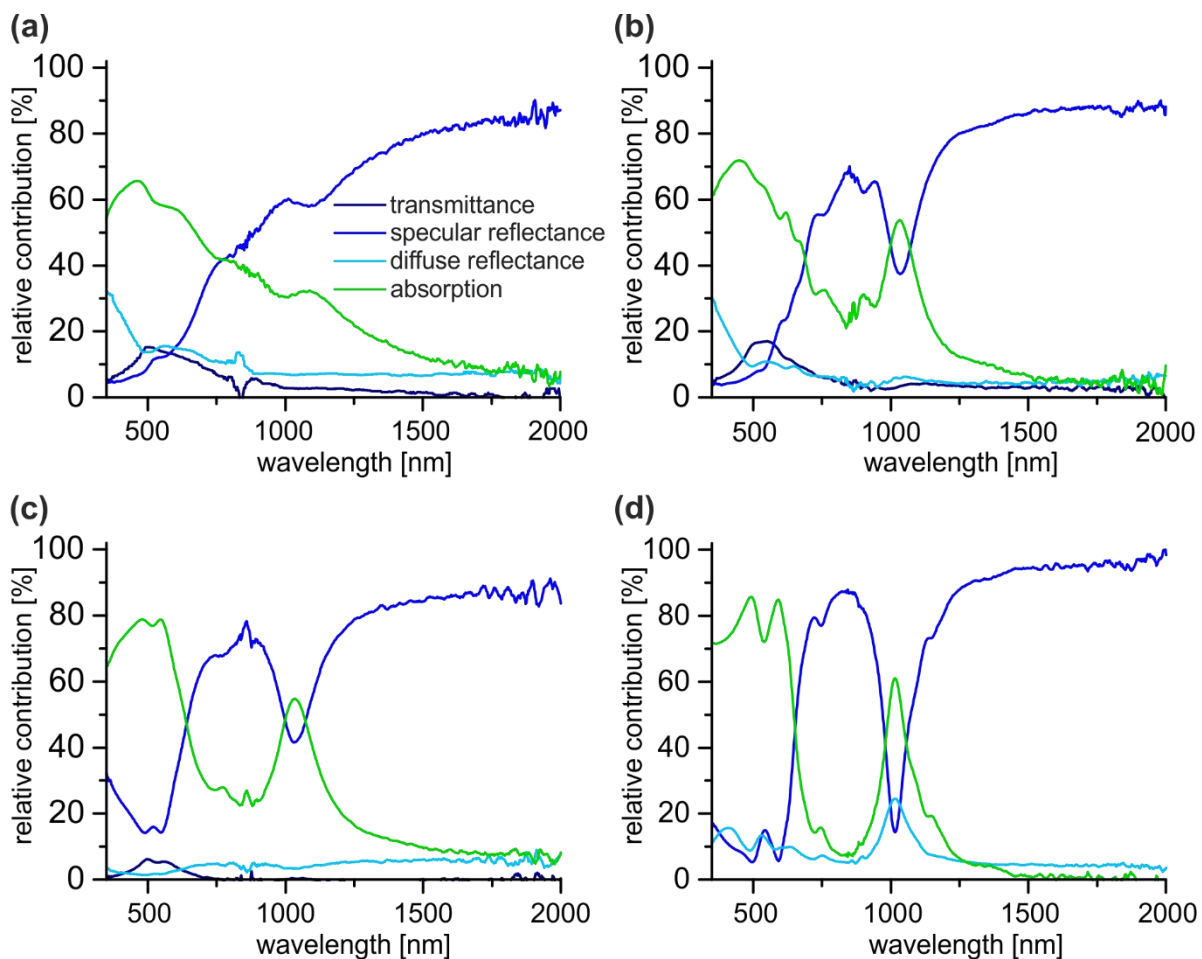


**Figure S8.3.** Influence mirror thickness. Transmittance, specular reflectance, diffuse reflectance and absorption for MIM structures with  $p = 570$  nm,  $t_2 = 30$  nm,  $t_3 = 80$  nm and (a)  $t_1 = 13$  nm (b)  $t_1 = 21$  nm (c)  $t_1 = 40$  nm (d)  $t_1 = 100$  nm.

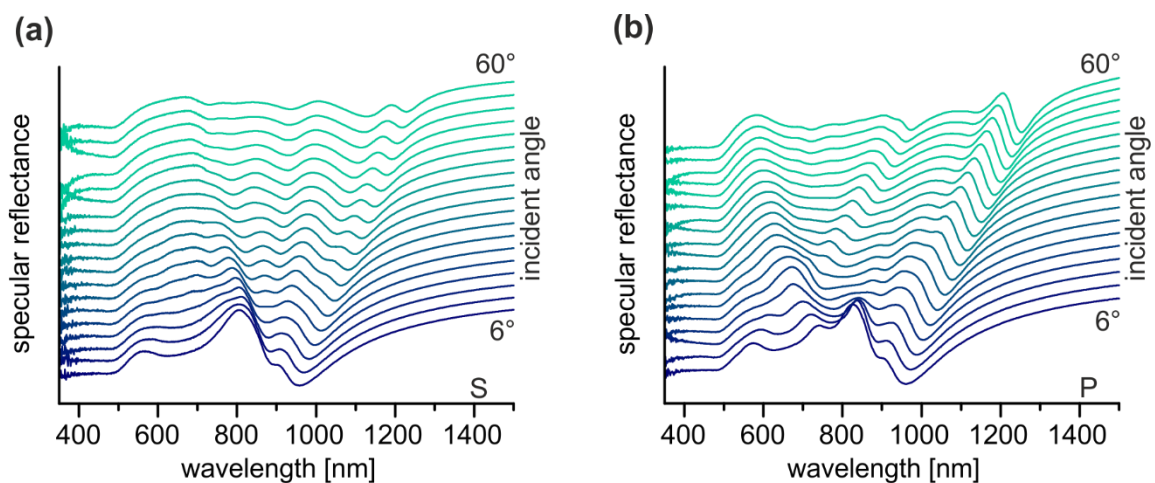


**Figure S8.4.** Angle-resolved reflectance measurements with (a) s-polarized and (b) p-polarized light of an isolated gold nanohole array with  $p = 570$  nm.

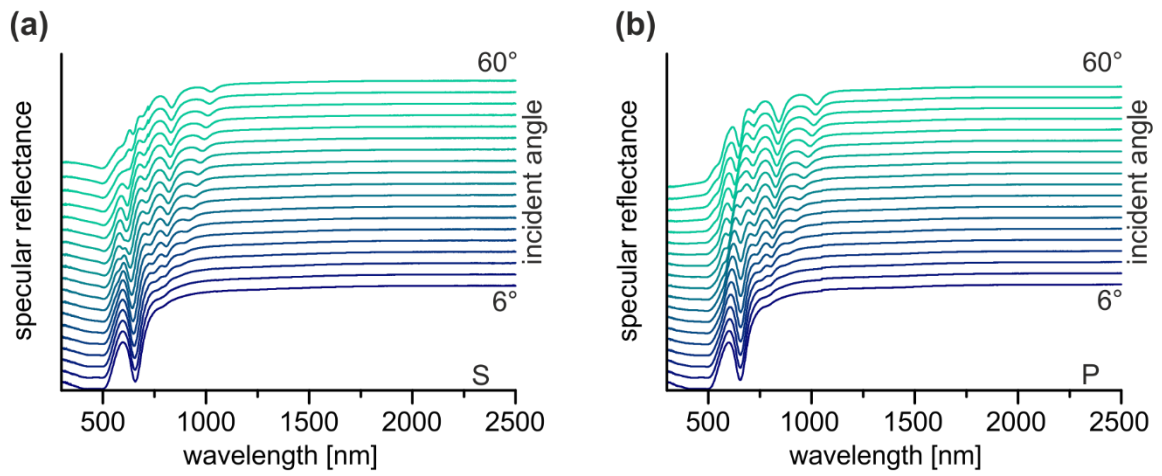


**Figure S8.5.** Angle-resolved reflectance measurements with (a) s-polarized and (b) p-polarized light of a MIM structure with  $p = 375$  nm,  $t_1 = 100$  nm,  $t_2 = 40$  nm and  $t_3 = 90$  nm.

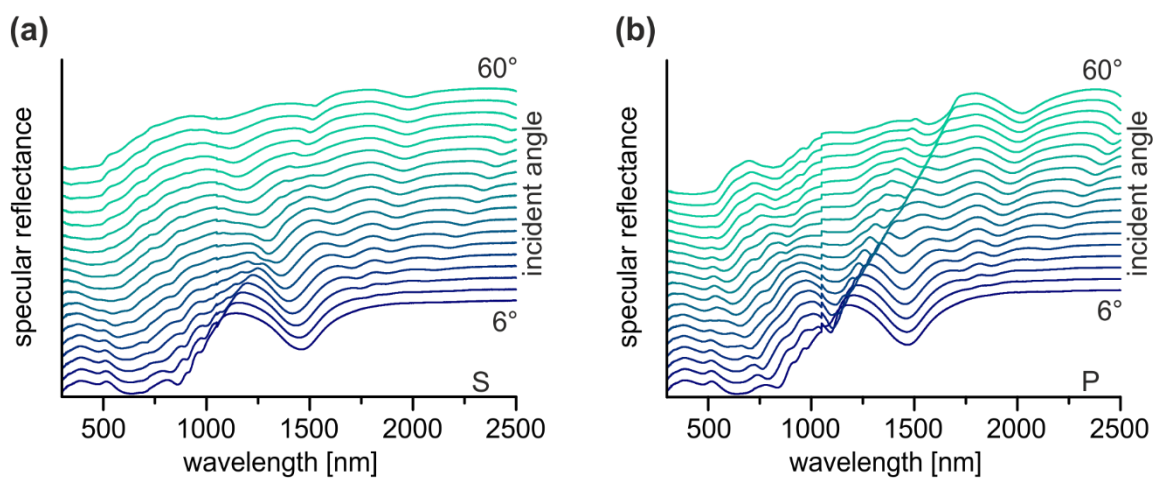


**Figure S8.6.** Angle-resolved reflectance measurements with (a) s-polarized and (b) p-polarized light of a MIM structure with  $p = 1040$  nm,  $t_1 = 100$  nm,  $t_2 = 40$  nm and  $t_3 = 90$  nm.

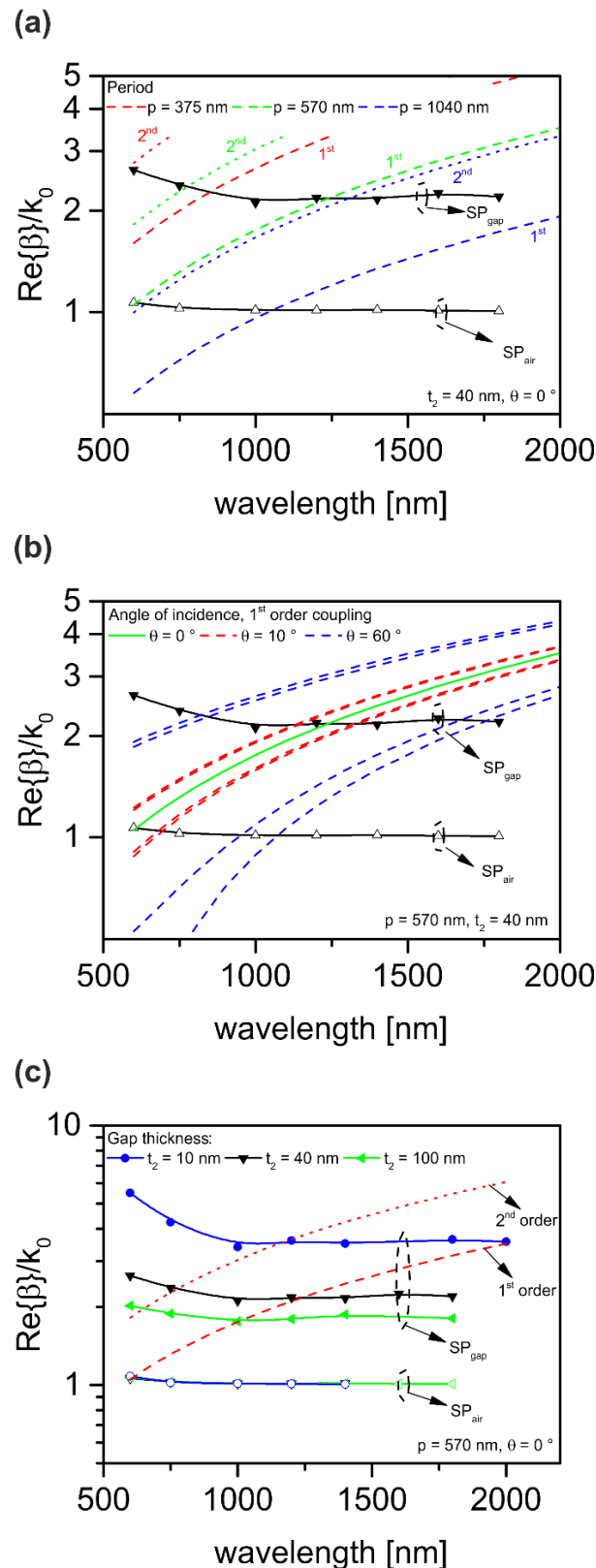


**Figure S8.7.** Analytically derived dispersion curves of the two SPP modes present in the MIM structures. (a) Influence of the lattice period at normal incidence. (b) Influence of the angle of incidence for  $p = 570$  nm. Assumed coupling via all (0,1), (1,0), (1,1), (0,1), (1,0) and (1,1) orders. The plane of incidence was assumed to be parallel with (0,1) and (0,1) orders. (c) Influence of the spacer thickness for  $p = 570$  nm at normal incidence.  $\beta$  is the propagation constant of guided modes,  $k_0$  is the light wavenumber in vacuum.

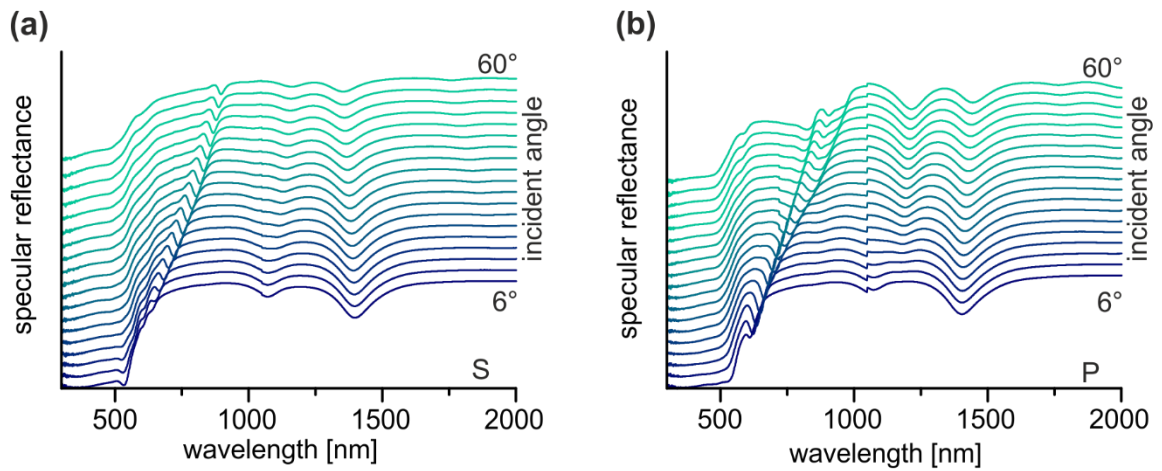


**Figure S8.8.** Angle-resolved reflectance measurements with (a) s-polarized and (b) p-polarized light of a MIM structure with  $p = 570$  nm,  $t_1 = 100$  nm,  $t_2 = 1$  nm and  $t_3 = 90$  nm.

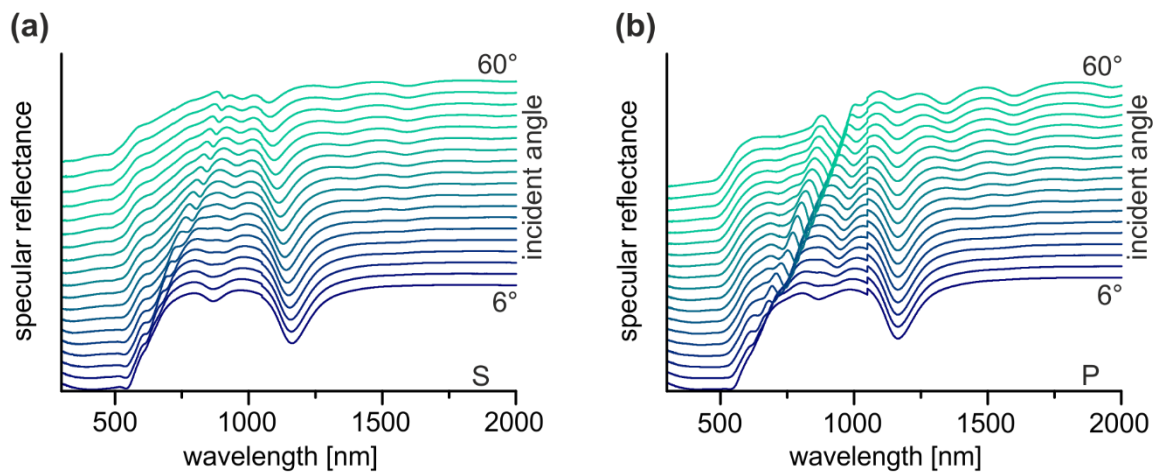


**Figure S8.9.** Angle-resolved reflectance measurements with (a) s-polarized and (b) p-polarized light of a MIM structure with  $p = 570$  nm,  $t_1 = 100$  nm,  $t_2 = 15$  nm and  $t_3 = 90$  nm.

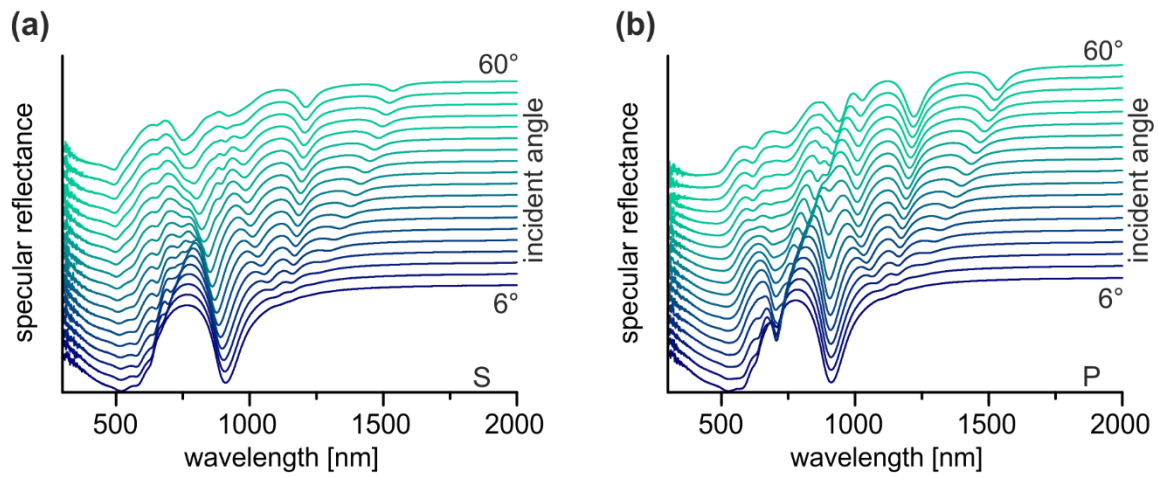


**Figure S8.10.** Angle-resolved reflectance measurements with (a) s-polarized and (b) p-polarized light of a MIM structure with  $p = 570$  nm,  $t_1 = 100$  nm,  $t_2 = 50$  nm and  $t_3 = 90$  nm.

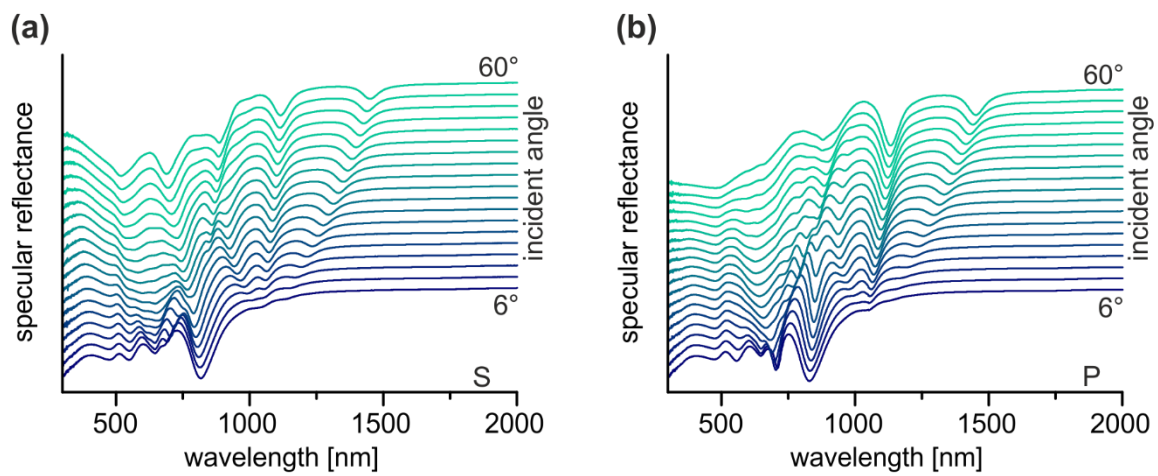


**Figure S8.11.** Angle-resolved reflectance measurements with (a) s-polarized and (b) p-polarized light of a MIM structure with  $p = 570$  nm,  $t_1 = 100$  nm,  $t_2 = 77$  nm and  $t_3 = 90$  nm.

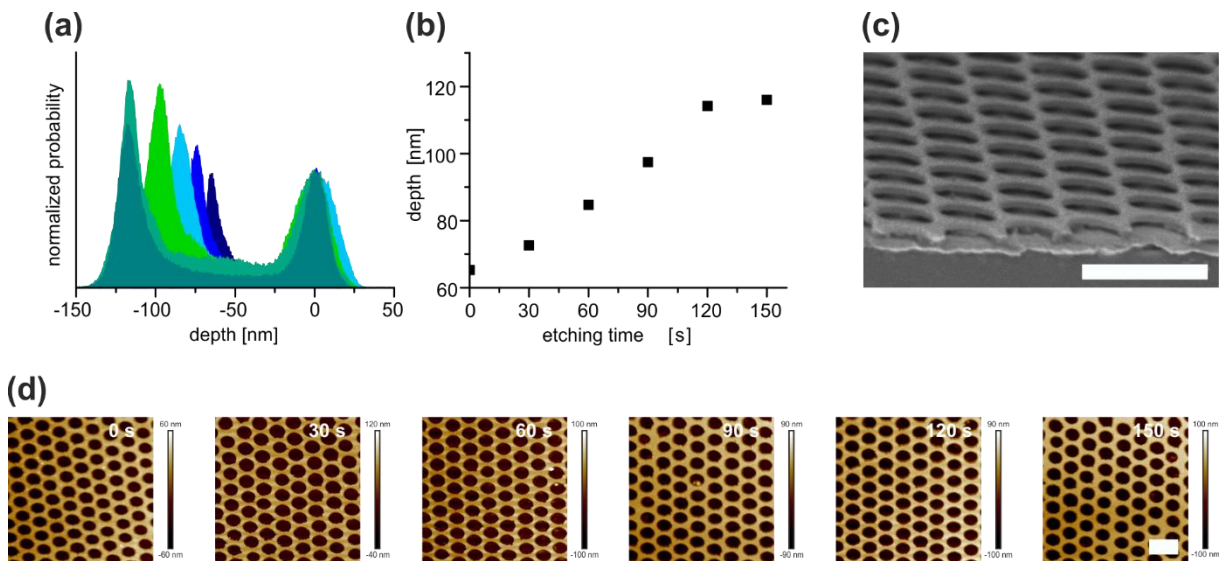


**Figure S8.12.** Plasma etching of MIM structure. (a) Depth profile of the MIM structure measured with AFM after consecutive etching steps. (b) Depth of the plasma etched MIM structure with increasing etching time. (c) Side-view SEM image of the MIM structure etched for 150 s. (d) AFM images of the MIM structure after each etching step, Scale bars are 1  $\mu\text{m}$ .

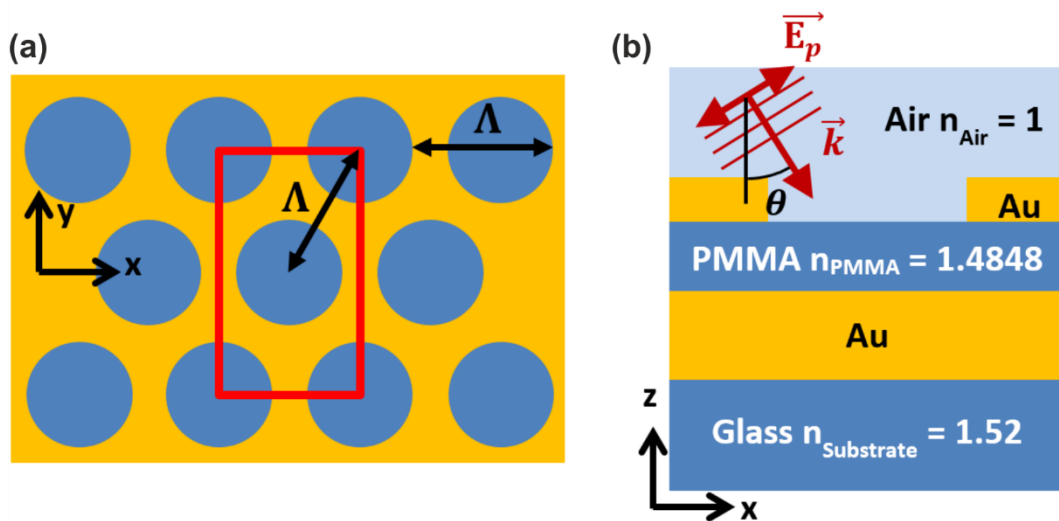


**Figure S8.13.** Schematic of geometry used in FDTD simulation for hexagonal nanomeshes with a rectangular unit cell. (a) Top view. The red rectangle indicates simulation volume with Bloch boundary conditions. A vertical cross-section is shown in (b) with the definition of the angle of incidence  $\theta$  and E-field orientation  $E_0$  for p-polarization.

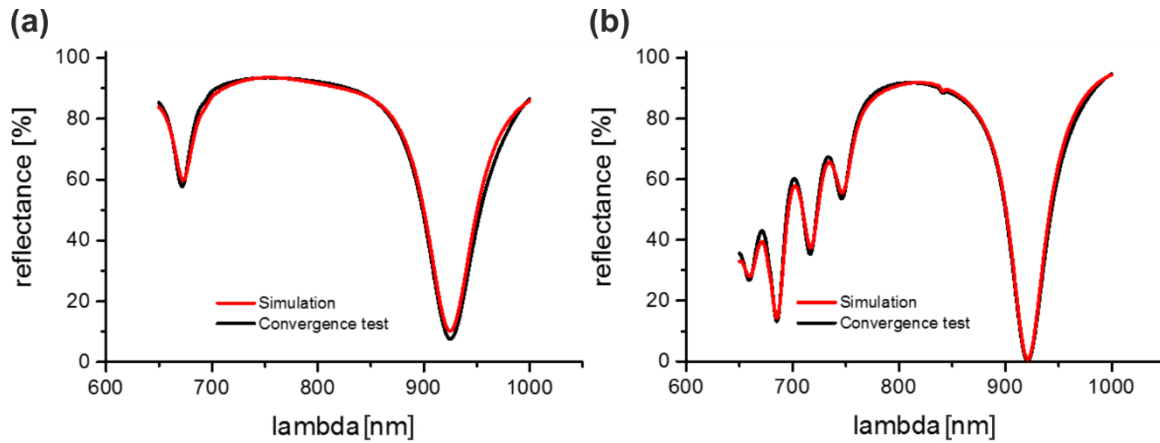


**Figure S8.14.** Convergence of the simulation was tested on selected by increase of mesh resolution. Simulations were run with a uniform mesh of  $(x,y,z) = (5 \text{ nm}, 5 \text{ nm}, 2 \text{ nm})$  unit cell size. The Mesh size was reduced to  $(x,y,z) = (2 \text{ nm}, 2 \text{ nm}, 2 \text{ nm})$  for selected configurations to confirm the convergence of results. Here, the convergence test for the shorter wavelength part of the spectrum is shown for the geometry used to study near field distribution in Figure 8.4 for (a) normal incident light and (b) excitation with  $\Theta = 22^\circ$  angle of incidence.

## 9 Plasmonic Nanomeshes: Their Ambivalent Role as Transparent Electrodes in Organic Solar Cells

Christian Stelling,<sup>1</sup> Chetan R. Singh,<sup>2</sup> Matthias Karg,<sup>3</sup> Tobias König,<sup>4\*</sup> Mukundan Thelakkat,<sup>2\*</sup> and Markus Retsch<sup>1\*</sup>

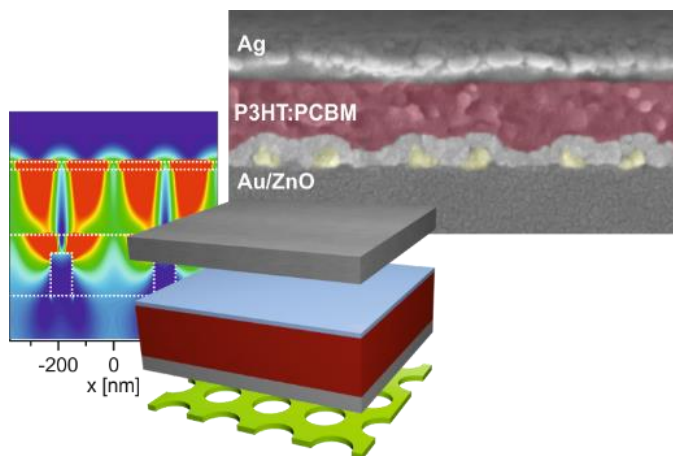
<sup>1</sup>Physical Chemistry – Polymer Systems, University of Bayreuth, 95440 Bayreuth, Germany

<sup>2</sup>Applied Functional Polymers, Macromolecular Chemistry I, University of Bayreuth, 95440 Bayreuth, Germany

<sup>3</sup>Physical Chemistry I, Heinrich-Heine-University, 40204 Düsseldorf, Germany

<sup>4</sup>Institute of Physical Chemistry and Polymer Physics, Leibniz-Institut für Polymerforschung Dresden e. V., 01069 Dresden

<sup>4</sup>Germany and Cluster of Excellence Centre for Advancing Electronics Dresden (CFAED), Technische Universität Dresden, 01062 Dresden, Germany



Published in *Scientific Reports* 7, 42530 (2017).

Reproduced with permission from Nature Publishing Group.

## Abstract

In this contribution, the optical losses and gains attributed to periodic nanohole array electrodes in polymer solar cells are systematically studied. For this, thin gold nanomeshes with hexagonally ordered holes and periodicities ( $P$ ) ranging from 202 nm to 2560 nm are prepared by colloidal lithography. In combination with two different active layer materials (P3HT:PC<sub>61</sub>BM and PTB7:PC<sub>71</sub>BM), the optical properties are correlated with the power conversion efficiency (PCE) of the solar cells. A cavity mode is identified at the absorption edge of the active layer material. The resonance wavelength of this cavity mode is hardly defined by the nanomesh periodicity but rather by the absorption of the photoactive layer. This constitutes a fundamental dilemma when using nanomeshes as ITO replacement. The highest plasmonic enhancement requires small periodicities. This is accompanied by an overall low transmittance and high parasitic absorption losses. Consequently, larger periodicities with a less efficient cavity mode, yet lower absorptive losses were found to yield the highest PCE. Nevertheless, ITO-free solar cells reaching ~ 77 % PCE compared to ITO reference devices are fabricated. Concomitantly, the benefits and drawbacks of this transparent nanomesh electrode are identified, which is of high relevance for future ITO replacement strategies.

## 9.1 Introduction

Transparent conducting electrodes (TCEs) are inevitable in modern electro-optical devices such as organic light-emitting diodes, touch displays, photodetectors or solar cells. However, materials that combine a high optical transparency and a high electrical conductivity are very rare.<sup>1</sup> The state-of-the-art transparent electrode materials are conducting oxides like indium tin oxide (ITO). Such oxides offer a high transmittance surpassing 90 % over the whole visible range, and a low sheet resistance down to  $10 \Omega/\square$ .<sup>2</sup> However, a lot of effort is put into the development of alternative electrode materials due to the well-known drawbacks of ITO: Besides the scarcity and thus high costs of indium, the conductivity of ITO strongly depends on its thickness. Additionally, ITO is very brittle, limiting the beneficial properties of polymer solar cells, which are their applicability for low-cost roll-to-roll processing onto flexible substrates.<sup>3</sup> The use of carbon nanotubes<sup>4</sup>, thin metal films<sup>5</sup>, solution-processed metal

nanowires<sup>6</sup>, metal grids prepared by lithography<sup>7,8</sup>, printing<sup>9</sup> or cracked templates<sup>10,11</sup> and metal nanohole arrays<sup>12-14</sup> have been discussed to replace ITO.

However, carbon nanotube grids still suffer from low stability under ambient conditions, while metal nanowire networks and thin metal films are limited due to their reduced transmittance compared to ITO.<sup>7,15</sup> Furthermore, solution processed nanowires exhibit a high resistance at junctions and easily cause electrical short-circuits due to wires penetrating through the blocking layer.<sup>16</sup>

A promising alternative to ITO could be periodic metal nanohole arrays, also referred to as nanomeshes. Due to their exceptional optical properties such as extraordinary optical transmittance (EOT)<sup>17</sup> they have been suggested as transparent conducting electrodes for both inorganic<sup>18</sup> and organic<sup>19</sup> solar cells. This is based on their ability to support surface plasmon polaritons (SPP).<sup>20-22</sup> The role of surface plasmons in the performance of thin film solar cells has extensively been studied in the past years.<sup>23-28</sup> Surface plasmons have been proposed to trap incident light at the metal/semiconductor interface and thus enhance the light absorption in photovoltaic devices due to an increased interaction time between the light and the active layer and an enhanced field intensity in the device. Yet, there is still a controversy whether or not nanomesh plasmonic electrodes are better suitable candidates as TCE by combining both their transmission and plasmonic properties. Unambiguous and consistent reports on clear plasmonic contributions, exceeding the improvements obtainable by simple scattering mechanisms are scarce.

Usually the better suitability of such nanomeshes is demonstrated just by testing them in devices and comparing with ITO references. An increase in the power conversion efficiency was shown for a silver nanohole array in a small-molecule solar cell compared to an unpatterned silver film and ITO as reference.<sup>29</sup> In that case, the active layer was in direct contact with the 12 nm thick nanohole array (400 nm period), which was prepared by colloidal lithography. The enhanced efficiency of such devices can originate from plasmonic enhancement in direct proximity to the nanomesh as well as from an increase in the interfacial area between hole and electron conductor.

Beside their application as transparent electrodes, the introduction of nanohole arrays as back reflectors in organic solar cells resulted in an enhanced device absorption by coupling of the light to SPP modes in experimental<sup>30</sup> and numerical studies<sup>31-33</sup> for ultrathin active layers of P3HT blended with fullerenes.

Some work has been done on integrating nanohole arrays as transparent electrodes for polymer solar cells. Randomly ordered nanoholes showed high losses in the  $J_{SC}$  due to the limited

transmittance of the electrodes.<sup>34,35</sup> Nevertheless, the IPCE measurements hint at a contribution of SPPs to the device performance. Numerical studies show the excitation of a guided mode localized in the P3HT:PC<sub>61</sub>BM active layer at long wavelengths beyond the absorption edge of P3HT.<sup>19</sup>

Zhu et al. used colloidal lithography to fabricate an electrode with a thickness of 18 nm, a hole diameter of 357 nm and an initial particle diameter of 430 nm.<sup>36</sup> The reduction in  $J_{SC}$  compared to the state-of-the-art electrode ITO was attributed to the reduced transparency.

Morfa et al. described the influence of the hole diameter on the sheet resistance of bare Ag nanohole arrays prepared by nanosphere lithography followed by plasma etching to reduce the initial particle diameter.<sup>37</sup> Short etching times yield high sheet resistances due to a discontinuous metal structure or wire thicknesses in the range of the mean free path of the electrons in silver. Longer etching times, on the contrary, result in a rapidly decreased transmittance. This demonstrates a fundamental dilemma and it is not clear up to now whether periodically structured metal electrodes can provide a net improvement.

For polymer solar cells, Chou et al. reported higher efficiencies for a subwavelength square array of nanoholes.<sup>38</sup> The bulk heterojunction devices with P3HT:PC<sub>61</sub>BM as active layer showed a drastic decrease in reflectance when incorporating the nanohole array into the device. By choosing an appropriate active layer thickness, which supports a coupling between the front and back-electrode, the incident light was confined in the active layer of the device. Therefore, the absorption of the device was radically boosted, exceeding even the efficiency of the reference ITO device. This effect was not maintained for the bare array or devices with a PMMA layer of the same thickness.

Overall, the distinct optical loss mechanisms related to parasitic absorption and reflectance for nanohole array electrodes have not been studied systematically and clarified properly. It is therefore not possible to evaluate the advantages and shortcomings of periodic nanohole electrodes on a broader scale. This, however, will be of great importance, if nanohole electrodes were to be considered as ITO replacements in current and future optoelectronic devices.

Therefore, in this paper, we focus on two main aspects, which are decisive for light management in any solar cell. First, we vary the periodicity of gold nanohole array from 202 nm up to 2560 nm and thereby fully address the relevant optical range from visible to near-infrared. Secondly, we investigate the interplay of different optical and electrical properties of these electrodes in photovoltaic devices with two different and well-known bulk-heterojunction photoactive layers, P3HT:PC<sub>61</sub>BM and PTB7:PC<sub>71</sub>BM in an inverted solar cell device architecture. P3HT:PC<sub>61</sub>BM was selected as it is the most studied material composition in

polymer photovoltaic research.<sup>39</sup> On the other hand, up to 9 % power conversion efficiency has been reported with a highly optimized PTB7:PC<sub>71</sub>BM system.<sup>40</sup> We have purposefully selected these material systems as universal prototypes in which the absorption edge of donor polymers varies from the visible to the near-infrared region. We rationalize our findings by finite-difference-time-domain (FDTD) simulations to provide a full understanding of the optical properties and assess the potential of metal nanomeshes as transparent conducting electrodes.

## 9.2 Results and Discussion

We fabricated our large area nanohole arrays via colloidal lithography with a metal layer thickness of 50 nm.<sup>41-44</sup> We used non-close-packed polystyrene particle monolayers prepared by self-assembly at the liquid/air interface and subsequent dry etching of the particles.<sup>42</sup> These monolayers then act as templates for the deposition of a gold layer by thermal evaporation. Finally, the particle template is removed yielding the hexagonally ordered nanohole array. In this periodic arrangement, the localized excitation of the surface plasmon resonance of the metallic nanoholes interferes with the far-field from the Bragg diffraction mode of the lattice (Rayleigh anomaly) leading to a Fano-type surface lattice resonance with narrow and asymmetric line shape.<sup>45,46</sup> The spectral position of the SPP resonances thereby depends on the predefined periodicity  $P$  (center-to-center distance between the holes).<sup>17</sup>  $P$  is given by the initial diameter of the polystyrene particles. Using polystyrene particles with diameters of 202 nm, 375 nm, 570 nm, 1040 nm and 2560 nm we were able to cover the optical range from visible to near-infrared. SEM images of the resulting gold patterns are shown in Figure 9.1a. The diameter of the holes  $d$  was adjusted to a constant  $d/P$  value of approximately 0.8 to obtain a constant area fraction. Consequently, around 40 % of the device area, independent of the periodicity, was covered by gold. The sheet resistance for Au was in the range of 8 – 18  $\Omega/\square$  for this surface coverage.<sup>37</sup> Further increasing the diameter of the holes would result in higher sheet resistances and might cause a reduction in the charge extraction in the solar cell devices due to the limited diffusion length of the charge carriers.<sup>37</sup> Since the sheet resistance of the nanomesh electrodes is comparable to standard ITO substrates, differences in the device performance can be solely attributed to the optical and plasmonic properties of these electrodes. Figure 9.1b and c depict the optical properties of the uncoated nanohole arrays with a systematic variation in periodicity on a glass substrate.

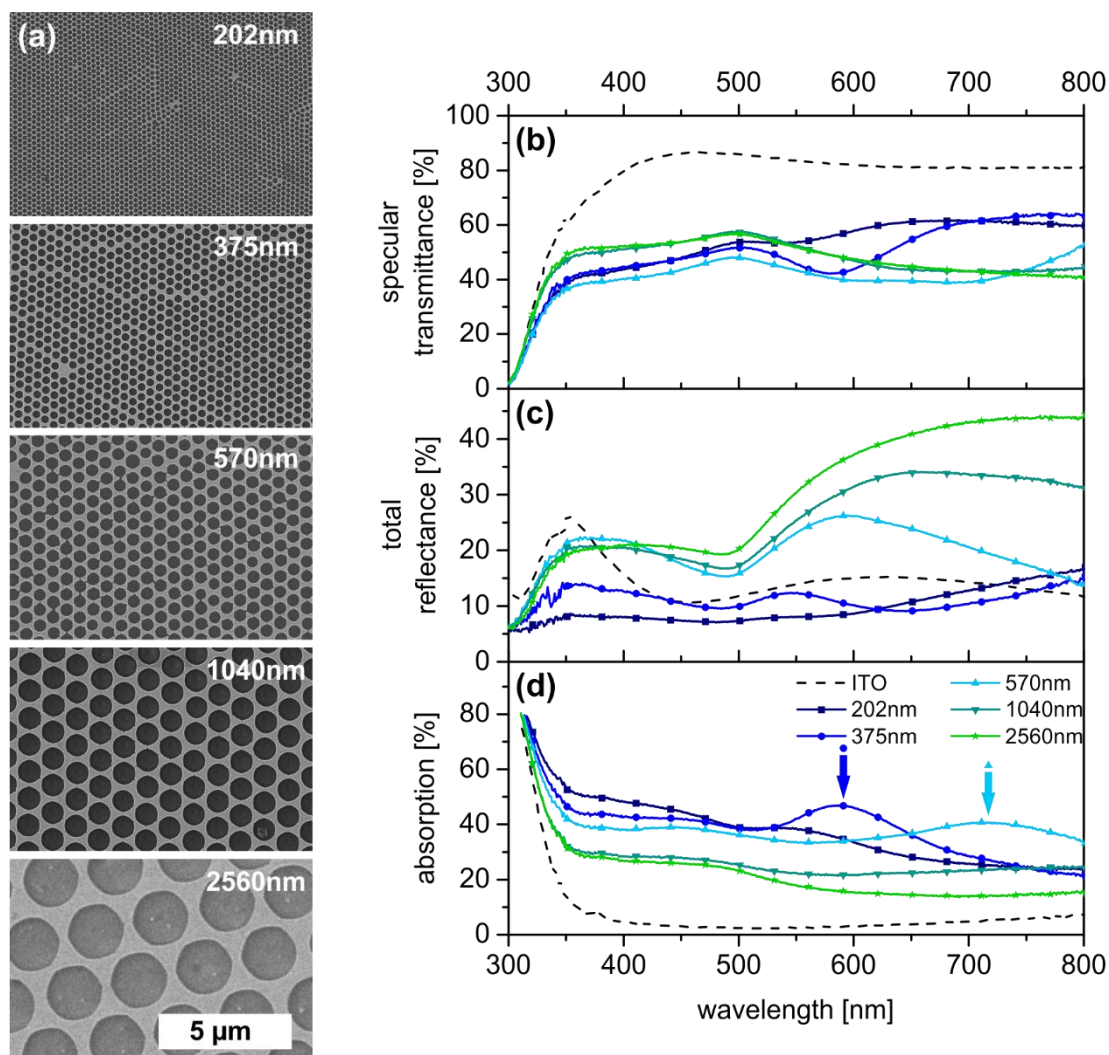


**Figure 9.1.** Electron microscopy and optical characterization of gold electrodes with constant gold area fraction. The corresponding hole diameters are listed in Table 9.1. (a) SEM images of gold nanohole arrays with different periodicities. The numbers given in (a) indicate the corresponding periodicity  $P$ . (b) Specular transmittance, (c) total reflectance and (d) absorption spectra of ITO (dashed line) and nanohole arrays (solid lines). The arrows indicate the positions of the SPP resonances.

For all periodicities, the transmittance ranges between 40 – 60 % in a wavelength range of 350 nm to 800 nm and is therefore significantly lower compared to the reference ITO electrode which has more than 80% transmittance. (Figure 9.1b). However, the transmittance data only provide limited information for tailoring the light management in a solar cell device. In particular, for plasmonic structures the discrimination between scattering, reflection and absorption is essential. Thus, the optical measurements were performed in an integrating sphere with the light incident onto the gold structures through the glass substrate. The wavelength dependent contribution of the total reflectance and absorption are shown in Figure 9.1c and d,

respectively. At wavelengths below 370 nm, all nanohole arrays are less reflective than ITO, due to the different band transitions of gold and ITO. Yet, their strong absorption at higher wavelengths results in an overall lower transmittance.

At the same time one can clearly discern periodicity-dependent changes of the optical properties. The nanohole arrays with  $P = 202$  nm and  $P = 375$  nm exhibit a lower reflectance compared to ITO across the whole range of interest. With increasing periodicity the reflectance increases, whereas the absorption decreases. This behavior is reminiscent of isolated plasmonic particles, which also show a size-dependence of their scattering to absorption ratio.<sup>24</sup> Additionally, these overall trends are superimposed by characteristic dips in the transmittance spectra. These originate from the excitation of SPP modes and are based on dipolar mode oscillations (simulated spectra of the pure nanomeshes and electric field distributions at the respective resonance wavelengths are given in Figure S9.1 and Figure S9.2). These transmittance minima correspond to slightly redshifted maxima in the absorption spectra (highlighted in Figure 9.1d) and thus show an asymmetric signature of the Fano resonance line shape. The SPP resonance strongly shifts to higher wavelength with increasing periodicities. Hence, in the relevant wavelength range for organic solar cells studied here (300 nm – 800 nm), the plasmonic resonances are visible only for the periods  $P = 375$  nm at 585 nm and for  $P = 570$  nm at 715 nm. Moreover, for the smallest period ( $P = 202$  nm) no resonance is discernible due to high losses in the gold near the intraband transition.

The fundamental question we want to address is, whether the expectedly high optical losses caused by the lower transmittance compared to the ITO reference, can be compensated by potential plasmonic enhancement effects. From a solar cell light management point of view, the resonance wavelength of the SPP mode should overlap with the absorption of the active medium. In that case, the enhancement of the electric field due to the resonance may result in additional absorption in the photoactive material. In a functional photovoltaic device, the light management will be further complicated by the interaction of the SPP mode with the metallic back-electrode. This is known to result in an additional mode known as mirror charged mode, cavity mode (metal-active layer-metal) or magnetic mode.<sup>47-49</sup>

Solar cells were fabricated using two different photoactive layers (P3HT:PC<sub>61</sub>BM and PTB7:PC<sub>71</sub>BM) on top of nanomesh electrodes introduced above. The exact inverted cell layout is given in Figure 9.2a and b for the nanomesh devices and in Figure S9.3 for the ITO reference device. Figure 9.2c shows the J-V curves under illumination of the P3HT:PC<sub>61</sub>BM devices for all periodicities (dark current characteristics are shown in Figure S9.4). The solar cell performance for each case was checked for reproducibility and consistency by repeating the

experiment on different days. Table 9.1 summarizes the best and averaged (in parenthesis) solar cell performance parameters obtained for each case. The reference solar cell devices on an ITO electrode showed a power conversion efficiency (PCE) of 2.6 % for the P3HT:PC<sub>61</sub>BM photoactive layer. In general, all nanohole array based solar cells showed a reduced PCE in comparison to the reference solar cell.

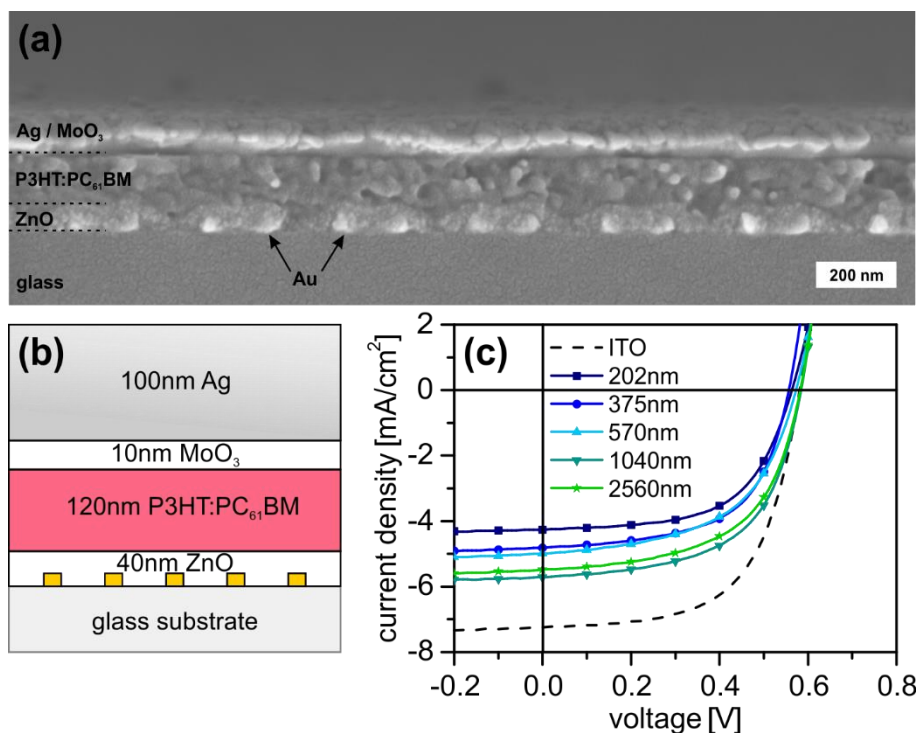


**Figure 9.2.** P3HT:PC<sub>61</sub>BM solar cells based on gold nanohole arrays. (a) SEM cross-section of a P3HT:PC<sub>61</sub>BM device with  $P = 202$  nm (a cross-section measured with the backscattered electron (BSE) detector is given in Figure S9.5). (b) Schematic illustration of the inverted device structure with a gold nanohole electrode. (c) Current-density – voltage characteristics under illumination of solar cells built on ITO (dashed) and gold nanohole arrays with different periodicities.

Compared to the ITO reference the  $J_{SC}$  dropped from 6.8 mA/cm<sup>2</sup> to 4.2 mA/cm<sup>2</sup> for the smallest periodicity. Nevertheless, the  $J_{SC}$  and consequently the PCE increased monotonically with  $P$  up to a maximum for 1040 nm followed by a decrease at 2560 nm. The maximum PCE for the P3HT:PC<sub>61</sub>BM active layer with nanomesh electrode ( $P = 1040$  nm) was 2.0 %, which is ~ 77 % of the ITO reference device. It should also be noted that within each case, the open circuit voltage ( $V_{OC}$ ) and the fill factor (FF) values remained nearly constant. This suggests the absence of excessive leakage currents and that the ZnO layer fully covered the nanomeshes. Besides that, the observed high FF value also indicates that the metal nanohole array was homogeneously closed. The nanomeshes offered a comparable electrical conductivity relative

to the conventional ITO electrode. Finally, even for the largest apertures ( $\sim 2100$  nm), the solar cells are not restricted by the charge carrier diffusion length in the ZnO blocking layer. Thus, we conclude that the nanomesh based solar cells were not electrically limited and that any deviations from the ITO reference were optically driven.

**Table 9.1.** Optimum and average of five (in parenthesis) P3HT:PC<sub>61</sub>BM device parameters. *P*: nanomesh periodicity, *d*: hole diameter, AF<sub>Au</sub>: area fraction of gold, R<sub>sh</sub>: nanomesh sheet resistance, J<sub>SC</sub>: short-circuit current density, V<sub>OC</sub>: open circuit voltage, FF: fill factor and PCE: power conversion efficiency of P3HT:PC<sub>61</sub>BM devices.

<i>P</i> [nm]	<i>d</i> [nm]	AF <sub>Au</sub> [%]	R <sub>sh</sub> [Ω/□]	J <sub>SC</sub> [mA/cm <sup>2</sup> ]	V <sub>OC</sub> [V]	FF [%]	PCE [%]
<b>ITO reference</b>	-	-	17.4	7.3 (6.8)	0.58 (0.59)	61 (62)	2.6 (2.5)
<b>202</b>	155	46	15.7	4.3 (4.2)	0.56 (0.56)	60 (60)	1.4 (1.4)
<b>375</b>	293	46	10.0	4.6 (4.6)	0.57 (0.56)	58 (53)	1.5 (1.4)
<b>570</b>	462	43	8.5	5.1 (5.1)	0.57 (0.56)	55 (53)	1.6 (1.5)
<b>1040</b>	853	37	17.3	5.7 (5.7)	0.59 (0.58)	58 (60)	2.0 (2.0)
<b>2560</b>	2077	37	8.5	5.4 (5.4)	0.58 (0.58)	58 (58)	1.8 (1.8)

Therefore, changes in J<sub>SC</sub> can be rationalized by the optical properties of the fully assembled solar cell devices (Figure 9.3). The absorption (*A*) of the solar cells was calculated from the total reflectance (*R*) measurements via  $A = 1 - R$ . In the range from 400 nm to 750 nm, the overall device absorption (Figure 9.3a) is significantly higher than that of the reference device with ITO (dashed line). The smaller the period *P*, the greater the absorption compared to the reference device, which is in good accordance with the absorption measurements of the pure nanomeshes (Figure 9.1d). Furthermore, an additional absorption peak appears close to the absorption edge of P3HT (600 nm – 650 nm) for the nanomesh based devices, which is not visible for the ITO reference device. This peak shifts red from 625 nm to 700 nm for increasing lattice periods. It is most pronounced for *P* = 1040 nm and disappears again for *P* = 2560 nm. We attribute this additional absorption to light trapping caused by the electrode grating.

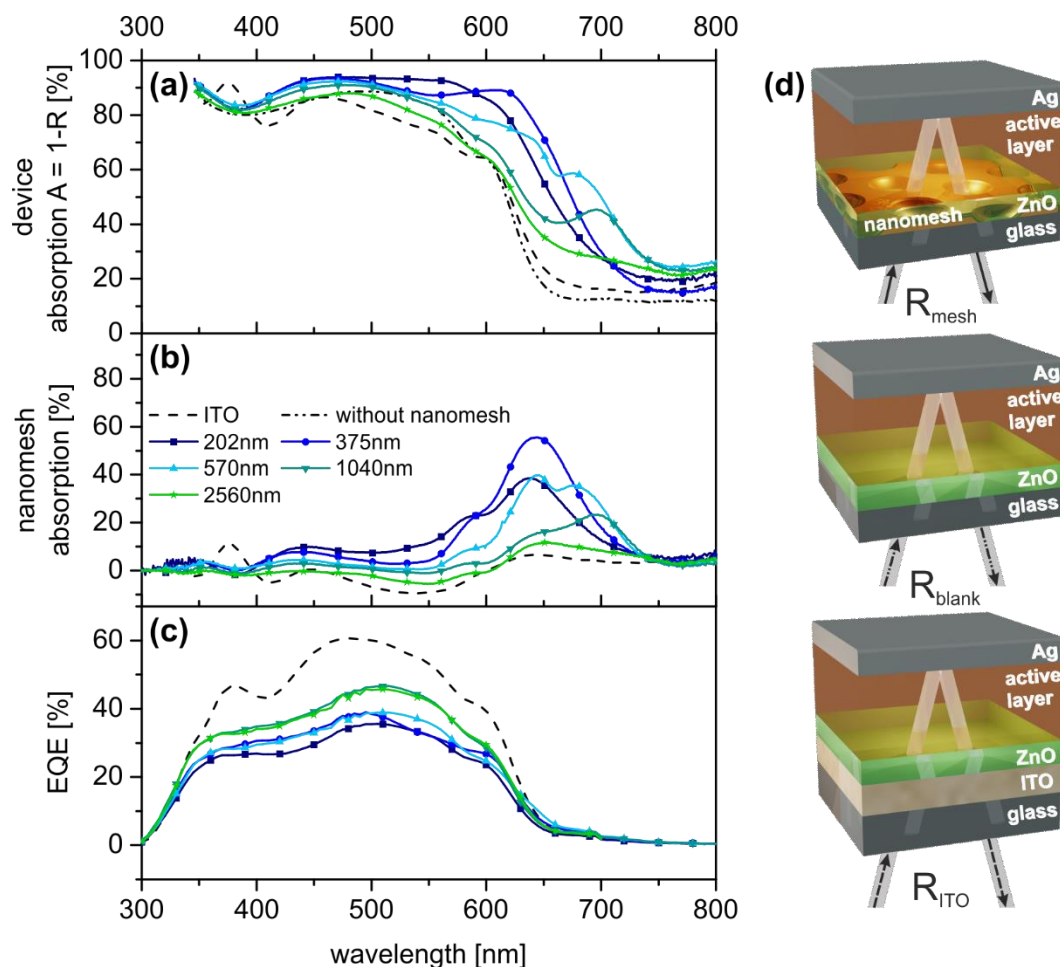


**Figure 9.3.** Influence of nanohole arrays on absorption and photocurrent generation in P3HT:PC<sub>61</sub>BM solar cells. (a) Absorption spectra of P3HT:PC<sub>61</sub>BM solar cells with gold nanohole electrodes with different periodicities (solid lines), of the same solar cell without the nanomesh (dash-dotted line), and of the P3HT:PC<sub>61</sub>BM reference device on ITO (dashed line). (b) Contribution of the nanohole electrode to the device absorption. The nanomesh absorption is obtained by subtracting the absorption ( $A = 1 - R$ ) of the same solar cell device without a nanomesh electrode ( $R_{\text{blank}}$ , dash-dotted line, Figure 9.3d) from the device absorption with nanomesh electrode ( $R_{\text{mesh}}$ , solid line). (c) EQE spectra of the P3HT:PC<sub>61</sub>BM solar cells with nanomesh electrodes (solid lines) compared to the ITO reference cell (dashed line). (d) Schematic presentation of the solar cell devices used for the reflectance measurements with (top) and without (center) the nanohole array electrode and with the ITO electrode (bottom).

To single out the contribution of the nanomesh electrodes to the device absorption we calculated the nanomesh absorption. This was done by subtracting the absorption of the device stack without the nanomesh electrode ( $A_{\text{blank}} = 1 - R_{\text{blank}}$ ) from the absorption of the device stack with the nanohole array electrode ( $A_{\text{mesh}} = 1 - R_{\text{mesh}}$ ) and is displayed in Figure 9.3b and d. This is the most insightful optical characterization as it provides a direct measure of the absorption within the device (based on the absorption properties of the photoactive layer and the reflective back-electrode) and the contribution of the nanohole electrode. As surface plasmons are highly

sensitive towards the refractive index environment, the absorption of nanohole arrays in the device differs from the absorption of the neat metal arrays. Thus, a correlation between the device performance and the optical properties of the pure meshes is not always directly possible. One can infer quite clearly that the absorption of the device is mainly dictated by the photoactive layer. From 300 nm to 550 nm only a slight broadband offset in the absorption can be assigned to the nanohole array. However, approaching the absorption band-edge of the photoactive polymer a strong increase of the entire device absorption can be seen for all but the largest periodicity  $P = 2560$  nm. The maximum of the nanomesh contribution to the absorption was found for  $P = 375$  nm. However, this additional absorption does not contribute to the device performance as inferred from the external quantum efficiency (EQE). Figure 9.3c shows EQE only in the absorption range of the photoactive layer. Since no enhancement of the EQE in the wavelength range from 550 nm to 750 nm is observed, it can be concluded that the high absorption within the nanohole arrays does not lead to photon to electron conversion. Moreover, the EQE is reduced for nanomesh based solar cells in the whole visible range compared to the ITO reference device. The smaller the grating period and thus the larger the additional absorption due to the nanomesh, the lower the EQE of the device. Therefore, the increasing PCE for larger periodicities can rather be assigned to the decrease of the parasitic absorption losses, which are in good agreement with Figure 9.1d. Additionally, for the largest periodicity ( $P = 2560$  nm) the reflectance losses at the nanomesh front electrode result in a decreased device absorption. Thus, a periodicity of  $P = 1040$  nm presents the best trade-off to minimize both the parasitic absorptive and the reflectance losses.

In order to capitalize on the increased absorption between 600 nm and 700 nm due to the nanohole electrode, we prepared solar cell devices based on a low band-gap polymer PTB7 and the fullerene derivative PC<sub>71</sub>BM. The PTB7:PC<sub>71</sub>BM blend absorbs up to a wavelength of 750 nm, thus covering the wavelength range of the maximum nanomesh absorption in Figure 9.3b. The inverted device structure and the J-V curves of the PTB7:PC<sub>71</sub>BM devices are shown in Figure 9.4.

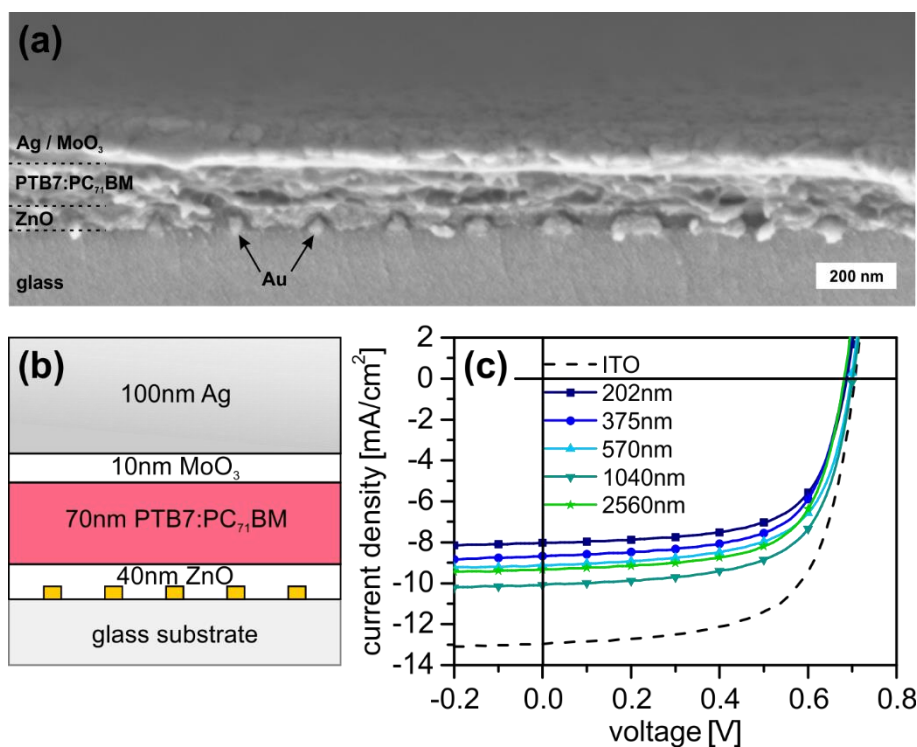


**Figure 9.4.** Device characteristics of PTB7:PC<sub>71</sub>BM solar cells based on gold nanohole arrays. (a) SEM cross-section of a PTB7:PC<sub>71</sub>BM device with  $P = 202$  nm. (b) Schematic illustration of the inverted device structure with a gold nanohole electrode. (c) Current-density – voltage characteristics under illumination of solar cells built on ITO (dashed line) and gold nanohole array TCEs with different periodicities.

A similar trend compared to the P3HT:PC<sub>61</sub>BM solar cells was observed for the solar cell parameters of the PTB7:PC<sub>71</sub>BM devices with the various periodicities of the nanomesh TCE (Table 9.2). The  $J_{SC}$  drops from 12.8 mA/cm<sup>2</sup> to 7.7 mA/cm<sup>2</sup> for the smallest periodicity. Increasing  $P$  monotonically increases the  $J_{SC}$ , which again decreases beyond  $P = 1040$  nm. The maximum PCE was 4.6 % for  $P = 1040$  nm compared to 6.0 % for the reference solar cell devices based on ITO. Again, no excessive leakage currents were observed for the nanohole devices and the open circuit voltage ( $V_{OC}$ ) and the fill factor (FF) values were nearly constant for all periodicities. The corresponding device absorption is given in Figure 9.5a.

**Table 9.2.** Optimum and average of five (in parenthesis) PTB7:PC<sub>71</sub>BM device parameters. *P*: nanomesh periodicity, *d*: hole diameter, AF<sub>Au</sub>: area fraction of gold, R<sub>sh</sub>: nanomesh sheet resistance, J<sub>sc</sub>: short-circuit current density, V<sub>oc</sub>: open circuit voltage, FF: fill factor and PCE: power conversion efficiency of PTB7:PC<sub>71</sub>BM devices.

<i>P</i> [nm]	<i>d</i> [nm]	AF <sub>Au</sub> [%]	R <sub>sh</sub> [Ω/□]	J <sub>sc</sub> [mA/cm <sup>2</sup> ]	V <sub>oc</sub> [V]	FF [%]	PCE [%]
<b>ITO reference</b>	-	-	17.4	12.9 (12.8)	0.71 (0.69)	65 (66)	6.0 (5.9)
<b>202</b>	155	46	13.4	7.9 (7.7)	0.69 (0.68)	66 (67)	3.6 (3.4)
<b>375</b>	293	46	8.8	8.7 (8.6)	0.68 (0.68)	66 (67)	3.9 (3.9)
<b>570</b>	462	43	8.5	9.2 (8.8)	0.70 (0.70)	65 (65)	4.2 (4.1)
<b>1040</b>	853	37	13.9	10.2 (9.6)	0.70 (0.69)	65 (65)	4.6 (4.3)
<b>2560</b>	2077	37	11.7	9.3 (9.3)	0.68 (0.68)	67 (63)	4.2 (4.0)

Compared to the P3HT:PC<sub>61</sub>BM devices, a similar trend in the device absorption was obtained for the PTB7:PC<sub>71</sub>BM devices. The absorption steadily decreases with increasing lattice periodicity. This can be attributed to the decreasing plasmonic absorption and increasing reflectance of the nanohole arrays. In contrast to P3HT:PC<sub>61</sub>BM, the absorption of the PTB7:PC<sub>71</sub>BM nanomesh devices hardly exceeds the absorption of the ITO reference device in the range up to 700 nm, where the active layer is strongly absorbing. Instead, for large periodicities the total absorption decreases compared to the ITO reference device. Again, the overall device absorption profile is strongly dictated by the absorption properties of the photoactive polymer, which extends up to the absorption edge (750 nm) of PTB7:PC<sub>71</sub>BM blend. Surprisingly, the additional absorption peaks evoked by the plasmonic properties of the nanohole arrays are now strongly redshifted compared to those in the P3HT:PC<sub>61</sub>BM systems. For *P* = 375 nm, *P* = 570 nm and *P* = 1040 nm additional absorption peaks are visible at the absorption edge of the polymer between 700 nm and 750 nm. We note that the highest nanomesh absorption is now observed for the *P* = 570 nm electrode instead of the *P* = 375 nm for the P3HT:PC<sub>61</sub>BM blends (Figure 9.5b). Interestingly, the absorption of the nanohole electrode with *P* = 202 nm incorporated in the PTB7:PC<sub>71</sub>BM device stack exhibits a spectrally flat behavior similar to ITO, while a distinct absorption peak is visible for the same structure in

the P3HT:PC<sub>61</sub>BM device. Again, the absorption related to the plasmonic electrode is absent for the largest grating period ( $P = 2560$  nm).

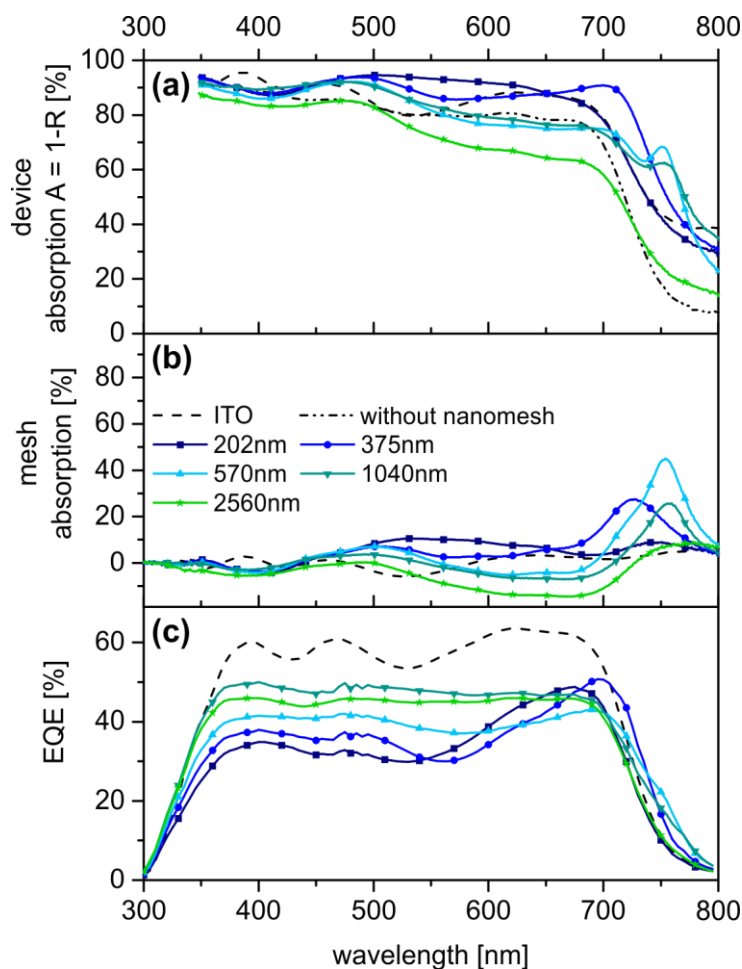


**Figure 9.5.** Influence of nanohole array on absorption and photocurrent generation in PTB7:PC<sub>71</sub>BM solar cells. (a) Absorption spectra of PTB7:PC<sub>71</sub>BM solar cells with gold nanohole electrodes for different periodicities (solid lines), of the same solar cell without the nanomesh (dash-dotted line), and of the PTB7:PC<sub>71</sub>BM reference device on ITO (dashed line). (b) Contribution of the nanohole electrode to the device absorption. The nanomesh absorption is obtained by subtracting the absorption ( $A = 1 - R$ ) of the same solar cell device without a nanomesh electrode ( $R_{\text{blank}}$ , dash-dotted line) from the device absorption with nanomesh electrode ( $R_{\text{mesh}}$ , solid line, compare Figure 9.3d). (c) EQE spectra of the PTB7:PC<sub>71</sub>BM solar cells.

Similar to the P3HT:PC<sub>61</sub>BM devices, the EQE of the PTB7:PC<sub>71</sub>BM devices is also reduced compared to the ITO reference device. However, among the nanomesh devices the EQE increases in a broad range from 350 nm to 650 nm for larger periodicities due to a decrease of the parasitic absorption losses (Figure 9.5c). Moreover, for PTB7:PC<sub>71</sub>BM the EQE of the devices with  $P = 202$  nm and  $P = 375$  nm exhibit asymmetric line shapes with a strong increase in the EQE above 550 nm, whereas larger grating periods yield rather flat EQE spectra. For

wavelengths above 720 nm, in a range where the absorption of the PTB7:PC<sub>71</sub>BM blend is already strongly reduced, the EQE of the nanohole devices even surpasses the EQE of the ITO reference device.

This EQE enhancement spectrally coincides with the absorption peaks assigned to the plasmonic resonances and redshifts with increasing periodicity of the nanomesh electrode. Thus, we attribute this increase in EQE above 550 nm to the light trapping behavior of the plasmonic electrode. Consequently, the plasmonic resonances induced by nanohole arrays indeed contribute to the photocurrent of the device. Therefore, we can claim that plasmonic absorption enhancement is possible via these periodically structured electrodes. However, the gain in EQE is not sufficient to outweigh the inevitable transmission losses in the range from 350 nm – 700 nm, where the polymer is highly absorbing. Compared to the ITO device, the EQE spectra of the nanohole devices are only enhanced above 720 nm, where the absorption of the polymer is the limiting factor for the device efficiency. For the largest periodicity  $P = 2560$  nm, no enhancement in the EQE can be observed presumably due to its predominantly reflecting behavior at the wavelength range of interest. This trend strongly indicates that for large lattice periodicities, the plasmonic influence is negligible and the electrodes have to be optimized for their overall transmittance in the first place.

The comparison between the P3HT:PC<sub>61</sub>BM and PTB7:PC<sub>71</sub>BM devices reveals an intriguing dilemma when trying to make use of plasmonic enhancement and replacing the ITO electrode simultaneously. Whereas the resonance wavelength of the pure meshes is strongly dependent on the grating periodicity, the overall device absorption is more strongly determined by the absorption of the photoactive layer. The previously broadband SPP resonances become strongly confined to the narrow spectral range, which is defined by the absorption edge of the active layer material. Thus, although the same electrode periodicities have been used for both blend systems, the high plasmonic absorption between 600 nm and 650 nm of the P3HT:PC<sub>61</sub>BM devices was redshifted to the band-edge of PTB7:PC<sub>71</sub>BM devices (700 nm – 750 nm), where the exciton conversion is again less efficient. Even worse, the optimum coupling was observed for  $P = 375$  nm and  $P = 570$  nm. Yet, the optimum PCE is found for  $P = 1040$  nm. This demonstrates even more drastically that losses in the transmittance cannot be counteracted by a plasmonic enhancement.

To understand the impact of the nanomesh optics on the two different photoactive material systems in more detail, the electric field distributions of the plasmonic modes were simulated by the finite-difference time-domain (FDTD) method (Figure 9.6). The simulated device absorption spectra for P3HT:PC<sub>61</sub>BM (Figure 9.6a) and PTB7:PC<sub>71</sub>BM (Figure 9.6f)

qualitatively match the experimental trend (for transmittance and reflectance spectra see Figure S9.6 and Figure S9.7). Especially, the experimentally observed redshift of plasmonic absorption from P3HT:PC<sub>61</sub>BM to the PTB7:PC<sub>71</sub>BM is clearly supported by the simulation curves. In the region of strong photoactive layer absorption, the device absorption decreases with increasing nanohole periodicities. At the absorption edge pronounced absorption peaks are visible, which redshift with  $P$  and become less intense.

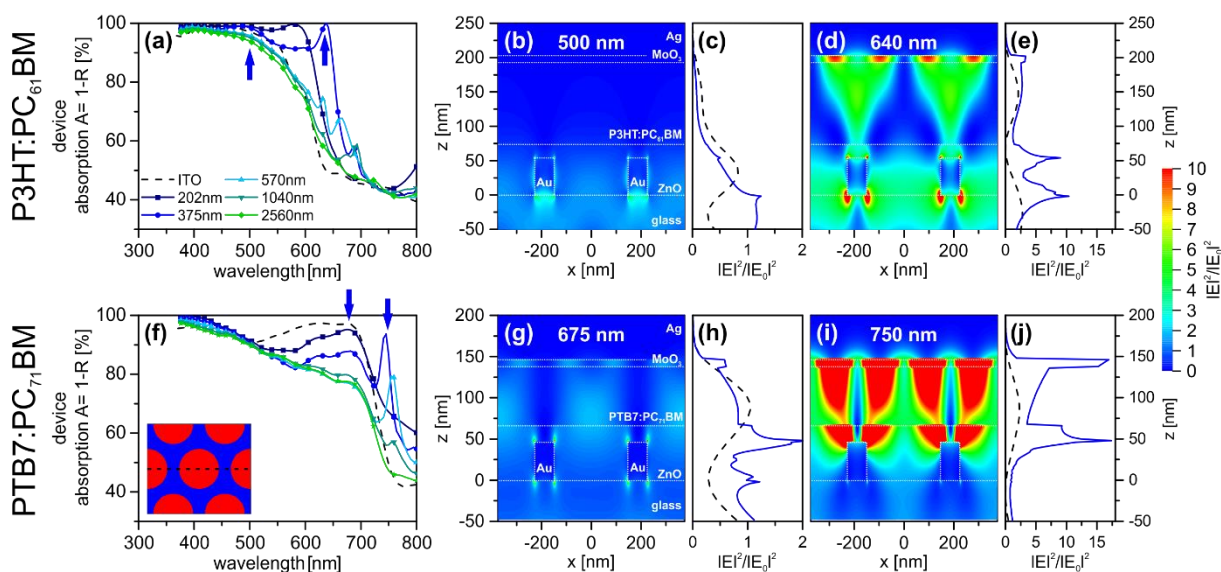


**Figure 9.6.** FDTD simulation of the P3HT:PC<sub>61</sub>BM (top row, a - e) and PTB7:PC<sub>71</sub>BM (bottom row, f - j) solar cell devices. Simulated spectra of (a) P3HT:PC<sub>61</sub>BM and (f) PTB7:PC<sub>71</sub>BM solar cells with gold nanohole electrodes and different periodicities are compared to those of ITO reference devices. The arrows indicate the two characteristic incident wavelengths used for the simulation of the electric field enhancement as shown in (b), (d) (g) and (i). Electric field intensity  $|E|^2$  distributions normalized to the incident electric field intensity  $|E_0|^2$  for P3HT:PC<sub>61</sub>BM at 500 nm (b) and 640 nm (d) and for PTB7:PC<sub>71</sub>BM at 675 nm (g) and 750 nm (i). The electric field enhancement shown in (b), (d), (g) and (i) were evaluated along the cross-section (dashed line) in the inset of (f) for  $P = 375$  nm in all cases. In (c), (e), (h) and (j) electric field enhancement averaged over the  $xy$ -plane of the unit cell is depicted along the  $z$ -coordinate for the respective wavelength for the ITO device (dashed line) and the nanomesh device (solid line).

The electric field distribution was simulated in three dimensions and plotted along the cross-section (dashed line) shown in the inset of Figure 9.6f for both active layer materials at two different characteristic wavelengths (bold arrows in Figure 9.6a and f) for a nanohole electrode with  $P = 375$  nm. The enhancement of the electric field intensity  $|E|^2$  in the device structure compared to the incident light intensity  $|E_0|^2$  is depicted for the P3HT:PC<sub>61</sub>BM devices in Figure 9.6b and d and for the PTB7:PC<sub>71</sub>BM devices in Figure 9.6g and i. In Figure 9.6c, e, h and j the corresponding electric field profiles  $|E|^2/|E_0|^2$  averaged over the whole unit cell along the layer

stack direction are given for the nanomesh devices (solid lines) compared to the ITO reference devices (dashed lines). The electric field distributions for the ITO reference devices are depicted in Figure S9.8.

At first, we want to assess the field distribution at a wavelength, which is lower than the absorption edge and dominated by the active medium absorption. Therefore, the field distribution was calculated at 500 nm (Figure 9.6b) and 675 nm (Figure 9.6g) for P3HT:PC<sub>61</sub>BM and PTB7:PC<sub>71</sub>BM, respectively. In each case, a nanohole array with  $P = 375$  nm was simulated, since this periodicity demonstrated a strong contribution of the nanohole absorption in either case (Figure 9.3a and Figure 9.5a). At these wavelengths, the corresponding photoactive layers absorb very strongly, and the solar cells are mainly limited by parasitic absorption and reflectance losses. For P3HT:PC<sub>61</sub>BM (Figure 9.6b) the simulation shows the scattering of the incoming light at the nanomesh with a close confinement of the electric field to the edges of the gold structure and a field profile, which exponentially decays into the active layer. The nanomesh is strongly reflecting resulting in high normalized field intensities exceeding unity in the glass layer (Figure 9.6c). In general, owing to the high attenuation of the photoactive layer, the electric field intensity in the layer stack is mainly reduced compared to the incident light intensity. Moreover, the electric field intensity in the photoactive layer is reduced for the nanomesh device relative to the ITO reference device. This gives rise to a decreased absorption in the nanomesh device at this wavelength. For the PTB7:PC<sub>71</sub>BM active layer at 675 nm (Figure 9.6g) a dipolar plasmon resonance is excited, which is weakly coupling to the silver back-electrode. This can be inferred from the field enhancement in the photoactive layer and the MoO<sub>3</sub> layer (Figure 9.6h). Nevertheless, the electric field intensity in the photoactive layer of the nanomesh device does not surpass the ITO reference device, which features a maximum of the field profile in the photoactive layer. Consequently, the contribution of the plasmonic resonance to the photocurrent of the device is negligible. This corroborates the experimental finding that the optical properties of the device are predominantly governed by the photoactive layer. A high absorption in the photoactive layer attenuates the coupling between the nanomeshes and the back-electrode and consequently it inhibits the evolution of confined plasmonic modes in the wavelength region of interest. However, to get some considerable improvements, these confined plasmonic modes are required to efficiently generate a surplus of excitons to outweigh the losses originating from the reduced transmittance through the nanohole electrode.

Field distribution simulation was also carried out near the absorption edge of the respective photoactive systems: at 640 nm and 750 nm for P3HT:PC<sub>61</sub>BM and PTB7:PC<sub>71</sub>BM,

respectively. Contrary to the field distribution observed within the absorption range of the photoactive layer discussed above, in the region of the absorption edge of the respective photoactive layers the electric field is less confined to the nanomesh electrode. Instead, the electric field intensity within the active layer of the devices is enhanced with respect to the incident intensity. For P3HT:PC<sub>61</sub>BM the electric field in the photoactive layer is moderately enhanced by a factor of 1.2 when excited at 640 nm, attributed to the resonance of the gold structure. Mirror charges are induced at the back-electrode with high field intensities occurring in the MoO<sub>3</sub> layer near the Ag surface (Figure 9.6e). Symmetrically enhanced electric fields at the edges of the gold structure indicate a strong coupling of the incident light with the plasmonic resonance. The localization of the electric field inside the active layer clearly indicates the presence of a cavity mode at this wavelength.<sup>19</sup> Inside the photoactive layer of the nanomesh device the electric field intensity even exceeds the intensity observed in the photoactive layer of the ITO reference device. Thus the light entrapment at this wavelength could indeed contribute to a plasmonically driven enhanced exciton generation.

An even stronger electric field enhancement was found for the PTB7:PC<sub>71</sub>BM device around the absorption maximum of the metal electrode at 750 nm in Figure 9.6i, showing an enhancement factor of up to 15 in the MoO<sub>3</sub> layer and 5.6 averaged over the photoactive layer. We assign this higher electric field enhancement to the smaller distance (70 nm) between the two metallic electrodes in the PTB7:PC<sub>71</sub>BM devices compared to that (120 nm) in the P3HT:PC<sub>61</sub>BM devices. The plasmonic resonance emerging from the nanohole electrode is enhanced by the presence of the Ag back-electrode, which depends on the length of the cavity between the electrodes.<sup>19,50</sup> For thinner devices the coupling between the structured front and the flat back-electrode is expected to be stronger. Although the 70 nm photoactive layer thickness used here may not be the optimum thickness to attain a maximum EQE enhancement at the absorption edge, even an optimized active layer thickness would not prevent the reflectance and absorption losses of the gold structure at the more relevant lower wavelengths (300 – 600 nm).

The low field intensity at the gold/glass interface (Figure 9.6j) points towards a low reflectance and absorption of the gold nanomesh. Here the electrode predominantly couples the incident light forward into the photoactive layer. Consequently, the losses caused by the gold nanomesh are minimal at this wavelength leading to the desired light concentration in the photoactive layer. Whereas PTB7 is only weakly absorbing at 750 nm, the plasmonic field enhancement still leads to a higher exciton generation in the active layer compared to the ITO device. This manifests itself in a higher EQE as shown in Figure 9.5c. At an even higher wavelength of

800 nm, which is off-resonance, one can still observe a field enhancement in the active layer (Figure S9.9). However, it is more confined to the ZnO rather than the active layer. In combination with the low polymer absorption at this wavelength no additional exciton generation and thus no contribution to the photocurrent in the EQE spectrum is seen. Simulated field distribution maps at the absorption maximum of all other periodicities for both photoactive layers also demonstrate the evolution of a cavity mode (see Figure S9.10 and Figure S9.11). While this can be excited with a broad range of periodicities, the coupling strength decreases with increasing  $P$ .

The discrepancy between losses in the short wavelength region and EQE enhancement at long wavelengths has already been described for Au nanowire electrodes<sup>7</sup> and nanoparticle arrays placed on the ITO electrode.<sup>51</sup> While the particles reduced the efficiency at small wavelength due to absorption and reflectance losses, a slightly enhanced efficiency was found at the absorption edge of the active layer attributed to a diffractive scattering or collective plasmonic mode. This scattering mode can only exist at the absorption edge of the active layer as the electric field from the particles would be suppressed by a higher attenuation of the polymer.<sup>52</sup> Instead, nanostructured back contacts result in an EQE enhancement pinned to the absorption edge of the polymer, but naturally without transmittance losses.<sup>26,53-56</sup>

To further clarify the nature of the cavity resonance, additional FDTD simulations were conducted in which we substituted the gold of a nanomesh with  $P = 375$  nm by ITO (Figure S9.12). ITO does not show any plasmonic resonances in the wavelength range of interest and is purely scattering the incident light due to the periodic nanostructure. Thus, the absence of the absorption maximum at 750 nm clearly indicates that this resonance is of plasmonic origin.

### 9.3 Conclusion

In summary, we systematically investigated the chances and limitations of thin plasmonic nanomeshes as transparent conducting electrodes for polymer solar cells. We, therefore, prepared gold nanohole arrays by colloidal lithography covering periodicities from 202 nm up to 2560 nm. These plasmonic nanohole arrays support SPP modes, which are governed by the underlying periodicity, and cover a broad optical range.

The nanohole electrodes were incorporated into organic solar cells consisting of two different photoactive layer polymer blends, the standard material P3HT:PC<sub>61</sub>BM and the low band-gap

material PTB7:PC<sub>71</sub>BM. No losses in the  $V_{OC}$  and FF of the devices indicated the absence of excessive leakage currents and high conductivities of the metal meshes. This renders such electrodes electrically comparable to the ITO reference. For both photoactive polymers, we found appreciable PCEs in our ITO-free devices reaching up to 77% of the reference solar cells. This decreased PCE was not surprising based on the strongly reduced transmittance of the nanohole electrode. Interestingly, the PCE increased with the grating period of the nanomeshes. An optimum was found in both polymer blend cases for  $P = 1040$  nm, which was attributed to an optimum balance between low losses by parasitic absorption and low losses by increasing the reflectivity of the nanomesh.

Plasmonic field enhancement due to the excitation of SPP and cavity modes within the solar cell stack was expected to be able to counteract these losses. We indeed did observe additional absorption peaks in the spectra of the nanomesh devices but only at the absorption edge of the respective polymer. Using FDTD simulation we were able to assign these to the excitation of a cavity mode. However, since this enhanced mode only exists at or below the absorption edge of the particular polymer, no enhancement of the photocurrent was observable for P3HT:PC<sub>61</sub>BM. For PTB7:PC<sub>71</sub>BM the cavity mode led to an EQE enhancement beyond 720 nm, however, this additional contribution was marginal compared to parasitic absorption and reflection losses at lower wavelengths. Consequently, surface plasmon resonances play an ambivalent role in the device optimization of polymer solar cells. They are capable of improving the absorption within a small spectral region. However, the broadband losses at any other wavelength cannot be compensated. To replace ITO without any losses in PCE, traditional methods to increase the overall transmittance such as decreasing the metal layer thickness or reducing the metal surface coverage are expected to have a greater impact (as long as the electrical properties are not compromised). Nevertheless, we want to conclude that this approach is still capable of producing ITO-free solar cells with reasonable PCE's based on standard photoactive material systems.

#### 9.4 Experimental Section

**Materials:** Polystyrene particles were purchased from *Microparticles GmbH* (Berlin) or synthesized using emulsifier-free emulsion polymerization. P3HT (Rieke Metals – 4002-EE), PTB7 (Solarmer – ZP002), PC<sub>61</sub>BM (Solenne) and PC<sub>71</sub>BM (American Dye Source) were

obtained from commercial suppliers and used without any further purification. The thickness and the sheet resistivity of our reference ITO substrates were 213 nm and  $10 \Omega/\square$ , respectively.

**Fabrication of Au nanomeshes:** Monolayers of polystyrene particles were prepared according to the procedure of Retsch et al.<sup>42</sup> Cationically functionalized glass slides were spin-cast with a 3 wt% particle dispersion at a speed of 4000 rpm. Subsequently, the coated glass substrates were immersed in a 0.1 mM SDS solution in MilliQ. The aqueous phase was adjusted to pH 12 by adding a few drops of  $\text{NH}_3$ . A monolayer was formed at the liquid/air interface by self-assembly of the detaching particles. The monolayer was transferred to a  $1 \times 1$  inch glass substrate and dried in air. The monolayers were etched in a plasma reactor MiniFlecto (*Plasma Technology GmbH*, Herrenberg, Germany) with 75 % argon and 25 % oxygen at 80 W at a pressure of 0.14 mbar to obtain non-close-packed monolayers. A 3 nm chromium layer and 50 nm gold were deposited using a Balzers BA360 thermal evaporation chamber. The layer thickness was monitored via a SQM 160 microbalance (*Sigma Instruments, Schaefer Technologie GmbH*). Afterwards, the particles were removed using Scotch® tape (3M) giving the nanohole arrays. The Au substrates were cleaned for 10 min in an ultrasonic bath with a 2 % aqueous Hellmanex (*Hellma GmbH*, Mühlheim, Germany) solution in MilliQ water. The surfactant was extensively rinsed off with MilliQ water, and the substrates were placed in the ultrasonic bath in ethanol for 10 minutes and dried with compressed air.

**Solar cell fabrication:** Solar cell devices were prepared by spin-coating a zinc acetate solution (109.75 mg zinc acetate dehydrate, 30.5  $\mu\text{L}$  ethanol amine and 1 ml methoxyethanol) onto cleaned substrates with patterned nanomeshes, followed by 150 °C baking for 5 min in air to convert zinc acetate to zinc oxide. The reference devices were on ITO glass substrates. The film thickness of the ZnO films was around 40 nm. Subsequently, the substrates were transferred to a glovebox for the deposition of the photoactive layer in a nitrogen environment. P3HT:PC<sub>61</sub>BM films (~115 nm) were prepared by spin-coating (850 rpm) 80  $\mu\text{l}$  of a solution containing 16.8 mg of P3HT and 13.2 mg of PC<sub>61</sub>BM in 1 ml of chlorobenzene. Subsequently, the P3HT:PC<sub>61</sub>BM films were annealed at 135°C for 15 min. PTB7:PC<sub>71</sub>BM films (~80 nm) were prepared by spin-coating (1000 rpm) 90  $\mu\text{l}$  of a solution containing 12 mg PTB7, 19.2 mg PC<sub>71</sub>BM and 50  $\mu\text{l}$  of 1,8-diiodooctane (DIO) in 1 ml of o-xylene. The films were dried in a glovebox anti-chamber for 30 min to remove residual DIO. The respective active layer thicknesses were adjusted to the optimum charge carrier mobility in the devices. Top electrodes consisting of MoO<sub>3</sub> (10 nm) capped by Ag (150 nm) were deposited by vacuum evaporation at  $\sim 1 \times 10^{-6}$  mbar.

**Characterization:** I-V measurements were performed under an inert environment with a Keithley 2400 source measure unit under  $100 \text{ mW/cm}^2$  illumination from an AM 1.5 class A solar simulator. The active area of  $9 \text{ mm}^2$  was defined by the overlap of a black mask aperture area, the ITO or nanomesh electrode, and the evaporated top electrode. External quantum efficiency (EQE) measurements were performed under both dark and white light bias conditions at short-circuit conditions via a Bentham PVE 300 assembly unit. More details have been published elsewhere.<sup>57</sup> UV/VIS spectra were measured using a Cary 5000 UV-Vis-NIR Spectrophotometer (*Agilent Technologies*) with attached Diffuse Reflectance Accessory between 300 and 1200 nm at an angle of incidence of  $8^\circ$  with an UV-bandgap of 3 nm, an IR-bandgap of 12 nm, a data interval of 1 nm, and a scan speed of 600 nm/min. The sheet resistance of the nanomeshes was measured with a Lucas Signatone SYS-301 and a SP4 probe head. SEM images were taken on an LEO 1530 Gemini Field Emission SEM (*Carl Zeiss AG*, Oberkochen, Germany) and an Ultra plus Field Emission SEM (*Carl Zeiss AG*, Oberkochen, Germany). The images were evaluated with the software ImageJ.<sup>58</sup>

**FDTD Simulation:** To determine the refractive index of the glass substrate, ZnO, MoO<sub>3</sub>, P3HT:PC<sub>61</sub>BM and PTB7:PC<sub>71</sub>BM we used an M2000 spectroscopic ellipsometer from *J.A. Woollam Co.* in the wavelength range from 245 nm to 1600 nm (D2 and QTH lamps). Ellipsometric data from all samples were acquired at five different angles of incidence in five-degree steps. To determine the refractive index of all materials we used a general oscillator layer model within the CompleteEASE (Version 5.07) software. All modeling approximation were physical reasonable (parametrization to fulfill Kramers–Kronig relations) and showed a mean square error (MSE) below five. The optical response in transmission and reflection at normal incidence and unpolarized light was simulated using a commercial software from *Lumerical Solutions, Inc.* (FDTD Solutions, Version 8.11.422). We used a hexagonal hole structure with periodic boundary condition (BC) in later direction and perfect match layer (PML) BC in beam direction with a linear polarized plane wave source. Hole diameters, periodicity, the amount of multilayer materials and thickness were obtained from the experiment. In beam direction, the FDTD simulation total length was chosen to be  $4 \mu\text{m}$  with transmission monitors located at both ends. The simulation setup has been placed in the center of the FDTD simulations, and the plane wave source was injected starting from the glass layer. For a broadband source simulation ( $\lambda = 300 - 800 \text{ nm}$ ), the FDTD software approximates the refractive index of the materials by a polynomial function (the refractive indices determined via spectral ellipsometry and the FDTD approximations are given in Figure S9.13 – Figure S9.17). All optical constants were approximated with an RMS error below 0.21. An anisotropic mesh

overwrite region were used according to the specific periodicity and hole diameter (mesh in lateral direction: between 2 nm mesh for  $P = 202$  nm and 6 nm mesh for  $P = 2560$  nm, mesh in beam direction: always 2 nm). All simulations reached the auto shut-off level of  $10^{-5}$  before reaching 1000 fs simulation time. To determine the electric field distribution and surface charge densities, we simulated the model at the plasmonic mode frequency at a pulse length of  $\sim 20$  fs (optimized for long pulse length).

### Acknowledgements

This work was funded by the German Research Foundation (DFG) by the SFB840. C.S. acknowledges support from the Elite Network Bavaria (ENB). The authors thank Fabian Nutz for the particle synthesis and Dr. Beate Förster and Martina Heider from the Bayreuth Institute of Macromolecular Research (BIMF) for their support using the scanning electron microscopy facilities. M.T. and C.R.S. also acknowledge the financial support by the Bavarian State Ministry for Environment and Consumer Protection (UMWELTnanoTECH) and Bavarian State Ministry for Education, Culture, Science and Arts (Solartechnologies Go Hybrid). T.K. acknowledges support from Leibniz-Institut für Polymerforschung (IPF) Dresden e. V. and Cluster of Excellence Centre for Advancing Electronics Dresden (CFAED). We also thank Prof. Sven Hüttner for providing the optical constants of MoO<sub>3</sub> layer.

### References

1. Kumar, A. & Zhou, C. The race to replace tin-doped indium oxide: which material will win? *ACS Nano* **4**, 11-14 (2010).
2. Kim, H., Gilmore, C. M., Piqué, A., Horwitz, J. S., Mattoussi, H., Murata, H., Kafafi, Z. H. & Chrisey, D. B. Electrical, optical, and structural properties of indium–tin–oxide thin films for organic light-emitting devices. *J. Appl. Phys.* **86**, 6451-6461 (1999).
3. Cairns, D. R., Witte, R. P., Sparacin, D. K., Sachsman, S. M., Paine, D. C., Crawford, G. P. & Newton, R. R. Strain-dependent electrical resistance of tin-doped indium oxide on polymer substrates. *Appl. Phys. Lett.* **76**, 1425-1427 (2000).
4. Geng, H. Z., Kim, K. K., So, K. P., Lee, Y. S., Chang, Y. & Lee, Y. H. Effect of acid treatment on carbon nanotube-based flexible transparent conducting films. *J. Am. Chem. Soc.* **129**, 7758-7759 (2007).
5. O'Connor, B., Haughn, C., An, K.-H., Pipe, K. P. & Shtein, M. Transparent and conductive electrodes based on unpatterned, thin metal films. *Appl. Phys. Lett.* **93**, 223304 (2008).
6. De, S., Higgins, T. M., Lyons, P. E., Doherty, E. M., Nirmalraj, P. N., Blau, W. J., Boland, J. J. & Coleman, J. N. Silver Nanowire Networks as Flexible, Transparent,

- Conducting Films: Extremely High DC to Optical Conductivity Ratios. *ACS Nano* **3**, 1767-1774 (2009).
7. van de Groep, J., Gupta, D., Verschuuren, M. A., Wienk, M. M., Janssen, R. A. & Polman, A. Large-area soft-imprinted nanowire networks as light trapping transparent conductors. *Sci. Rep.* **5**, 11414 (2015).
  8. Kang, M.-G., Kim, M.-S., Kim, J. & Guo, L. J. Organic Solar Cells Using Nanoimprinted Transparent Metal Electrodes. *Adv. Mater.* **20**, 4408-4413 (2008).
  9. Galagan, Y., J.M. Rubingh, J.-E., Andriessen, R., Fan, C.-C., W.M. Blom, P., C. Veenstra, S. & M. Kroon, J. ITO-free flexible organic solar cells with printed current collecting grids. *Sol. Energy Mater. Sol. Cells* **95**, 1339-1343 (2011).
  10. Rao, K. D., Hunger, C., Gupta, R., Kulkarni, G. U. & Thelakkat, M. A cracked polymer templated metal network as a transparent conducting electrode for ITO-free organic solar cells. *Phys. Chem. Chem. Phys.* **16**, 15107-15110 (2014).
  11. Hunger, C., Rao, K. D. M., Gupta, R., Singh, C. R., Kulkarni, G. U. & Thelakkat, M. Transparent Metal Network with Low Haze and High Figure of Merit applied to Front and Back Electrodes in Semitransparent ITO-free Polymer Solar Cells. *Energy Technol.* **3**, 638-645 (2015).
  12. Wu, W. & Tassi, N. G. A broadband plasmonic enhanced transparent conductor. *Nanoscale* **6**, 7811-7816 (2014).
  13. Cheng, K., Cui, Z., Li, Q., Wang, S. & Du, Z. Large-scale fabrication of a continuous gold network for use as a transparent conductive electrode in photo-electronic devices. *Nanotechnology* **23**, 425303 (2012).
  14. Kwon, N., Kim, K., Sung, S., Yi, I. & Chung, I. Highly conductive and transparent Ag honeycomb mesh fabricated using a monolayer of polystyrene spheres. *Nanotechnology* **24**, 235205 (2013).
  15. Maurer, J. H., Gonzalez-Garcia, L., Reiser, B., Kanelidis, I. & Kraus, T. Templated Self-Assembly of Ultrathin Gold Nanowires by Nanoimprinting for Transparent Flexible Electronics. *Nano Lett.* **16**, 2921-2925 (2016).
  16. Lee, J.-Y., Connor, S. T., Cui, Y. & Peumans, P. Solution-Processed Metal Nanowire Mesh Transparent Electrodes. *Nano Lett.* **8**, 689-692 (2008).
  17. Ebbesen, T. W., Lezec, H. J., Ghaemi, H. F., Thio, T. & Wolff, P. A. Extraordinary optical transmission through sub-wavelength hole arrays. *Nature* **391**, 667-669 (1998).
  18. Chi, Y.-M., Chen, H.-L., Lai, Y.-S., Chang, H.-M., Liao, Y.-C., Cheng, C.-C., Chen, S.-H., Tseng, S.-C. & Lin, K.-T. Optimizing surface plasmon resonance effects on finger electrodes to enhance the efficiency of silicon-based solar cells. *Energy Environ. Sci.* **6**, 935-942 (2013).
  19. Du, Q. G., Ren, H., Wu, L., Bai, P., Png, C. E., Sun, X. W., Kam, C. H. & Martijn de Sterke, C. Light absorption mechanism in organic solar cells with hexagonal lattice nanohole aluminum transparent electrodes. *J. Opt.* **17**, 085901 (2015).
  20. Couture, M., Liang, Y., Poirier Richard, H. P., Faid, R., Peng, W. & Masson, J. F. Tuning the 3D plasmon field of nanohole arrays. *Nanoscale* **5**, 12399-12408 (2013).
  21. Schwind, M., Kasemo, B. & Zoric, I. Localized and propagating plasmons in metal films with nanoholes. *Nano Lett.* **13**, 1743-1750 (2013).
  22. Park, T.-H., Mirin, N., Lassiter, J. B., Nehl, C. L., Halas, N. J. & Nordlander, P. Optical Properties of a Nanosized Hole in a Thin Metallic Film. *ACS Nano* **2**, 25-32 (2008).
  23. Petoukhoff, C. E., Shen, Z., Jain, M., Chang, A. & O'Carroll, D. M. Plasmonic electrodes for bulk-heterojunction organic photovoltaics: a review. *J. Photonics Energy* **5**, 057002 (2015).

24. Karg, M., König, T. A. F., Retsch, M., Stelling, C., Reichstein, P. M., Honold, T., Thelakkat, M. & Fery, A. Colloidal self-assembly concepts for light management in photovoltaics. *Mater. Today* **18**, 185-205 (2015).
25. Atwater, H. A. & Polman, A. Plasmonics for improved photovoltaic devices. *Nat. Mater.* **9**, 205-213 (2010).
26. Singh, C. R., Honold, T., Gujar, T. P., Retsch, M., Fery, A., Karg, M. & Thelakkat, M. The role of colloidal plasmonic nanostructures in organic solar cells. *Phys. Chem. Chem. Phys.* **18**, 23155-23163 (2016).
27. Min, C. J., Li, J., Veronis, G., Lee, J. Y., Fan, S. H. & Peumans, P. Enhancement of optical absorption in thin-film organic solar cells through the excitation of plasmonic modes in metallic gratings. *Appl. Phys. Lett.* **96**, 3 (2010).
28. Zeng, B., Kafafi, Z. H. & Bartoli, F. J. Transparent electrodes based on two-dimensional Ag nanogrids and double one-dimensional Ag nanogratings for organic photovoltaics. *J. Photon. Energy* **5**, 057005 (2014).
29. Luhman, W. A., Lee, S. H., Johnson, T. W., Holmes, R. J. & Oh, S. H. Self-assembled plasmonic electrodes for high-performance organic photovoltaic cells. *Appl. Phys. Lett.* **99**, 103306 (2011).
30. Ostfeld, A. E. & Pacifici, D. Plasmonic concentrators for enhanced light absorption in ultrathin film organic photovoltaics. *Appl. Phys. Lett.* **98**, 113112 (2011).
31. Zeng, B. B., Gan, Q. Q., Kafafi, Z. H. & Bartoli, F. J. Polymeric photovoltaics with various metallic plasmonic nanostructures. *J. Appl. Phys.* **113**, 063109 (2013).
32. Bai, W., Gan, Q., Song, G., Chen, L., Kafafi, Z. & Bartoli, F. Broadband short-range surface plasmon structures for absorption enhancement in organic photovoltaics. *Opt. Express* **18**, A620-A630 (2010).
33. Liu, K., Zeng, B., Song, H., Gan, Q., Bartoli, F. J. & Kafafi, Z. H. Super absorption of ultra-thin organic photovoltaic films. *Opt. Commun.* **314**, 48-56 (2014).
34. Reilly, T. H., van de Lagemaat, J., Tenent, R. C., Morfa, A. J. & Rowlen, K. L. Surface-plasmon enhanced transparent electrodes in organic photovoltaics. *Appl. Phys. Lett.* **92**, 243304 (2008).
35. Takatori, K., Nishino, T., Okamoto, T., Takei, H., Ishibashi, K. & Micheletto, R. Indium-free organic thin-film solar cells using a plasmonic electrode. *J. Phys. D-Appl. Phys.* **49**, 185106 (2016).
36. Zhu, J., Zhu, X., Hoekstra, R., Li, L., Xiu, F., Xue, M., Zeng, B. & Wang, K. L. Metallic nanomesh electrodes with controllable optical properties for organic solar cells. *Appl. Phys. Lett.* **100**, 143109 (2012).
37. Morfa, A. J., Akinoglu, E. M., Subbiah, J., Giersig, M. & Mulvaney, P. Transparent metal electrodes from ordered nanosphere arrays. *J. Appl. Phys.* **114**, 054502 (2013).
38. Chou, S. Y. & Ding, W. Ultrathin, high-efficiency, broad-band, omni-acceptance, organic solar cells enhanced by plasmonic cavity with subwavelength hole array. *Opt. Express* **21**, A60-A76 (2013).
39. Dang, M. T., Hirsch, L. & Wantz, G. P3HT:PCBM, Best Seller in Polymer Photovoltaic Research. *Adv. Mater.* **23**, 3597-3602 (2011).
40. He, Z., Zhong, C., Su, S., Xu, M., Wu, H. & Cao, Y. Enhanced power-conversion efficiency in polymer solar cells using an inverted device structure. *Nat. Photonics* **6**, 593-597 (2012).
41. Kosiorek, A., Kandulski, W., Chudzinski, P., Kempa, K. & Giersig, M. Shadow Nanosphere Lithography: Simulation and Experiment. *Nano Lett.* **4**, 1359-1363 (2004).

42. Retsch, M., Zhou, Z., Rivera, S., Kappl, M., Zhao, X. S., Jonas, U. & Li, Q. Fabrication of Large-Area, Transferable Colloidal Monolayers Utilizing Self-Assembly at the Air/Water Interface. *Macromol. Chem. Phys.* **210**, 230-241 (2009).
43. Ai, B., Yu, Y., Möhwald, H., Zhang, G. & Yang, B. Plasmonic films based on colloidal lithography. *Adv. Colloid Interface Sci.* **206**, 5-16 (2014).
44. Ye, X. & Qi, L. Two-dimensionally patterned nanostructures based on monolayer colloidal crystals: Controllable fabrication, assembly, and applications. *Nano Today* **6**, 608-631 (2011).
45. Genet, C., van Exter, M. P. & Woerdman, J. P. Fano-type interpretation of red shifts and red tails in hole array transmission spectra. *Opt. Commun.* **225**, 331-336 (2003).
46. Luk'yanchuk, B., Zheludev, N. I., Maier, S. A., Halas, N. J., Nordlander, P., Giessen, H. & Chong, C. T. The Fano resonance in plasmonic nanostructures and metamaterials. *Nat. Mater.* **9**, 707-715 (2010).
47. Mayer, M., Tebbe, M., Kuttner, C., Schnepf, M. J., König, T. A. & Fery, A. Template-assisted colloidal self-assembly of macroscopic magnetic metasurfaces. *Faraday Discuss.* **191**, 159-176 (2016).
48. Fei Guo, C., Sun, T., Cao, F., Liu, Q. & Ren, Z. Metallic nanostructures for light trapping in energy-harvesting devices. *Light-Sci. Appl.* **3**, e161 (2014).
49. Lindquist, N. C., Luhman, W. A., Oh, S. H. & Holmes, R. J. Plasmonic nanocavity arrays for enhanced efficiency in organic photovoltaic cells. *Appl. Phys. Lett.* **93**, 123308 (2008).
50. Parsons, J., Hendry, E., Sambles, J. R. & Barnes, W. L. Localized surface-plasmon resonances and negative refractive index in nanostructured electromagnetic metamaterials. *Phys. Rev. B* **80**, 245117 (2009).
51. Diukman, I., Tzabari, L., Berkovitch, N., Tessler, N. & Orenstein, M. Controlling absorption enhancement in organic photovoltaic cells by patterning Au nano disks within the active layer. *Opt. Express* **19 Suppl 1**, A64-71 (2011).
52. Tsai, S. J., Ballarotto, M., Romero, D. B., Herman, W. N., Kan, H. C. & Phaneuf, R. J. Effect of gold nanopillar arrays on the absorption spectrum of a bulk heterojunction organic solar cell. *Opt. Express* **18**, A528-A535 (2010).
53. Li, X., Choy, W. C. H., Ren, X., Xin, J., Lin, P. & Leung, D. C. W. Polarization-independent efficiency enhancement of organic solar cells by using 3-dimensional plasmonic electrode. *Appl. Phys. Lett.* **102**, 153304 (2013).
54. Petoukhoff, C. E. & O'Carroll, D. M. Absorption-induced scattering and surface plasmon out-coupling from absorber-coated plasmonic metasurfaces. *Nat. Commun.* **6**, 7899 (2015).
55. Hsiao, Y.-S., Chien, F.-C., Huang, J.-H., Chen, C.-P., Kuo, C.-W., Chu, C.-W. & Chen, P. Facile Transfer Method for Fabricating Light-Harvesting Systems for Polymer Solar Cells. *J. Phys. Chem. C* **115**, 11864-11870 (2011).
56. Li, X. H., Sha, W. E. I., Choy, W. C. H., Fung, D. D. S. & Xie, F. X. Efficient Inverted Polymer Solar Cells with Directly Patterned Active Layer and Silver Back Grating. *J. Phys. Chem. C* **116**, 7200-7206 (2012).
57. Singh, C. R., Li, C., Mueller, C. J., Huttner, S. & Thelakkat, M. Influence of Electron Extracting Interface Layers in Organic Bulk-Heterojunction Solar Cells. *Adv. Mater. Interfaces* **3** (2016).
58. Rasband, W. S. *ImageJ*, U. S. National Institutes of Health, Bethesda, Maryland, USA, <http://imagej.nih.gov/ij> (1997-2016).

## 9.5 Supplementary Information

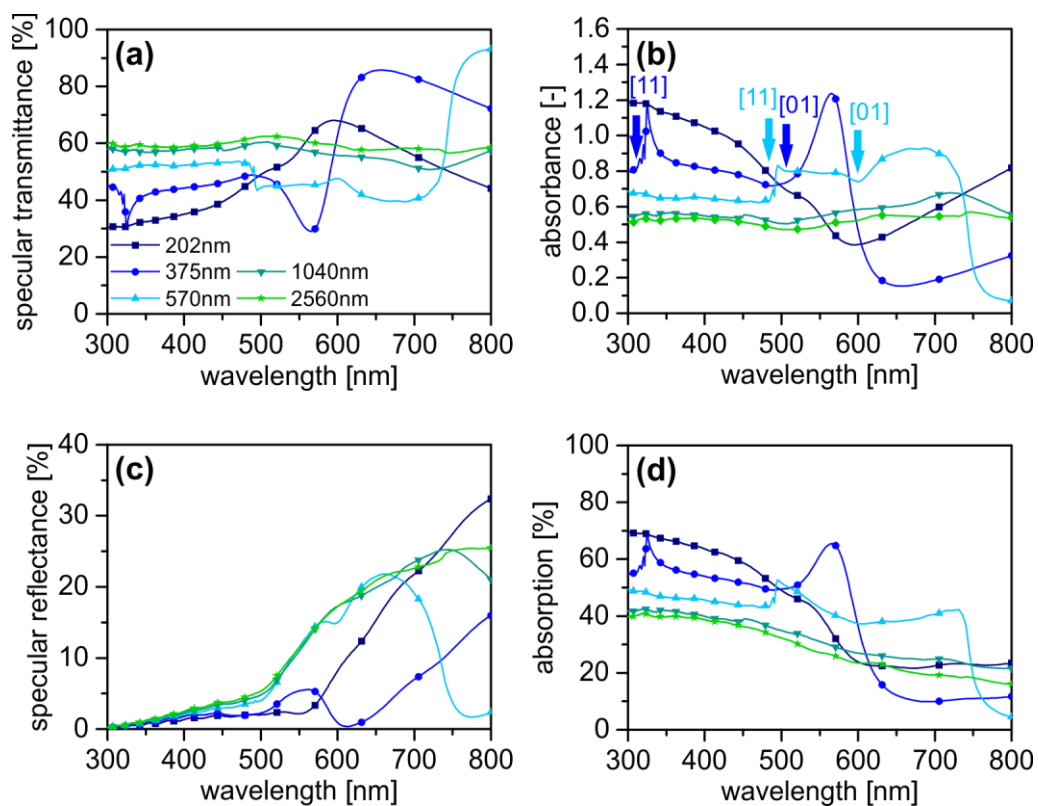


**Figure S9.1.** FDTD simulation of the pure nanomeshes on glass normalized to the glass substrate with variable periodicity  $P$  and constant gold area fraction of 40 %. Normal incident specular transmittance (a), absorbance (b), specular reflectance (c) and absorption (d) spectra calculated with unpolarized light. The arrows in (b) indicate the Bragg diffraction modes for  $P = 375$  nm and  $P = 570$  nm.

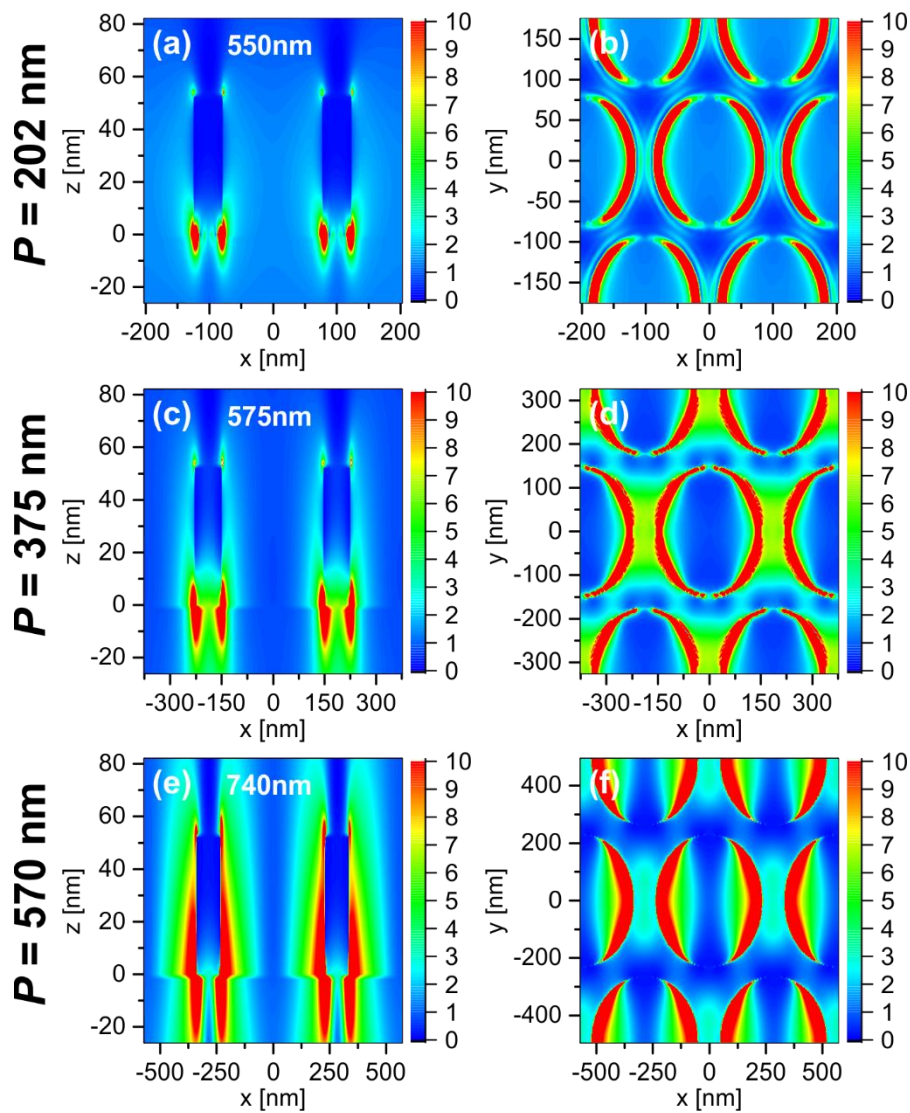


**Figure S9.2.** Simulated electric field distributions  $|E|^2/|E_0|^2$  for the pure nanomeshes with variable periodicity on glass. Cross-section electric field profile (a) and top view electric field profile (b) for  $P = 202$  nm and a wavelength of 550 nm. Cross-section electric field profile (c) and top view electric field profile (d) for  $P = 375$  nm and a wavelength of 575 nm. Cross-section electric field profile (e) and top view electric field profile (f) for  $P = 570$  nm and a wavelength of 740 nm.

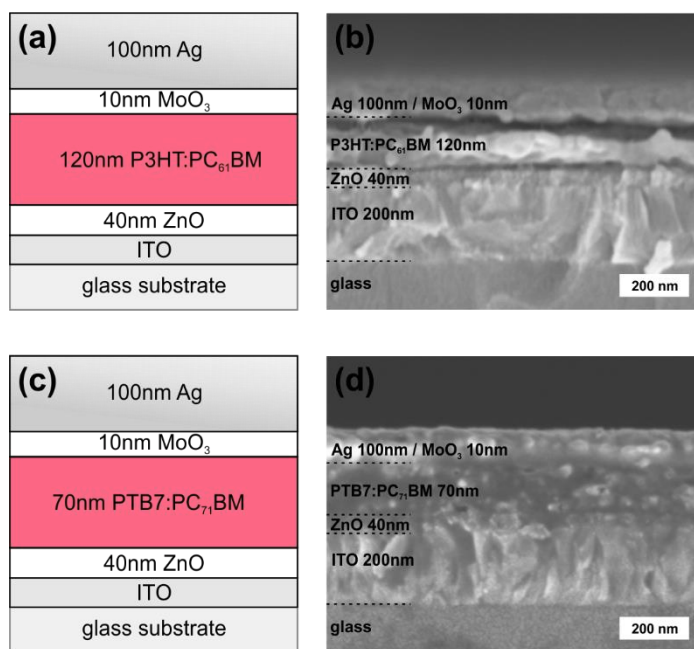


**Figure S9.3.** ITO reference devices. Schematic illustration of the ITO reference device structure with (a) P3HT:PC<sub>61</sub>BM and (c) PTB7:PC<sub>71</sub>BM active layer. SEM cross-section of the ITO reference device with (c) P3HT:PC<sub>61</sub>BM and (d) PTB7:PC<sub>71</sub>BM active layer.

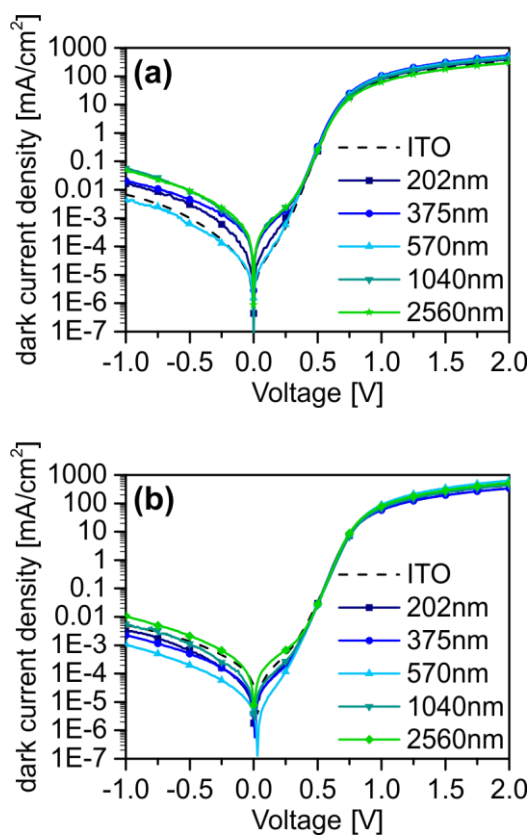


**Figure S9.4.** Dark current-density characteristics. Dark current-density - voltage curves of (a) P3HT:PC<sub>61</sub>BM and (b) PTB7:PC<sub>71</sub>BM solar cells for different hole-to-hole distances on nanomesh electrode.

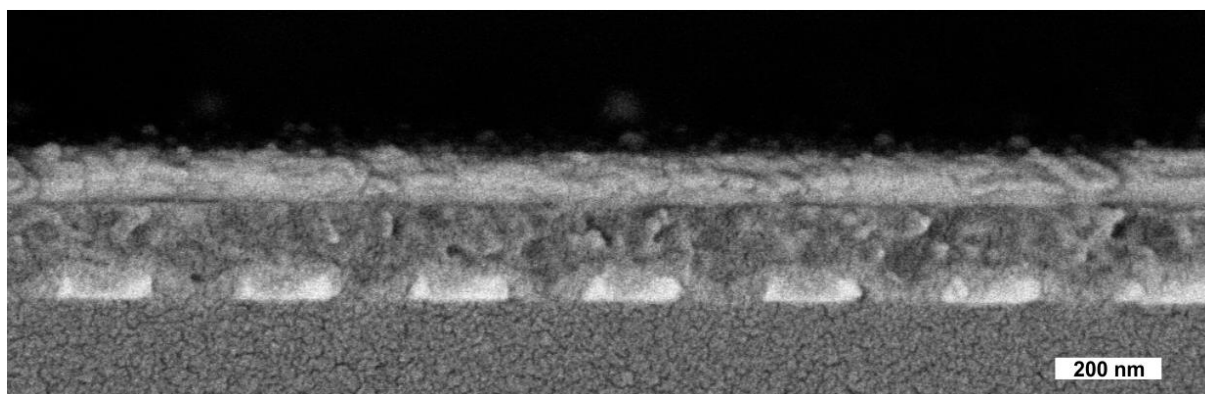


**Figure S9.5.** BSE image of nanomesh solar cell. SEM cross-section of the nanomesh device with P3HT:PC<sub>61</sub>BM active layer and  $P = 202$  nm measured with the backscattered electron (BSE) detector.

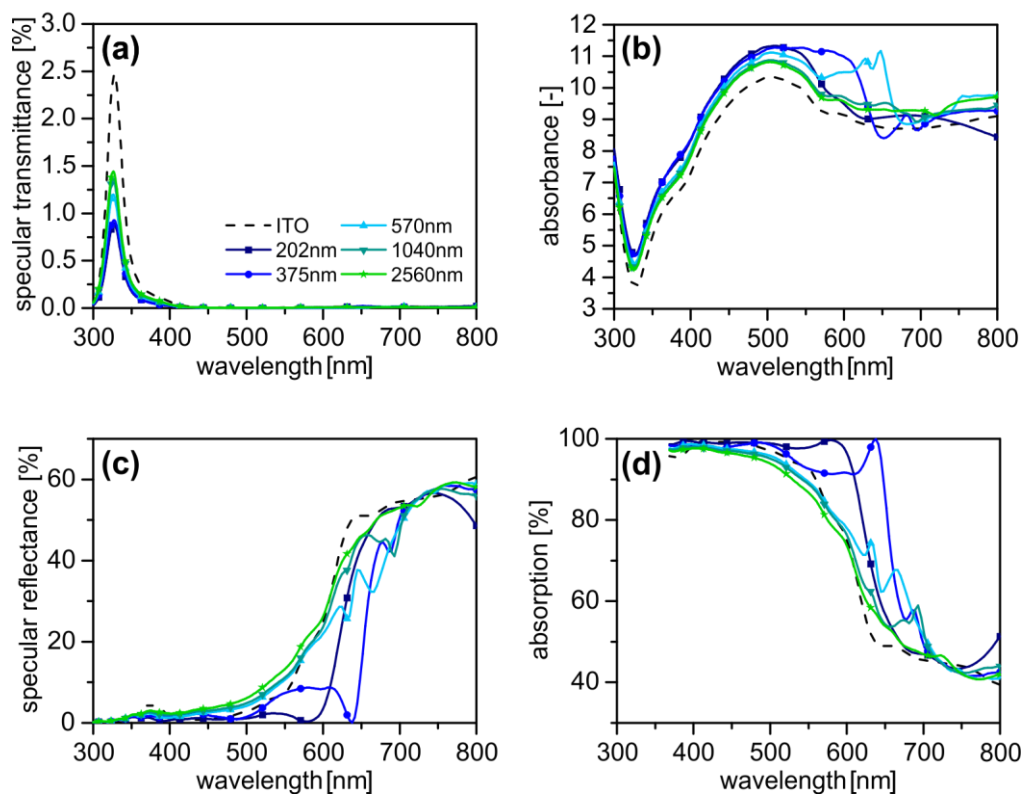


**Figure S9.6.** FDTD simulation of the P3HT:PC<sub>61</sub>BM solar cell devices with gold nanohole electrodes and different periodicities compared to ITO reference devices. Normal incident specular transmittance (a), absorbance (b), specular reflectance (c) and absorption (d) spectra.

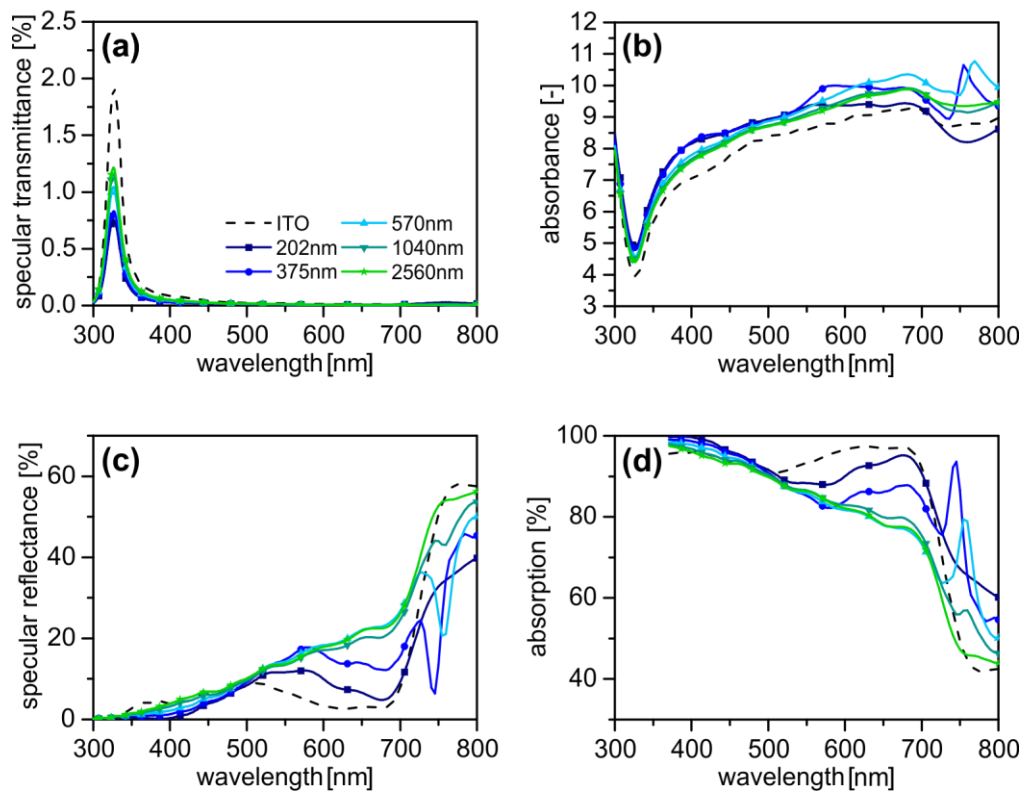


**Figure S9.7.** FDTD simulation of the PTB7:PC<sub>71</sub>BM solar cell devices with gold nanohole electrodes and different periodicities compared to ITO reference devices. Normal incident specular transmittance (a), absorbance (b), specular reflectance (c) and absorption (d) spectra.

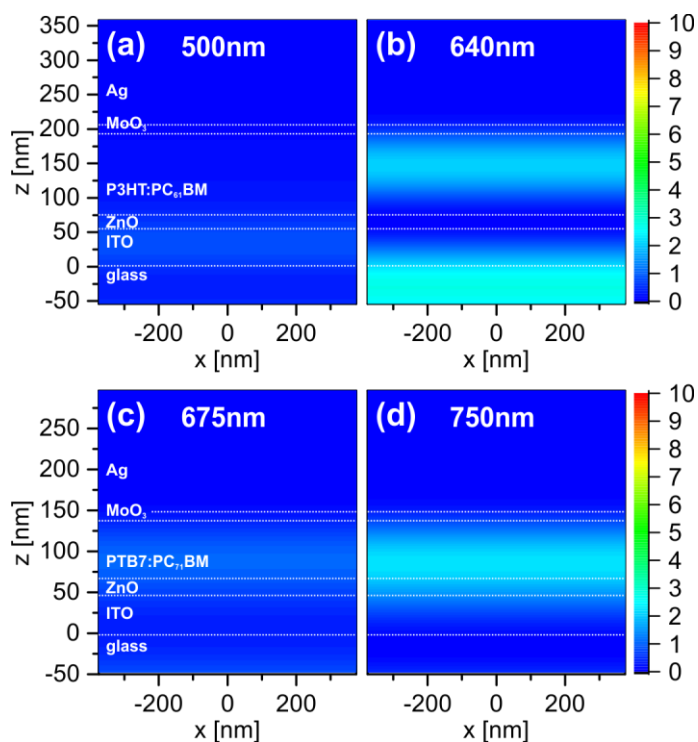


**Figure S9.8.** Electric field distributions of ITO reference devices. Cross-section electric field distributions  $|E|^2/|E_0|^2$  of the ITO reference devices for P3HT:PC<sub>61</sub>BM at 500 nm (a) and 640 nm (b) and for PTB7:PC<sub>71</sub>BM at 675 nm (c) and 750 nm (d).

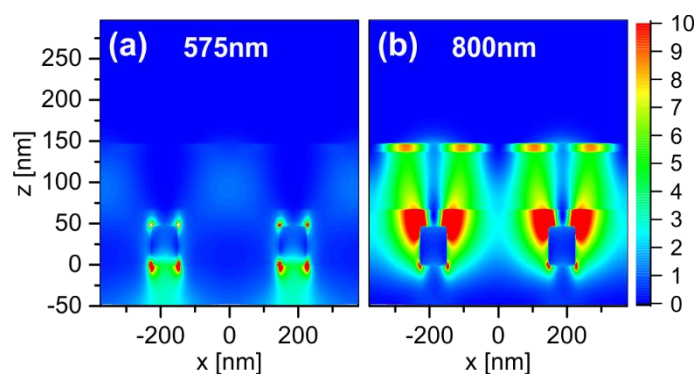


**Figure S9.9.** FDTD simulation of the PTB7:PC<sub>71</sub>BM solar cell device with a gold nanomesh electrode and  $P = 375$  nm. Cross-section electric field distributions  $|E|^2/|E_0|^2$  at 575 nm (a) and 800 nm (b).

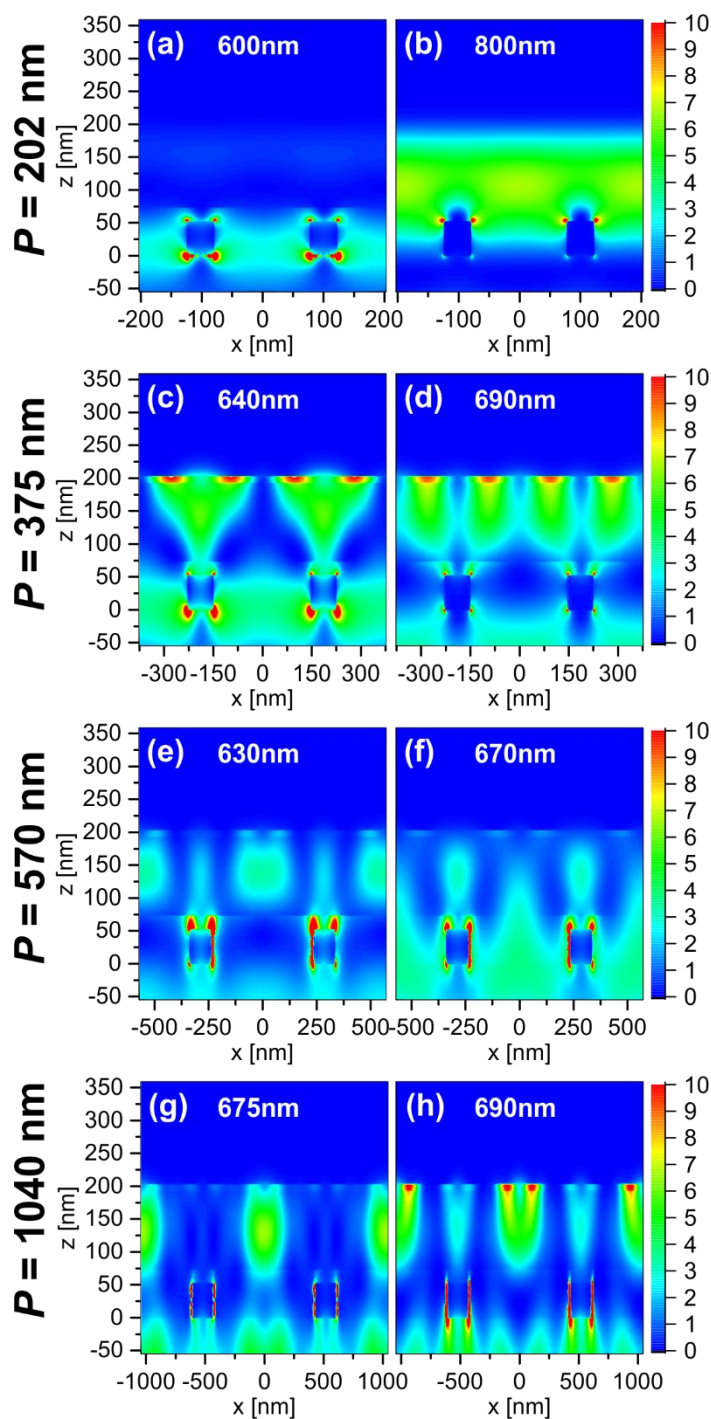


**Figure S9.10.** FDTD simulation of the P3HT:PC<sub>61</sub>BM solar cell devices with gold nanomesh electrodes and variable nanomesh periodicities. Cross-section electric field distributions  $|E|^2/|E_0|^2$  at 600 nm (a) and 800 nm (b) for  $P = 202$  nm, at 640 nm (c) and 690 nm (d) for  $P = 375$  nm, at 630 nm (e) and 670 nm (f) for  $P = 570$  nm, at 675 nm (g) and 690 nm (h) for  $P = 1040$  nm.

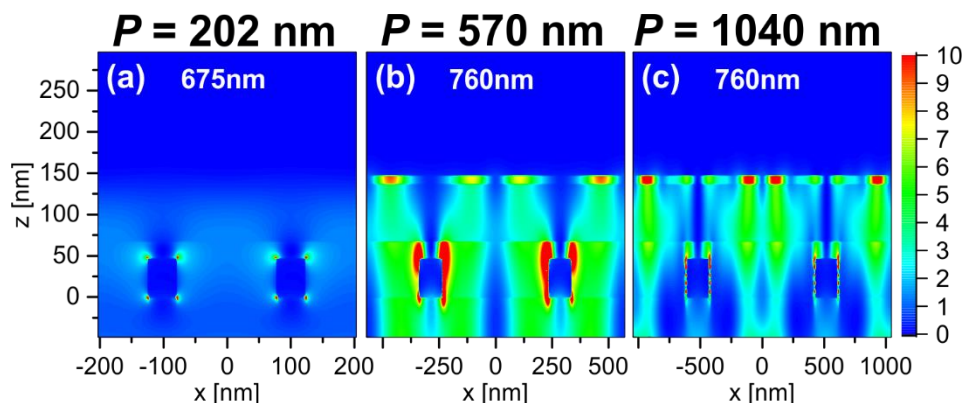


**Figure S9.11.** FDTD simulation of the PTB7:PC<sub>71</sub>BM solar cell devices with gold nanomesh electrodes and variable nanomesh periodicities. Cross-section electric field distributions  $|E|^2/|E_0|^2$  at 675 nm for  $P = 202$  nm (a), at 760 nm for  $P = 570$  nm (b), at 760 nm for  $P = 1040$  nm (c).

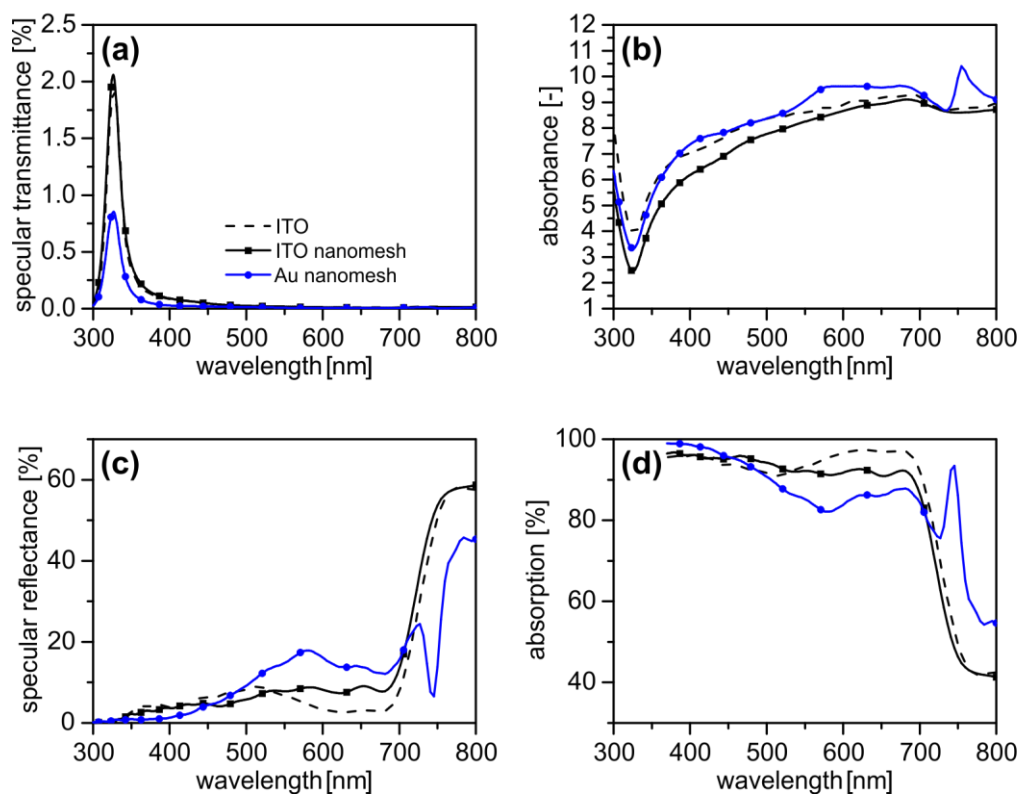


**Figure S9.12.** FDTD simulation of PTB7:PC<sub>71</sub>BM solar cell devices with gold nanomesh electrodes and ITO nanomesh electrodes with  $P = 375$  nm compared to the planar ITO reference device. Normal incident specular transmittance (a), absorbance (b), specular reflectance (c) and absorption (d) spectra.

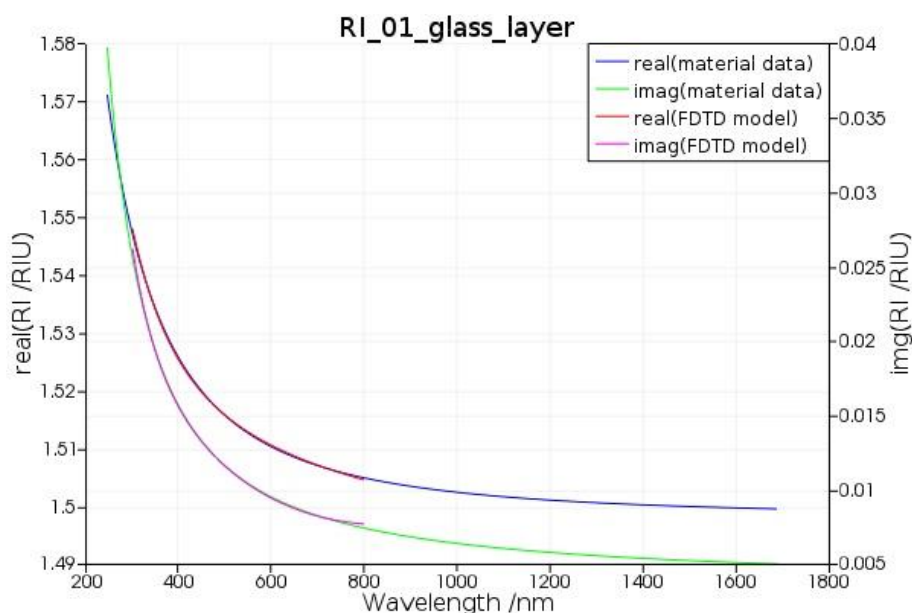


**Figure S9.13.** Refractive index of glass. Complex refractive index (RI) of the glass layer (standard microscopy slides, *Menzel*, Braunschweig, Germany) determined with spectral ellipsometry (material data) and FDTD approximation with a polynomial function (FDTD model). For further usage the raw data (material data) will be available at <http://refractiveindex.info/>.

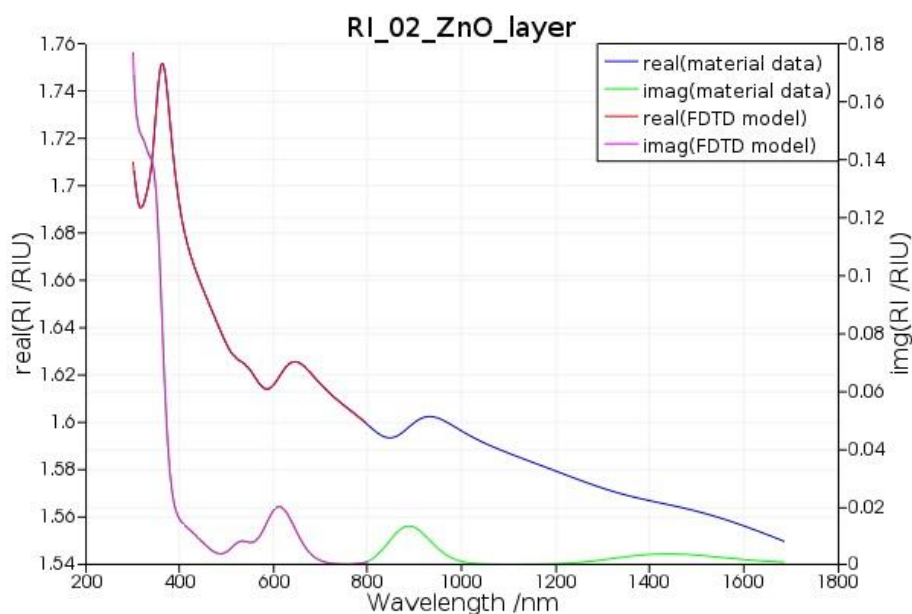


**Figure S9.14.** Refractive index of ZnO. Complex refractive index (RI) of the ZnO layer determined with spectral ellipsometry (material data) and FDTD approximation with a polynomial function (FDTD model).

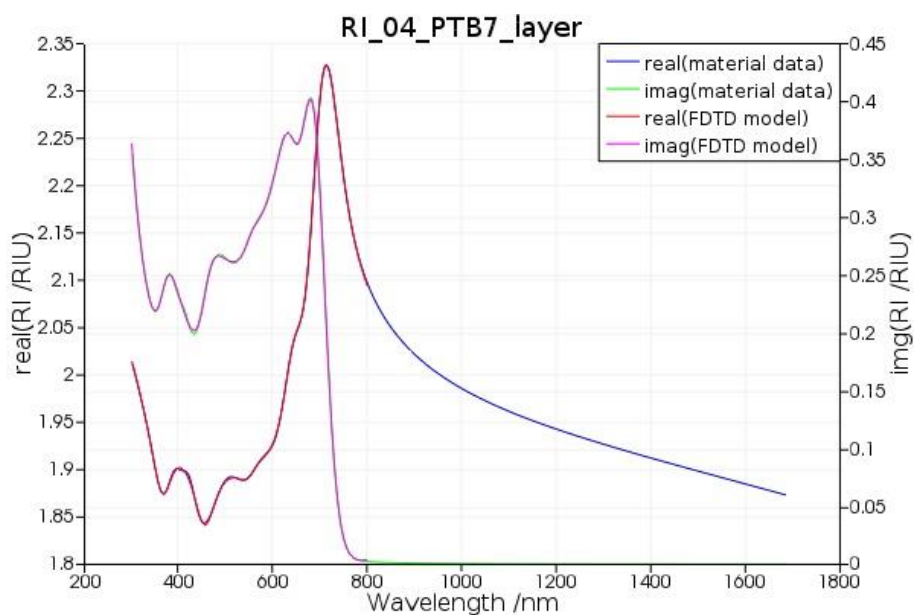


**Figure S9.15.** Refractive index of PTB7:PC<sub>71</sub>BM. Complex refractive index (RI) of the PTB7:PC<sub>71</sub>BM layer determined with spectral ellipsometry (material data) and FDTD approximation with a polynomial function (FDTD model).

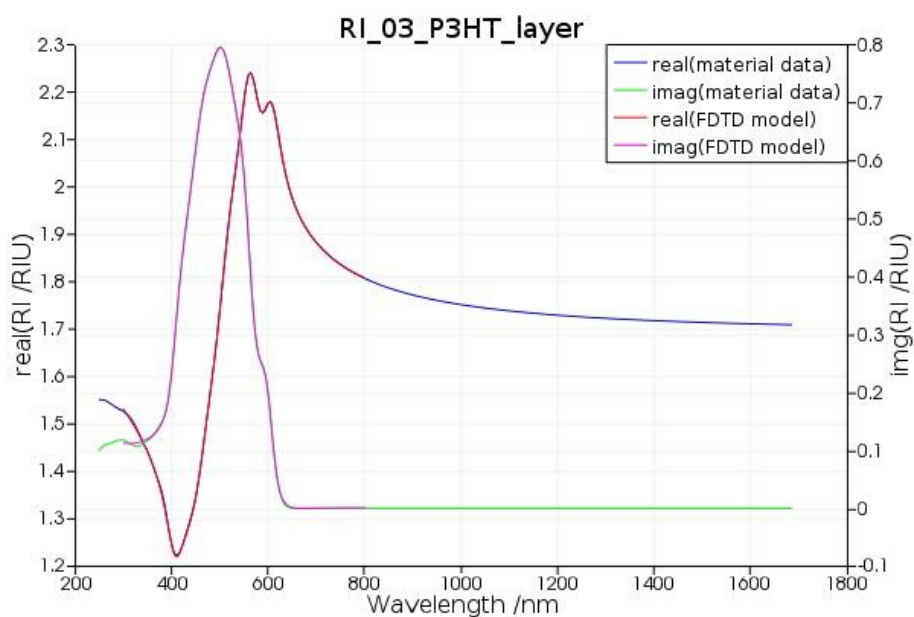


**Figure S9.16.** Refractive index of P3HT:PC<sub>61</sub>BM. Complex refractive index (RI) of the P3HT:PC<sub>61</sub>BM layer determined with spectral ellipsometry (material data) and FDTD approximation with a polynomial function (FDTD model).

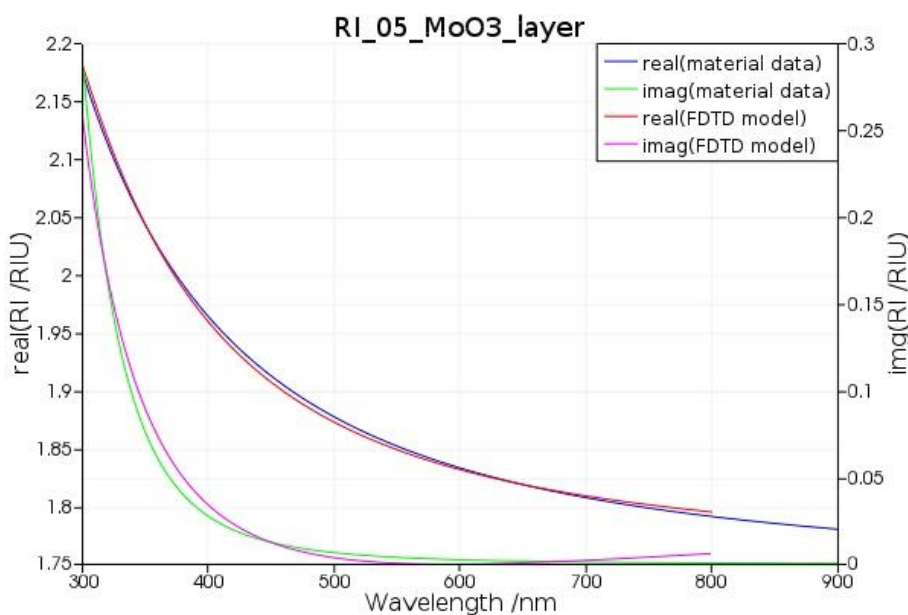


**Figure S9.17.** Refractive index of MoO<sub>3</sub>. Complex refractive index (RI) of the MoO<sub>3</sub> layer determined with spectral ellipsometry (material data) and FDTD approximation with a polynomial function (FDTD model).

**Gold** was taken from Johnson and Christy (JC) [Johnson, P. B.; Christy, R. W. Optical Constants of the Noble Metals. *Phys. Rev. B* 1972, 6, 4370-4379.]

**Ag** was taken from Hagemann et al. (CRC) [Hagemann, H. J.; Gudat, W.; Kunz, C. Optical Constants from the Far Infrared to the X-Ray Region: Mg, Al, Cu, Ag, Au, Bi, C, and Al<sub>2</sub>O<sub>3</sub>. *J. Opt. Soc. Am. A* 1975, 65, 742-744.]

**ITO** from was taken from the CompleteEASE (Version 5.07) refractive index database.



## 10 Outlook

The concepts presented in this thesis consort to the tremendous efforts that have been made in the field of photonic and plasmonic crystals during the last decades. In the ongoing race of miniaturization, colloidal crystals play an essential role due to their ability to manipulate light analogously to electrons in semiconductors. To realize the dream of purely photonic circuits, colloidal self-assembly could offer a cost-effective alternative to conventional lithography techniques. Apart from optical circuits, many applications of colloidal assemblies or their replica are already within reach such as molecular sensing devices, structural coloration or dirt-repellant and antifouling coatings.<sup>1,2</sup>

A plethora of synthesis and assembly protocols are available for spherical colloidal particles with engineered optical properties. However, much work has still to be done to overcome the inherent drawbacks of colloidal assembly. Point defects and grain boundaries caused by vacancies or impurities dramatically deteriorate the optical performance of a photonic crystal. Thus, considerable effort is put into the development of large-scale and defect-free fabrication of colloidal crystals. At the same time, hierarchical structures and highly defined defects have to be introduced to channel and manage light with low losses. The defects can facilitate the nanoscale light generation, waveguiding or light localization.<sup>1</sup> Likewise, the specific introduction of defects into phononic crystals would allow for the engineered propagation and localization of acoustic waves. Template-directed self-assembly could enable these low-defect, hierarchical assemblies.<sup>3</sup> Further work has to be conducted to expand the accessible lattice symmetries, not only in two-dimensions but also in three-dimensional colloidal crystals.

Moreover, the existing self-assembly methods have to be extended to active building blocks, allowing for stimuli-responsive architectures that are switchable by for example light or current. For this, efficient synthesis and purification strategies for more complex building blocks and anisotropic particles have to be established. For example, plasmonic nanoparticles or fluorescent particles self-assembled into gold nanohole arrays might yield highly efficient sensing or lasing devices, respectively. Moreover, the modification of the single particle e.g. by introducing binding sites can push the concept of directed self-assembly to the next level.<sup>4,5</sup>

Similarly, plasmonic structures prepared by colloidal assembly open up huge possibilities for future applications and often directly rival purely dielectric colloidal crystals. Nevertheless, at this point, the high absorption losses of plasmonic structures are the most prominent impediment to their application. While the careful incorporation of metal nanoparticles into

thin-film solar cells proved beneficial for the power conversion efficiency, it is more challenging to implement plasmonic grating structures as transparent conductive electrodes. Minimizing the high losses of plasmonic structures by optimizing the structure and materials remains one of the most important goals in plasmonic research. Furthermore, the interaction of plasmonic structures and absorbing materials has to be further understood to be able to deliberately design efficient optical devices.

However, for both, dielectric and plasmonic colloidal structures, numerous obstacles still have to be resolved to be able to compete with conventional technologies.

### References

1. Cong, H., Yu, B., Tang, J., Li, Z. & Liu, X. Current status and future developments in preparation and application of colloidal crystals. *Chem. Soc. Rev.* **42**, 7774-7800 (2013).
2. Vogel, N., Retsch, M., Fustin, C. A., Del Campo, A. & Jonas, U. Advances in colloidal assembly: the design of structure and hierarchy in two and three dimensions. *Chem. Rev.* **115**, 6265-6311 (2015).
3. Ozin, G. A. & Yang, S. M. The race for the photonic chip: Colloidal crystal assembly in silicon wafers. *Adv. Funct. Mater.* **11**, 95-104 (2001).
4. Duguet, E., Desert, A., Perro, A. & Ravaine, S. Design and elaboration of colloidal molecules: an overview. *Chem. Soc. Rev.* **40**, 941-960 (2011).
5. Gröschel, A. H., Schacher, F. H., Schmalz, H., Borisov, O. V., Zhulina, E. B., Walther, A. & Müller, A. H. Precise hierarchical self-assembly of multicompartment micelles. *Nat Commun* **3**, 710 (2012).

---

## List of Publications

1. Stelling, Christian; Bernhardt, Christoph; Retsch, Markus.  
"Subwavelength Etched Colloidal Monolayers: A Model System for Tunable Antireflective Coatings"  
*Macromolecular Chemistry and Physics* **2015**, *216*, 1682-1688.
2. Vega-Flick, Alejandro; Duncan, Ryan A.; Wallen, Sam P.; Boechler, Nicholas; Stelling, Christian; Retsch, Markus; Alvarado-Gil, Juan J.; Nelson, Keith A.; Maznev, Alexei A.  
"Vibrational dynamics of a two-dimensional microgranular crystal"  
*Physical Review B* **2017**, *96*, 024303.
3. Hummel, Miriam E. J.; Stelling, Christian; Kopera, Bernd A. F.; Nutz, Fabian A.; Karg, Matthias; Retsch, Markus; Förster, Stephan.  
"Ordered Particle Arrays via a Langmuir Transfer Process: Access to Any Two-Dimensional Bravais Lattice"  
*Langmuir* **2019**, *35*, 973-979.
4. Stelling, Christian; Mark, Andreas; Papastavrou, Georg; Retsch, Markus.  
"Showing particles their place: deterministic colloid immobilization by gold nanomeshes"  
*Nanoscale* **2016**, *8*, 14556-14564.
5. Stelling, Christian; Retsch, Markus.  
"Nanomeshes at Liquid Interfaces: From Free-Standing Hole Arrays toward Metal-Insulator-Metal Architectures"  
*Advanced Materials Interfaces* **2018**, *5*, 1800154.
6. Stelling, Christian; Fossati, Stefan; Dostalec, Jacob; Retsch, Markus.  
"Surface plasmon modes of nanomesh-on-mirror nanocavities prepared by nanosphere lithography"  
*Nanoscale* **2018**, *10*, 17983-17989.
7. Stelling, Christian; Singh, Chetan R.; Karg, Matthias; König, Tobias A. F.; Thelakkat, Mukundan; Retsch, Markus.  
"Plasmonic nanomeshes: their ambivalent role as transparent electrodes in organic solar cells"  
*Scientific Reports* **2017**, *7*, 42530.

8. Karg, Matthias; König, Tobias A. F.; Retsch, Markus; Stelling, Christian; Reichstein, Paul M.; Honold, Tobias; Thelakkat, Mukundan; Fery, Andreas.  
"Colloidal self-assembly concepts for light management in photovoltaics"  
*Materials Today* **2015**, *18*, 185-205.
9. Nellist, Michael R.; Chen, Yikai; Mark, Andreas; Gödrich, Sebastian; Stelling, Christian; Jiang, Jingjing; Poddar, Rakesh; Li, Chunzeng; Kumar, Ravi; Papastavrou, Georg; Retsch, Markus; Brunschwig, Bruce S.; Huang, Zhuangqun; Xiang, Chengxiang; Boettcher, Shannon W.  
"Atomic force microscopy with nanoelectrode tips for high resolution electrochemical, nanoadhesion and nanoelectrical imaging"  
*Nanotechnology* **2017**, *28*, 095711.
10. Vega-Flick, Alejandro; Duncan, Ryan A.; Wallen, Sam P.; Boechler, Nicholas; Stelling, Christian; Retsch, Markus; Alvarado-Gil, Juan J.; Nelson, Keith A.; Maznev, Alexei A.  
"Contact-based and spheroidal vibrational modes of a hexagonal monolayer of microspheres on a substrate"  
*Wave Motion* **2017**, *76*, 122-133.

## List of Contributions

1. Stelling, Christian; Singh, Chetan R.; Karg, Matthias; König, Tobias A. F.; Thelakkat, Mukundan; Retsch, Markus.  
Oral presentation: “Plasmonic Nanomeshes in Organic Solar Cells: a Fundamental Dilemma“  
Australian Colloid and Interface Symposium (**2017**), Coffs Harbour, Australia
2. Stelling, Christian; Mark, Andreas; Papastavrou, Georg; Retsch, Markus.  
Poster presentation: “Electrostatic Particle Immobilization in Gold Nanomeshes“  
Australian Colloid and Interface Symposium (**2017**), Coffs Harbour, Australia
3. Stelling, Christian; Mark, Andreas; Papastavrou, Georg; Retsch, Markus.  
Poster presentation: “Electrostatic Particle Immobilization in Gold Nanomeshes“  
International Conference on Self-Assembly in Confined Spaces (**2016**), San Sebastián, Spain
4. Stelling, Christian; Retsch, Markus.  
Poster presentation: “Functional Mesostructures by Colloidal Self-Assembly“  
26<sup>th</sup> European Doctoral School on Metamaterials (**2014**), Jena, Germany



## Danksagung

An dieser Stelle möchte ich mich bei allen bedanken, die durch ihre Unterstützung zum Gelingen dieser Arbeit beigetragen haben.

Zunächst gilt mein Dank meinem Doktorvater Prof. Dr. Markus Retsch für die Möglichkeit an diesem spannenden Projekt arbeiten zu dürfen, die intensive Betreuung aber auch die Freiheit, eigene Projekte verfolgen zu können.

Ich danke allen meinen Kooperationspartnern, allen voran Prof. Dr. Mukundan Thelakkat, Andreas Mark, Miriam Hummel und Chetan R. Singh für die tolle Arbeit und viele erhellende Diskussionen, ohne die diese Arbeit nicht möglich gewesen wäre. Fabian Nutz danke ich außerdem für Synthese der Polystyrol dispersionen.

Ein großes Dankeschön an alle meine Praktikanten Tanja Feller, Anne Weckwerth, Sven Dietler, Andreas Karg, Tobias Lauster, Marius Schöttle, Kai Herrmann und Felix Wenzel sowie an meine Hiwis Flora Bitterlich und Sebastian Goller, die mir sehr viel, oft frustrierende Arbeit abgenommen haben.

Thanks to Jacek Jasieniak for giving me the possibility to join his research group at Monash University and to his group for the warm welcome and the great support during my visit.

Mein Dank gilt auch dem Elitenetzwerk Bayern für die finanzielle und ideelle Förderung.

Ein großes Dankeschön auch an Elisabeth Düngfelder und Jennifer Hennessy für die immer sehr zuvorkommende Hilfe bei administrativen Dingen, an Stephan Hauschild für die Unterstützung in IT-Fragen und an Karlheinz Lauterbach und Julia Moßner für die stete Versorgung mit Gasflaschen und die nicht selbstverständliche Chemikalienentsorgung. Zudem danke ich Martina Heider und Beate Förster für die Unterstützung an den Elektronenmikroskopen sowie Markus Hund für die Hilfe am Rasterkraftmikroskop und mit der Aufdampfanlage.

Allen Mitarbeitern des Lehrstuhls PC1 danke ich für die tollen Jahre und die angenehme Atmosphäre innerhalb und außerhalb der Uni. Besonders die Abende in der Confiserie Klein werden mir in Erinnerung bleiben. Danke Jenny! Vielen Dank vor allem an meine Laborkollegen Tobias Honold, Andreas Karg, Tobias Lauster, Steffen Dütz und ganz besonders Patrick Hummel für das sehr angenehme Arbeitsklima und die vielen lustigen Momente.

Vielen lieben Dank dir, Kirsten, für die viele Geduld und Unterstützung, vor allem an langen Abenden im Labor!

## Danksagung

---

Ganz besonders danken möchte ich zum Schluss meiner Familie, die mich während meines gesamten Studiums unterstützt und mir in jeder Hinsicht den Rücken frei gehalten hat.

## **(Eidesstattliche) Versicherungen und Erklärungen**

(§ 8 Satz 2 Nr. 3 PromO Fakultät)

*Hiermit versichere ich eidesstattlich, dass ich die Arbeit selbständig verfasst und keine anderen als die von mir angegebenen Quellen und Hilfsmittel benutzt habe (vgl. Art. 64 Abs. 1 Satz 6 BayHSchG).*

(§ 8 Satz 2 Nr. 3 PromO Fakultät)

*Hiermit erkläre ich, dass ich die Dissertation nicht bereits zur Erlangung eines akademischen Grades eingereicht habe und dass ich nicht bereits diese oder eine gleichartige Doktorprüfung endgültig nicht bestanden habe.*

(§ 8 Satz 2 Nr. 4 PromO Fakultät)

*Hiermit erkläre ich, dass ich Hilfe von gewerblichen Promotionsberatern bzw. –vermittlern oder ähnlichen Dienstleistern weder bisher in Anspruch genommen habe noch künftig in Anspruch nehmen werde.*

(§ 8 Satz 2 Nr. 7 PromO Fakultät)

*Hiermit erkläre ich mein Einverständnis, dass die elektronische Fassung der Dissertation unter Wahrung meiner Urheberrechte und des Datenschutzes einer gesonderten Überprüfung unterzogen werden kann.*

(§ 8 Satz 2 Nr. 8 PromO Fakultät)

*Hiermit erkläre ich mein Einverständnis, dass bei Verdacht wissenschaftlichen Fehlverhaltens Ermittlungen durch universitätsinterne Organe der wissenschaftlichen Selbstkontrolle stattfinden können.*

.....  
Ort, Datum, Unterschrift